Probing the Mechanisms of Action and Resistance of Mixed-ligand Platinum(II) Complexes with Dual-stage Antiplasmodium Activity

Fatima-Zahra Ishmail

Thesis presented for the degree of

DOCTOR OF PHILOSOPHY

in the Department of Chemistry

UNIVERSITY OF CAPE TOWN

Supervisors

Professor Kelly Chibale, Dr Kathryn Wicht, Dr John Woodland, and the late Professor Timothy Egan

May 2024

Declaration

Probing the Mechanisms of Action and Resistance of Mixed-ligand Platinum(II) Complexes with Dual-stage Antiplasmodium Activity

I, Fatima-Zahra Ishmail, declare the following:

1. That all the work reported in this thesis titled above is my own, both in concept and execution, apart from the normal guidance of my supervisors.
2. That where input from others is provided, they are acknowledged.
3. That where the work of others is cited in this thesis, it is acknowledged and referenced.
4. That none of the above-titled thesis has been, is being, or is to be submitted for another degree at the University of Cape Town or any other university.
5. I grant the University of Cape Town a free license to reproduce this work, in whole or in part, for research.

I hereby present this thesis for examination for the degree of Doctor of Philosophy (PhD) in Chemistry.

Signed at the University of Cape Town on 25 April 2024.

Signed by candidate

Candidate signature:
Fatima-Zahra Ishmail

Dedication

In memory of Professor Timothy Egan, who started this academic journey with me but sadly could not walk me over the finish line.

Though not physically here, your wisdom and love for science can be seen in every idea and finding within the pages of this thesis. Your passion for knowledge and dedication to sharing all that you know have been an inspiration and the fuel I needed to keep going. Through your mentorship, I have learned to persevere, to carry myself with integrity and to strive for scientific excellence.

Though you are no longer with us, you have left a scientific legacy that lives on in all the lives that you have touched through your teaching. You have also left an unforgettable mark in the malaria field, which will be an inspiration for generations to come. This thesis is only but a small tribute to your influence and passion for science. This work is also a testament to the impact that you have had on my journey as a young scientist.

I thank you, for always having an open-door policy and approaching every question as an opportunity to enthusiastically discuss science. You were never judgmental of what I did or did not know. I thank you for allowing me to learn under your mentorship and for believing in me.

Acknowledgments

Professor Timothy Egan- Thank you for allowing me to work on this project and for always having an open-door policy. Thank you for your positive thinking and your ability to make no problem seem unsolvable. I am grateful for your constant willingness to sit down and talk through the scientific roadblocks rationally. You have taught me to think independently as a scientist and to strive to produce research of the highest standards. Thank you for your mentorship and for making sure that all the necessary support systems are in place in your absence.

Professor Kelly Chibale- Thank you for your mentorship and for providing me with all the tools and resources needed to complete my PhD. Thank you for allowing me to be a part of your research group and for making it a comfortable and non-judgmental space for learning and growing as a young scientist. You have been a role model and an inspiration, and I cannot express my gratitude enough. You have created a space in your academic group where we as students have access to countless resources, webinars, seminars, and workshops that have allowed me to grow exponentially and have opened my mind tremendously as a scientist. I appreciate your guidance and your constant encouragement to be a better scientist. The motivational talks you have given me in our one-on-one meetings will forever be something I will reflect on in moments of doubt.

Dr Kathryn Wicht- Thank you for your support and for imparting your knowledge to me during my PhD. journey. You have pushed me to do my best and to try again after countless failed experiments. Thank you for being hands-on and patient in the cell culture lab as I learned new assays. I am grateful for your calmness and reassurance, which made culturing clones easier. Thank you for the countless sit-downs and words of encouragement. You have been an inspiration for women in science and I am truly grateful to have been mentored by you.

Dr John Woodland- Thank you for adding a deeper level of thought to this project, you have pushed me to enhance my understanding and to think beyond the surface. Thank you for always encouraging me to take the initiative and adding some much-needed humor and/or puns (in the form of a comment) to my progress reports and chapter drafts. These were always appreciated and a mood uplifter. Thank you for your patience and willingness to help throughout my PhD journey. I am grateful for your illuminating enthusiasm and positivity that have made this PhD. easier.

The Haem Team- Dr Roxanne Mohunlal, Larnelle Garnie, Leah Amod, Nicole Teixera, Ghannish Soogary, and Keletso Maepa, you have all been so much more than just lab mates. Thank you for your friendship and for making my PhD years even more enjoyable! Thank you for all the fun discussions, lunches, and support you all have given me that contributed significantly to my sanity.

KC academic group and H3D- To all past and present members of the KC academic group and H3D team, thank you for all your help and support in the synthesis lab. Our interactions were vital to my growth as a scientist, and I am grateful to have had the opportunity to work with and learn from you all.

Ferdinand Ndubi- Thank you for your friendship, our many discussions about life that took my mind off the chemistry, and for always sharing your fruit during lunch.

Natalia Shakela- My “sister twin”, there aren't enough words to express my gratitude for you and our friendship. Throughout this journey you have been more than just my friend, you have been my support system, my cheerleader, and the voice of kindness. Beyond the academic space, your friendship has been a source of pure joy. Whether it was celebrating the small victories or surviving the many synthetic storms together, your presence has made this journey all the more meaningful.

Dr Godwin Dziwornu- To merely say thank you, will not do justice to your mentorship and friendship. Nonetheless, thank you for taking me under your wing and sharing your knowledge and synthetic tricks with me. Your encouragement and belief in me have motivated me and pushed me to strive for success even when the challenges seemed too big. Your willingness to listen to my ideas and your insightful feedback has undoubtedly added to the quality of my work in this thesis. Thank you for being a support system during some of the most difficult times.

Sarah Harries- Thank you for your friendship, support, and help during the gDNA extraction of my resistant clones.

Other contributors

Thank you to my funders: NRF, Harry Crossley, KW Johnston Bequest, and Kelly Chibale for providing me with financial support to complete my PhD.

Thank you to members of the ADME and DMPK groups at H3D for running the solubility, microsomal metabolic stability, permeability, plasma protein binding, and pharmacokinetic studies reported in this thesis.

Thank you to Professor Lyn-Marie Birkholtz, Dr Dina Coertzen, and Sizwe Tshabalala for running the SYBR Green and gametocyte activity whole-cell assays reported in this thesis.

Thank you to Professor David Fidock and his team at Columbia University for conducting the whole-genome sequencing experiments reported in this thesis.

I am grateful to the admin staff, Deidre Brooks, Joanne Polzin, Deidre Van Rooyen, Elaine Rutherfoord-Jones, Marché Jaftha, and Melony Geldenhuys for their assistance.

Family members

To my parents, Shireen and Emeraan Ishmail, thank you for giving me the best education and for always believing in me. For always supporting me and smothering me with unconditional love. Thank you for teaching me to be a go-getter and to never give up in the face of difficulties.

To my husband, Muhammad Jawad Abrahams, thank you for your unwavering support and encouragement. It has been a difficult 4.5 years, filled with challenges and grief but you have taught me to be resilient, strong, and to persevere. Thank you for being a pillar of strength and for always being patient and kind. You have been a voice of reason and a sounding board when I needed one most. You have taught me that every problem has a solution. Thank you for listening to me talk about synthesis and cell culturing as though you completely understood. Lastly, thank you for accompanying me to campus on the weekends and public holidays and for sacrificing for me and with me. I am grateful to be able to do life with you.

Conferences

1. Keystone Symposium, D2 Malaria: Confronting Challenges from Drug Discovery to Treatment. Beaver Run Conference Center, Breckenridge, Colorado, USA (10th – 13th April 2022)
2. H3D symposium, A Spectrum of Opportunities in Infectious Disease Drug Discovery to Enhance Global Health. Webersburg Estate, Stellenbosch, South Africa (25th – 13th October 2022)
3. Young Chemists' Symposium, University of Western Cape, South Africa (15th September 2023)

Abstract

Malaria remains one of the largest parasitic disease burdens worldwide, with the vast majority of that burden occurring on the African continent. The ongoing high number of malaria cases and deaths is in part attributable to the emergence and spread of resistance to most clinical chemotherapeutics. With the reported development of partial resistance to the current front-line artemisinin-based combination therapies, there is an increased risk of malaria morbidity and mortality as limited replacement treatments are currently available. For that reason, it is essential to invest in the discovery of compounds with novel mechanisms of action (MoA), dual-stage activity, and with immutable targets. Until now, drug discovery has typically focused on the development of antimalarials that are entirely organic in composition. This has left the field of inorganic medicinal chemistry and transition metal-based chemotherapeutics underexplored and underrepresented.

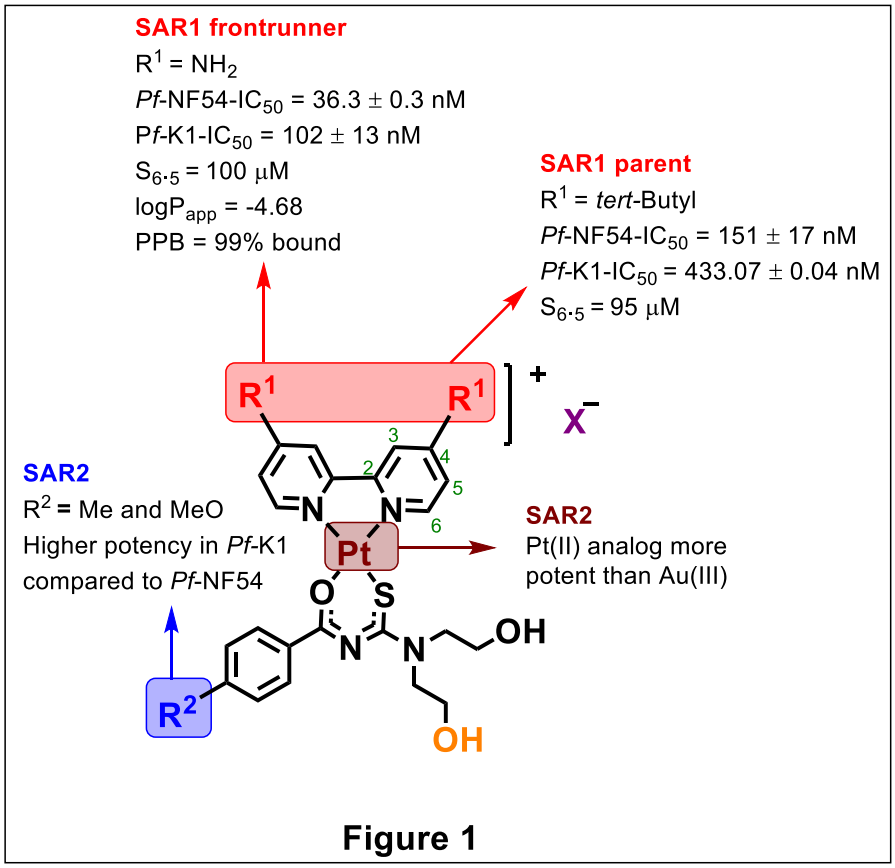

Figure 1

This thesis focuses on further expanding the atomic repertoire of antimalarials to transition metal complexes to identify compounds with dual-stage activity and novel MoA. Several

mixed-ligand platinum(II) complexes and one gold(III) complex were synthesized. Six chemical modifications were explored, and the structure-activity relationships (SARs) and structure-property relationships (SPRs) of those changes were evaluated to identify the most efficacious and non-toxic analogs.

Analysis of the SAR of these platinum(II) complexes revealed that whole-cell potency in the asexual blood stage (ABS) was driven by the presence of an electron-donating substituent in the 4,4-position of the bipyridine ligand. The majority of the complexes had IC_{50} values below 1 μM against both the chloroquine-sensitive (*Pf*-NF54) and multidrug-resistant (*Pf*-K1) strains. Substituting the 4,4-position on the bipyridine with an amine, as shown in **Figure 1**, yielded a four-fold increase in potency compared to the *tert*-butyl analog. Further SAR analysis suggested that substitution with a methyl in the 5,5'-position of the bipyridine was favored over the 4,4'-position. For the exchange of the transition metal from platinum(II) to gold(III) in a *tert*-butyl substituted analog, a decrease of 25-fold was observed for whole-cell potency. This suggested that, at least for the tested analog, a platinum(II) center was favored for antiplasmodium potency. Five of the synthesized derivatives displayed dual-stage activity with a *tert*-butyl substituent in the R^1 position giving rise to analogs with the highest gametocyte potency. The complexes also exhibited no significant cytotoxicity against the Chinese hamster ovarian cell line (selectivity index > 10) and demonstrated good solubilities ($S_{6.5}$ > 90 μM).

Compounds with appreciable *in vitro* ABS activity and good solubility were progressed to microsomal metabolic stability studies in which a range of stabilities was observed in both human liver microsomes (HLM, 24–72% remaining after 30 minutes of incubation) and mouse liver microsomes (MLM, 33–94% remaining after 30 minutes of incubation). However, the complexes were generally more stable in MLM than in HLM. A frontrunner complex ($R^1 = NH_2$, **4f**) with excellent whole-cell potency, solubility, and microsomal metabolic stability in MLM was probed for its *in vivo* pharmacokinetic (PK) parameters, *in vitro* apparent permeability ($logP_{app}$), and plasma protein binding capacity. A disconnect between the high *in vitro* ABS potency and the *in vivo* PK analysis of complex **4f** was observed, which was rationalized by the low volume of distribution and high plasma protein binding of this complex.

With the planar geometry of these complexes as the rationale for the MoA studies, it was hypothesized that they might inhibit the formation of hemozoin through π-π stacking interactions. To this end, their capacity to inhibit the synthetic form of hemozoin (β-hematin) was first determined in an extracellular detergent-mediated β-hematin inhibition assay. The complexes displayed comparable or superior inhibition of β-hematin formation activities to the positive control compound, chloroquine. Subsequently, two complexes were selected for the

cellular heme fractionation assay in which both complexes were observed, surprisingly, not to inhibit hemozoin formation in the parasite.

Lastly, resistance selections were conducted using two prioritized complexes to further probe their mechanism of resistance (MoR) and possible MoA. Recrudescence occurred after 17 days in one of the flasks under drug pressure from 3 x IC_{50} of **4f**. Whole-genome sequencing identified several copy number variations (CNVs) and single nucleotide polymorphisms (SNPs) either shared by the four isolated clones or unique to each clone. Most notably, these CNVs and SNPs suggested that resistance was likely driven by the *Pf*-multidrug-resistance 1 (*Pfmdr1*) in three of the clones or SNPs of kinesin-13 for the most resistant clone. While *Pfmdr1* amplifications are a well-known mechanism of resistance (MoR), kinesin-13 is novel and has not been reported in the literature as a potential MoR or validated *Plasmodium* target.

The dual-stage potency displayed by a subset of compounds and the high susceptibility of the *Pf*-K1 strain to the SAR2 complexes discussed in this thesis provides a basis for further optimization of this chemical series. Hence, additional chemical modifications could be made to fine-tune the chemical space for improved potency and pharmacological properties of this chemical series. Furthermore, successful resistance selections have led to the identification of a novel MoR (kinesin-13). Thus, future work could explore the plausibility of kinesin-13 as a druggable target for antiplasmodium agents, in which supplementary genetic approaches could be employed.

List of Abbreviations

ABS- Asexual blood-stage

ACT- Artemisinin-based combination therapy

ADME- Adsorption, distribution, metabolism and excretion

AEEA- *N*-amino-ethyl-ethanolamine

AL- Artemether-lumefantrine

AM- Artemether

ART- Artemisinin

AS- Artesunate

ATR-FTIR- Attenuated total reflection-Fourier transform infrared

BC- Before Christ

Bpy- Bipyridine

CAR- Cellular accumulation ratio

CHO- Chinese hamster ovarian

CL_{int}- Intrinsic clearance

CL_s- Clearance

COD- 1,5-Cyclooctadiene

CQ- Chloroquine

CQR- Chloroquine-resistant

CQS- Chloroquine-sensitive

CV- Cyclic voltammetry

CYP450- Cytochrome P450

DCM- Dichloromethane

dfppy- 2-(2,4-difluorophenyl)pyridine

DFR- Dihydrofolate reductase

DHA- Dihydroartemisinin

DHPS- Dihydropteroate synthase

DMF- Dimethylformamide

DMSO- Dimethyl sulfoxide

DV- Digestive vacuole

EG- Early-stage gametocytes

Et_3N- Triethylamine

EtOH- Ethanol

F- Bioavailability

FQ- Ferroquine

HAP- Histoaspartic protease

HATU- Hexafluorophosphate azabenzotriazole tetramethyl uranium

HCT- Hematocrit

HIV- Human immunodeficiency virus

HLM- Human liver microsomes

HMBC- Heteronuclear multiple bond correlation

HPLC- High-performance liquid chromatography

HSAB- Hard and soft acid and base

HSQC- Heteronuclear single quantum coherence

HTS- High-throughput screening

i.v.- Intravenous

IC_{50}- Half-maximal inhibitory concentration

ITNs- Insecticide-treated nets

LG- Late-stage gametocytes

MB- Methylene blue

MDR- Multidrug-resistant

MeCN- Acetonitrile

MeOH- Methanol

MLM- Mouse liver microsomes

MMS- Microsomal metabolic stability

MMV- Medicines for Malaria Venture

MMV048- MMV390048

MoA- Mechanism of action

MoR- Mechanism of resistance

MS- Mass spectrometry

MT- Microtubule

NA- Not applicable

NBD- 4-nitrobenzo-2-oxa-1,3-diazole

ND- Not determined

NDP- No drug pressure

NMR- Nuclear magnetic resonance

P- Parasitemia

p.o.- per oral

PAMPA- Parallel artificial membrane permeability assay

P_{app}- Apparent permeability

pbt- 2-phenylbenzothizole

Pf- Plasmodium falciparum

PGMs- Platinum group metals

PI4K- Phosphatidylinositol 4-kinase

PK- Pharmacokinetic

pLDH- *Plasmodium* lactate dehydrogenase

PPB- Plasma protein binding

pq- 2-phenylquinoline

pRBCs- Parasitized red blood cells

Pv- Plasmodium vivax

RBCs- Red blood cells

RI- Resistance index

ROS- Reactive oxygen species

SAR- Structure-activity relationship

SI- Selectivity index

SP- Sulfadoxine-pyrimethamine

SPR- Structure-property relationship

$T_{1/2}$- Half-life

TB- Tuberculosis

V_{frac}- Fractional volume

V_{ss}- Steady-state volume of distribution

WGS- Whole-genome sequencing

WHO- World Health Organization

βH/ βHI- β-hematin/ β-hematin inhibition

Contents

Chapter 1: Introduction and Literature Review

1.1. Chapter overview

Malaria is a life-threatening disease that has placed a huge burden on the world and, more specifically, on the African continent's health system and its economy. It has caused centuries of suffering, despite continuous attempts to reduce the disease burden and eradicate the disease. Over the decades, many resources and much research have gone into discovering new ways to control and eradicate malaria through pesticides, mosquito nets, vaccines, and chemotherapies. This chapter will provide the overall context for this thesis related to malaria and the search for novel treatments.

1.2. History of malaria and its disease burden

Malaria is one of the world's oldest infectious diseases and has posed an enormous global burden for centuries.[1] Historic artifacts such as Mesopotamian clay tablets, Egyptian remains, and Indian writings dated 1500–800 BC, have shown evidence of the disease being prevalent in the pre-modern era.[2] It is caused by unicellular protozoa of the *Plasmodium* genus,[3] and affects several vertebrates including reptiles, birds, and humans.[4] To date, over 200 *Plasmodium* species that infect several host species have been identified.[5] Within these 200 species, only five infect humans, with *Plasmodium falciparum* (*Pf*) and *Plasmodium vivax* (*Pv*) being the most virulent.[6,7]

The malaria parasite was first discovered in 1880 by Alphonse Laveran.[8] Almost two decades later, in 1897, Ronald Ross identified mosquitos as the vectors responsible for transmitting infection amongst birds.[9] Subsequently, one year later, Italian scientists found that human malaria was also transmitted via mosquito vectors.[9] From here, the life cycle of the parasite was elucidated, starting with Henry Shortt and Cyril Garnham who discovered the liver schizont stage of *Plasmodium cynomolgi* in a Rhesus monkey in 1947.[10] The sexual stages of the parasite life cycle were discovered by William MacCallum in 1897 when he was studying birds infected with parasites in their blood.[11] Lastly, the final stages of the life cycle were discovered by Wojciech Krotoski in 1982.[9]

Despite malaria being a worldwide concern, most of the disease burden falls on the African continent which has the highest morbidity and mortality rates. The latest World Malaria Report, published in 2023 by the World Health Organization (WHO), states that there was a global increase of five million malaria cases in 2022 compared to 2021. The death toll was also up by 6% at 608 000 deaths in 2022.[12] This is further depicted in the incidence map shown in **Figure 1.1** where a high occurrence of malaria was still seen in 2023 and most significantly in economically poor countries, mainly in the Global South.

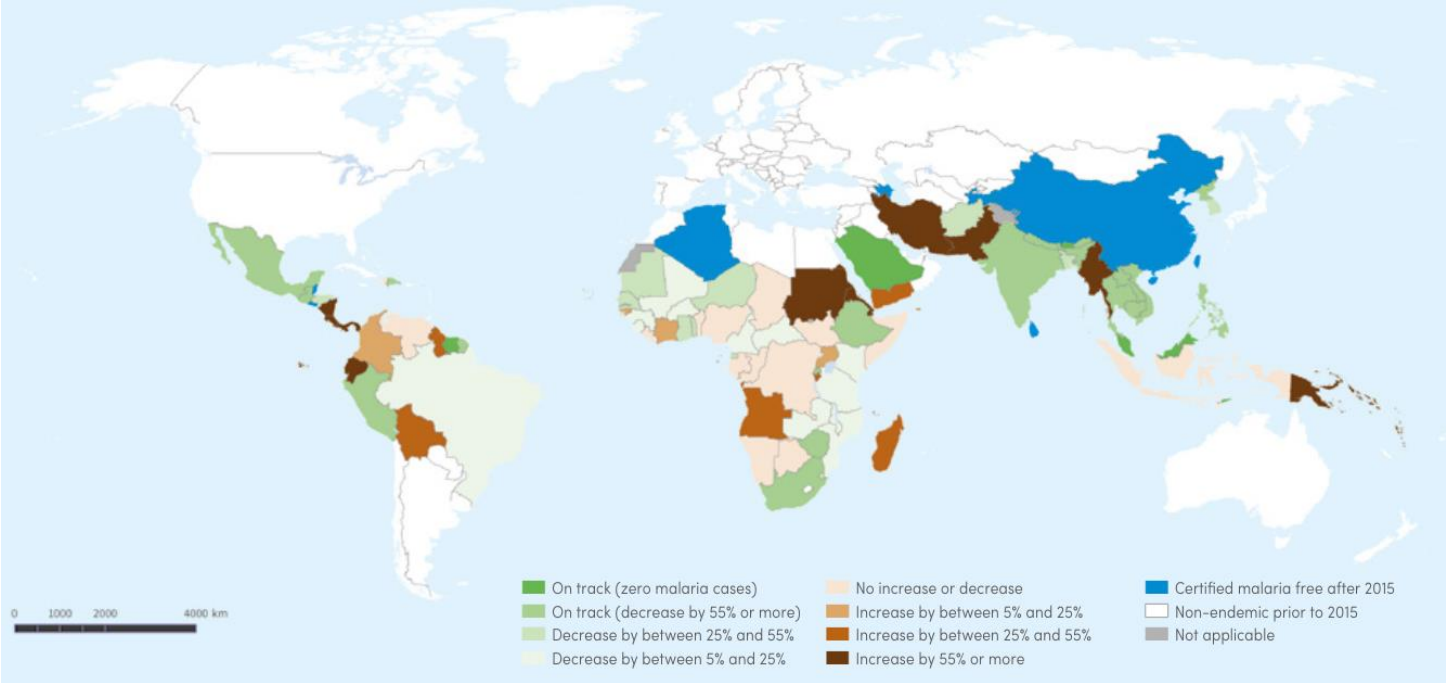

Figure 1.1. World map of malaria-endemic countries showing the progress made since 2015 towards the GTS (Global Technical Strategy 2016–2030). Republished from the 2023 World Malaria Report.[12]

1.3. The malaria parasite life cycle and molecular drug targets

1.3.1. Life cycle

The malaria parasite progresses through several stages during its life cycle. Transmission from the mosquito vector begins when a female *Anopheles* mosquito takes a blood meal from a human host, injecting sporozoites into the host's bloodstream as shown in **Figure 1.2**.[13] These sporozoites migrate to the liver, where they undergo mitotic replication in hepatocytes. The liver cells then rupture, releasing merozoites into the bloodstream which enter the asexual blood stage (ABS) or the sexual stage of the life cycle. The ABS occurs in red blood cells (RBCs) where merozoites sequentially develop into the ring stage, trophozoite stage, and then the schizont stage. Merozoites are released when the RBCs rupture and proceed to infect other healthy RBCs. During the sexual stage of the life cycle, the ring form of the parasite develops into female and male gametocytes of which there are early-stage (EG) and late-stage gametocytes (LG). During this sexual stage, the parasite goes through a seven-to-ten-day maturation period during which the gametocytes progress from stages I to V, occupying RBCs as well.[14] Thus, stages I to IV are considered immature or early-stage gametocytes, and stage V parasites are considered mature or late-stage gametocytes. To complete the life cycle, LGs are ingested by the mosquito vector during another blood meal after which these gametocytes undergo gametogenesis producing male and female gametes. The fusion of a male and female gamete results in the formation of a zygote after which mitotic division occurs, prompting the sequential development into ookinetes, oocytes, and sporozoites.[15] These sporozoites migrate to the mosquito's salivary glands where the transmission to the human host occurs again.[14]

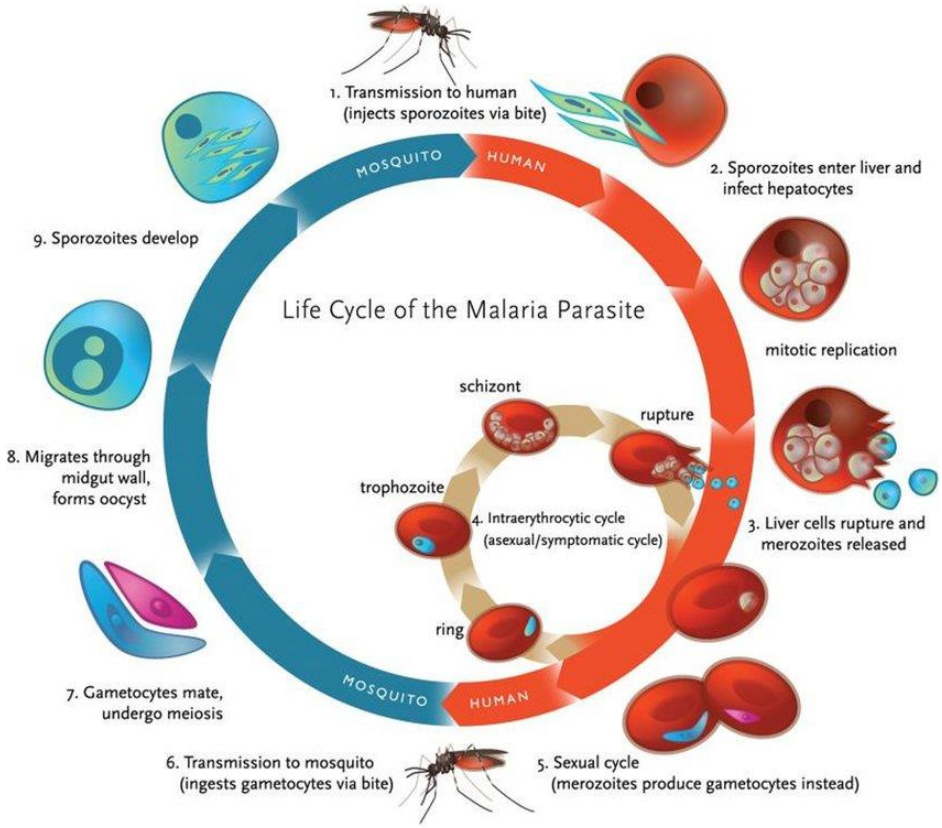

Figure 1.2. *Plasmodium* life cycle. Republished from Vale *et al.* under the Creative Commons Attribution license (CC BY), Copyright (2024).[13]

1.3.2. Antimalarial drug targets

Liver stage

During the pre-erythrocytic stage of the parasite life cycle, sporozoite development and migration can be blocked at each step using chemoprophylaxis as shown in **Figure 1.3**.[16] Chemoprophylaxis involves the administration of a drug to prevent disease development.[17] Drugs that have been approved to be clinically used against the liver stage include atovaquone-proguanil, sulfadoxine-pyrimethamine, primaquine, and tafenoquine.[18] Although the MoA of many of these drugs during the liver stage is largely unknown,[19] primaquine has been shown to act via the generation of hydroxylated-primaquine metabolites which ultimately lead to the production of toxic reactive oxygen species (ROS); namely, H_2O_2.[20]

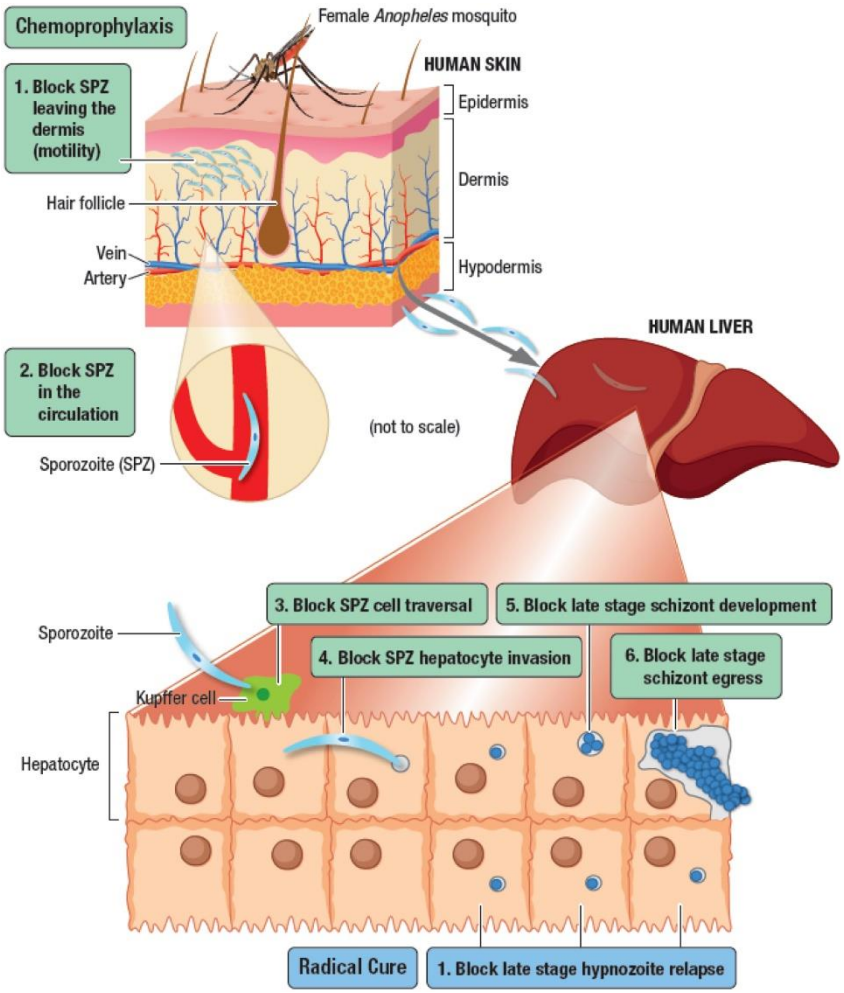

Figure 1.3. The pre-erythrocytic stage of the *P. falciparum* and *P. vivax* life cycle. The image shows that each step of the liver stage can be targeted using chemoprophylaxis as shown in green boxes. Republished from Valenciano *et al*. under the Creative Commons Public Domain Mark 1.0 copyright.[16]

Additionally, studies have shown that drugs targeting kinases such as the adenosine monophosphate-activated protein kinase (AMPK) reduce hepatic infection.[21, 22] Furthermore, a study by Stanway *et al*. identified metabolic subsystems that could be potential drug targets. These included the type II fatty acid synthesis and elongation pathways as well as the tricarboxylic acid, amino sugar, heme, lipoate, and shikimate metabolic processes.[23]

Asexual blood stage (ABS)

Many of the clinically-available antimalarial drugs inhibit only the ABS. The major metabolic pathways that are targeted by most of these drugs include oxidative stress, fatty acid synthesis, nucleic acid synthesis, and heme detoxification.[24] During the trophozoite ABS, approximately 80% of host hemoglobin is ingested through the cytostome which transports it into the parasite digestive vacuole (DV) as shown in **Figure 1.4**.[25] In the DV, proteolytic enzymes (plasmepsin I, II, and IV, histoaspartic protease (HAP), falcipains 2 and 3, and falcilysin) break down hemoglobin into small peptides used for nutrients, and toxic free heme.[26,27] For each molecule of hemoglobin digested, four heme molecules are liberated.

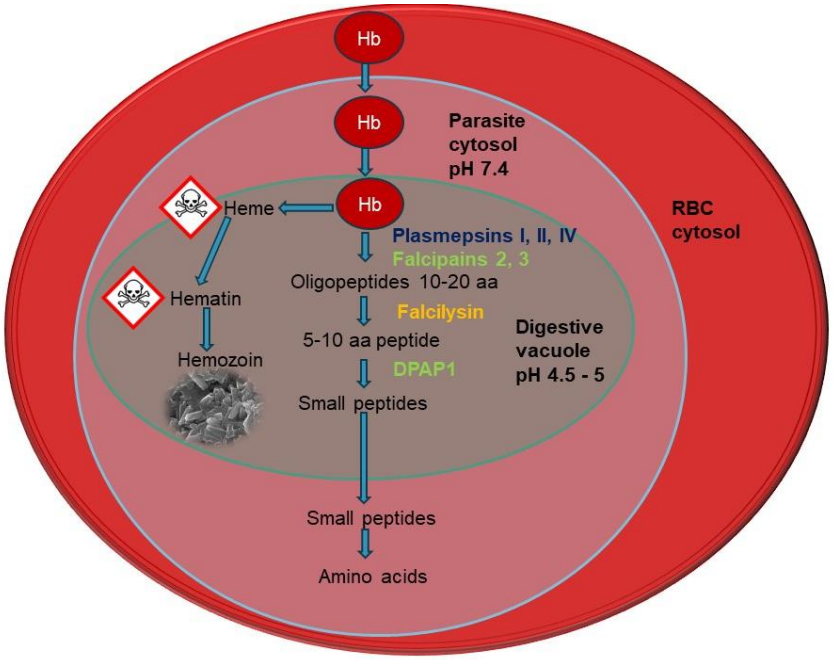

Figure 1.4. The hemoglobin degradation process that takes place in the parasite's digestive vacuole converts toxic heme into crystalline hemozoin. The relevant enzymes that facilitate this process are shown as well as the pH differences between each cellular compartment. Abbreviation: aa- amino acids.

Therefore, to avoid lipid peroxidation and subsequent death, the parasite converts free heme into the inert, non-toxic biomineral, hemozoin.26 In the presence of an inhibitor of hemozoin formation, such as chloroquine, redox-active toxic heme accumulates, producing detrimental amounts of ROS and resulting in DNA damage.27 The mechanism of hemozoin formation has been debated extensively but the prevailing theory is that it occurs via lipid-mediated biocrystallization.[29,30] Additionally, hemozoin can also be synthesized *in vitro* by incubating

monomeric hematin (at 37 °C and pH 4.8) to produce its synthetic form, β-hematin,[27] which is chemically and spectroscopically identical to hemozoin.[31] Concerning known inhibitors of hemozoin formation, the most prominent class of antimalarials with this MoA are the quinolines,[27] which are further discussed in **Section 1.4.2.1**.

Sexual stage: Production of gametocytes

The sexual stage of the parasite life cycle involves the production of gametocytes which are essential for transmitting the parasite from the human host back to the mosquito vector.[32] As mentioned above, there are five stages (I-V) of the gametocyte life cycle.[33] Each stage is morphologically distinct as shown in **Figure 1.5**, with stages I-IV sequestered in the bone marrow and stage V circulating in the blood vessels.[34] **Figure 1.5** also shows the stage-specific protein expression highlighting their potential as drug targets. *Pfs*16, with an unknown function, is expressed during both EG (I-V) and LG (V). It has been reported that disruption of this protein leads to decreased gametocyte production and the ability of male gametes to exflagellate.[35] Additionally, disruption of the gene encoding for the PfMDV-1 protein, also with unknown function, decreases the production of male gametocytes.[36]

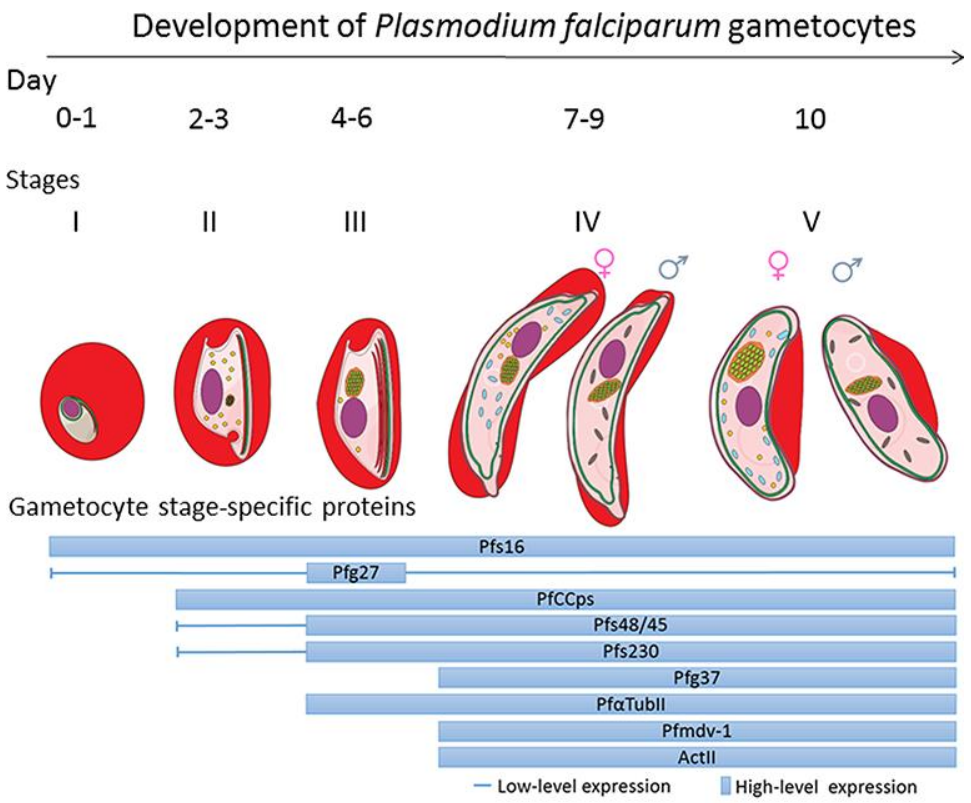

Figure 1.5. *P. falciparum* gametocyte morphology and stage-specific protein expression, highlighting them as potential targets. The bar represents that the protein is expressed at high levels during the respective stage and the full line indicates low levels of expression. Reproduced from Ngwa *et al.* under the Creative Commons Attribution 3.0 Unported License.[34]

Furthermore, Abugri *et al*. provide a summary of potential targets for gametocyte drug discovery, some of which are discussed here.[37] Hitz *et al*. highlighted the importance of PfCK2α (casein kinase 2) for the maturation of gametocytes, making it a potential drug target.[38] Additionally, Baker *et al*. report on another *P. falciparum* protein kinase G, PfPKG, which was found to be a target of the gametocyte stage in their study.[39]

Despite there being several possible targets during the gametocyte stage, there are only a small number of compounds with reliable gametocytocidal activity. Only primaquine is currently clinically recommended by the WHO.[40] However, with the help of high-throughput screening (HTS) and the development of assays that screen for compounds with gametocyte activity, new transmission-blocking compounds have been identified from both the Medicines for Malaria Venture (MMV) library,[41,42] and other diverse library sets.[43,44]

Following the above discussion, the past and present methods and drugs used to treat malaria are discussed in detail in the next section, highlighting their stage specificity and MoA.

1.4. Malaria treatment and resistance

1.4.1. Treatment

Over the many years that malaria has been a threat to the global health system, tremendous efforts have been made to treat and eradicate the disease. This includes the use of insecticides, mosquito nets, vaccines, and chemotherapeutics.

The use of insecticide-treated nets (ITNs) over beds and indoor residual spraying (IRS) has been employed to prevent malaria transmission and infection.[45,46] Both methods employ the use of insecticides and are used for vector control. Additionally, ITNs act as a physical barrier between the host and the vector and are treated with a chemical that is toxic to mosquitoes. Only two chemical insecticides have been approved for use in ITNs, namely pyrroles and pyrethroids. These insecticides either kill the mosquito or disorientate it, reducing its ability to effectively find and feed on a human host.[47] When used community-wide, ITNs have been shown to not only offer personal protection against mosquito bites, but can also decrease the survival rate, frequency of feeding, and the overall density of mosquitos in the community.[48,49] However, this method is not completely preventative, as it is mainly only used at night while sleeping, and general wear and tear of the net can leave the host vulnerable if not properly maintained.

An additional form of prevention, recommended by the WHO, is the use of a malaria vaccine. The development of a malaria vaccine began in the 1960s with seminal studies conducted in mice using irradiated sporozoites (sporozoites inactivated with UV light).[50] Significant progress has been made since then, leading to the prequalification of the RTS,S/AS01 (pre-erythrocytic) vaccine for *P. falciparum* prevention in children living in areas with moderate to high malaria transmission.[51] RTS,S/AS01 is a recombinant protein vaccine that targets the circumsporozoite protein and was approved by the WHO for use in children aged 5 to 17 months.[52] This marked the first recommended use of a malaria vaccine by the WHO.

A second malaria vaccine, R21/Matrix-M, was developed at the University of Oxford and is also a pre-erythrocytic candidate vaccine. It is a virus-like particle comprised of HBsAg (hepatitis B surface antigen) fused to the C-terminus and central repeats of the circumsporozoite protein.[53] Phase III clinical trials have shown that the R21/Matrix-M vaccine has a 75% efficacy against clinical malaria,[51] and has also received prequalification by the WHO.[54]

These vaccines induce a cellular immune response that effectively prevents the development of liver schizonts in the short term. However, constant rupturing of single schizonts can still lead to the progression of the parasites to the blood stage, resulting in severe infection or death.[55] Thus the use of chemotherapeutics is still important in the fight against malaria as no effective vaccine has been developed against the blood stage yet. Thus, the extensive repertoire of drugs developed and used as chemotherapeutics is discussed in the next section.

1.4.2. Malaria chemotherapeutics

Four major classes of drugs are used to treat malaria; namely, quinoline-based compounds, antifolates, artemisinin derivatives, and antimicrobials.

One of the very first drugs used to treat malaria was quinine (**Figure 1.6**), which is historically one of the first chemical compound to treat an infectious disease.[56] Quinine is naturally found in the bark of *Cinchona* trees,[57] and was primarily used as an antimalarial up until the 1920s when more effective treatments were discovered.[56] Furthermore, attempts to synthesize quinine were unsuccessful but paved the way for German chemists to discover new antimalarials based on quinine's chemical structure.[58] Consequently, methylene blue (MB, **Figure 1.6**) was introduced as the first synthetic antimalarial in 1891 by Guttmann and Ehrlich.[59] However, due to the toxicity of MB, further investigation and modification of the chemical scaffold was necessary and led to the discovery of 8-aminoquinolines,[60] as discussed below.

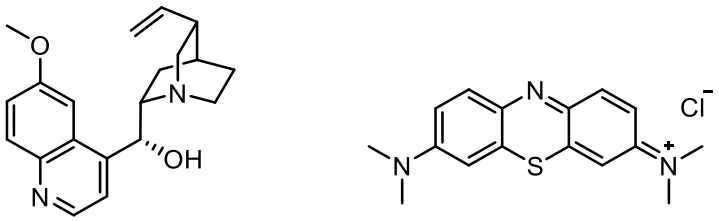

Figure 1.6. Chemical structures of quinine (left) and methylene blue (right).

1.4.2.1. Quinoline-based compounds

Pamaquine (**Figure 1.7**), discovered in 1926, was the first clinically-used 8-aminoquinoline but was shortly replaced by its less toxic derivative, primaquine (**Figure 1.7**).[60] As mentioned in **Section 1.3.2**, primaquine exhibits liver stage and gametocyte activity and is currently one of the clinically-used 8-aminoquinolines.[61] The high potency and reduced toxicity exhibited by

primaquine led to the modification of side chains in several other heterocycles, leading to the synthesis of quinacrine (**Figure 1.7**).[62] However quinacrine was later found to have adverse side effects such as discoloration of the skin, and its further use was terminated.[63] Thus, with the need for an effective drug, further research on the quinoline scaffold led to the discovery of 4-aminoquinolines.

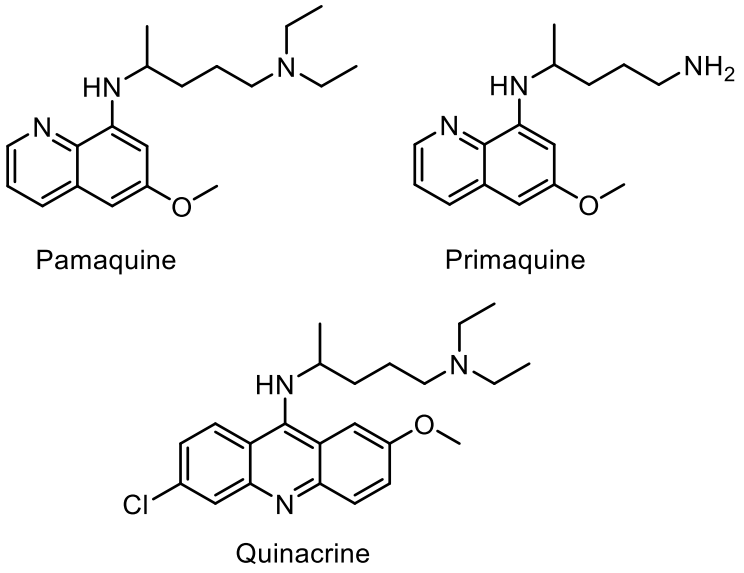

Figure 1.7. Chemical structures of the antimalarial drugs pamaquine, primaquine and quinacrine.

Hans Andersag from Bayer laboratories in Germany synthesized a 4-aminoquinoline known as resochin which was initially thought to be too toxic for further clinical use.[64] However, additional toxicology and pharmacology studies later showed that it was safe for use in humans.[65] A few years later, during World War II, the Americans came into possession of a derivative of resochin in North Africa, known as sontoquine (**Figure 1.8**). This led to their synthesis of the very well-known antimalarial drug, chloroquine (CQ, **Figure 1.8**).[65,66] However it was shortly after found that resochin and CQ were structurally identical, with CQ being superior to all previously used chemotherapeutics.[66] The immense success and widespread use of CQ for decades led to the emergence of CQ-resistance (CQR) in *P. falciparum* and *P. vivax*, as will be further discussed in **Section 1.4.3**.[67]

Since the discovery of CQ, the quinoline scaffold has dominated the antimalarial drug discovery field.[68] Among these quinoline derivatives that have been clinically employed are mefloquine, amodiaquine, and piperaquine as shown in **Figure 1.8**.

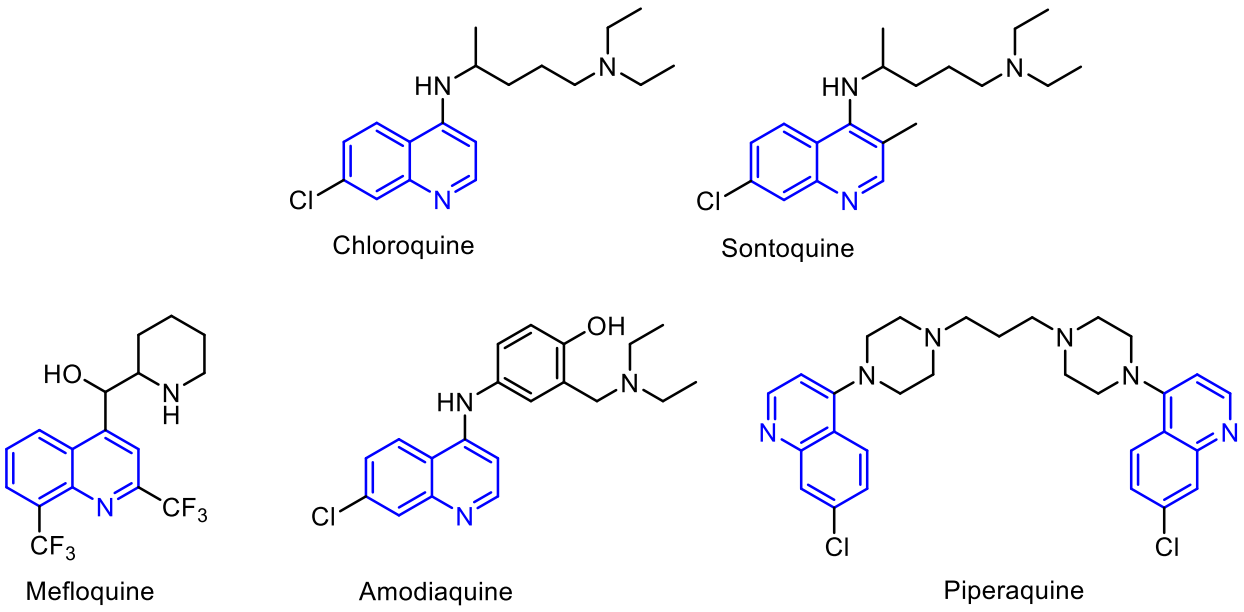

Figure 1.8. Popular quinoline-based antimalarial drugs. The quinoline motif is highlighted in blue.

Many of these quinoline compounds act via the inhibition of hemozoin formation. For example, CQ is a weak diprotic base that exists in pH-dependent proportions of a neutral, mono-protonated (CQH^+), and di-protonated (CQH_2^{2+}) species within the parasite. When basic CQ enters the acidic DV (pH ~5), the equilibrium shifts to predominantly form the CQH_2^{2+} species which can no longer diffuse across the membrane, 'trapping' diprotic CQ and resulting in its accumulation.[69,70] In the DV, CQH_2^{2+} intercalates between the crystal packing of hemozoin and can bind to hematin. This forms a toxic dimer predominantly through π-π stacking interactions, preventing further crystallization of hemozoin. Further studies have shown that CQ forms a heme μ-oxo dimer in solution, driven by the irreversible oxidation of iron(II) to iron(III).[71,72] This process of inhibiting hemozoin formation also leads to the accumulation of toxic heme which causes lysis of the parasite's membrane and halts the vacuole's protease functions,[73] ultimately leading to parasite death. Thus, the π-π stacking interaction between the porphyrin ring of heme and the quinoline ring of CQ is essential for the accumulation of the heme-drug complex within RBCs and has become a common factor when designing inhibitors of hemozoin formation.[74]

1.4.2.2. Non-quinoline-based compounds

Antifolates

Another main class of antimalarial drugs is the folate inhibitors. The parasitic folate metabolism is essential for survival due to its importance in DNA synthesis.[75] There are two classes of antifolate drugs; the first inhibits dihydropteroate synthase (DHPS, class I) and the second inhibits dihydrofolate reductase (DHFR, class II).[76] Proguanil (DHFR inhibitor), shown in **Figure 1.9**, was reported as one of the very first antifolate drugs to treat malaria.[77] It was later found that it cyclizes into its active metabolite, cycloguanil.[78] Additionally, pyrimethamine (**Figure 1.9**, DHFR inhibitor), first discovered as an antitumor agent, was later found to be structurally similar to cycloguanil by Falco *et al*. leading to its identification as an antimalarial antifolate agent.[79,80] However, when used in combination with atovaquone (**Figure 1.9**, another clinically-used antimalarial), proguanil instead doesn't act as a DHFR inhibitor but reduces the amount of atovaquone required.[77] Atovaquone is a naphthoquinone that is structurally analogous to parasitic ubiquinone, a protein cofactor found in the mitochondria that supports electron transport.[81]

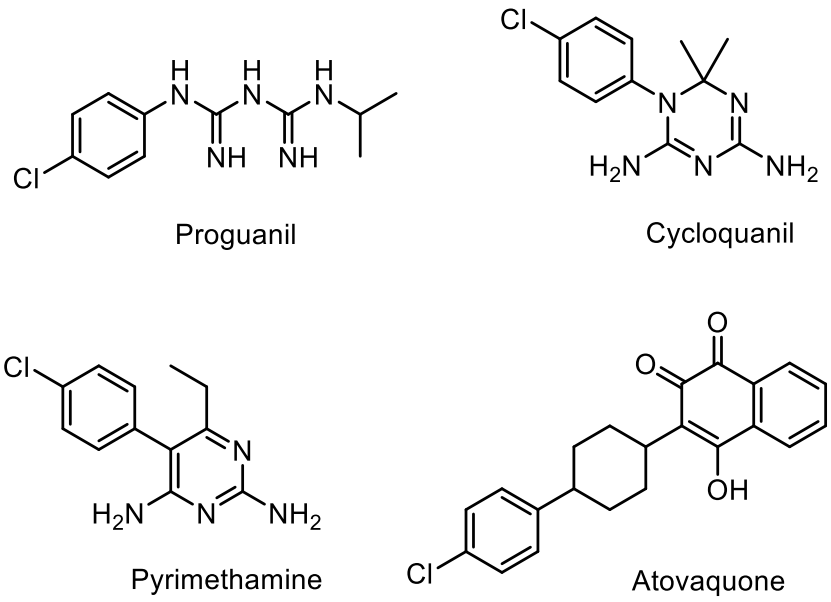

Figure 1.9. Class II antifolate drugs that inhibit dihydrofolate reductase during the parasite's essential folate pathway.

The class I antifolate DHPS inhibitors are comprised of sulfa drugs and the discovery that they inhibit the folate pathway led to their use as antimalarials. Within this group of compounds are

the sulfonamides and sulfones such as sulfadoxine and sulfanilamide shown in **Figure 1.10**. Shortly after their discovery as DHPS inhibitors, it was found that they have a synergistic effect with those that inhibit DHFR and were since used in antifolate combinations such as sulfadoxine-pyrimethamine (SP).[76]

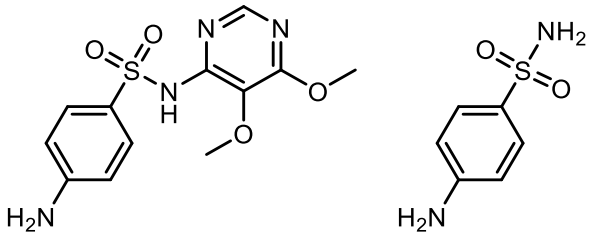

Sulfadoxine Sulfanilamide

Figure 1.10. Sulfa drugs sulfadoxine and sulfinamide that have been used as antifolate antimalarial drugs in combination with class II drugs.

However, with the increasing ineffectiveness of CQ and SP, caused by resistance to these drugs, there was a need for alternative treatments, leading to the use of artemisinin and its derivatives.

Artemisinin

Currently, the front-line treatment for malaria is the artemisinin-based combination therapy (ACT) regimen. Artemisinin (ART, **Figure 1.11**) was first discovered by Chinese scientists in the 1960s in their search for new effective antimalarials.[82] ART was originally extracted from the Chinese herb known as sweet wormwood or *Artemisia annua*.[83] The herb was used to treat malaria symptoms for many years before its active ingredient was identified as a sesquiterpene lactone with an endoperoxide bridge.[84] Originally, the administration of ART as a tablet was not effective due to its poor solubility and absorption.[85] However, with combined efforts via “Project 523”, several Chinese scientists prepared ART derivatives in the 1970s with improved efficacy and bioavailability; these included dihydroartemisinin (DHA), artemether (AM), and artesunate (AS), as shown in **Figure 1.11**.[83]

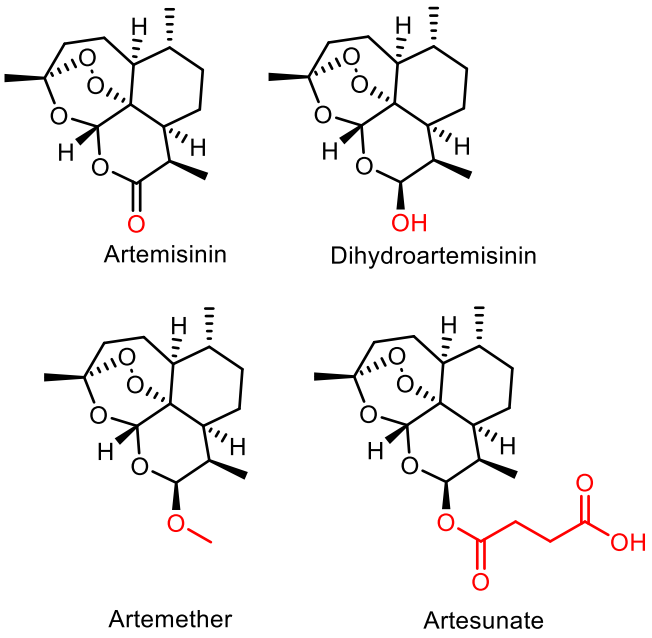

Figure 1.11. Chemical structure of artemisinin and its derivatives. The differences in chemical structure between the derivatives are shown in red.

One drawback to using ART and its derivatives (often collectively referred to as ARTs) as monotherapy for short periods is that malaria parasites are only temporarily cleared, which has been attributed to the short half-life of ARTs, leading to the emergence of resistant parasite strains.[85] Thus, ARTs have been used in combination with longer-acting antimalarials as shown in **Figure 1.12**.[86] Current drug combinations include AM-lumefantrine (AL) as the first choice and AS-amodiaquine as the second choice. Other much less used options include combinations of DHA-piperaquine, atovaquone-proguanil (brand name Malarone), and quinine with doxycycline or clindamycin which are known antibiotics. Severe infections require injections, mainly of AS but quinine is sometimes used.[87] The use of ACT therapy has assisted in the prevention of recrudescence after ART use and has delayed the acquisition of drug resistance.[88]

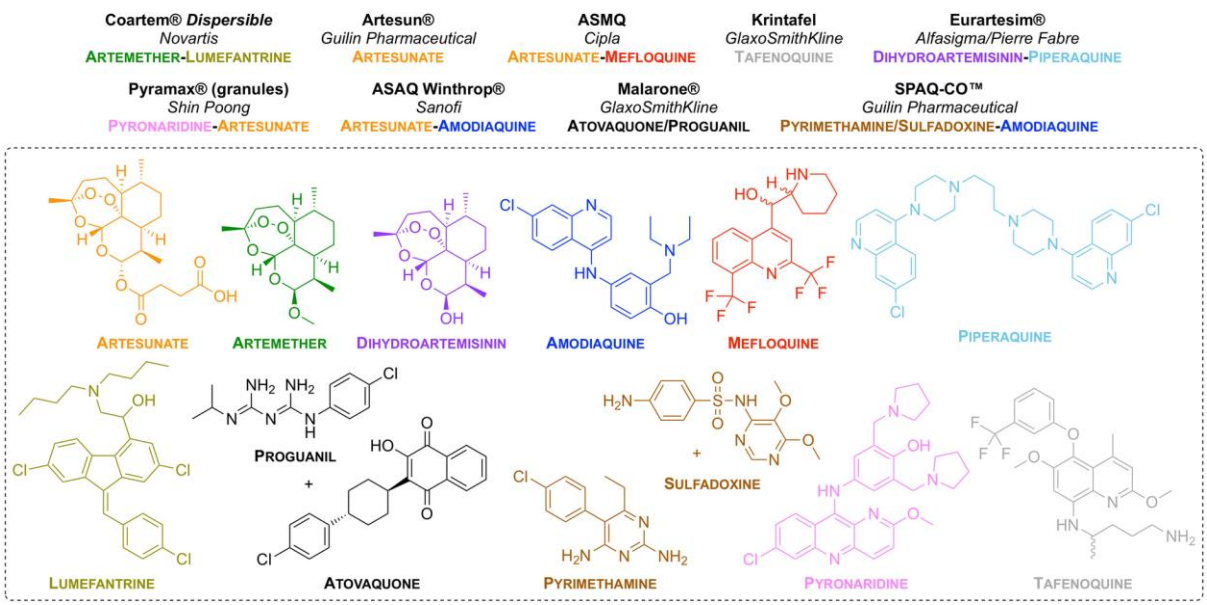

Figure 1.12. Summary of clinically-used combination therapy for the treatment of malaria. Republished from Tse *et al*. under the Creative Commons Attribution 4.0 International license.[77]

Concerning its MoA, ART is thought to be activated via a heme iron-catalyzed reductive cleavage of the endoperoxide bond which generates carbon-centered radicals. These radicals react with essential parasite proteins via alkylation, causing parasite death.[89] Since low levels of free heme are only available during the trophozoite stage, ART is relatively inactive during the ring stage of the ABS.[90] However it has also been found that the formation of heme-ART adducts inhibits the formation of hemozoin, complementing the harmful effect of the formed radicals upon ART activation.[90]

From the above sections, it is clear that there is an abundance of available drugs that act against the ABS and a scarcity of those that act against the liver stage and more significantly against the gametocyte stage, as is also summarized in **Figure 1.13**. This emphasizes the need for novel compounds that act against both the liver and gametocyte stages of the life cycle.

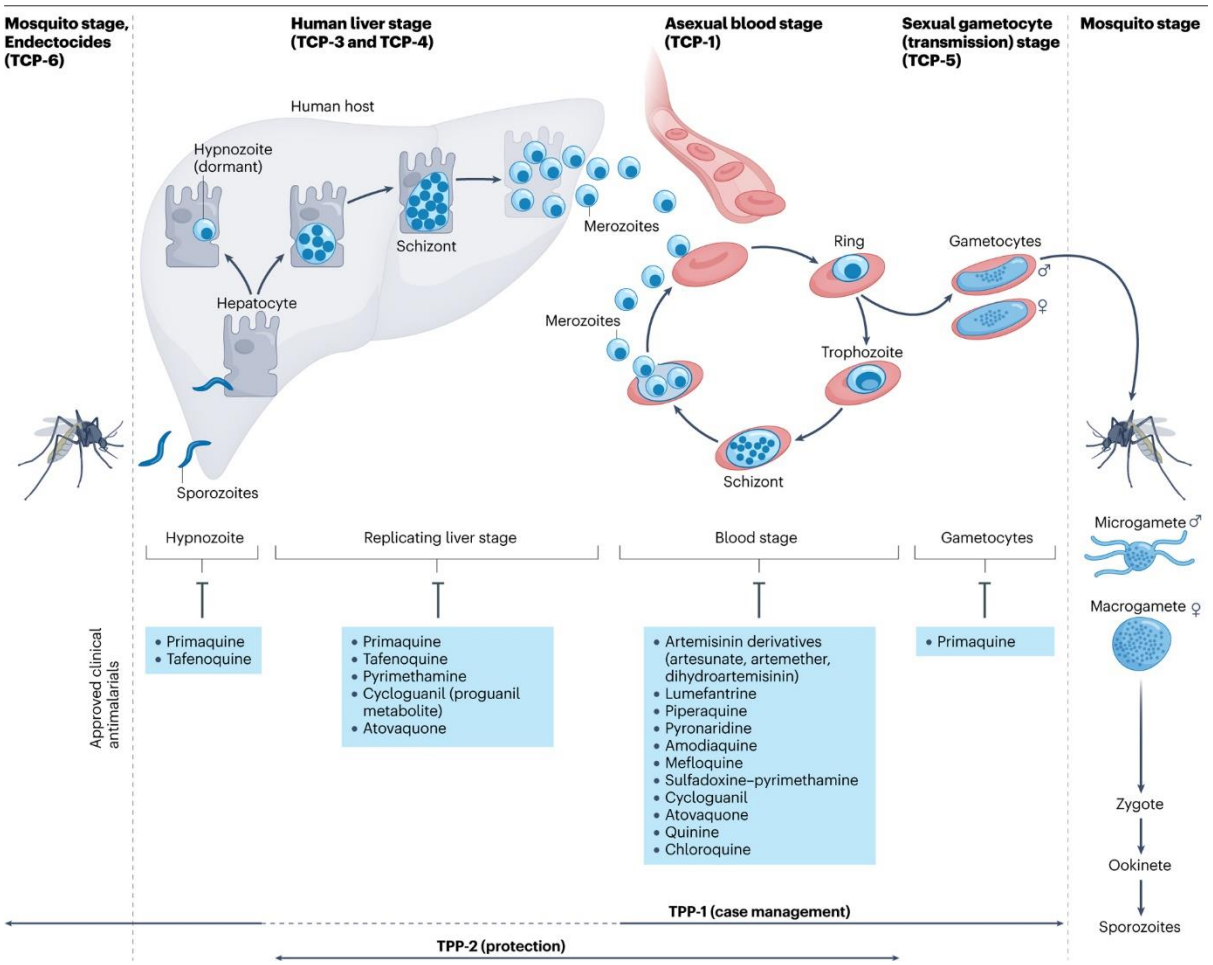

Figure 1.13. Summary of antimalarial drugs and the stage of the life cycle they act against, highlighting the scarcity of active drugs against gametocytes. Republished from Siqueira-Neto *et al.*[87] under the Creative Commons Attribution 4.0 International license.

As mentioned in the above section, the emergence of drug resistance has been a major hindrance in the control of malaria. Thus, the next section discusses the genetic contributors to drug resistance of the most frequently used antimalarials.

1.4.3. Drug resistance

The extensive use of many of the above-mentioned antimalarial drugs (quinolines: CQ, mefloquine, primaquine, piperaquine, and sulfadoxine-pyrimethamine) has provided immense selection pressure for human malaria parasites to evolve mechanisms of resistance (MoR).[91] Thus the emergence of resistance has been a major contributor to the constant high morbidity and mortality rates mentioned in **Section 1.2**. The likeliness of resistance emerging against a particular drug varies, as some drugs are more prone to becoming ineffective than others. This

is exemplified by the drugs CQ and atovaquone, where resistance to CQ emerged after decades of its widespread use, while resistance to atovaquone emerged parallel to its initial clinical use.[92]

CQ was the gold standard for antimalarials for several years due to its high efficacy and low cost. However, its pharmacological potency was diminished when CQR emerged, leading to the re-emergence of malaria and the spread of CQR strains of the parasite in Southeast Asia and South America.[93,94] CQR parasite strains have shown decreased accumulation of the drug in the DV, mediated by the energy-dependent efflux out of the DV. Thus, the efflux of CQ is dependent on the generation and hydrolysis of ATP.[95] As mentioned in **Section 1.4.2.1**, CQ accumulates in the DV as a CQH_2^{2+} species.[70] However, CQR parasites can transport protonated CQ out of the DV, preventing its accumulation.[96] This is facilitated by the K76T mutation in the *Plasmodium falciparum* chloroquine resistance transporter (*pfcrt*) gene which was discovered by a genetic cross between CQ-sensitive (CQS) and CQR strains. Furthermore, mutations in the *Plasmodium falciparum* multidrug drug resistance gene 1 *pfmdr1*), which encodes for an ABC transporter (ATP-binding cassette, P-glycoprotein homolog) have been associated with resistance to mefloquine, quinine, and ART derivatives.[97]

After the spread of *Pf*-CQR strains, treatment regimens shifted to the use of sulfonamide, sulfadoxine, and pyrimethamine. Resistance to pyrimethamine has been associated with progressive and cumulative mutations in the dihydrofolate reductase (*dhfr*) gene which decreases the drug's binding affinity.[98] Similarly, resistance to the sulfa drugs involves mutations in the dihydropteroate synthase (*dhps*) gene.[99] This mutation has been shown to reduce the conversion of sulfadoxine to dihydropteroate.[99] With the development of resistance to many of the quinoline and SP drugs, ACT was recommended as the front-line treatment, although resistance to ART also started to emerge.

ART resistance was first recognized in 2007 in western Cambodia and was characterized by delayed parasite clearance in AS-treated patients.[100] Thus, due to delayed clearance, ART resistance is more accurately referred to as partial drug resistance.[101] The delayed clearance phenotype has been attributed to the loss of susceptibility to ART during the early ring stage (0–3 h) of the ABS of the parasitic life cycle.[102] ART resistance is highly stage-specific as no resistance has been observed at the later asexual blood stages (late ring and trophozoite stage) of the parasite life cycle. This has been associated with nonsynonymous mutations in the *kelch 13* gene (*pfk13*) and, more specifically, in the propeller region of this gene.[103] It has been suggested that this *kelch 13* mutation mediates ART resistance by reducing activation of the drug and increasing the capacity of the parasite to remove damaged proteins.[104] Reduced drug activation has been associated with mutations that lead to lower levels of the

Kelch 13 protein, reducing hemoglobin catabolism and endocytosis. Consequently, this leads to less Fe(II)PPIX which catalyzes endoperoxide cleavage and reduces ART activation.[105]

From the above discussion, it is clear that the constant development of drug-resistant strains of *P. falciparum* and the decreased effectiveness of most clinically-used drugs requires critical development of new antimalarial chemotherapeutic drugs.[106,107] It is crucial to develop compounds that target resistant strains of the malaria parasite, have dual-stage activity, and act against novel targets. In pursuit of malaria drug discovery, chemotypes used in other disease areas can be exploited and optimized as novel antimalarial compounds. Most relevant to this thesis are metal complexes which are briefly discussed in the following sections.

1.5. Metals in medicine

The use of metals as therapeutic agents dates back over a millennium. They were used in ancient practices to improve health and promote healing. For example, silver was used as early as 69 BC to heal wounds.[108] The ancient seers in India used processed metals such as mercury, gold, silver, lead, copper, and zinc to treat several diseases over 5 000 years ago.[109] Additionally, copper was used as far back as 2 500 BC in Egypt and China to sterilize water.[110]

The use of metal complexes in modern medicine began with the discovery of the therapeutic nature of the well-known anticancer platinum-based compound, cisplatin.[110] Cisplatin (**Figure 1.14**) was first discovered by Rosenberg who realized its pharmacological properties against *Escherichia coli*.[111] The subsequent approval of cisplatin for clinical use in 1978 led to the discovery of its anticancer properties, first in mice and then in humans.[112] Due to its high efficacy but also its toxicity, several derivatives of cisplatin were synthesized in attempts to improve its pharmacological profile; namely, carboplatin, oxaliplatin, satraplatin, and picoplatin, all shown in **Figure 1.14**.[113]

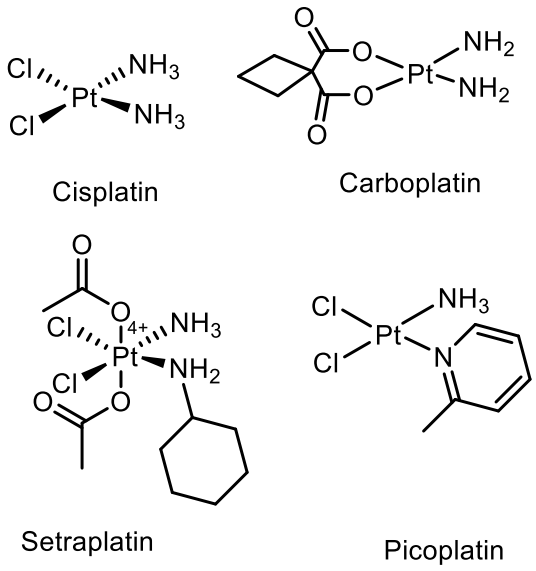

Figure 1.14. Cisplatin and its less toxic derivatives, carboplatin, setraplatin, and picoplatin, are used for cancer treatment.

The modern use of gold began in 1890 with the discovery of its antibacterial properties against TB.[114] Additionally, gold salts have often been used to treat rheumatoid arthritis.[115] Further studies of gold complexes identified auranofin (**Figure 1.15**), a gold(I)-containing compound that was approved for clinical use in 1985 to treat rheumatoid arthritis.[116] Auranofin is still used today and has even entered clinical trials as an anticancer chemotherapeutic.[117]

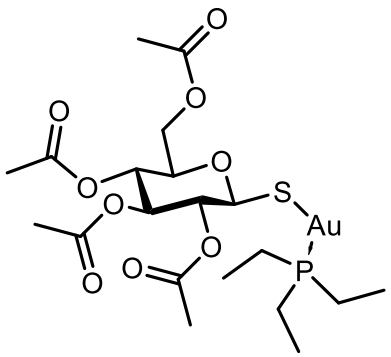

Figure 1.15. Chemical structure of the gold(I) arthritis medication, auranofin.

The extensive and successful use of transition metal complexes in cancer therapy has prompted researchers to investigate their potential against other disease areas. Metal complexes containing vanadium and zinc have been shown to treat insulin resistance,[118] and

many transition metal complexes including zinc, copper, and iron have exhibited antimicrobial activity against both gram-positive and gram-negative strains.[119] Iridium complexes have shown anti-inflammatory properties with many metal complexes reducing the harmful effects of free radicals.[120] Furthermore, Mjos and Orvig provide an extensive review on an array of metallodrugs and their therapeutic applications in diabetes, gastrointestinal disorders, and cardiovascular disorders to name a few. Additionally, this review discusses the use of metal complexes as radiopharmaceuticals and photochemotherapeutic metallodrugs in cancer therapy.[121] This review also highlights one of the important advantages of using inorganic chemistry in drug discovery as metallomics can be employed for target validation. However, most relevant to this thesis is the display of antiparasitic activity by compounds with several transition metal centers,[122–124] which is further discussed in **Section 1.5.2.**

1.5.1. Advantages of metals in medicine

The use of transition metal complexes as therapeutic agents offers several advantages over its purely organic alternatives. Transition metals have the added advantage of being neutral, cationic, or anionic species that can easily be changed with ligand coordination. Metals also have access to several different oxidation states that can influence their ability to interact with different charged molecules.[125] Additionally, the MoA of metal complexes in living organisms can differ from that of organic compounds. For example, metal complexes have been shown to introduce artificial oxidative stress through the production of ROS in cancer cells where they have also catalyzed redox-related stress.[126] Lastly, metal complexes are also able to adopt several geometries that are not available to organic scaffolds. Depending on the oxidation state of the metal, these include square planar, square-pyramidal, trigonal-bipyramidal, and octahedral, compared to organic compound geometries being limited to linear, trigonal planar, or tetrahedral. Furthermore, with the ability to fine-tune the attached ligands, the pharmacological properties can often be tweaked without the need for longer synthetic protocols.[127]

1.5.2. Metalloantimalarials

Considering the substantial success exhibited by CQ and its analogs, the derivatization of metalloantimalarials naturally began with CQ as an organic scaffold. This was not only due to the high potency of the quinoline scaffold, but also to investigate if complexation would result in compounds that do not share cross-resistance with CQ.

Sanchez-Delgado *et al*. were among the first groups to synthesize transition metal (Rh and Ru) complexes using a CQ scaffold. These complexes, shown in **Figure 1.16** exhibited comparable *in vitro* antiplasmodium activity to CQ (IC_{50} = 72 ± 9 nM) in the *P. berghei* species with IC_{50} values of 73 ± 33 nM and 18 ± 7 nM for $[Rh(COD)Cl]_2$ and $[RuCl_2(CQ)]_2$, respectively.[128] Additionally, these complexes were assayed against Balb/C mice infected with *P. berghei* (tested at a dose of 2.8 mg/kg/day) in which a reduction in parasitemia of 73% and 94% was observed for the $[Rh(COD)Cl]_2$ and $[RuCl_2(CQ)]_2$ complexes, respectively. Furthermore, $[RuCl_2(CQ)]_2$ exhibited a five-fold increase in activity *in vitro* compared to CQ when tested against the FCB1 strain of *P. falciparum*.[128] Further work done by the same group, attempted to synthesize ruthenium complexes of higher potency as shown in **Figure 1.16**, [(*p*-cymene)Ru(II)Cl_2(CQ)]Cl, [(benzene)Ru(II)(Cl)(H_2O)(CQ)]Cl. Therefore, the ancillary ligand was changed from 1,5-cyclooctadiene (COD) to varying arenes.[129] These $Ru^{II}(\eta^6$-arene) CQ derivatives displayed appreciable antiplasmodium activity in the CQS strains FcB1, PFB, and F32 but, most notably, they showed enhanced activity against the Dd2, K1, and W2 CQR strains of *P. falciparum*.[130]

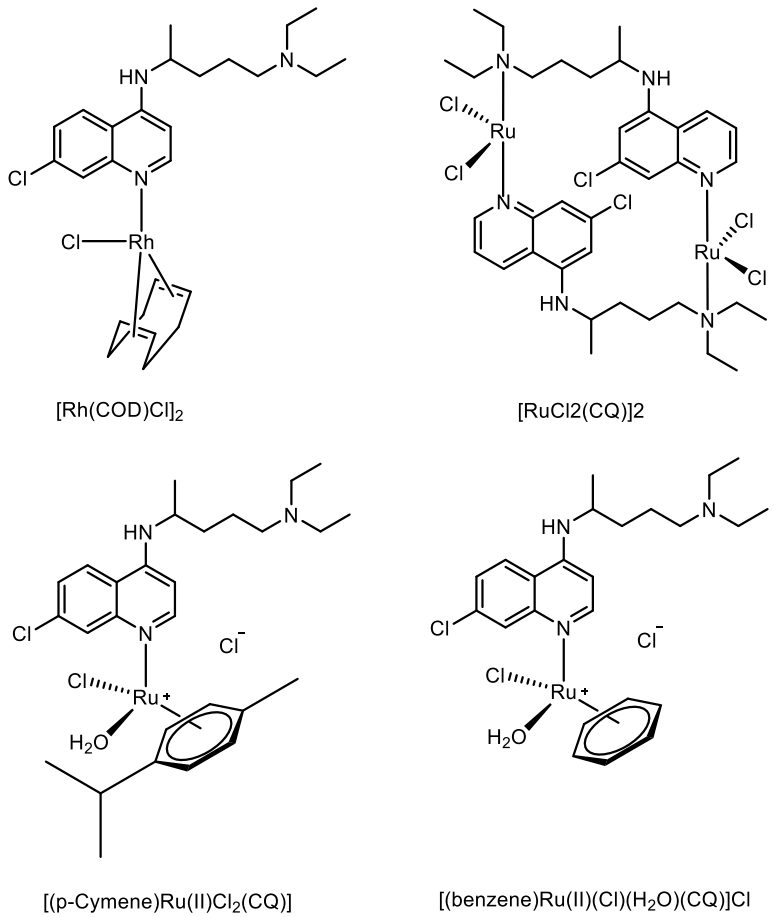

Figure 1.16. Chemical structures of some of the very first CQ-derived metal complexes synthesized by Sanchez-Delgado *et al*.[128]

From here, scientists were inspired by the improved activity of metal complexes, leading to the development of other quinoline-based metal complexes including the complexation of gold,[131] iridium,[132] and platinum[133] to CQ.

However, most significant to the metalloantimalarial field was the discovery that ferrocene metal complexes exhibited promising medicinal properties.[134] This led to the derivatization of CQ to a ferrocenyl-containing complex, ferroquine (FQ, **Figure 1.17**).[135] FQ was designed to overcome CQR,[136] and showed whole-cell potency against both CQS and CQR strains of *P. falciparum*. Despite the extensive structure-activity relationship (SAR) studies carried out with 120 of its derivatives, FQ has remained the lead ferrocenyl-containing CQ derivative,[137] as a more potent analog is yet to be found. Furthermore, FQ is currently in phase IIb clinical trials in combination with artefenomel (an antiparasitic trioxolane agent).[138]

The derivatization of CQ with a metallic moiety such as the ferrocenyl scaffold has contributed to the superior antimalarial properties displayed by FQ. This has in part been attributed to its difference in basicity, lipophilicity, and pK_a values compared to its organic parent. The pK_a of FQ at vacuole pH results in a ten-fold increase in its DV accumulation compared to CQ, where it acts partially via hemozoin inhibition.[139] Reports have also suggested that the lipophilicity of FQ is 100 times that of CQ at cytosolic pH where at pH 5, it accumulates fifty-fold more than CQ in the DV. It has therefore been hypothesized that the increased activity of FQ may be attributed to its ability to target hemozoin lipid sites more proficiently than CQ.[139] It has been suggested that the increased lipophilicity of FQ can be attributed to an intramolecular hydrogen bond between the *tertiary* amine and the 4-amino moiety in the quinoline ring.[139] This results in a folded conformation that increases transport of FQ through cell membranes.[137]

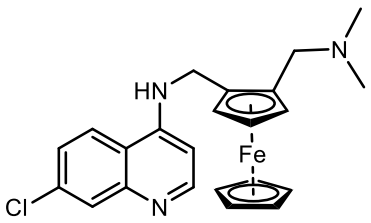

Figure 1.17. Structure of FQ.

The second MoA of FQ involves the formation of hydroxyl radicals under the oxidizing conditions of the parasite DV, as shown below by **Equation 1.1**, preventing the formation of merozoites.[139,140] Thus, FQ inhibits the formation of hemozoin, produces ROS, and results in

lipid peroxidation, ultimately leading to the death of the malaria parasites.

$$Fe(II) + H_2O_2 \rightarrow FQ(III) + HO^- + HO \quad \textbf{Equation 1.1}$$

Another study conducted by Salas *et al*. reports on the antiplasmodium activity of a series a chloroquine-bridged ferrocenyl derivatives in which the complexes shown in Figure **1.18** retained whole-cell potency in the *Pf*-Dd2 and *Pf*-K1 CQR strains.[141]

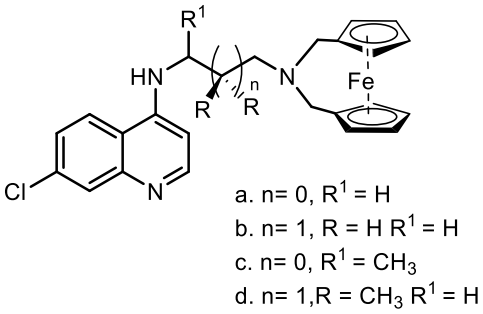

Figure 1.18. Chloroquine-bridged ferrocenyl derivative synthesized by Salas *et al*. with retained activity in the *Pf*-Dd2 and *Pf*-K1 strains.[141]

However, FQ has been the gold standard of metalloantimalarials for many years. Among the other quinoline organic frameworks used in attempts to synthesize metal complexes include mefloquine[142,143] and amodiaquine, although CQ derivatives dominate the literature.[144–147] However, other organic scaffolds have also been used in the development of transition metal complexes that exhibit antiplasmodium activity and will be discussed in the following section.

1.5.3. Metalloantimalarials based on non-quinoline scaffolds

Among the non-quinoline metalloantimalarials are those derived from ART. Delhaes *et al*. synthesized four ART ferrocene derivatives shown in **Figure 1.19**. The compounds were synthesized as isomers and their *in vitro* antiplasmodium activity was tested as a mixture against strains *Pf*-HB3 (CQS), *Pf*-SGE2 (CQS), and *Pf*-Dd2 (CQR). However, the

complexation of ART or DHA did not improve their pharmacological profile compared to ART or DHA in either of the strains tested.[148]

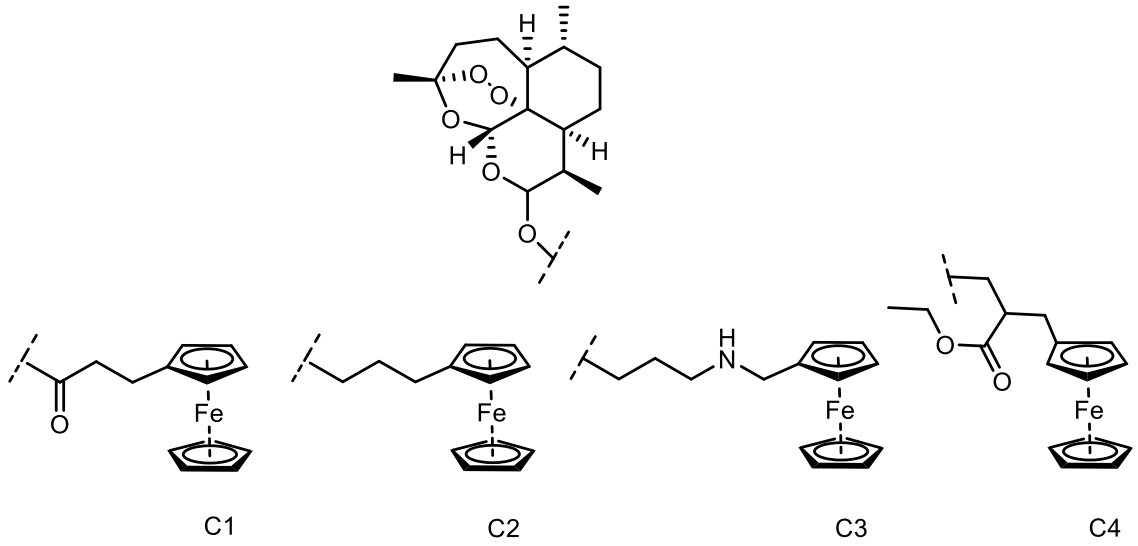

Figure 1.19. Artemisinin ferrocene derivatives synthesized by Delhaes *et al*.[148]

A very recent study done by Albertyn *et al.* reports on ruthenium-containing ART derivatives as shown in **Figure 1.20**. For this, the ART scaffold was derivatized with an *N,N'*-coordinated ruthenium *p*-cymene or a ferrocene complex. The novel ligands were therefore either an artemisinyl-triazole pyridine or a pyridyl amido artesunate.[149] These ruthenium complexes were synthesized as isomers and their whole-cell potency was tested as a mixture.

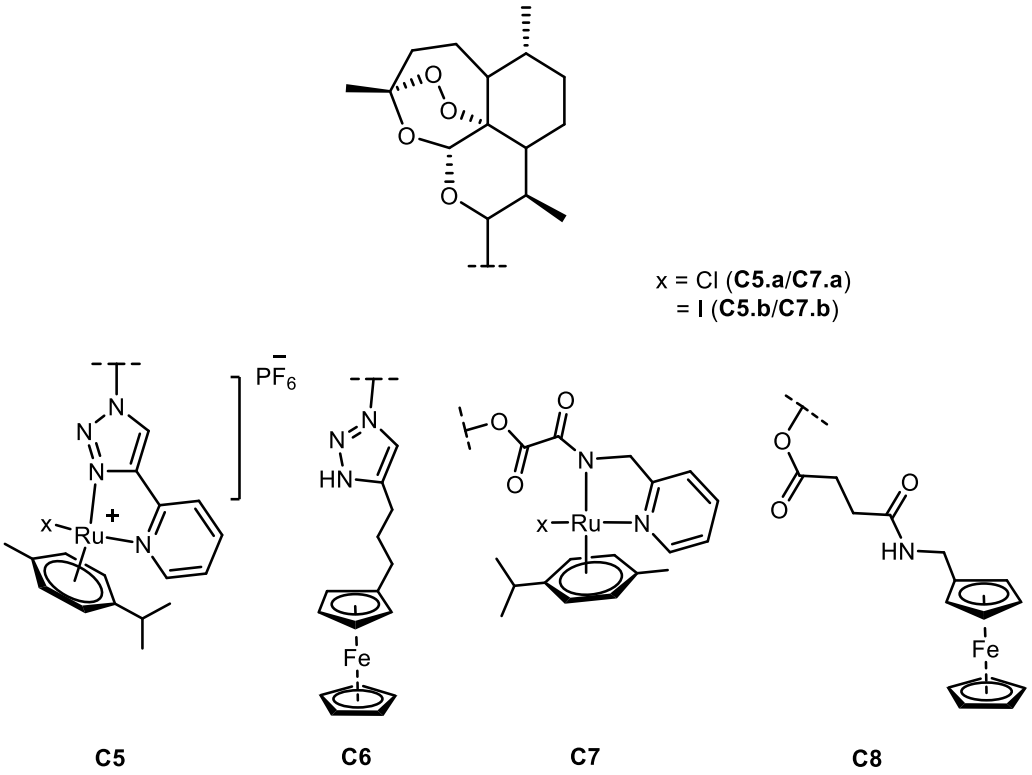

Figure 1.20. Artemisinin-derived metal complexes were synthesized by Albertyn *et al*. and evaluated for their antiplasmodium activity.[149]

The ruthenium complexes (**C5.a-b** and **C7a-b**) displayed antiplasmodium potency in the nanomolar range (14–245 nM) but were all less potent than the ART ligands. The ferrocenyl-containing compounds (**C6** and **C8**) did, however, exhibit higher *in vitro* potency than ART and DHA.

Among the scaffolds that have been used in the investigation of metalloantimalarials include the benzimidazoles, synthesized by Rylands *et al*.[150] In their study, the metal complexes displayed sub-micromolar potency against the *Pf*-NF54 and *Pf*-K1 strains with the most potent analogs shown in **Figure 1.21**. It can also be seen that the metal complexes exhibited enhanced activity compared to their organic ligands **L1** and **L2**. However, these complexes did not inhibit the formation of β-hematin, and it was proposed to have a novel MoA, although this was not evaluated further.[150]

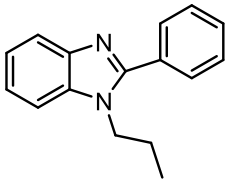

L1:
Pf-NF54 IC_{50} = 22 320 ± 0.16 nM

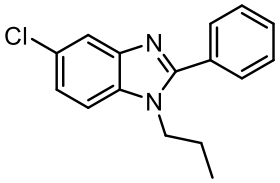

L2:
Pf-NF54 IC_{50} = 20 640 ± 0.81 nM

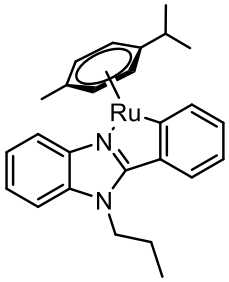

C9:
Pf-NF54 IC_{50} = 12 ± 0.01 nM
Pf-K1 IC_{50} = 2.68 ± 0.15 nM

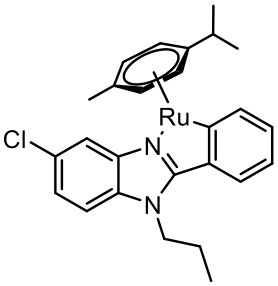

C10:
Pf-NF54 IC_{50} = 59 ± 0.04 nM
Pf-K1 IC_{50} = 1.85 ± 0.27 nM

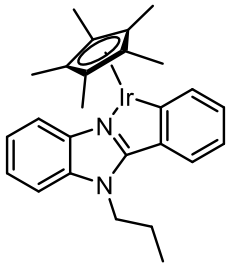

C11:
Pf-NF54 IC_{50} = 19 ± 0.01 nM
Pf-K1 IC_{50} = 4.31 ± 0.27 nM

Figure 1.21. Ruthenium and iridium benzimidazole derivatives synthesized by Rylands *et al*. were shown to exhibit potent antiplasmodium activity and were proposed to have a novel MoA.[150]

Additionally, Chellan *et al*. synthesized a series of rhodium(III), ruthenium(II), and iridium (III) metal complexes containing ligands derived from sulfadoxine.[151] These complexes exhibited sub-micromolar potency against the *Pf*-3D7 and *Pf*-Dd2 strains of the parasite with the most active complexes shown in **Figure 1.22**. These complexes also showed dual-stage activity with potency against the ABS and LG stage of the malaria parasite whereas sulfadoxine was inactive.[151]

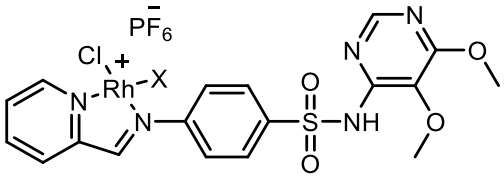

C12: X = Cpxph
3D7-IC_{50} = 0.34 ± 0.06 μM
Dd2-IC_{50} = 0.52 ± 0.18 μM
LG-IC_{50} = 0.93 ± 0.36 μM

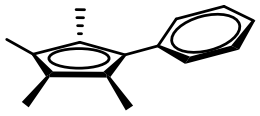

Cpxph

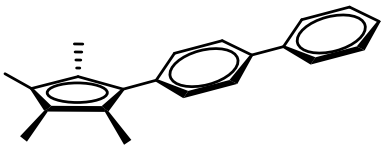

Cpxbiph

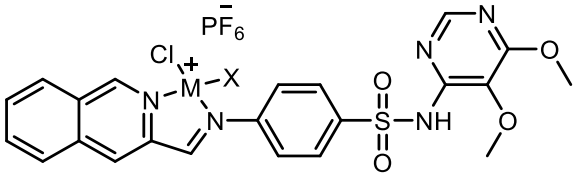

C13: M = Rh, X = Cpxph
3D7-IC_{50} = 0.38 ± 0.24 μM
Dd2-IC_{50} = 0.54 ± 0.19 μM
LG-IC_{50} = 1.10 ± 0.09 μM

C14: M = Rh, X = Cpxbiph
3D7-IC_{50} = 0.44 ± 0.09 μM
Dd2-IC_{50} = 0.65 ± 0.03 μM
LG-IC_{50} = 1.48 ± 0.39 μM

C15: M = Ir, X = Cpxbiph
3D7-IC_{50} = 0.25 ± 0.04 μM
Dd2-IC_{50} = 0.17 ± 0.07 μM
LG-IC_{50} = 1.23 ± 0.29 μM

Figure 1.22. The most potent rhodium(III) and iridium(III) sulfadoxine derivatives synthesized by Chellan *et al*. that exhibited dual-stage antiplasmodium activity.[151]

Furthermore, several other organic scaffolds have been employed in the investigation of novel metalloantimalarials, including Schiff-base phenolates,[152] amine phenols,[153] ferrocenyl sugars,[154] ferrocenyl chalcones,[155] flavones,[156] and pyridyl esters,[157] to name a few.

As mentioned in **Section 1.4.1**, one of the advantages of complexation chemistry is the ability to easily alter the attached ligand for a desired pharmaceutical outcome. Medicinal inorganic chemistry is not only limited to the use of well-known pharmacophores in the field of study, but organic scaffolds can be selected based on other favorable chemical properties as will be discussed for bipyridines.

1.5.4. Bipyridine and their metal complexes with antiplasmodium activity

Although bipyridine has largely been considered a biologically inactive scaffold until recently, more details on it will be provided in the subsequent discussion on bipyridine metals. It should, however, be mentioned here that despite the bipyridines not being extensively studied for their pharmaceutical properties, there are a few reports in the literature, two of which are discussed here.

A study done by Cabrera *et al*. reports on the antiplasmodium activity of a series of 3,5-substituted 2-aminopyridines.[158] The R substituent was varied between several different aryl moieties, of which the most active analogs are shown in **Figure 1.23** with their respective IC_{50} values. These bipyridine analogs therefore exhibit high potency against the multidrug-resistant *Pf*-K1 and drug-sensitive *Pf*-NF54 strains of malaria.[158]

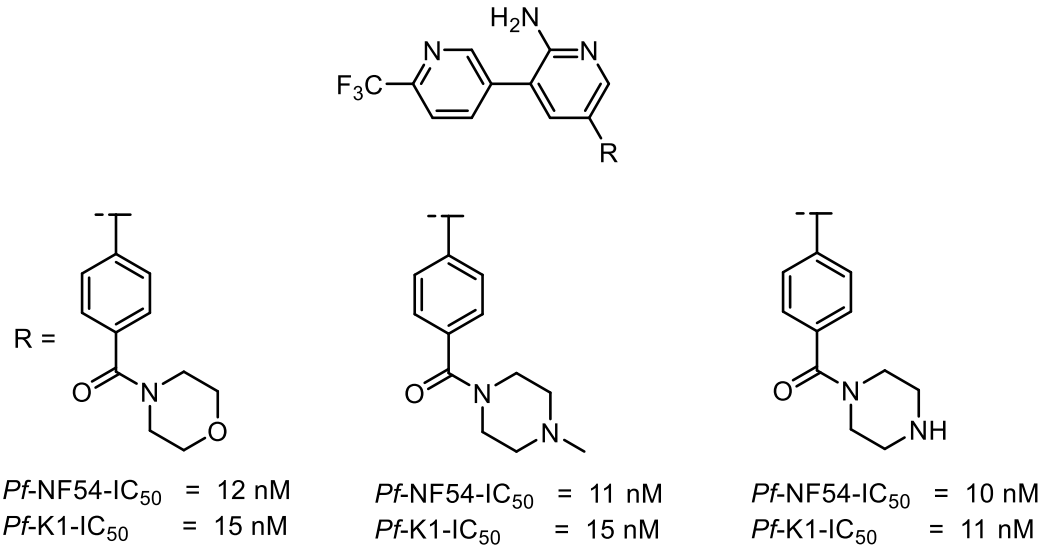

Figure 1.23. Analogs of bipyridine reported by Cabrera *et al.* that exhibit promising antiplasmodium activity.[158]

In another study, Liang *et al*. synthesized a series of bipyridine-sulfonamide compounds shown in **Figure 1.24**.[159] This series of compounds had over 20 analogs where the R^1 and R^2 substituents varied between aromatic carboxamides and phenyl sulfonamides. Many of the compounds exhibited nanomolar potency against *Pf*-3D7 (IC_{50} = 39 nM to 5880 nM) and inhibited phosphatidylinositol 4-kinase (PI4K) which is an essential enzyme during all stages of the *Plasmodium* life cycle.[159]

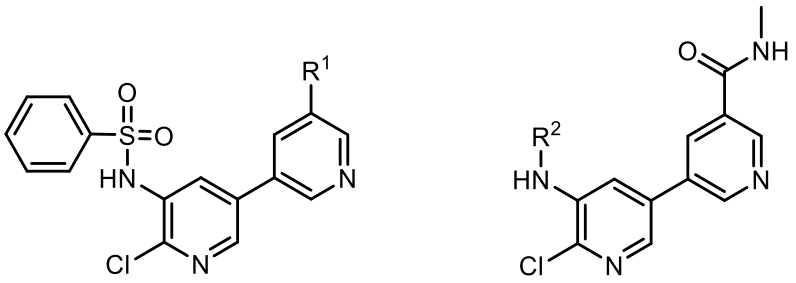

Figure 1.24. Analogs of bipyridine reported by Liang *et al.* that exhibit promising antiplasmodium activity and were found to be PI4K inhibitors.[159]

Concerning inorganic chemistry, bipyridine is one of the most widely used ligands in complexation chemistry. This is in part attributed to their redox stability as chelating ligands and neutrality that allows them to coordinate with cationic metals, without changing the charge.[160] Furthermore, the incorporation of bipyridine into metal complexes has been essential in understanding the thermodynamics and kinetics of coordination, bonding, photochemistry, photophysics, and electrochemistry of metal complexes.[161] There are a large number of reported bipyridine-containing metal complexes in the literature with a wide range of applications. However, only their pharmaceutical properties and more importantly their antiplasmodium properties are discussed here.

Shaik *et al*. synthesized mixed-ligand mononuclear Zn(II) complexes with a 2,2'-bipyridine ancillary ligand as shown in **Figure 1.25**.[162] These complexes exhibited promising antiplasmodium activity with sub-micromolar IC_{50} values between 0.011 μM and 0.140 μM.[162]

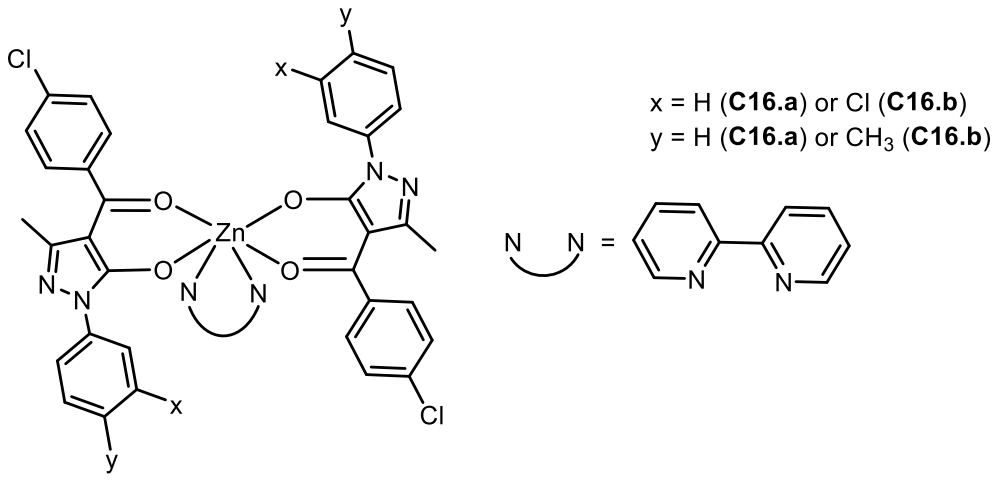

Figure 1.25. Mixed-ligand mononuclear Zn(II) complexes with 2,2'-pyridine as an ancillary ligand synthesized by Shaik, Jadeja, and Patel.[162]

Additionally, Kumari *et al*. recently synthesized a series of cyclometallated bipyridine iridium complexes shown in **Figure 1.26**.[163] The most active complex had a pq, $(C^N)_2$ chelator and an **L3,** N^N chelating ligand with IC_{50} values of 9.7 ± 1.5 nM, 12.2 ± 0.4 nM and 12.1 ± 0.9 nM against the *Pf*-3D7 (CQS), *Pf*-RKL9 (CQR), and *Pf*-R539T (ART-resistant) strains, respectively. These complexes also exhibited dual-stage activity, with promising *in vivo* gametocyte potency against *P. berghei* parasites. Furthermore, mechanistic studies indicated that these iridium complexes produce ROS which disrupts the mitochondrial membrane of the parasite.[163]

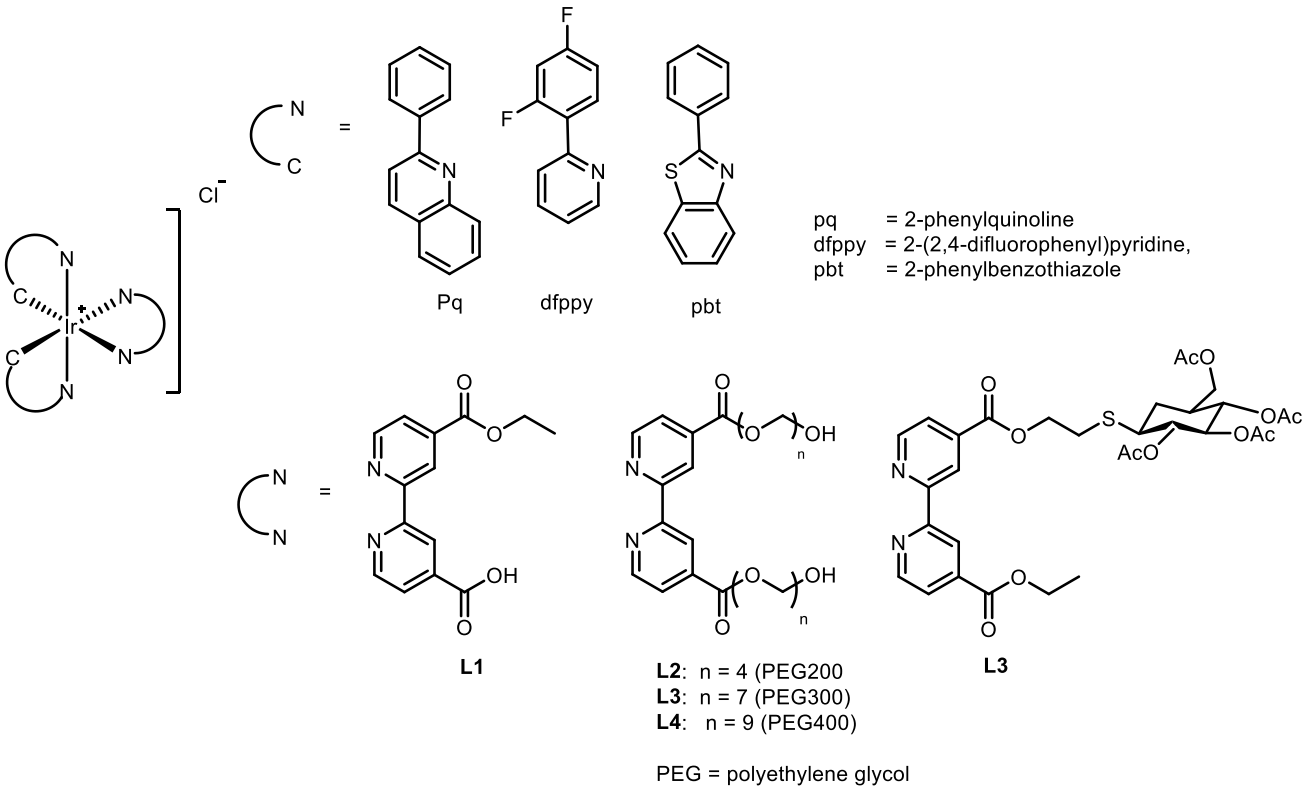

Figure 1.26. Cyclometallated bipyridine iridium complexes that were synthesized by Kumari *et al.* and exhibited antiplasmodium activity.[163]

In another study, Chellan *et al*. report on a series of half-sandwich rhodium and iridium bipyridyl complexes containing an ART pharmacophore shown in **Figure 1.27**.[164] These complexes exhibited whole-cell potency in the nanomolar range with enhanced activity compared to CQ

and ART. Furthermore, they were also active against LGs with IC_{50} values as low as 8 nM for an iridium analog with the Cp^{xph} ancillary ligand.[164]

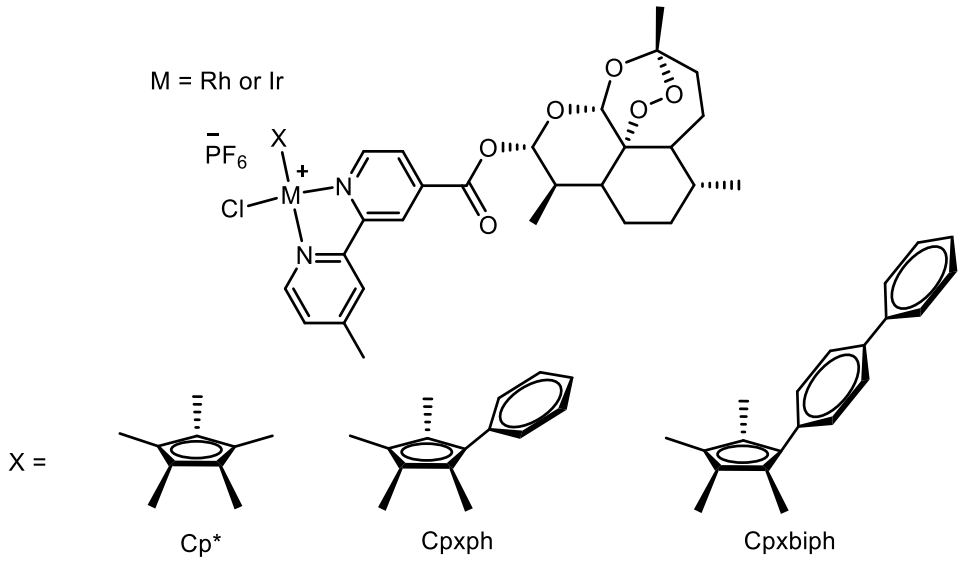

Figure 1.27. Half-sandwich rhodium and iridium bipyridyl complexes synthesized by Chellan *et al*. containing an artemisinin pharmacophore.[164]

1.5.5. Platinum antiplasmodium compounds

Platinum forms one of the six platinum group metals (PGMs) which also includes palladium, rhodium, ruthenium, iridium, and osmium. While iridium is among the most frequently studied elements among the PGMs for whole-cell potency, the above examples also highlight the extensive use of rhodium and ruthenium in antiplasmodium activity studies. On the other hand, the use of platinum in its medicinal capacity began with cisplatin as an anticancer agent as previously discussed.

However, in terms of its antiparasitic activity, platinum antiplasmodium agents have often been synthesized with a quinoline organic scaffold. One example is the platinum(II)-chloroquine phosphine complexes synthesized by Macedo *et al*. shown in **Figure 1.28**.[165] These complexes exhibited lower potency than CQ against the CQS-3D7 strain but displayed comparable activity against the CQR-W2 strain. However, unlike CQ these complexes displayed potency against the hepatic stage of *P. berghei* and reduced mitochondrial activity.[165]

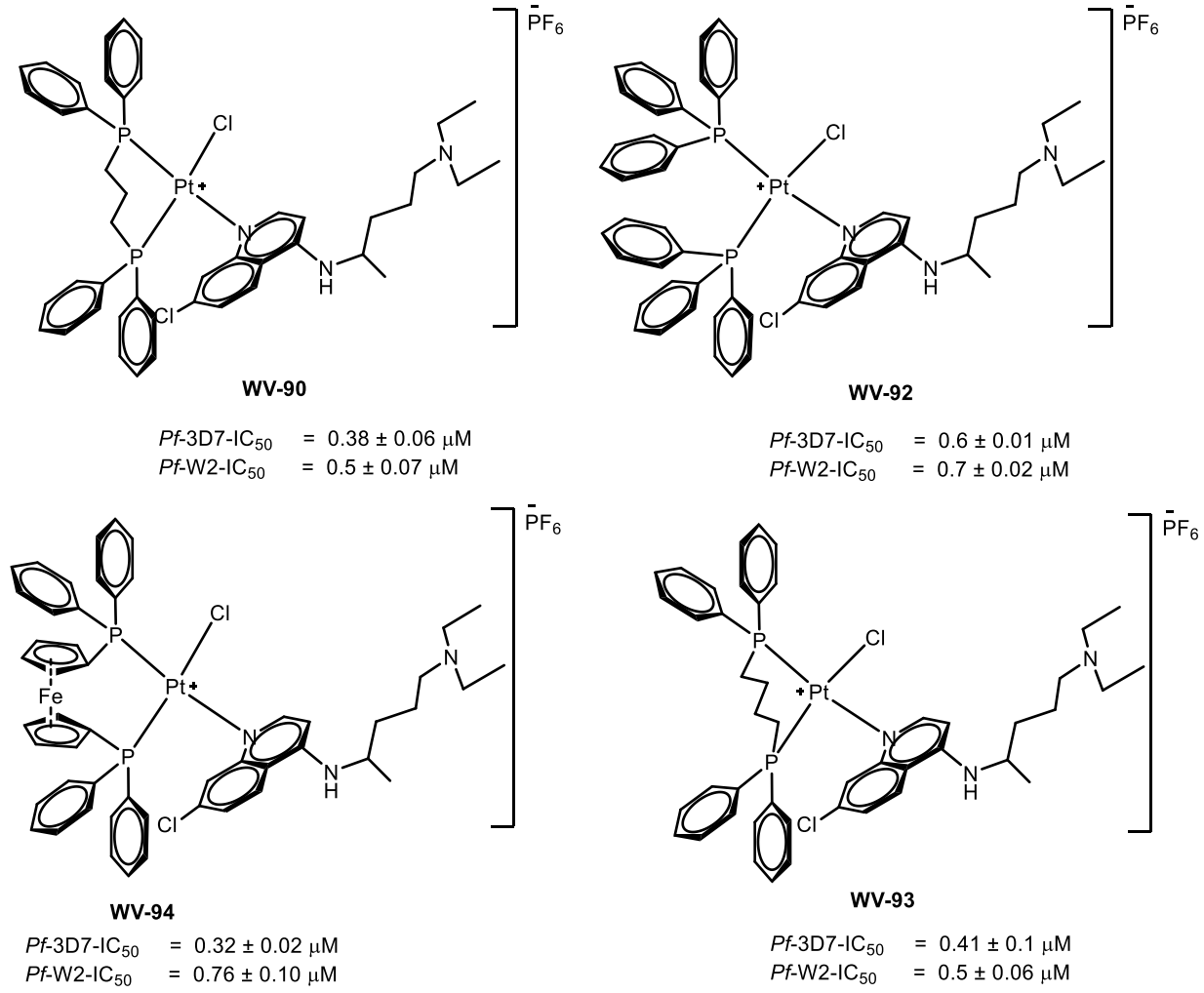

Figure 1.28. Platinum(II)-chloroquine phosphine complexes synthesized by Macedo *et al.* with antiplasmodium activity.[165]

Another study conducted by De Souza *et al.*[166] shows that a series of 7-aminochloroquinoline platinum(II) derivatives (**Figure 1.29**) inhibit parasite growth between 50% to 80% in mice infected with *P. berghei.* Furthermore, these complexes were found to be non-cytotoxic against mammalian macrophage cells.[166]

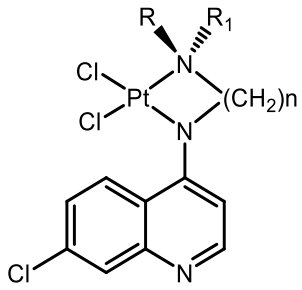

C17: n = 2, R = R_1 = H
C18: n = 3, R = R_1 = H
C19: n = 2, R = CH_2CCH; R_1 = H
C20: n = 2, R = R_1 = CH_2CCH
C21: n = 3, R = R_1 = CH_2CCH

Figure 1.29. A series of 7-aminochloroquinoline platinum(II) complexes that were synthesized by De Souza *et al.* and were found to inhibit parasite growth *in vivo* up to 80% in the *P. berghei* species.[166]

Furthermore, a very recent study by Liu *et al*. reports on a series of platinum(IV)-artesunate complexes, in which the analog in **Figure 1.30** exhibited high *in vivo* antimalarial potency against the *P. berghei* ANKA model.[167] A parasitemia of approximately 16% was observed ten days after the mice were treated with this platinum(IV) complex compared to a 36% parasitemia seen for the model.[167]

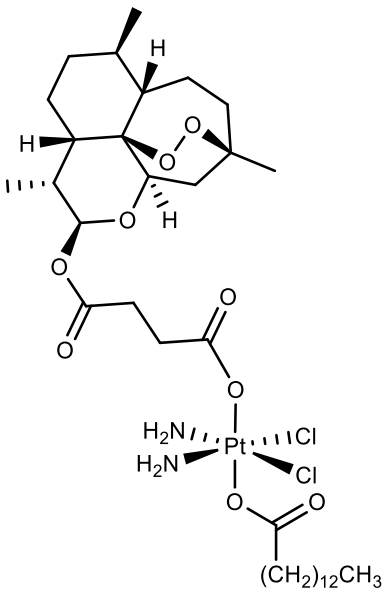

Figure 1.30. The most active platinum(IV)-artesunate complex synthesized by Chuyi Yu *et al.* exhibited *in vivo* antimalarial activity against the *P. berghei* ANKA model.[167]

The pharmaceutical properties of acyl thioureas are briefly discussed next, as it is an important scaffold used herein and in the work that has influenced this thesis.

1.6. The pharmaceutical application of acyl-thioureas

Thioureas have gained recognition for their potential medicinal application, showing antifungal,[168] antibacterial,[169] antioxidant,[170] and anti-epileptic properties.[171] The thiourea moiety has also been used to treat co-infections such as human immunodeficiency virus (HIV) and tuberculosis (TB),[172] among other medicinal applications.[173] To this end, Zahra *et al*. published a recent review article highlighting the pharmaceutical properties of several acyl-thiourea compounds.[174] This article brings to light the extensive investigation of thioureas in cancer research and the scarcity in the investigation of this scaffold as an antiplasmodium agent.

However, Verlinden *et al*.[175] reported on a series of alkylated (bis)urea and (bis)thiourea polyamine analogs that exhibit *in vitro* antiplasmodium activity against both drug-resistant (W2 and HB3) and drug-sensitive (3D7) strains of *P. falciparum*. In another study, Pingaew *et al.*[176] reported the bis-thiourea compound shown in **Figure 1.31** that exhibited antiplasmodium activity against the *Pf*-K1 strain with an IC_{50} value in the low micromolar range (1.92 μM).

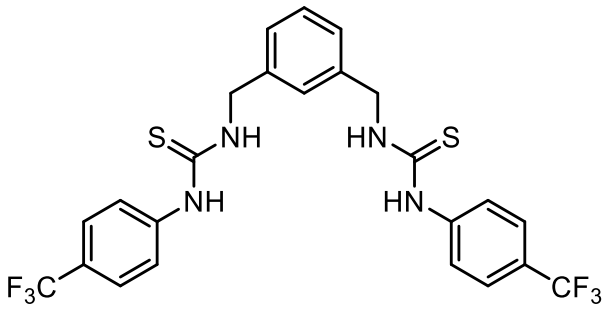

Figure 1.31. The bis-thiourea compound was synthesized by Pingaew *et al*. and evaluated for *in vitro* antiplasmodium activity.[176]

Additionally, Bissati *et al*. synthesized a series of oligoamine thioureas shown in **Figure 1.32** which exhibited whole-cell potency against the *Pf*-3D7 and *Pf*-Dd2 strains of malaria.[177] Most of these analogs had nanomolar potency with IC_{50} values between 150 nM and 650 nM. It was hypothesized that these compounds exert their potency via the inhibition of *P. falciparum* spermidine synthase.[177] Spermidine is a polyamine that is involved in several cellular processes and is essential for cell proliferation and differentiation in the parasite.[178]

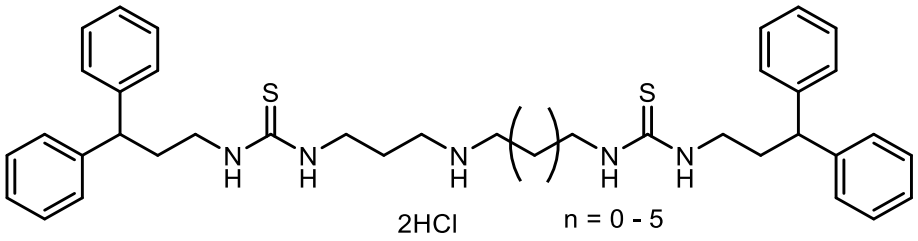

Figure 1.32. The general structure of the oligoamines synthesized by Bisatti *et al.* with antiplasmodium activity in the nanomolar range.[177]

Finally, the above summary of some of the metal complexes and ligands developed and studied for their antiplasmodium activity highlights the advantages of metal complexes in medicinal chemistry. Some of the complexes were found to be more potent against drug-resistant strains of *Plasmodium* with dual-stage activity and elicit their potency via novel MoAs. These data therefore show the scope and potential of metal complexes for development as antimalarials.

1.7. Prior research and motivation

As seen from the above examples, platinum complexes with antiplasmodium activity are often derived from known pharmacophore scaffolds. However, Egan and coworkers synthesized a series of 2,2'-bipyridine and 1,10-phenanthroline platinum(II) complexes,[179] in which the ligands exhibited no whole-cell potency. The design of the Egan *et al*. series was influenced by previous work conducted by Koch *et al*. who synthesized the series of platinum(II) complexes shown in **Figure 1.33**.[180] Koch and coworkers found that these acyl-thiourea-containing platinum(II) complexes were able to undergo concentration-dependent self-association in acetonitrile. It was proposed that the self-association occurred through π-π stacking interactions between dimers.[180]

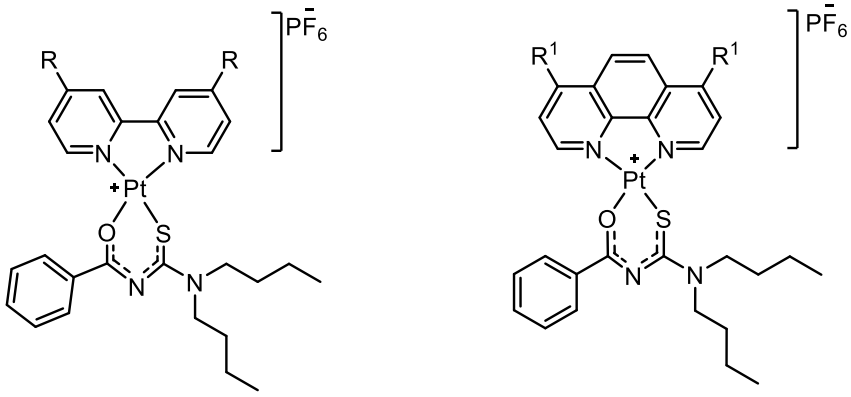

R = H (**C22.a**), Me (**C22.b**), *tert*-butyl (**C22.c**) R^1 = H (**C23.a**), Ph (**C23.b**)

Figure 1.33. The series of 2,2-bipyridine and 1,10-phenanthroline platinum(II) complexes synthesized by Koch *et al*. to investigate their self-association properties in solution.[180]

From here, Egan and coworkers hypothesized that the self-stacking capacity of the planar platinum complexes was similar to that of porphyrins. Thus, it was suggested that the complexes could associate with the heme porphyrin, Fe(III)PPIX, to inhibit the formation of β-hematin. The group then synthesized a similar series of platinum(II) complexes to the Koch study as shown in **Figure 1.34** and evaluated their whole-cell potency and capacity to inhibit β-hematin formation.[179]

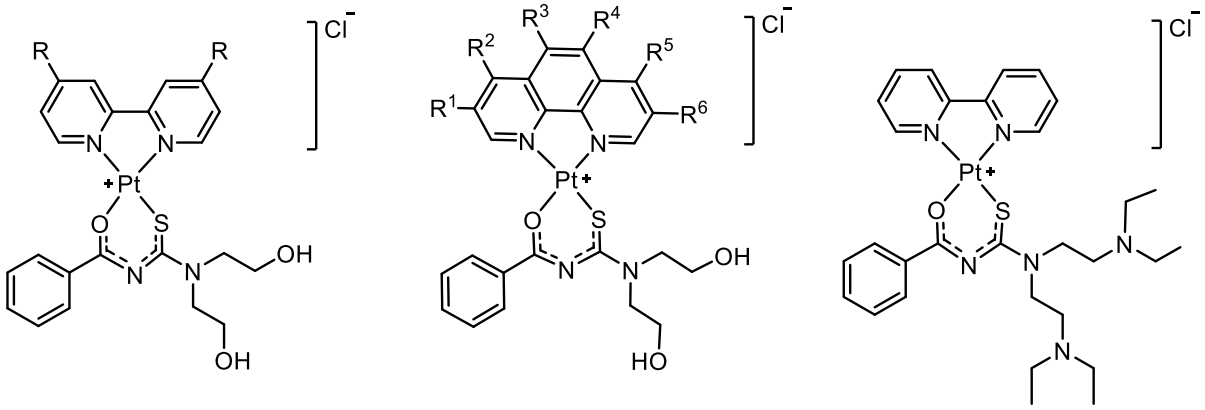

R = H (**C24.a**), Me (**C24.b**), *tert*-butyl (**C24.c**)

C26

	R^1	R^2	R^3	R^4	R^5	R^6
C25.a:	H	Me	H	H	H	H
C25.b:	H	H	Me	H	H	H
C25.c:	Me	Me	H	Me	Me	Me
C25.d:	H	H	Cl	H	H	H
C25.e:	H	H	NO_2	H	H	H

Figure 1.34. The series of mixed-ligand platinum(II) complexes that were synthesized by Egan and coworkers to evaluate their whole-cell potency against the malaria parasite and their capacity to inhibit the formation of β-hematin.[179]

As seen by the comparison of **Figures 1.33** and **1.34**, the bipyridine ligand substitutions in the two studies were identical, but the substitutions on the phenanthroline ligand differed. Additionally, the side chains in the two studies were also different as the Koch complexes had a dibutylamine chain on the acyl-thiourea ligand whereas the Egan complexes contained a diethanolamine chain. The Koch complexes also had hexafluorophosphate counterions compared to chloro counterions used in the Egan study.

Complexes **C24.a** to **C26** were evaluated for their *in vitro* antiplasmodium activity against the CQS (D10) and CQR (K1) strains of *P. falciparum* with their IC_{50} values listed in **Table 1.1**.[179] Egan *et al*. found that within their series of complexes, **C24.c** was the most active with a 4,4'-di-*tert*-butyl substituent on the bipyridine moiety.[179] However complex **C24.c** exhibited weak inhibition of β-hematin formation in their infrared (IR)-based assay and the MoA of the most active complex has since been unknown. It should be noted that the IR-based method relies on the detection of the sharp βH bands at 1660 and 1207 cm^{-1} in the IR spectrum when an inhibitor is not present (**Figure 1.35**). The results are represented as "+" (βH formation inhibitor) or "-" (not a βH formation inhibitor).[181]

Table 1.1. The IC_{50} values obtained in the Egan study where there were four independent repeats and two technical repeats (N, n = 4, 2). The inhibition of β-hematin formation activity of the complexes is also indicated.

Complex	*Pf*-D10-IC_{50} (nM)	*Pf*-K1-$IC5_0$ (nM)	Inhibition of β-hematin formation
C24.a	336 ± 76	295 ± 56	+
C24.b	295 ± 42	824 ± 102	-
C24.c	141 ± 29	119 ± 33	-
C25.a	282 ± 45	488 ± 130	+
C25.b	308 ± 64	557 ± 89	+
C25.c	602 ± 44	706 ± 95	+
C25.d	594 ± 93	666 ± 79	+
C25.e	2 927 ± 736	1 925 ± 309	+
C26	1 958 ± 85	2 378 ± 513	-

+: good inhibition activity, -: weak inhibition

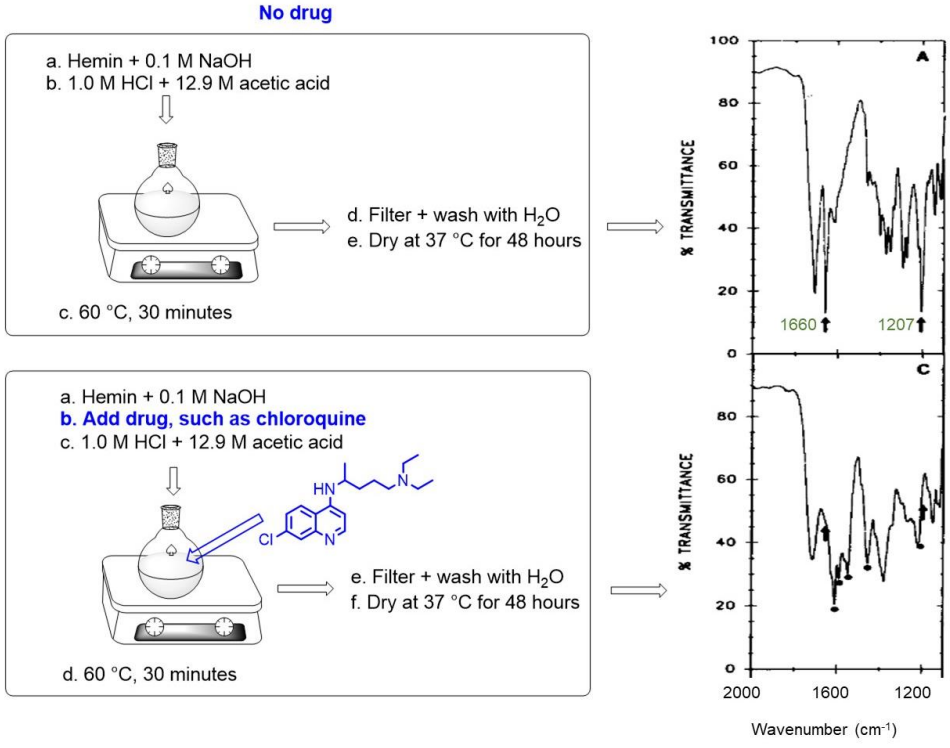

Figure 1.35. The summarized protocol for the infrared-based method of detecting β-hematin inhibition. The top panel illustrates the method for when no drug is added and the obtained infrared spectrum in which the bands at 1660 cm^{-1} and 1207 cm^{-1} for βH are observed. The bottom panel illustrates the instance in which CQ (a known inhibitor) is added and the bands corresponding to βH cannot be seen.

The disadvantages of the infrared (IR)-based assay are that it is qualitative, as βH cannot be quantified, and it requires a long drying period of 48 hours before obtaining the IR spectrum.[182] Additionally, another disadvantage to this method is the possible overlap of the functional group stretching bands of the tested compound with that of βH in the IR spectrum. This increases the susceptibility of the assay to produce false negative and positive results. Thus, Ncokazi and Egan developed a more robust method to identify β-hematin formation inhibitors that makes use of the ferrihemochrome method.[182] In this method, pyridine is added after incubation to a mixture of the test compound with hemin, NaOH, and sodium acetate. Pyridine then selectively binds to free hematin that has not formed βH. To identify whether a compound is indeed an inhibitor of β-hematin formation or not, the resulting heme pyridine, which is orange in color is spectroscopically quantified at 405 nm. However, since it was suggested that hemozoin formation is mediated through neutral lipids,[183] Carter *et al*.[28] developed an HTS assay that combines the use of lipid-mediated β-hematin formation, and the colorimetric detection described in the Ncokazi method above.[28] This is known as the NP-40 (Nonidet P-40) detergent-mediated assay and is considered more reliable than the formerly used infrared-based assay. For this assay, the detergent, NP-40 is used to mimic the lipid-water interface at which hemozoin is synthesized *in vivo*.[28] The NP-40 therefore promotes heme stacking and βH formation.[8] The assay conditions further mimic physiological conditions as compounds are incubated at 37 °C in pH ~4.9, making this method a robust way of screening for potential inhibitors of hemozoin formation. This has been demonstrated for the well-known clinical drugs, CQ and amodiaquine.[9]

1.8. Techniques for deconvolution of mechanisms of action and resistance

In addition to the NP-40 detergent-mediated βH inhibition assay described above, several other techniques have been developed to identify the possible MoA(s) and MoR(s) of experimental antiplasmodium compounds. A brief background to two of these assays, relevant for this thesis, is provided in the following sections.

1.8.1. Cellular heme fractionation assay

Identified βH inhibitors from the extracellular βH inhibition assay can be validated as bone fide hemozoin inhibitors in a cellular heme fractionation assay. This assay evaluates potential inhibition of hemozoin formation within the parasite using the method developed by Combrinck *et al*.[11] This whole-cell assay differs from the βH inhibition assay in that it quantifies the amount of three heme species (hemoglobin, free heme, and hemozoin) within the parasite after

incubation with the test compounds. However, the quantification technique is similar to that described for the βH inhibition assay above (the so-called hemochrome method) as its underlying principle is the binding of pyridine to unsequestered heme. The assay is conducted over four days and involves several steps as summarized in **Figure 1.36**.

The assay begins with treating synchronous rings of *Pf* with the test compound at concentrations below and above its IC_{50} value to elicit a dose-dependent effect. The cells are incubated for 24 to 39 hours, allowing the surviving parasites to progress to trophozoites after which they are harvested using saponin lysis. On day 3, the number of surviving parasites is counted using flow cytometry from which the concentration of heme iron in heme, hemoglobin, and hemozoin are quantified. On day 4, the three heme species are extracted from the trophozoites during a fractionation process that isolates each species via the stepwise addition of several buffers and reagents. Pyridine is added as part of the fractionation step and the absorbance of the pyridine-heme complex is measured on a multi-well plate reader. The absorbance maxima are used to calculate the percentage of each heme species in the wells. Due to its lengthy protocol and the limitation of testing only one compound per 24-well plate, the assay is not considered to be high throughput and usually only a subset of compounds are prioritized for this assay.

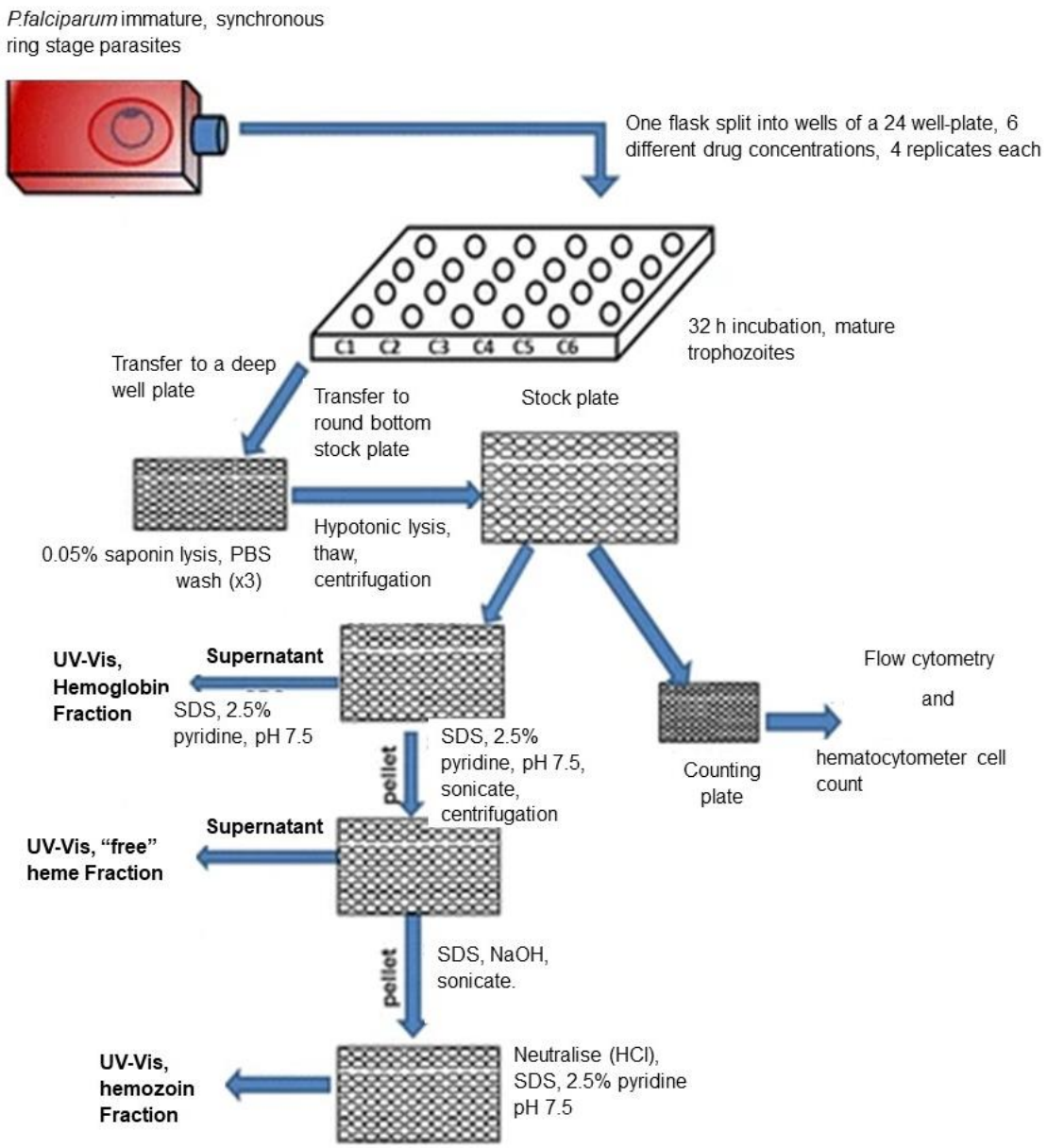

Figure 1.36. Schematic representation of the heme fractionation assay. Reproduced from Combrinck *et al*.[184]

In the study by Combrinck *et al*., the above-described cellular heme fractionation assay was validated using the known inhibitors of hemozoin formation, CQ and amodiaquine.[184] Additionally, this method has been used to validate the inhibition of hemozoin formation as a MoA of other series including benzimidazoles,[185] ferroquine-derived polyamines,[186] a 3-trifluoromethyl-1,2,4-oxadiazole analog,[187] and tetrazole-based compounds,[188] to name a few.

1.8.2. Resistance selection

The emergence of drug resistance is a common natural and clinical phenomenon that occurs for most anti-infective agents. It is defined as the reduced susceptibility of the specific organism to the test compound, often caused by a genetic mutation.[189] With the development of a reliable continuous cell culture method by Trager and Jensen,[190] measuring drug resistance *in vitro* became possible under laboratory conditions, as was described by Nguyen-Dinh and Trager for CQ using the petri-dish method (**Figure 1.37**).[191] Resistance selections, coupled with genetic approaches, are beneficial as they can identify the resistance mechanism of a compound *in vitro*. Furthermore, they can also be used as a tool to identify the MoR of a compound, which is often related to the MoA

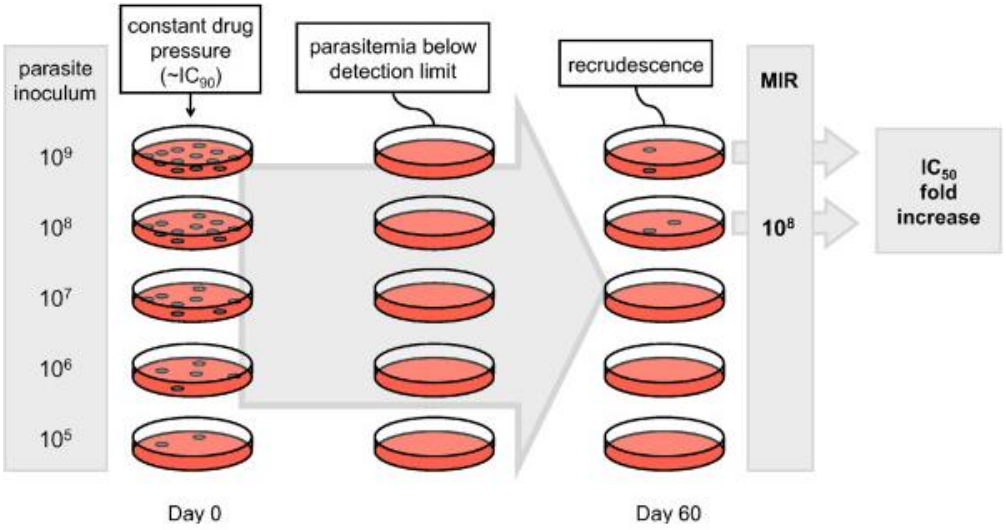

Figure 1.37. Standard protocol for *in vitro* resistance selection using various inoculum sizes in a petri dish. The minimal inoculum for resistance (MIR) represents the frequency of resistance and the IC_{50} fold increase indicates the extent of resistance. Republished from Ding *et al*.[189] under the Creative Commons Attribution 2.0 Generic.

During a resistance selection, parasites are cultured under sub-lethal concentrations of the test compound for a prolonged period, eliminating all sensitive parasites and allowing for the possible selection of resistant mutants. Additionally, parasites of varying inoculum sizes (10^5 to 10^9) can be cultured under drug pressure to determine the minimum inoculum for resistance (MIR) which ultimately identifies the frequency of resistance.[189] To optimize the chances of selecting for a resistant mutant, *in vitro* drug-resistant selections can be conducted either as a single step, stepwise, or using a pulse method.[192] The resistant selection process produces

a bulk culture of polyclonal cells; therefore, to isolate monoclonal populations, the bulk culture is cloned by limiting dilution. This dilution is based on a Poisson distribution in which the bulk culture is drastically diluted through serial dilution based on a statistical distribution of the cells in a suspension.[193] The diluted suspension is spread over a 96-well plate such that no more than half of the wells contain an individual parasite at the time of setup. Lastly, the gDNA of each clone and the parent strain (typically *Pf*-Dd2) is extracted from harvested trophozoites and whole-genome sequencing (WGS) is carried out.

As mentioned previously, the combined use of resistance selection and WGS can be a tool for identifying the target of a compound.[194] This is shown in a study conducted by Gilson *et al.* in which a series of 4-cyano-3-methylisoquinoline compounds were synthesized with antiplasmodium activity.[195] Selections using their most active compound and WGS of the isolated clones identified a single-point S374R mutation in the sodium efflux transporter gene, *Plasmodium falciparum* P-type ATPase 4 (*pfatp4*). This mutation was common to all clones and was identified as the target of the selection drug using additional target validation assays. In another study, Sonoiki *et al.* used resistance selections to identify *Plasmodium falciparum* cleavage and polyadenylation specificity factor subunit 3 (*Pf*CPSF3, which plays a role in endonuclease activity) as the target of one of their synthesized benzoxaborole compounds.[196]

1.9. Thesis rationale

The ongoing challenges of malaria on the global health system calls for a significant shift in research efforts. Many existing antimalarial compounds have single-stage activity and only act against the ABS of the parasite life cycle. Despite the remarkable progress made in malaria drug discovery over the years, a large portion of the research has focussed on organic scaffolds with well-defined MoAs. This has left a critical gap in the field which can be filled by metal complexes. The use of metals in antimalarial therapy has not only shown to improve the whole-cell potency of known pharmacophores but also to present novel MoA with the ability to withstand resistance (as highlighted in the discussion of FQ). As such, the rationale of this thesis is to fill the gap between malaria drug discovery and inorganic chemistry to further emphasize the advantages of metalloantimalarials. Furthermore, the work previously conducted in the Egan group has presented an inorganic scaffold with proven whole-cell potency against both the CQS and CQR strains of *P. falciparum* in which the compounds were rationally designed, considering a well-defined target (hemozoin formation inhibition). Thus, there is a need to expand on the previously synthesized metal-based chemical series towards a deeper understanding of SARs and structure-property relationships (SPRs) of this scaffold.

Additionally, their MoA can be further investigated using more advanced assays and approaches compared to the prior work.

1.10. Aims and objectives

The overall aim of this thesis was to design and synthesize new chemical matter with potential dual-stage antiplasmodium activity that can withstand resistance. Additionally, given the previous study from the Egan group, the work in this thesis aimed to resynthesize the mixed-ligand acyl-thiourea-bipyridine platinum(II) complexes. This was done to reevaluate their whole-cell potency and their capacity to inhibit β-hematin formation using the detergent-based assay. From here, several chemical modifications were made to further evaluate their SARs and SPRs to identify the most potent compounds with favorable drug-like properties. The MoA and MoR of these complexes were probed through several extracellular and whole-cell experiments, using phenotypic and genomic approaches.

1.10.1. Specific objectives

To accomplish the aims mentioned in **Section 1.10.1**, the specific objectives of this work were:

1. To resynthesize the three substituted bipyridine complexes from the Egan study and reevaluate their whole-cell potency and capacity to inhibit β-hematin formation.
2. To rationally design compounds based on structural modifications to enhance whole-cell potency and drug-like properties.
3. To synthesize a fluorescent probe of the mixed-ligand platinum(II) complexes to investigate its intracellular localization.
4. To determine the SAR and SPR profiles of the chemical series.
5. To probe the MoA of the complexes using a cellular heme fractionation assay to determine if they inhibit hemozoin formation within the *P. falciparum* parasite.
6. To analyze the ability of selected complexes to accumulate within the parasitic digestive vacuole via inoculum effect experiments.
7. To evaluate the photophysical properties of the fluorescent probe and its cellular localization using fluorescent microscopy studies.
8. To determine the electrochemical properties of the complexes and identify if they correlate to a possible MoA via oxidative stress.
9. To investigate the MoR of selected complexes using resistance selections and whole-genome sequencing of mutants.

Chapter 2: Design, Synthesis, and Characterization of Mixed-ligand Platinum(II) and Gold(III) Complexes

2.1. Introduction

This chapter describes the design, chemical synthesis, and characterization of the mixed-ligand platinum(II) and gold(III) complexes and their precursors. The synthesis started with previously reported complexes,[179] as described in **Section 1.7** and, from there, chemical modifications were explored based on the Craig plot to rationally design a series of compounds that allowed for subsequent evaluation of structure-activity relationships (SARs) and structure-property relationships (SPRs) arising from six sites of chemical modification. Certain mechanistic details of many reported synthetic reactions are well-known and have been referenced in this thesis. Selected compounds have been chosen as representatives for characterization and their ^{1}H-NMR spectra and HPLC-MS chromatograms are annotated herein.

2.2. Design

Since the primary design of the metal complexes synthesized herein stems from those previously reported.,[179] changes to six chemical regions on the original scaffold were explored and are numbered accordingly in **Figure 2.1.**

The substituent in the 4,4-position on the bipyridine ligand was varied (**1**), a substituent was added in the *para*-position of the acyl thiourea ligand (**2**), the position of the substituent on the bipyridine was changed from a position of 4,4'-dimethyl to 5,5'- and 6,6'-dimethyl (**3**), the chloride counterion was exchanged for nitrate and hexafluorophosphate (**4**), replacement of diethanolamine chain with *N*-amino-ethyl-ethanolamine (**5**) and, lastly, the platinum(II) metal center was changed to gold(III) (**6**). Several other metal centers have been employed in the development of metalloantimalarials[197] but, to keep the geometry around the metal center constant (square planar), a gold(III) replacement was chosen for this section of work. Gold has often been used as a therapeutic agent in other disease areas such as arthritis therapy,[198] cancer,[199] and malaria.[200] Furthermore, only one structural modification was conducted per numbered change to the chemical space, e.g. the 4,4'-di-*tert*-butyl remained constant for

change-**2** and change-**3** and the *para*-H constant for change-**4**. This was done so that the SARs and SPRs could be more accurately evaluated by referring to matched pairs.

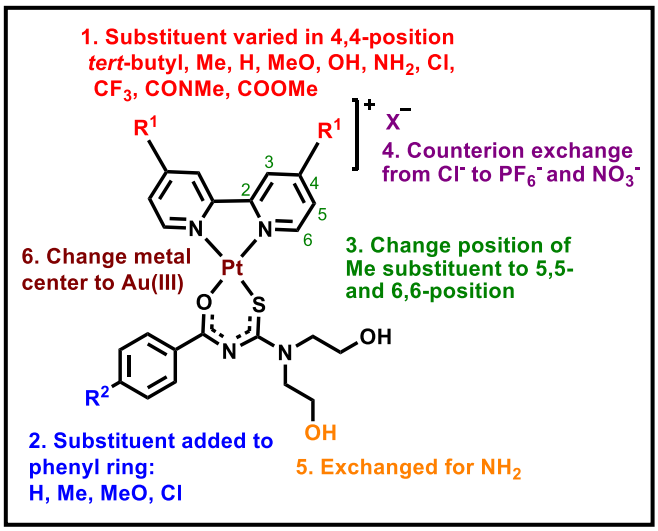

Figure 2.1. The six chemical modifications used to explore the SARs and SPRs of this series of metal complexes.

The R^1 and R^2 substituents (**Figure 2.1**) were selected from the four quadrants of the Craig plot (**Figure 2.2**). Two or more substituents per quadrant were prioritized to produce a chemical series that had sufficiently contrasting electronic and hydrophobic properties to span a range of potential physiochemical and biological properties. The Craig plot describes two physiochemical properties of a substituent, viz. the Hammett σ constant (electron-donating properties) and the Hansch–Fujita π parameter (hydrophobicity).[201] Silver nitrate and potassium hexafluorophosphate were selected for the counterion exchanges based on reagent availability and ease of synthesis. For chemical modification **3** (substitution on bipyridine), the methyl substituent was selected owing to the commercial availability of the necessary synthetic starting materials to evaluate the regio-specific biological activity.

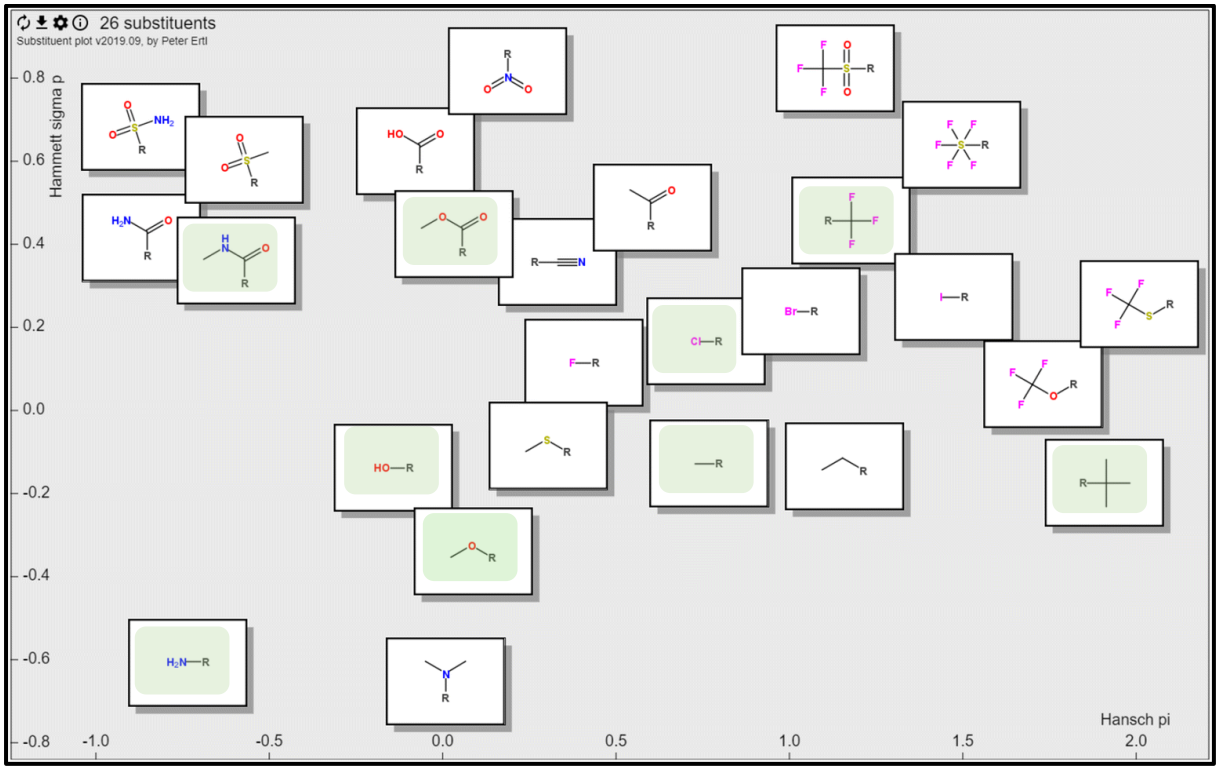

Figure 2.2. An illustration of a Craig plot[202] with the substituents used for the SAR studies in this work highlighted in green. A Craig plot allows for the visualization, analysis, and bioisosteric selection of substituents for drug design.[202]

2.3. Chemistry

The synthetic procedures for complexes **4a-4k** and their precursors follow methods reported in the literature and were adapted for the different analogs accordingly.[179]

2.3.1. Synthesis and characterization of thiourea ligands

For the synthesis of the acyl-thiourea ligands **1a-1d**, the respective benzoyl isothiocyanate was reacted with diethanolamine, resulting in the formation of compounds **1a-1d** with high yields (**Scheme 2.1**). The chemical structures of the ligands **1a-1d** were confirmed using ^{1}H-NMR spectroscopy (**Figure 2.3**) and HPLC-MS ESI. Compound **1d** was used without further purification in the subsequent reaction.

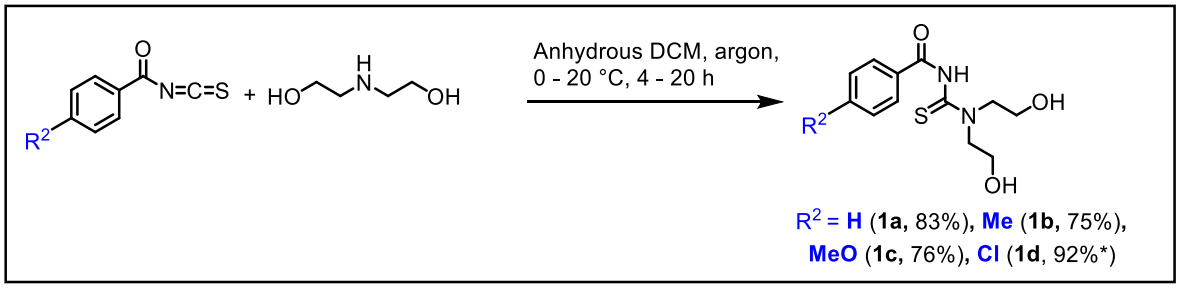

Scheme 2.1. Synthesis of acyl-thiourea ligands (compounds **1a-1d**) with varying R^2 substituents in the *para* position of the phenyl ring. Compound **1d** was isolated as a crude product (*) with a 92% yield and was taken forward to subsequent reactions without further purification.

The ^{1}H-NMR spectra of compounds **1a**-**1c** are consistent with the proposed structures in which all proton signals display the expected integration and multiplicities, as shown in **Figure 2.3**. The alkyl chain of compounds **1a-1c** gives rise to two sets of resonances due to the restricted rotation around the amine/thiocarbonyl bond. The proton signals of H-3,3' and H-4,4' in compound **1a** appear as a doublet and triplet at 7.9 ppm and 7.5 ppm, respectively, and the proton resonance of H-5 appears at 7.6 ppm. The increased electron density from the methyl and methoxy substituents in compounds **1b** and **1c**, respectively, gives rise to aromatic proton resonances that are further upfield compared to those in compound **1a**. Furthermore, the CH_3 proton resonances of **1c** (2.4 ppm) are more upfield than that of **1b** (3.8 ppm) due to the increased electron-donating ability of the methoxy relative to the methyl substituent.

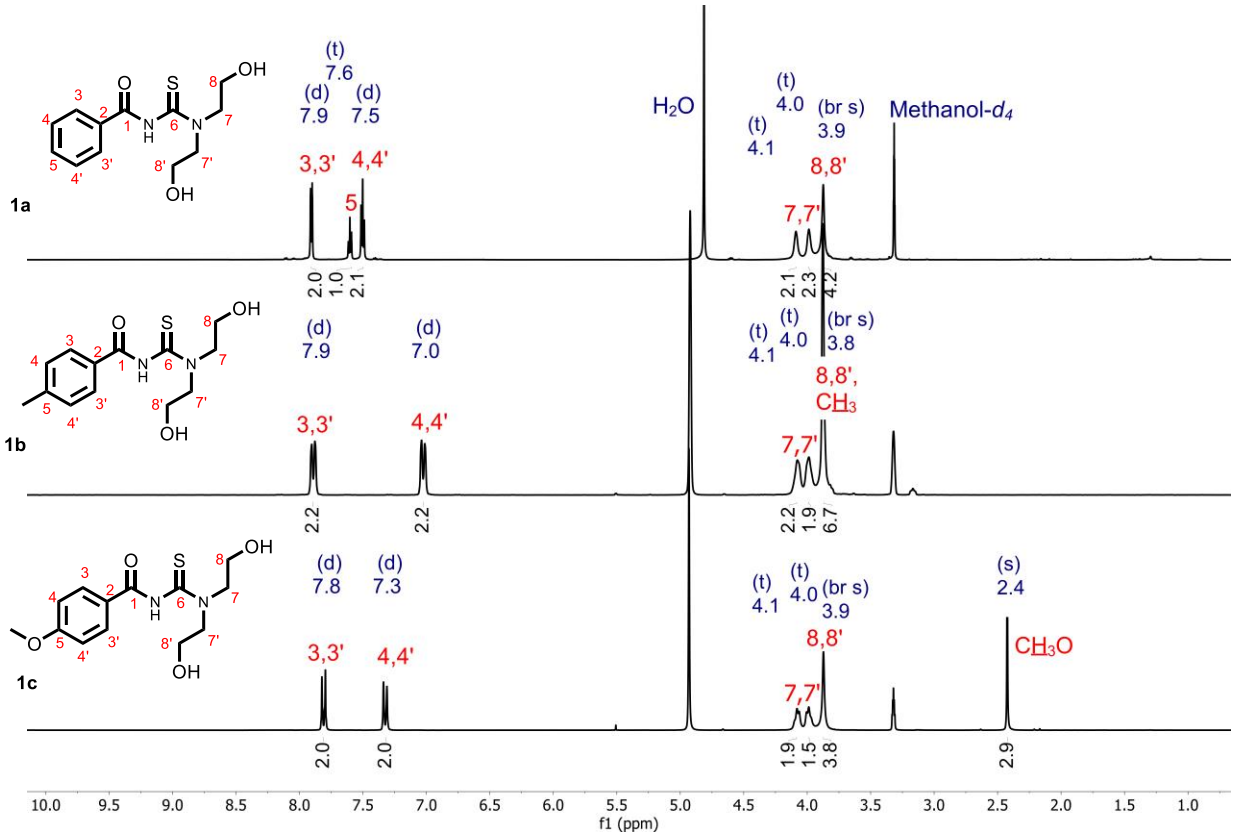

Figure 2.3. Stacked ^{1}H-NMR spectra of the acyl-thiourea ligands **1a-1c** in methanol-d_4**,** showing the proton chemical shifts in the different *para*-substituted analogs. The chemical shifts (in ppm) and peak multiplicities are displayed in blue, the integration values in black, and the proton assignments are displayed in red.

2.3.2. 4,4'-R[1]-2,2'-bipyridine

Substituted bipyridine analogs from the top left side of the Craig plot (electron-withdrawing, more lipophilic substituents) were also included in the series of synthesized compounds via [2,2'-bipyridine]-4,4'-dicarboxylic acid in a condensation reaction, giving rise to compounds *N*[4],*N*[4]'-dimethyl-[2,2'-bipyridine]-4,4'-dicarboxamide (**2a**) and dimethyl [2,2'-bipyridine]-4,4'-dicarboxylate (**2b**).(**Scheme 2.2.**). Triethylamine (Et_3N) was used as the base in combination with hexafluorophosphate azabenzotriazole tetramethyl uronium (HATU) as the coupling reagent. Compound **2a** was synthesized in the aprotic solvent dimethyl formamide (DMF), whereas compound **2b** was synthesized using methanol (MeOH) as the solvent and alcohol source for esterification.

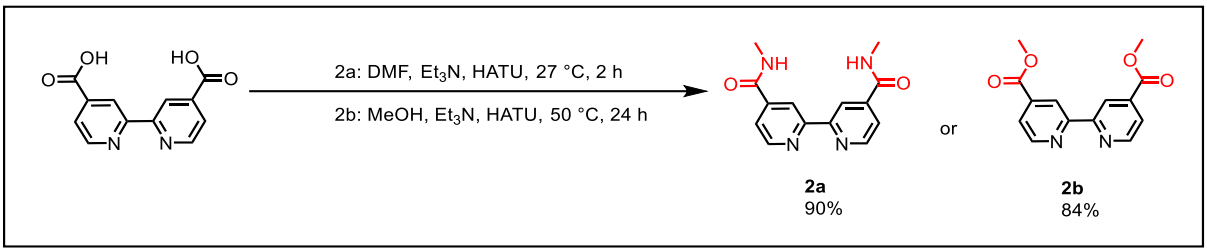

Scheme 2.2. Synthetic method for the methyl amide (**2a**) and methyl ester (**2b**).

The ^{1}H-NMR spectra of compounds **2a** and **2b** (**Figure 2.4**) both show a doublet, a doublet of doublets (H-a,a' and H-b,b') and a singlet (H-d,d') in the aromatic region, each integrating for two protons. The methyl proton signals appear at 2.85 ppm and 3.30 ppm (overlapping with the water peak) for the methyl amide (**2a)** and ester (**2b**), respectively, both integrating for six protons as expected. Additionally, the ^{1}H-NMR spectrum of **2a** has a doublet at 8.9 ppm, integrating for the two amide protons of the compound on each pyridyl ring, confirming successful amide coupling.

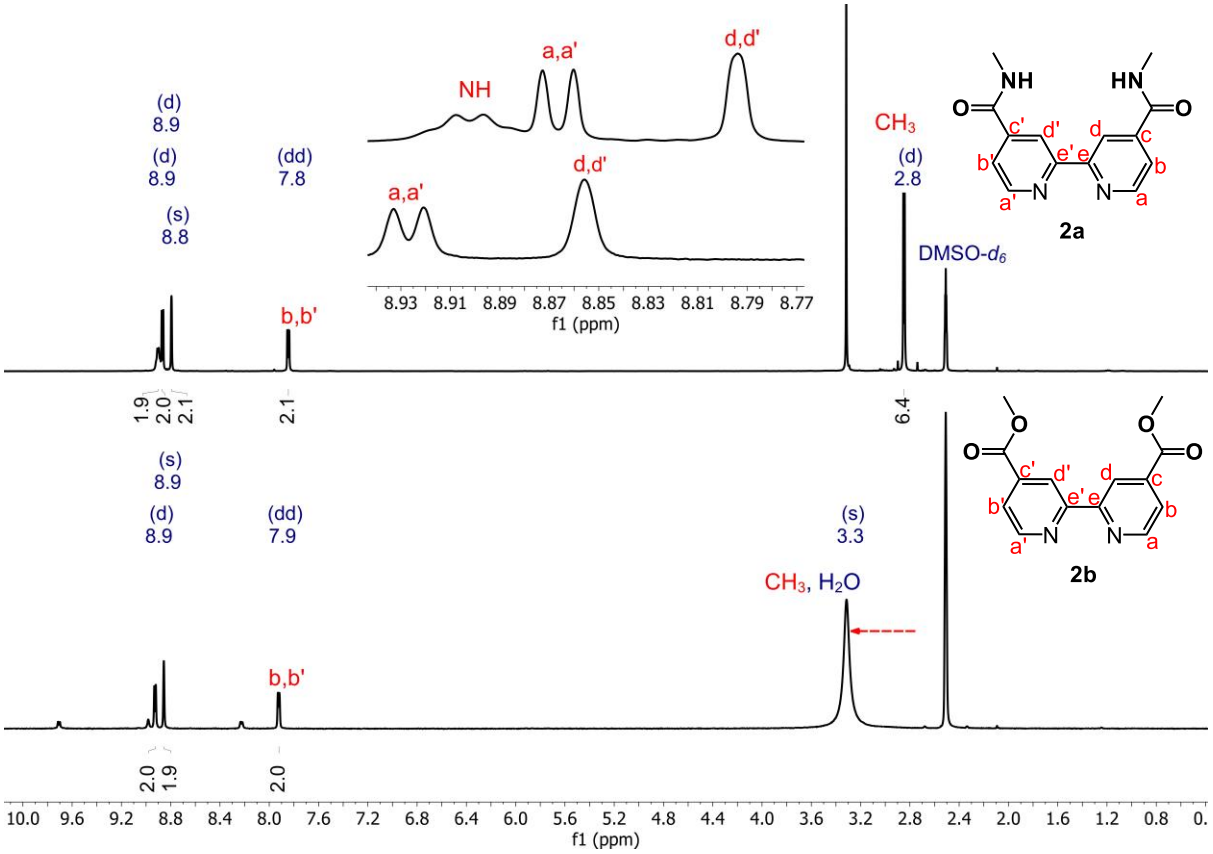

Figure 2.4. Stacked ^{1}H-NMR spectra of compounds **2a** (top) and **2b** (bottom) obtained in DMSO-d_6 show the aromatic protons of the two compounds in similar chemical environments as their chemical shifts are comparable. The methyl protons appear more downfield for compound **2b**, owing to the bonding of its carbon to the more electronegative oxygen, compared to nitrogen in **2a**, which results in a deshielding effect on the attached protons. The chemical shifts (in ppm) and peak multiplicities are displayed in blue, the integration values in black, and the proton assignments are displayed in red.

2.3.3. [$PtCl_2$(diimine)] complexes

The [$PtCl_2$(diimine)] precursor complexes (**3a** - **3j**) were synthesized according to the method described by Morgan *et al.*[203] which involves the addition of the relevant bipyridine to a solution of potassium tetrachloroplatinate in either acidified distilled water or neutral distilled water at 95 °C. The addition of 4 M HCl reduces the aquation of the [$PtCl_4$] species, improving the yield of the complex formed. Where R^1 = NH_2 and COOMe, HCl was omitted due to the likely protonation of NH_2 and hydrolysis of COOMe under acidic conditions, respectively. The [$PtCl_2$(diimine)] complexes were isolated as yellow or brown solids in moderate to high yields (**Scheme 2.3**). The poor solubility of complex **3c** in the available deuterated-NMR solvents (dimethyl sulfoxide-d_6, methanol-d_4, chloroform-d_2, acetone-d_6, and acetonitrile-d_3) prevented its complete characterization using NMR spectroscopy, but the compound was progressed to the next synthetic step. The crude products of complexes **3f** and **3j** were taken forward into the next synthetic step without further purification. Complex **3a** is used as a representative for the ^{1}H-NMR spectral analysis discussion of these precursor complexes (**Figure 2.5.**).

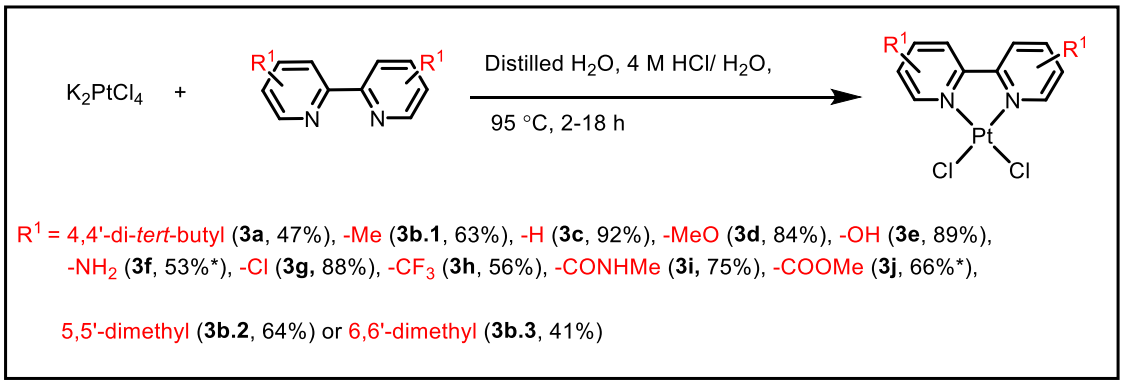

Scheme 2.3. Synthetic scheme for the [$PtCl_2$(diimine)] complexes. The asterisk represents compounds isolated as crude products.

In the ^{1}H-NMR spectrum of **3a**, platinum satellites are seen next to the proton signal of H-a,a', as indicated by the arrows in **Figure 2.5**. ^{195}Pt is NMR-active, caused by the spinning of its charged nucleus around an axis that generates a dipole moment that can be recorded by an NMR spectrometer. These satellites are not a result of proton-proton coupling but rather appear due to the coupling of H-a and H-a' to platinum. However, these satellites are not always visible and are not apparent in the spectra of the remaining [$PtCl_2$(diimine)] precursor complexes (compounds **3b** - **3j**), some of which are shown in **Figure 2.6**. In the ^{1}H-NMR spectrum of **3a**, two doublets corresponding to H-a,a' and H-d,d' are seen at 9.5 ppm and 7.9 ppm, respectively. A doublet of doublets is seen at 7.6 ppm corresponding to H-b,b' as they couple to H-a,a' and H-d,d' with coupling constants J = 6.0 Hz and 3.0 Hz, respectively. Each of these aromatic signals integrates for the expected two protons. There is an intense singlet in the aliphatic region at 1.4 ppm, integrating for the eighteen CH_3 protons.

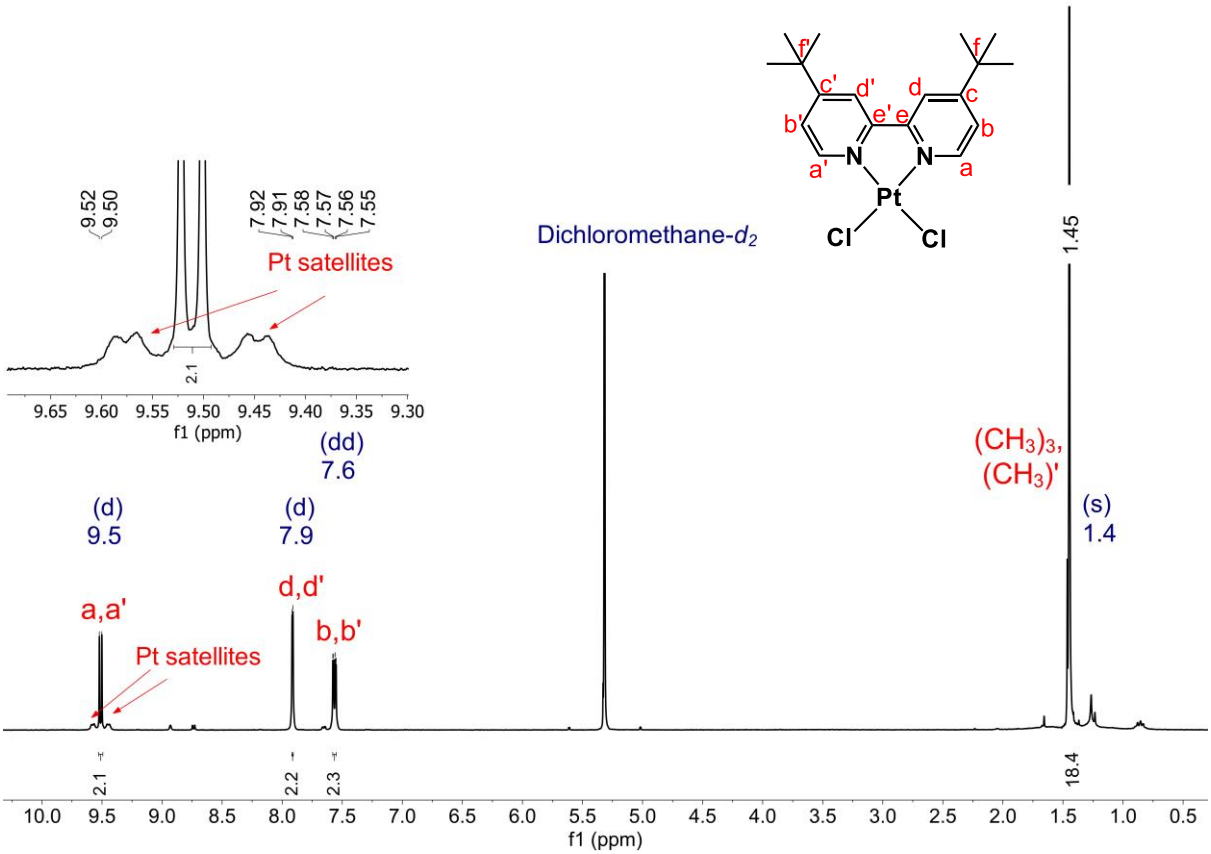

Figure 2.5.^{1}H-NMR spectrum of the [$PtCl_2$(diimine)] compound **3a** in dichloromethane-d_2 shows platinum satellites next to H-a,a'. The chemical shifts (in ppm) and peak multiplicities are displayed in blue, the integration values in black, and the proton assignments are displayed in red.

The ^{1}H-NMR spectra of the remaining 4,4-di-substituted [$PtCl_2$(diimine)] precursor complexes are shown in **Figure 2.6**. The [$PtCl_2$(diimine)] complexes with the more electron-withdrawing substituents have more deshielded proton signals than the analog containing the electron-donating OH substituent (**3e**). For all the [$PtCl_2$(diimine)] precursor complexes, each proton signal integrates for the two chemically equivalent protons on each pyridyl ring. In the ^{1}H-NMR spectrum of compound **3j**, the proton signals of unreacted precursor compound **2b** are indicated with an asterisk. Compound **3j** was therefore used as a crude mixture for the subsequent reaction to synthesize compound **4j** where impurities were removed using column chromatography.

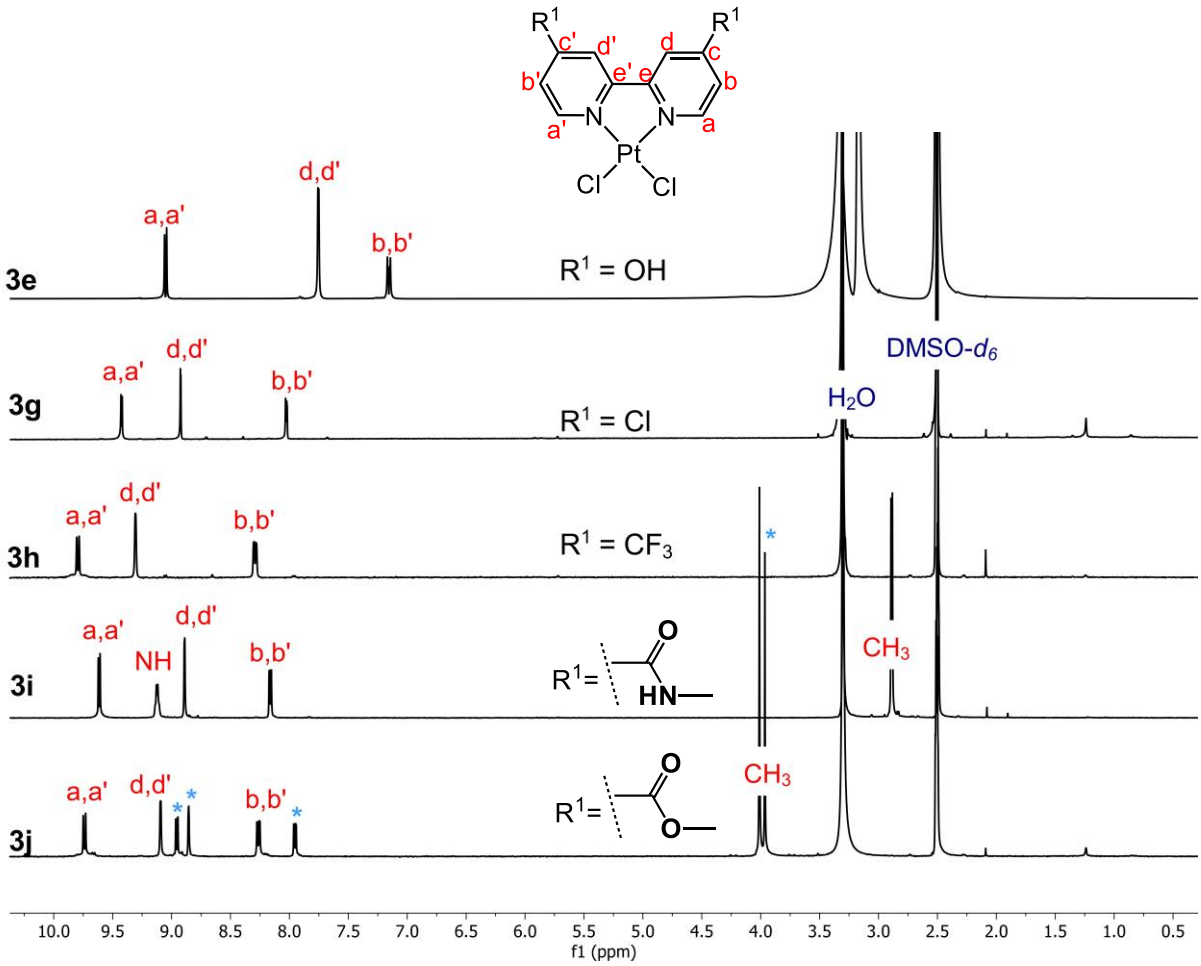

Figure 2.6. Stacked ^{1}H-NMR spectra of the [$PtCl_2$(diimine)] compounds in DMSO-d_6 showing the variation in the chemical shifts of analogs containing different substituents in the 4,4'-position of bipyridine. The asterisk indicates signals belonging to impurities from the ligand **2b**. The chemical shifts (in ppm) and peak multiplicities are displayed in blue, the integration values in black, and the proton assignments are displayed in red.

General spectroscopic analysis of metal complexes compared to their parent ligand shows that the resonance of protons on the carbon adjacent to the nitrogen undergo upfield shifts upon complexation. This is caused by a synergic effect which results in electrons from a filled π-orbital on the ligand being donated to an empty metal orbital. Subsequently, electrons from a filled d-orbital on the metal center are synergistically back-donated to an empty π*-antibonding orbital on the ligand.[204] This back-donation shields the surrounding aromatic protons, resulting in an upfield shift of their proton resonances. However, upon complexation of the 4,4′-di-substituted-2,2′-dipyridyls to the platinum metal center, all the aromatic protons shift downfield as represented in **Figure 2.7** by the dichloro analog, **3g**. This downfield shift is due to the electron-deficient metal center, likely caused by the inductive electron-withdrawing effect from the platinum-bound chloride ancillary ligands. The chloride ligands attract electrons more strongly than the pyridyl nitrogen atoms, deshielding the bipyridine protons and resulting in a downfield shift of their proton resonances.

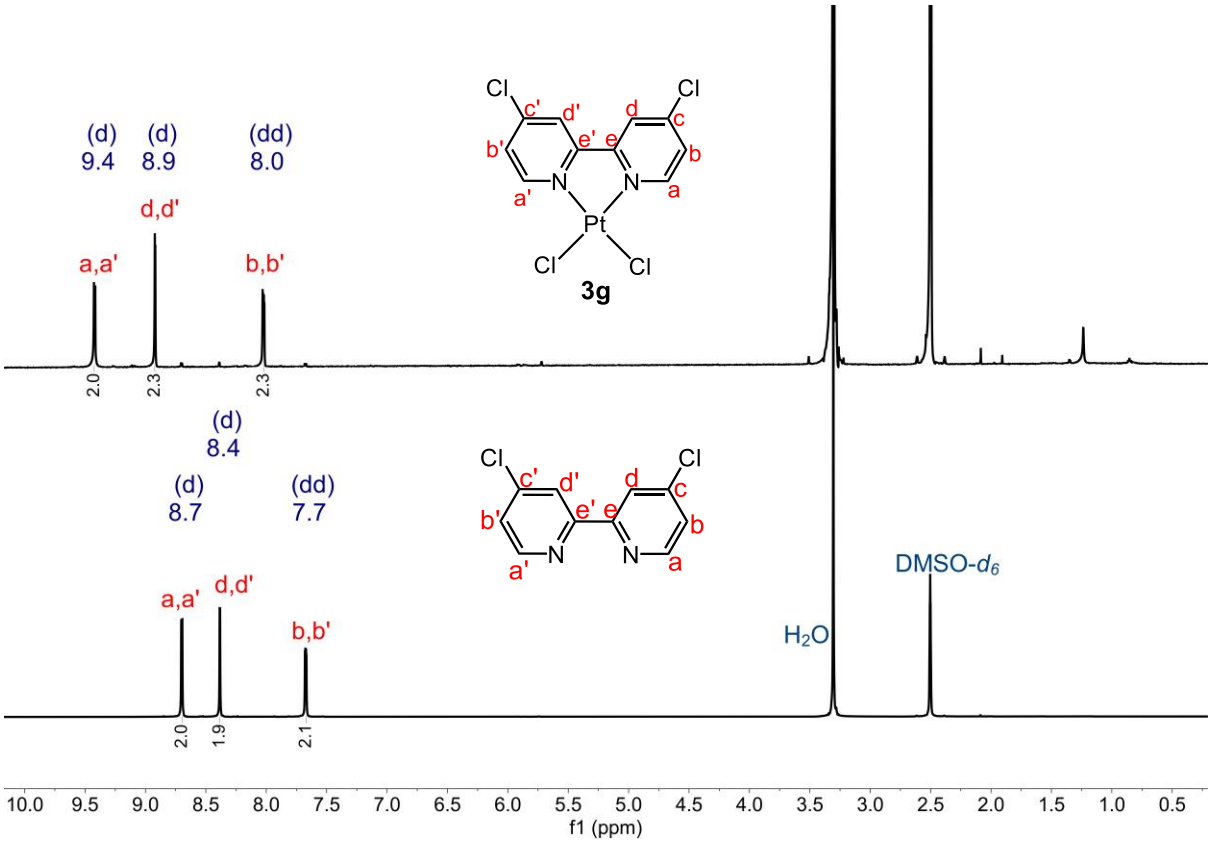

Figure 2.7. Stacked ^{1}H-NMR spectra of compound **3g** (top) and commercially purchased 4,4'-dichloro-2,2'-bipyridyldichloroplatinum(II) (bottom) in DMSO-d_6, showing the downfield shifts of the aromatic protons upon complexation of the bipyridine to the platinum(II) center. The chemical shifts (in ppm) and peak multiplicities are displayed in blue, the integration values in black, and the proton assignments are displayed in red.

When the position of the disubstituted methyl substituents was changed from the 4,4'- to the 5,5'-positions, there were no significant shifts in the proton resonances of H-a,a' and H-d,d' (**Figure 2.8**). However, moving the methyl to the 6,6'-position shifted the aromatic proton resonances upfield. This is likely caused by the methyl substituents being proximally closer to the platinum center in the 6,6'-position. Consequently, the electron-donating nature of the closer methyl substituent causes more backdonation and subsequently more shielding to the surrounding protons. The proton chemical shifts of the methyl group show a negligible shift across all three analogs and are observed next to the DMSO-d_6 solvent peak at 2.6 ppm.

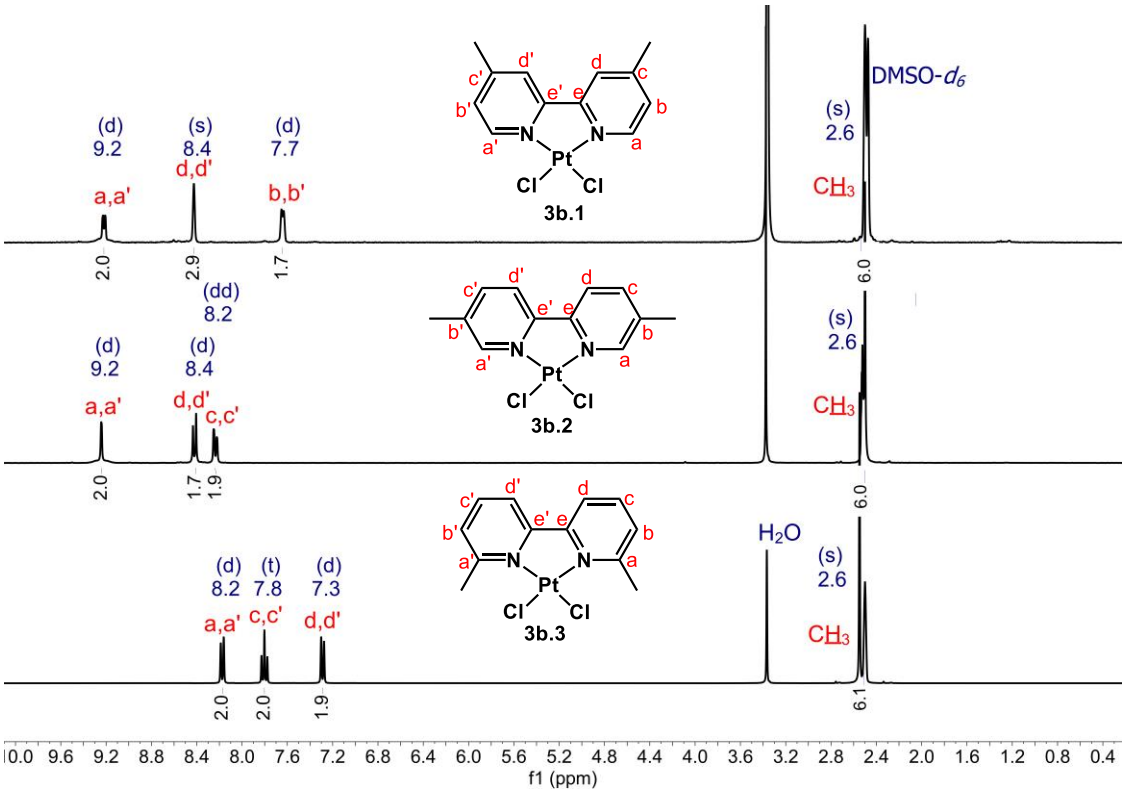

Figure 2.8. Stacked ^{1}H-NMR spectra of the methyl [$PtCl_2$(diimine)] compounds **3b.1**, **3b.2,** and **3b.3**, showing that moving the methyl groups to the 6,6'-position causes an upfield shift in the aromatic proton resonances. The CH_3 protons show a negligible difference in chemical shifts across all three analogs with its signal residing to the left of the DMSO-d_6 solvent signal at 2.6 ppm. The chemical shifts (in ppm) and peak multiplicities are displayed in blue, the integration values in black, and the proton assignments are displayed in red.

2.3.4. [Pt(diimine)(L-O,S)]$^+$ complexes

The [Pt(diimine)(L-O,S)]$^+$ complexes **4a-4j** were synthesized using methods previously described for analogs **4a**-**4c**.[179] The reaction proceeds with the dropwise addition of the relevant acyl-thiourea and Et_3N in either DMF, acetone, or MeCN to a suspension of the respective $PtCl_2$(diimine)] complex in the same solvents (**Scheme 2.4, A**). According to the hard and soft acids and base (HSAB) theory, platinum(II) is a soft acid and first reacts with the 'softer' sulfur before binding to the 'harder' oxygen atom upon deprotonation of the amine nitrogen (**Scheme 2.4, B**). Complexes **4a-4j** were isolated as yellow or brown solids in low to high yields.

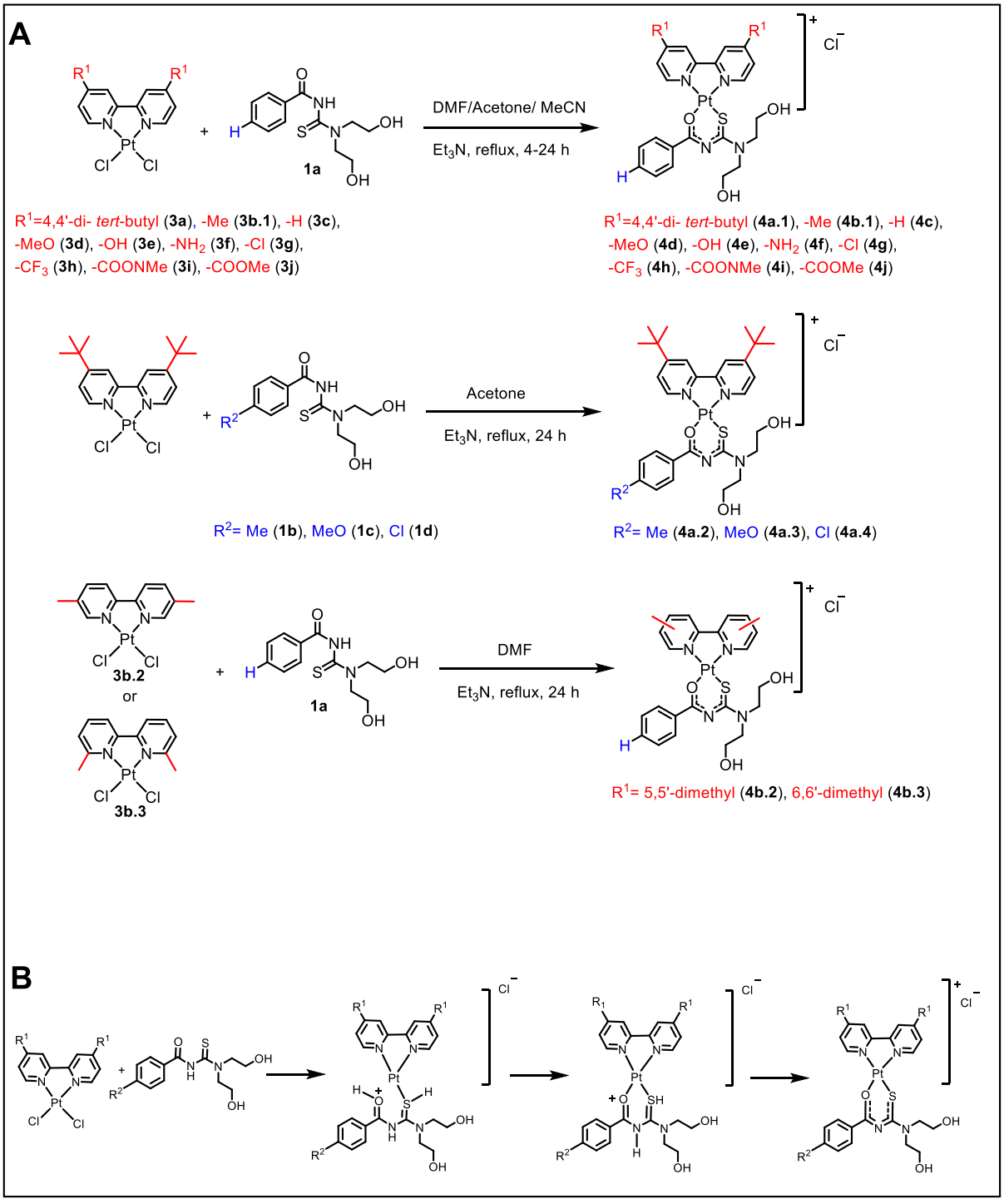

Scheme 2.4. A: Synthetic scheme for [Pt(diimine)(L-O,S)]$^+$ complexes, showing three of the six chemical modifications. B: Reaction mechanism highlighting the HSAB theory, in which the soft platinum(II) binds to the softer sulfur atom first before the harder oxygen atom.

Spectroscopic analyses of complexes **4a** - **4j** show all proton signals from both the bipyridine and acyl-thiourea moiety present with the correct integrations and multiplicities (**Chapter 7, Section 7.2.3.4**). Due to similar shifts being observed in the proton resonances of all the complexes, **4d** was selected for the characterization discussion of these $[Pt(diimine)(L\text{-}O,S)]^+$ complexes. The ^{1}H-NMR and ^{13}C-NMR spectra of **4d** (**Figures 2.9** and **2.10**) are presented as representatives for this discussion. Upon complexation of the acyl-thiourea ligand (**1a**) to the precursor complex (**3d**), the bipyridine aromatic proton signals (H-a,d,b) split into two sets (not observed in the precursor complexes (**3a - 3l**). This arises due to the loss of symmetry upon complexation, caused by the asymmetric acyl-thiourea moiety. Two triplets are seen at 5.2 ppm and 5.1 ppm, respectively, each integrating for one hydroxyl proton of the ethanolamine chain (**Figure 2.9**). These triplets are not seen in the ^{1}H-NMR spectra of the complexes obtained in methanol-d_4 (**4g**, **4h,** and **4a.2**) as these protons are exchangeable (**Section 7.2.3.4**).

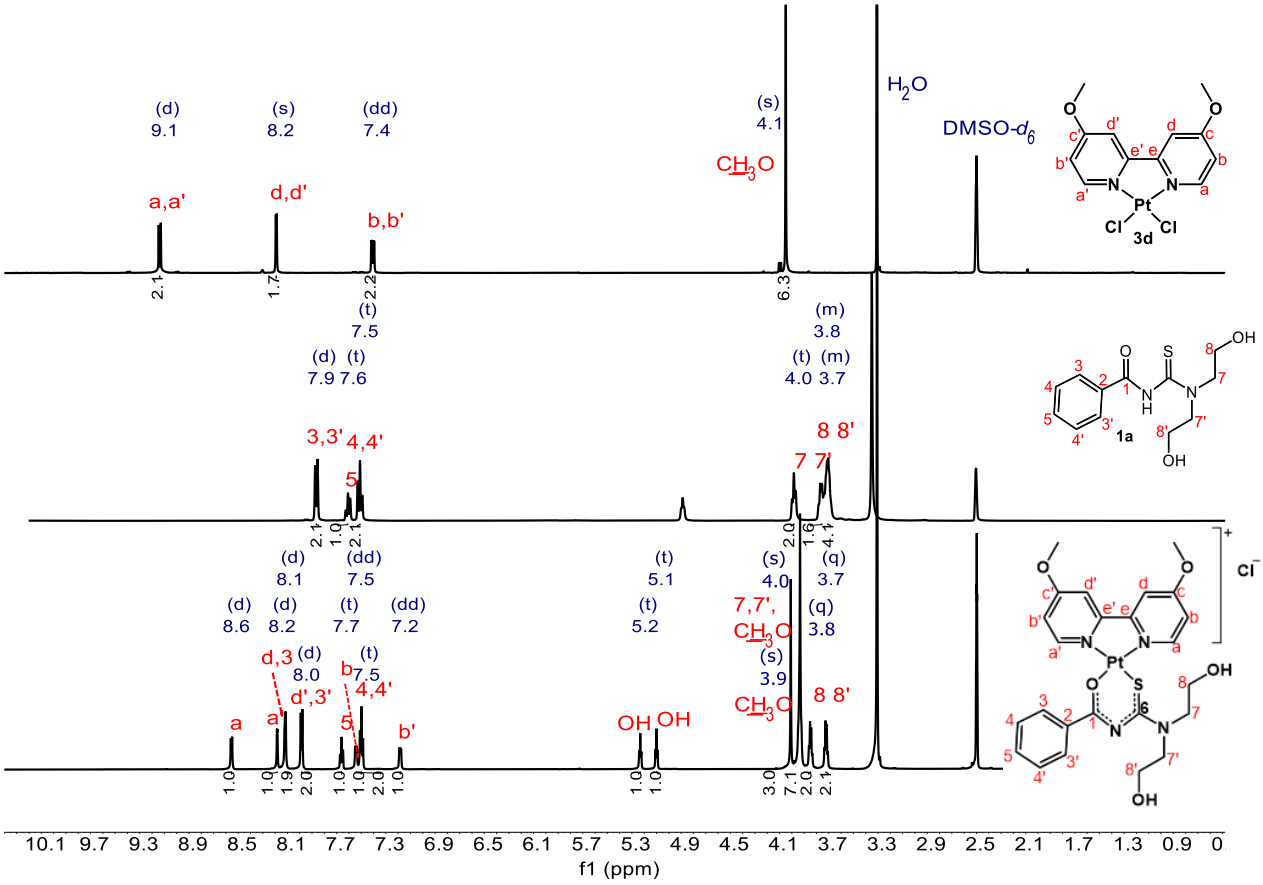

Figure 2.9. Stacked ^{1}H-NMR spectra of compounds **1a** (middle), **3d** (top), and complex **4d** (bottom) in DMSO-d_6, showing the change in chemical shift upon complexation. The chemical shifts (in ppm) and peak multiplicities are displayed in blue, the integration values in black, and the proton assignments are displayed in red.

Furthermore, analysis of the ^{13}C-NMR spectrum of **4d** (**Figure 2.10**) shows signals corresponding to the expected 24 carbon atoms, further confirming the presence of the suggested complex. Additionally, HPLC-MS analysis confirmed the presence of the parent ion with $[M\text{-}Cl]^+$ with a *m/z* 678.1 and a calculated value of 678.65.

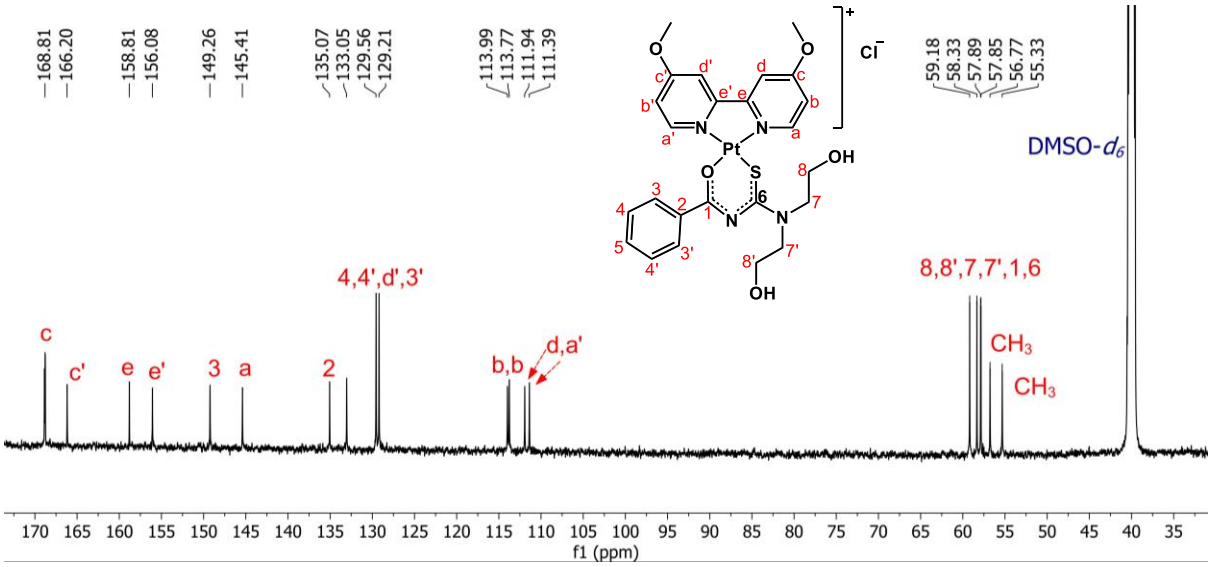

Figure 2.10.^{13}C-NMR spectrum of complex **4d** in DMSO-*d*$_6$ shows all the signals for the 24 expected carbon atoms. The chemical shifts are shown in black on top of the spectrum and carbon atom assignments in red.

In the ^{1}H-NMR spectra of complexes **4b.1** (2D-COSY NMR spectrum shown in **Figure 2.11**), **4d** (**Figure 2.10**), **4a.3** (not shown), and **4b.2** (not shown) the proton signals for H-7,7' appears as an intense "singlet", integrating for four protons as opposed to the expected triplet seen for the other complexes. This likely occurs because the proton resonances of these two sets of protons are indistinguishable at this resolution and cause an increase in intensity at 3.92 ppm. A representative 2D-COSY NMR spectrum of **4b.1** was obtained and is shown in **Figure 2.11**. The 2D-COSY NMR spectrum of **4b.1** attests to its structural integrity and confirms the correct assignment of protons H-7,7', as seen by the cross-peaks from H-7,7' to H-8 and H-8'.

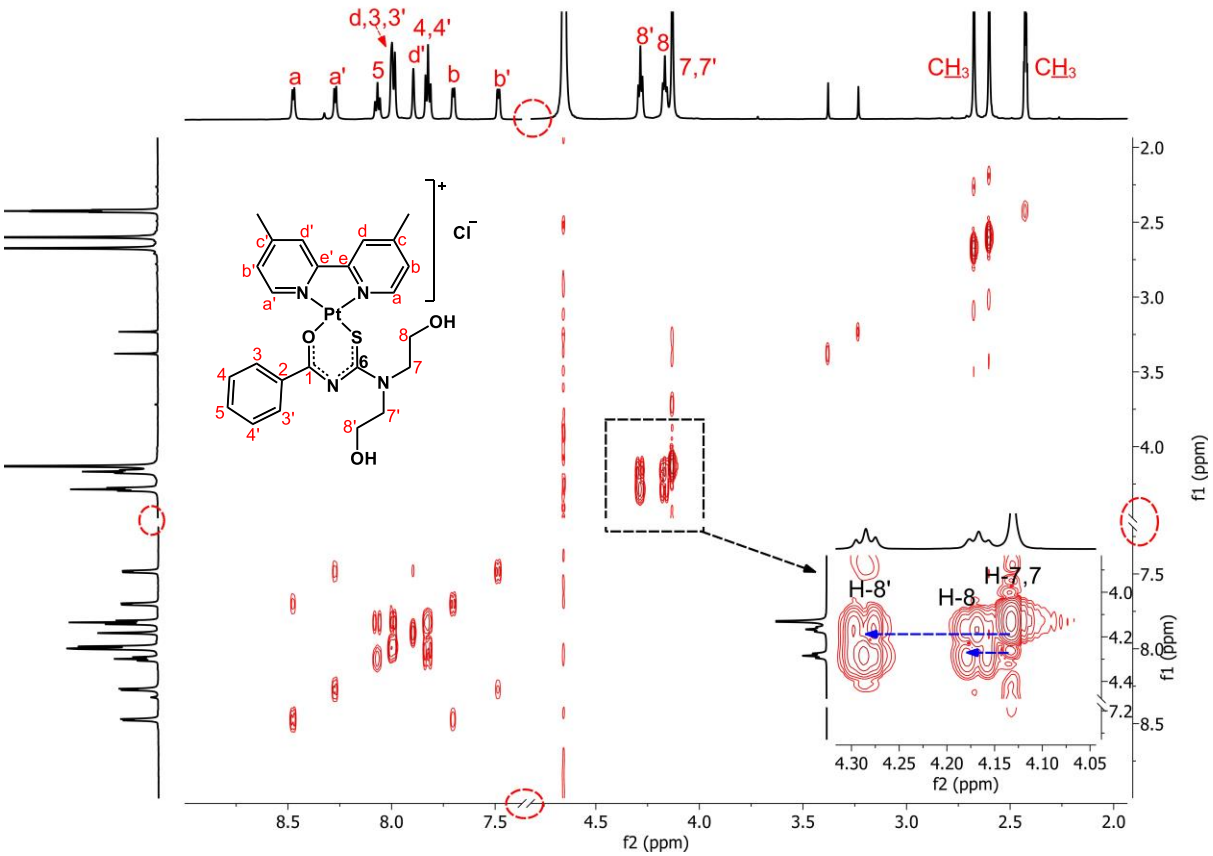

Figure 2.11.2D-COSY NMR spectrum of complex **4b.1** shows the cross-peaks between protons H-8,8' and H-7,7' (shown by the blue arrows), demonstrating that protons H-7 and H-7' have been correctly assigned to the intense "singlet" at 3.92 ppm. The circles represent regions of the spectrum containing no signals that were cut. The proton assignments are shown in red.

Complex **4j** (R^1 = COOMe) was poorly soluble in the available deuterated solvents, viz. dimethyl sulfoxide-d_6, methanol-d_4, acetone-d_6, acetonitrile-d_3, chloroform-d_2, deuterium oxide and a mixture of acetonitrile-d_3/deuterium oxide (1:1, v/v). Consequently, a comprehensive ^{1}H-NMR spectrum of annotatable resolution could not be obtained. The synthesis of **4j** could, therefore, only be supported using HPLC-MS which shows a peak with a retention time of 2.4 minutes and a *m/z* of 734.1 corresponding to $[M\text{-}Cl]^+$ (**Figure 2.12**).

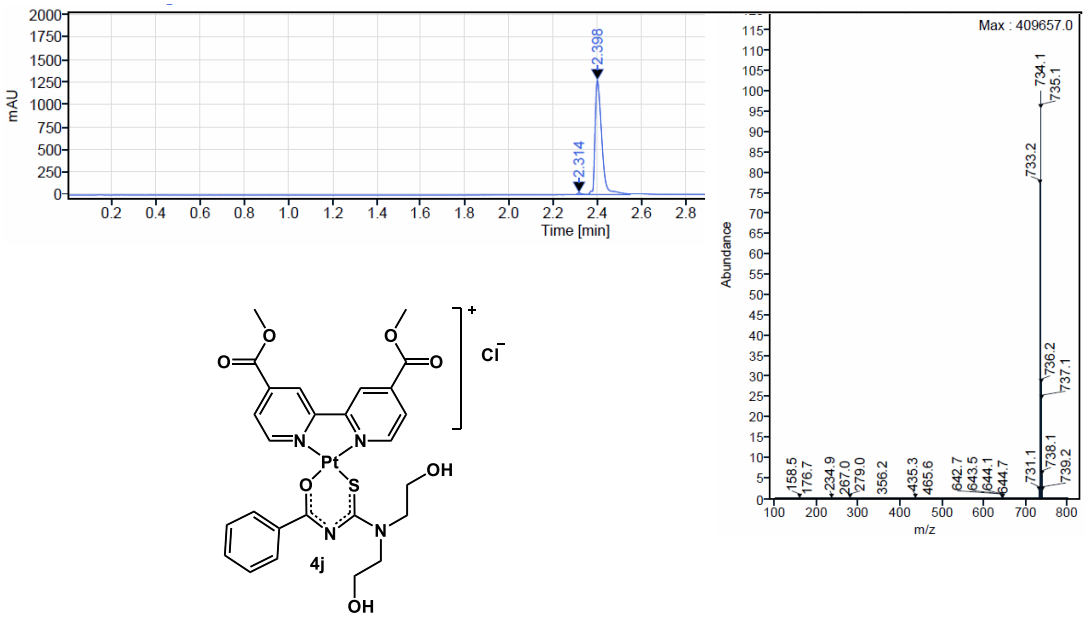

Figure 2.12 Chromatogram (top) and mass spectrum (right) of complex **4j,** showing that the mass of complex **4j** matches its calculated *m/z* of 734.6 in the positive ionization mode.

2.3.5. Counterion exchange

To improve a drug's solubility, stability, and overall pharmaceutical properties, a salt form of the drug/compound is often produced rather than the free base.[205] In this study, the series of complexes were synthesized as salts, presenting the opportunity to evaluate the biological effect of different counterions. The chloride counterion used as the standard for all the complexes was exchanged for different anions in a selected complex using simple salt metathesis reactions. The effects of this change on the pharmacological properties were evaluated. Although several salts are commercially available, NH_4PF_6 and $AgNO_3$ were selected due to their variability in both size and hydrophobicity (**Scheme 2.5**). Complex **4a.1** was reacted with either ammonium hexafluorophosphate (NH_4PF_6) or silver nitrate ($AgNO_3$) in a mixture of DCM:MeOH (1:1) or anhydrous MeOH, respectively. The resulting NH_4Cl and

AgCl salts were both insoluble in the organic solvents and precipitated out. These salts were filtered on celite, resulting in the isolation of the desired products **4a.5** and **4a.6** in the filtrate.

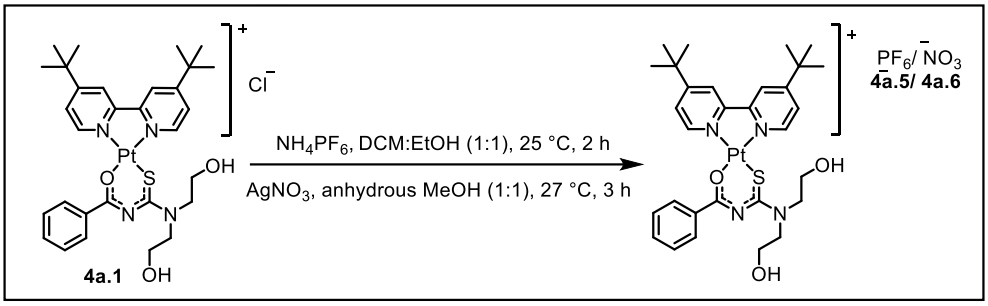

Scheme 2.5. Synthetic scheme for the counterion exchanges between Cl^- and PF_6^- or NO_3^-.

In the stacked ^{1}H-NMR spectra (**Figure 2.13**) of complexes **4a.1**, **4a.5** and **4a.6**, small shifts were observed for the aromatic protons compared to those seen for **4a.1** (**Table 2.1.**). Although these shifts were not very pronounced, they did support the exchange between counterions. **Figure 2.13** also confirms that the correct integrations and multiplicities were maintained across the analogs.

Table 2.1. ^{1}H-NMR chemical shifts between complexes with a Cl^- (**4a.1**), PF_6^- (**4a.5**) and NO_3^- (**4a.6**) counterion.

Complex	**4a.1**	**4a.5**	**4a.6**
Proton identity	**Chemical shift (ppm)**		
a	8.93	8.88	8.93
d	8.79	8.77	8.80
d'	8.69	8.66	8.69
a'	8.57	8.51	8.55
3,3'	8.15	8.11	8.15
b	8.11	8.08	7.77
b'	7.77	7.74	7.71
5	7.70	7.69	7.71
4,4'	7.55	7.55	7.56

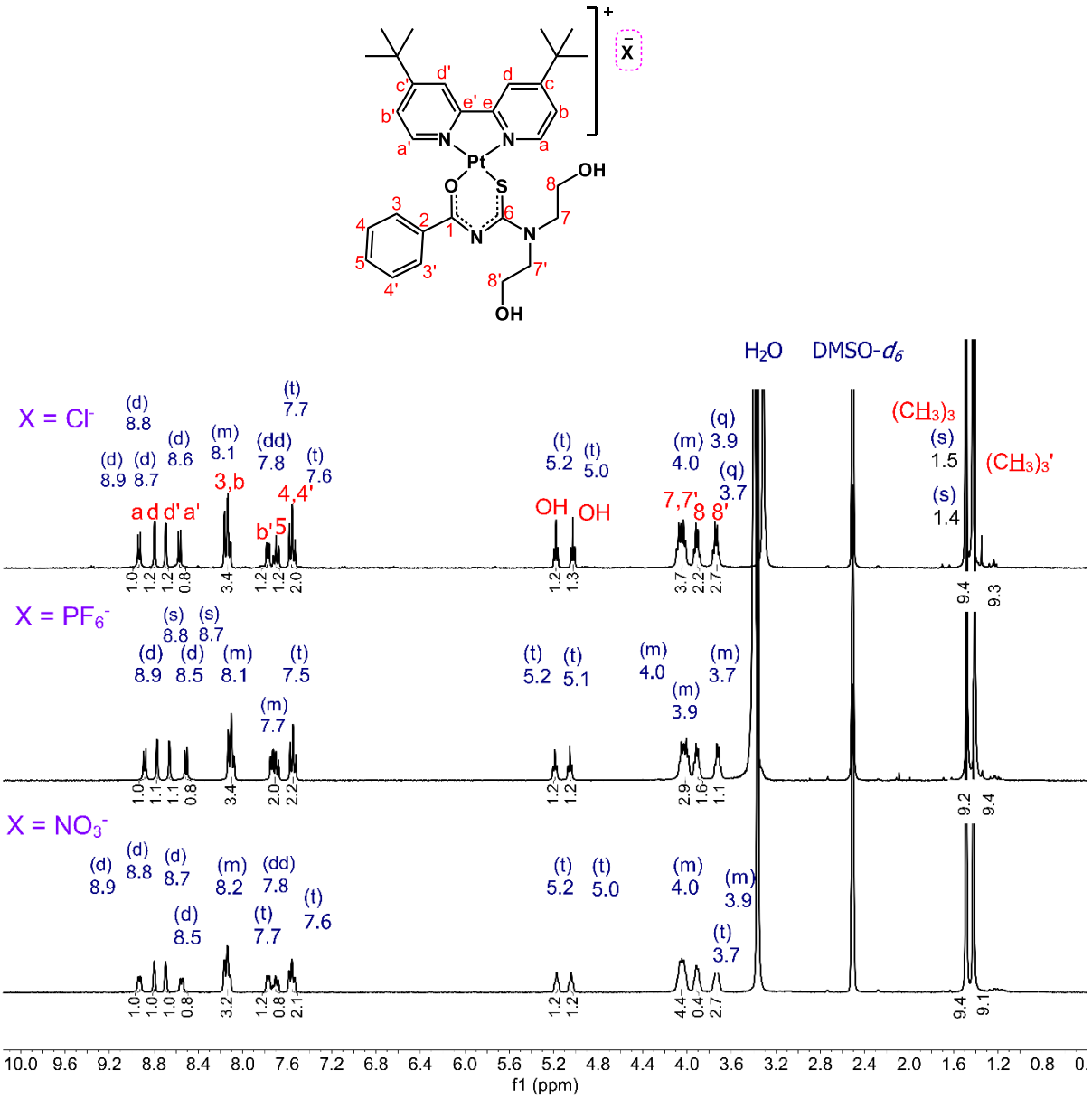

Figure 2.13. Stacked ^{1}H-NMR spectra of complexes **4a.1** (top), **4a.5** (middle), and **4a.6** (bottom) in DMSO-d_6, highlighting the aromatic chemical shifts that occurred due to the counterion exchanges between chloride and hexafluorophosphate and nitrate. The chemical shifts (in ppm) and peak multiplicities are displayed in blue, the integration values in black, and the proton assignments are displayed in red.

Additionally, a ^{19}F-NMR spectrum of **4a.5** was obtained (**Figure 2.14**) which further demonstrates the successful exchange between Cl^- and PF_6^-. Fluorine and phosphorus are both spin-active and all six fluorine atoms are equivalent. The doublet seen at -70.12 ppm is due to the coupling of fluorine to the ^{31}P nuclei.

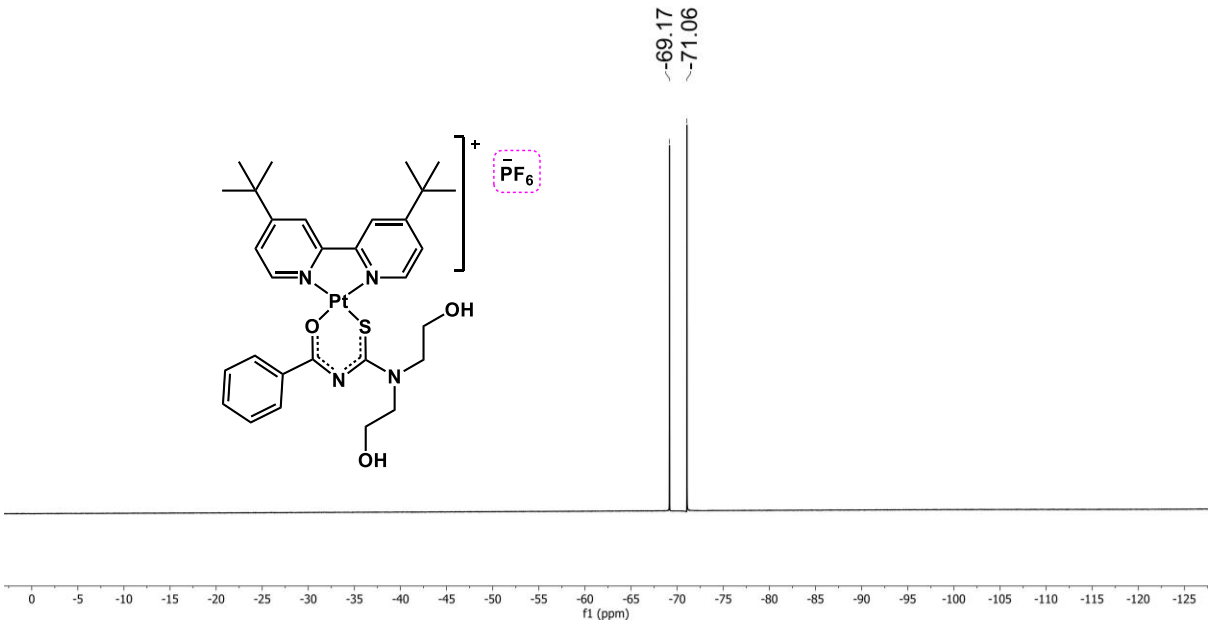

Figure 2.14.^{19}F-NMR spectrum of complex **4a.5** shows that the Cl^- was successfully exchanged for the PF_6^- counterion. Chemical shifts (in ppm) and multiplicities are shown in blue.

The success of the counterion exchanges was further confirmed using attenuated total reflection Fourier transform infrared (ATR-FTIR) spectroscopy. The IR spectra of complexes **4a.1**, **4a.5,** and **4a.6** are displayed in **Figure 2.15** and the respective wavenumbers of the functional groups are reported in **Table 2.2**. The OH stretching band appears at 3325 cm^{-1} for complex **4a.1** and shifts to higher wavenumbers of 3601 cm^{-1} and 3392 cm^{-1} in the spectra of complexes **4a.5** and **4a.6**, respectively. The pyridyl C=N band shifts from 1614 cm^{-1} in **4a.1** to 1619 cm^{-1} and 1621 cm^{-1} in complexes **4a.5** and **4a.6**, respectively. The aromatic C=C stretching bands shift slightly from 1500 cm^{-1}, 1512 $cm^{-1,}$ and 1482 cm^{-1} in **4a.1** to 1494 cm^{-1}, 1496 $cm^{-1,}$ and 1520 cm^{-1} in both **4a.5** and **4a.6**. These shifts in wavenumbers attest to the successful exchange of counterions. The exchange from Cl^- to PF_6^- is further suggested by the presence of the PF_6 strong stretching band at 833 cm^{-1} for **4a.5**. The NO_3^- stretching band for **4a.6** appears at 1396 cm^{-1} as a "shoulder" of the C-H bending band at 1408 cm^{-1}. This "shoulder" on the band at 1396 cm^{-1} is only seen in the spectrum of complex **4a.6**, whereas the C-H bending bands of complexes **4a.1** and **4a.5** are identical in character (sharp and strong). The correct assignment of the NO_3^- is further corroborated by reports in the literature in which the IR vibrational band of NO_3^- counterions are reported for metal complexes at 1383 cm^{-1}.[206,207]

Table 2.2. Reported IR wavenumbers (cm^{-1}) of various functional groups of compounds **4a.1, 4a.5**, and **4a.6** to confirm successful counterion exchange.

Functional group	**4a.1** (x=Cl^-)	**4a.5** (x=PF_6^-)	**4a.6** (x=NO_3^-)
	Band wavenumber (cm^{-1})		
OH	3325	3601	3392
N=C=O	2957	2960	2965
N=C=S	2866	2874	2872
C=N	1614	1619	1621
C=C	1500, 1512, 1482	1520, 1496, 1494	1520, 1496, 1494
C–H	1411	1411	1808
PF_6	-	833	-
NO_3	-	-	1396

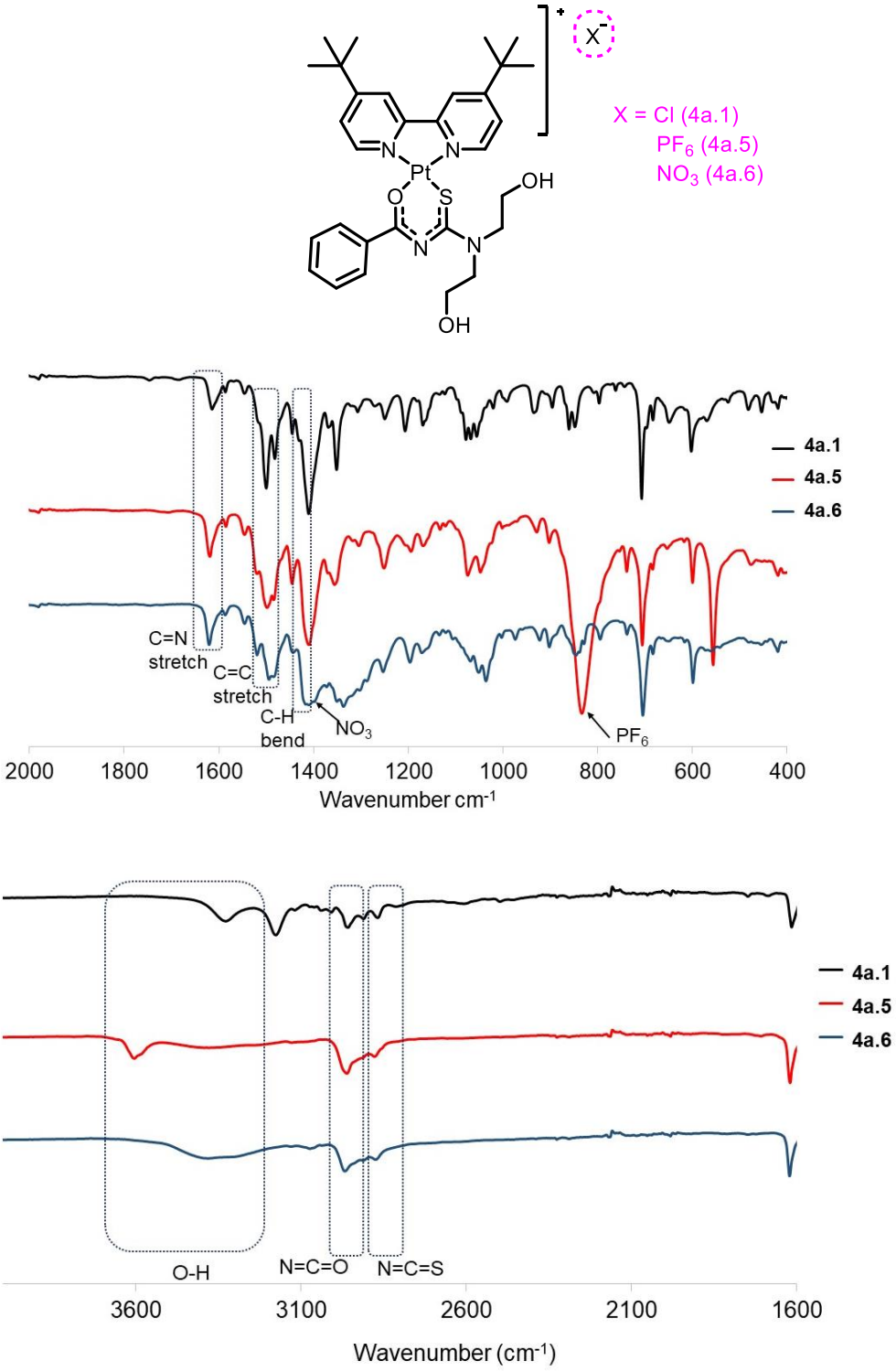

Figure 2.15. Infrared spectra of complexes **4a.1**, **4a.5**, and **4a.6**. Stretching region 1600-3600 cm^{-1} (bottom) and stretching range 400-2000 cm^{-1} (top). **4a.1** (x= Cl^-), **4a.5** (x=PF_6^-), **4a.6** (x=NO_3^-).

2.3.6. Synthesis of $[Au(diimine)(L\text{-}O,S)]^{2+}$ analog

The use of complexation chemistry presents another advantageous opportunity to alter the metal center and the oxidation state of the metal to evaluate SARs and SPRs. For the consistency of changing only one chemical space at a time, 4,4'-di-*tert*-butyl-2,2'-bipyridine was selected as the bipyridine ligand, and compound **1a** as the acyl-thiourea ancillary ligand. For this, potassium tetrachloroaurate(III) was reacted with 4,4'-di-*tert*-butyl-2,2'bipyridine in H_2O:MeOH (1:1) with potassium hexafluorophosphate (compound **3k**, **Scheme 2.6**) using a reported method with minor modification.[208] For complex **4k**, the reaction conditions used in the synthesis of the platinum(II) analog (**4a.1**) was first attempted with Et_3N and KPF_6 in acetone at 60 °C. However, these reaction conditions did not yield the desired complex.

Compound **3k** was subsequently reacted with compound **1a** in acetonitrile at 22 °C using caesium carbonate as the base and potassium hexafluorophosphate as the counterion salt. Unlike the platinum(II) analogs, gold(III) yields a charged $[AuCl_2(diimine)]^+$ species with one hexafluorophosphate counterion. Additional potassium hexafluorophosphate is thus added in the synthesis of **4k**, to further stabilize the formation of the desired square planar $[Au(diimine)(L\text{-}O,S)]^{2+}$ complex.

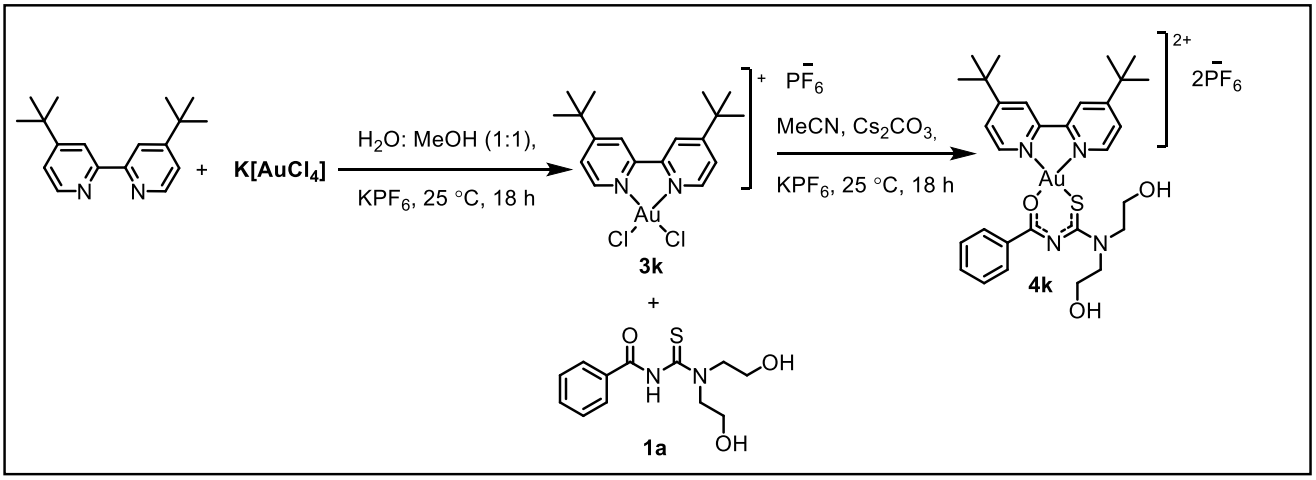

Scheme 2.6. Synthetic scheme of precursor complexes **3k** and the final gold(III) complex **4k**.

The ^{1}H-NMR spectrum of compound **3k** (**Figure 2.16**) shows a downfield shift in all the proton resonances due to the electron-poor gold metal center. Protons H-a,a', H-d,d' and H-b,b' appear as two doublets and a doublet of doublets at 9.3 ppm, 8.9 ppm, and 8.1 ppm, respectively, each integrating for two protons. The methyl protons appear as an intense singlet at 1.5 ppm, integrating for 18 protons.

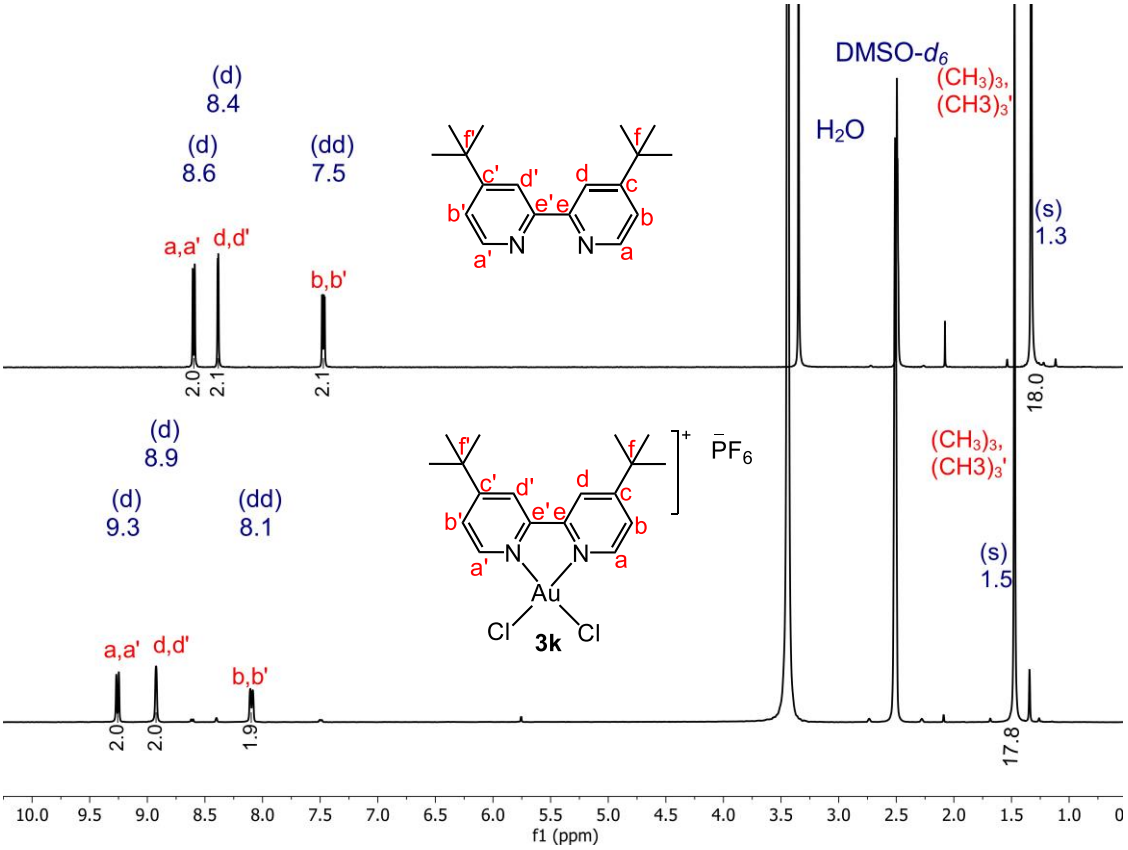

Figure 2.16. Stacked ^{1}H-NMR spectra of 4,4'-di-*tert*-butyl-2,2'bipyridine (top) and compound **3k** (bottom) in DMSO-d_6, showing the downfield shifts in the aromatic protons upon complexation caused by the positively charged gold(III) center. The chemical shifts (in ppm) and peak multiplicities are displayed in blue, the integration values in black, and the proton assignments are displayed in red.

The ^{1}H-NMR spectrum of **4k** (**Figure 2.17**) shows doublets for protons H-a,a', H-d, and H-3,3' at 8.74 ppm, 8.58 ppm and 8.05 ppm, respectively. Protons H-5 and H-4,4' appear as triplets at 7.56 ppm and 7.48 ppm, respectively, correlating to the expected integrations of one and two protons. The signals for the eight aliphatic protons appear as four triplets between 4.14-3.80 ppm, each integrating for the expected two protons. In the ^{1}H-NMR spectra of the platinum analogs of this series, each "equivalent" pyridyl proton appears as two separate signals, i.e. proton H-a appears as a separate signal from H-a'. However, in the ^{1}H-NMR

spectrum of the gold(III) analog (**4k**), the aromatic protons on each pyridyl ring only appear as one signal, integrating for two protons. The CH_3 signal at 1.41 ppm also presents as one singlet instead of two, as was seen in the platinum analogs. The presence of two PF_6^- counterions (**4k**) as opposed to one Cl^- counterion (**4a.1**) could explain this difference in the splitting of the aromatic signals in the different analogs.

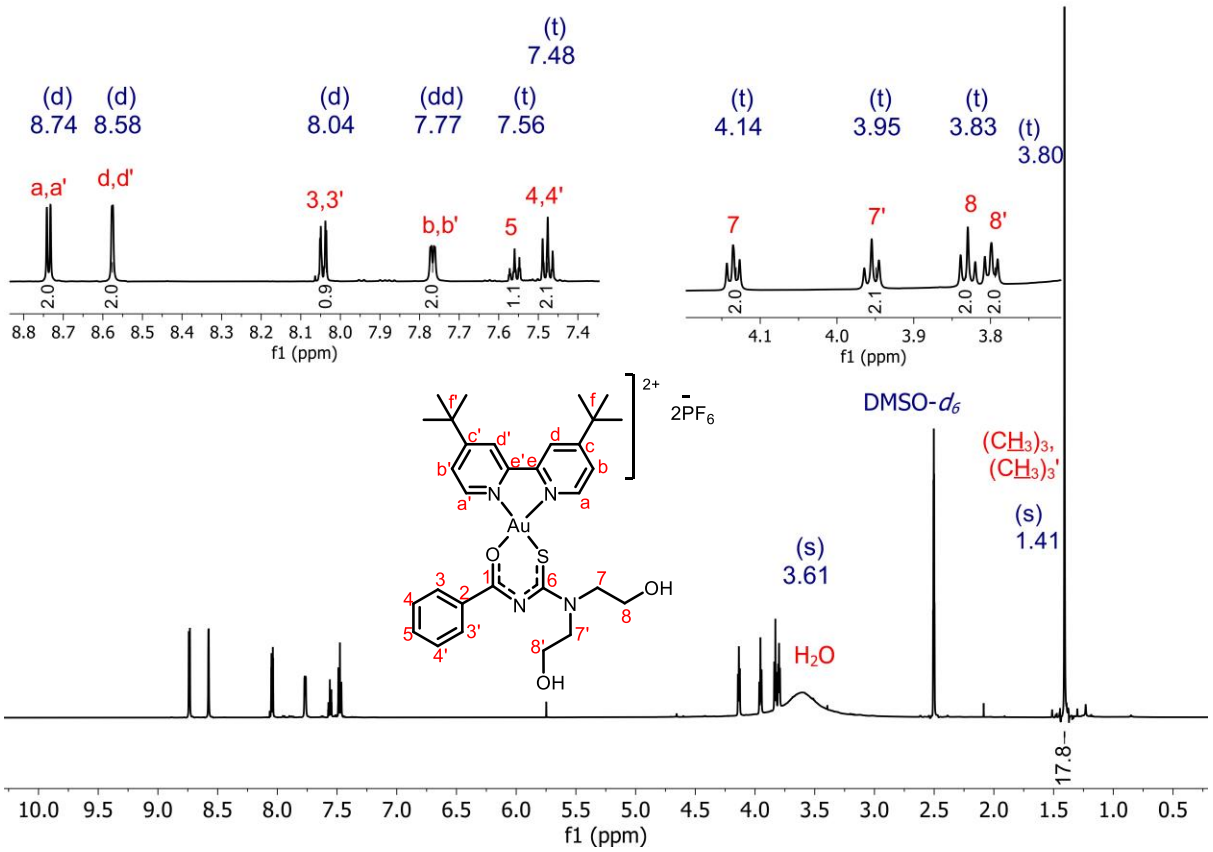

Figure 2.17. The ^{1}H-NMR spectrum of the [Au(diimine)(L-O,S)]$^{2+}$ analog, complex **4k**, in DMSO-d_6 showing the annotated signals. A downfield shift in the proton resonance of H_2O is observed from the expected 3.33 ppm (in DMSO) to 3.61 ppm, emphasizing its coordination to the complex in solution. The chemical shifts (in ppm) and peak multiplicities are displayed in blue, the integration values in black, and the proton assignments are displayed in red.

The ^{13}C-NMR spectrum was assigned using the 2D-NMR experiments, heteronuclear single quantum coherence (HSQC) and heteronuclear multiple bond correlation (HMBC) (**Figure 2.18**). HSQC was first used to accurately assign the carbon signals to their corresponding proton signals. HMBC was then used to annotate the remaining quaternary carbons either through strong three-bond correlations or weak two-bondcorrelations. The HMBC spectrum

for **4k** seen in **Figure 2.18** shows a strong three-bond correlation {8.04, 175.85} between proton H-3 and carbon C-1. The assignment of C-1 is further confirmed by the weak five-bond correlation {7.48, 175.85} seen for H-4 and C-1. C-2 was assigned by the presence of a strong bond correlation {7.48, 134.39} to H-4 and a weak four-bond correlation {7.55, 134. 64} to H-5.

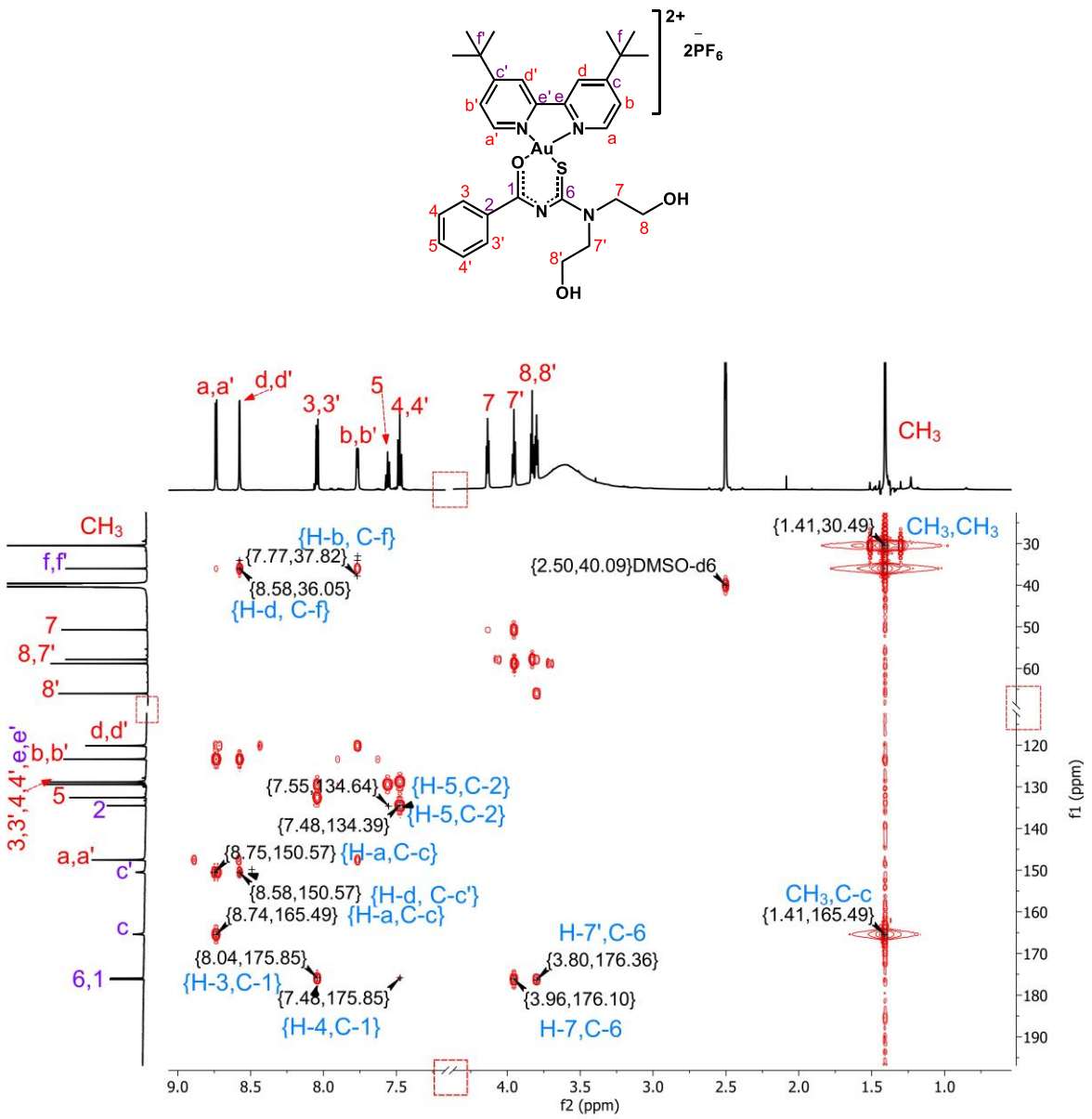

Figure 2.18. HMBC-NMR spectrum of complex **4k** showing strong three-bond and weak two-bond correlations used to assign quaternary carbons (purple), demonstrating that all 30 carbons are accounted for.

The assignment of C-6 was confirmed by the presence of strong three-bond correlations to both H-7 {3.80, 176.36} and H-7' {7.96, 176.10}. The intensity of the assigned C-c carbon is low, but the correct assignment is confirmed by the strong three-bond correlation to H-a {8.74, 165.49} and to the *tert*-butyl CH_3 protons {1.41, 165.49}. Carbon C-c' appears as a separate signal to C-c and is confirmed by another strong three-bond correlation to H-a' {8.75, 150.57} and a weak two-bond correlation to H-d {8.58, 150.57}. The fully assigned ^{13}C-NMR spectrum is shown in **Figure 2.19** and further attests to the correct structure of **4k**, as all 30 carbon atoms are accounted for.

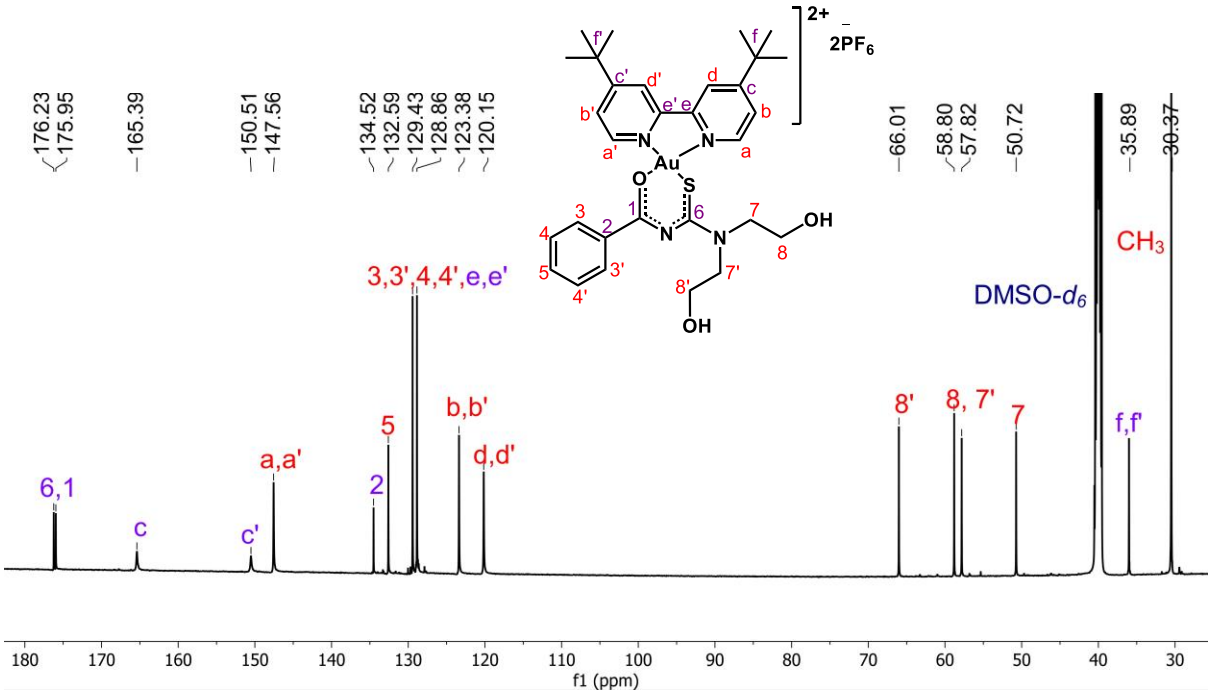

Figure 2.19. The ^{13}C-NMR spectrum of complex **4k** in DMSO-d_6, showing the assigned carbon signals which represent the 30 carbon atoms.

Despite the NMR data supporting the proposed structure of compound **4k**, two peaks were observed in the HPLC-MS chromatogram (**Figure 2.20**), irrespective of the mode (positive and negative) used to run the sample. Neither peak corresponded to the mass of the parent ion of **4k** ($[M\text{-}2PF_6]^+$, calculated to be 732.69). In positive ionization mode, the peaks were seen at retention times of 0.885 minutes and 1.018 minutes, correlating to the *m*/*z* values of 804.7 and 809.0, respectively. Compounds were dissolved in either HPLC-grade DMSO or MeOH to obtain the HPLC-MS spectra and injected through a column using a combination of water, MeCN, and formic acid as its mobile phase. These are all coordinating solvents and have the potential to either explicitly or partially bind to the metal center while it is in solution. To eliminate possible coordination by DMSO, the complex was dissolved in MeOH before

obtaining a chromatogram. Identical chromatograms were obtained, regardless of the dissolving solvent, one of which is shown in **Figure 2.20** (top). This suggested the coordination of one of the mobile phase solvents instead.

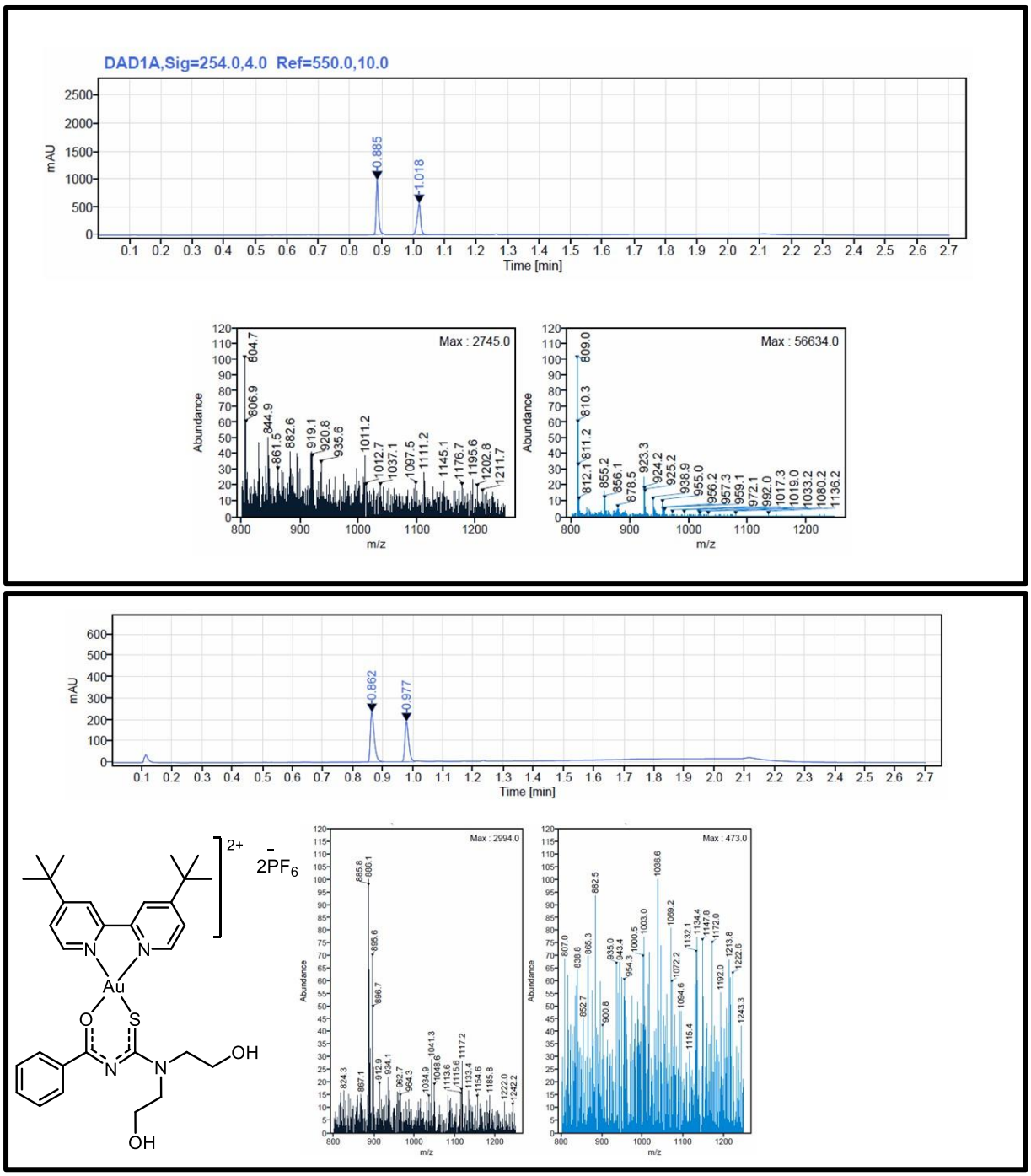

Figure 2.20. HPLC-MS chromatograms and mass spectrum of complex **4k** in positive (top) and negative (bottom) mode, respectively.

Upon further analysis of the observed *m/z* values (positive mode), it was apparent that each mass corresponded to one of two scenarios where either four water molecules or two water molecules and one MeCN molecule were coordinated to the gold(III) (**Figure 2.21**). In the negative mode (**Figure 2.20**, bottom), a peak at a retention time of 0.862 min. corresponds to the ion fragment (75%) with a *m/z* of 895.6. This mass corresponds to complex **4k** with four MeCN molecules co-ordinated, minus hydrogen ($[M+4MeCN-H)^+$). The peak with a retention time of 0.977 minutes, does not ionize in the negative mode and therefore its *m/z* value could not be determined.

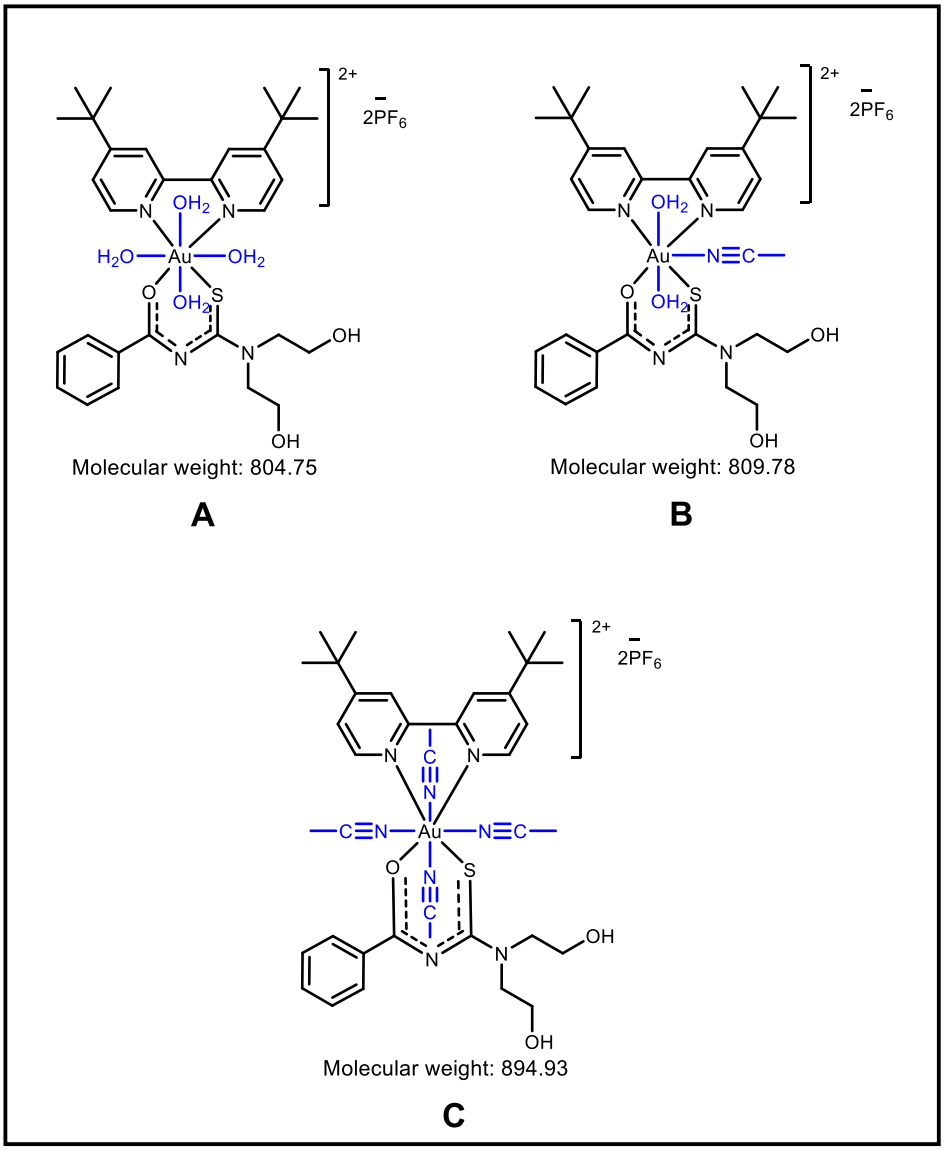

Figure 2.21. Possible chemical structures of **4k** when run through the HPLC-MS column using H_2O and MeCN as the mobile phase.

To further confirm that coordination occurred only in solution during the HPLC-MS run, ATR-FTIR was obtained for complex **4k** (**Figure 2.22**). Were complex **4k** isolated as a solid aqua species (**Figure 2.21, A**), a strong broad band in the O-H stretch region around 3400 cm^{-1} would have been seen. The absence of such a band confirms that no water molecules are explicitly bound to the metal center. Furthermore, no stretching band for acetonitrile is seen in the 2200-2300 cm^{-1} region either. The IR data, therefore, reiterates that there are no water or acetonitrile molecules ligated to the metal center and complex **4k** was isolated as shown in **Scheme 2.6**. Furthermore, the PF_6 stretching band is seen at 826 cm^{-1}, the C=N stretching band at 1632 cm^{-1}, C=C stretching band at 1585 cm^{-1}, and the aliphatic stretching band at 3415 cm^{-1}. These bands, corresponding to their respective functional groups, all appear in the same region as they do in the platinum analogs (**4a.1-3**). Although a square-planar geometry is preferred in gold(III) complexes, five-coordinate and six-coordinate gold((III) complexes in solution have been reported in the literature, suggesting that the phenomenon observed for **4k** in water/acetonitrile is feasible.[209]

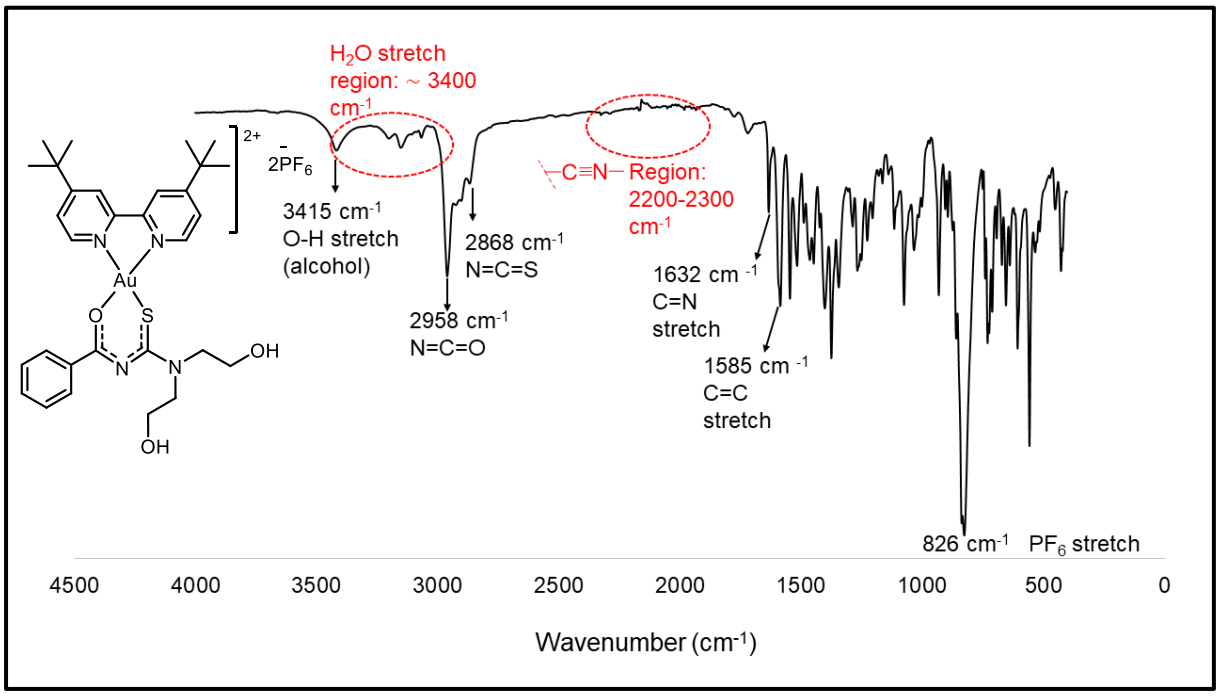

Figure 2.22. IR spectrum obtained for complex **4k**, showing that no bands corresponding to H_2O or MeCN are seen in the circled regions, indicative that neither of these molecules are ligated to **4k** in a solid state.

2.3.7. Fluorescent analogs and their precursors

One approach to studying the MoA of a compound is to investigate the cellular localization of that compound or a related analog. This can reveal crucial information on where within the studied organism the compound (or analog) accumulates and potentially acts.[210] One strategy to study cellular localization is to employ an extrinsic fluorescent reporter. There is an abundance of fluorescent reporters commercially available but selecting a reporter with suitable photochemical properties (good photostability, good fluorescence signal, and a good Stokes shift) is a critical decision to ensure that the subsequent biological analysis is worthwhile. The Stokes shift of a fluorophore refers to the difference between λ_{max} and λ_{em} and serves as an important parameter, as fluorophores with a small Stokes shift are susceptible to self-quenching.[211] The four fluorophores discussed in this section are shown in **Figure 2.23** with their reported excitation wavelengths.[212–215]

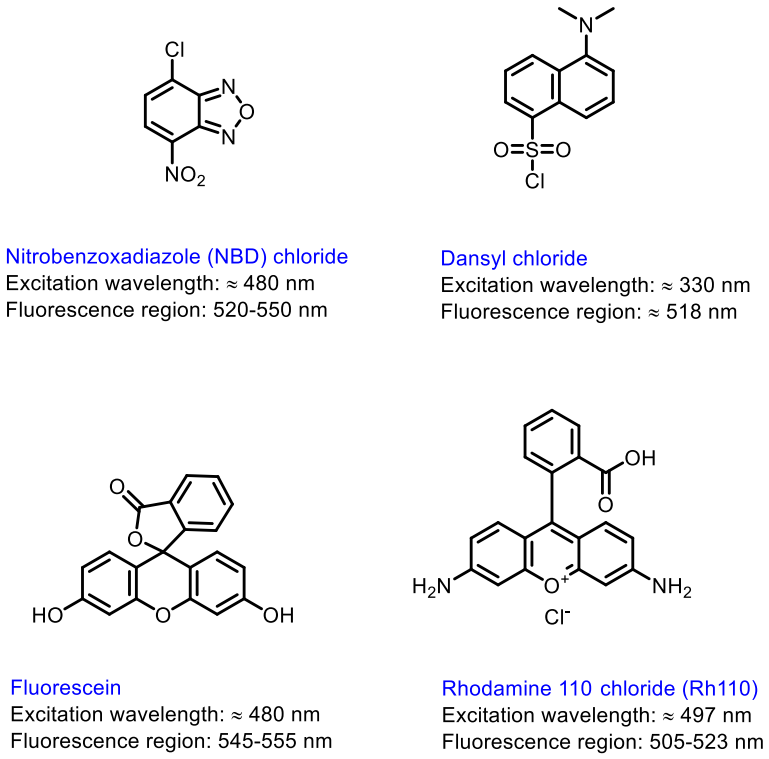

Figure 2.23. The chemical structures of fluorescent reporter starting materials with their reported approximate excitation wavelengths.[216–219]

Initially, 4-nitrobenzo-2-oxa-1,3-diazole (NBD), which has a large Stoke shift but is a very small compound, was selected as the fluorescent probe. NBD is an attractive fluorophore as its chemical labeling can often be done under mild conditions,[220] and it has an emission wavelength in the visible range.[221] NBD has also previously been used in the synthesis of fluorescent platinum compounds in cancer studies,[222–224] and has been studied in cellular localization experiments in *P. falciparum*.[225,226] Attachment of the NBD probe to an *N*-amino-ethyl-ethanolamine (AEEA) chain (compound **5**) was first attempted to subsequently attach this NBD-containing chain to the acyl-thiourea ligand (**1a**) and precursor complex (**3a**).

Several synthetic routes and reaction conditions were unsuccessfully attempted (**Scheme 2.7**). These reaction conditions were adapted from the literature where similar products were synthesized.[227–230] However, low-yield crude products were either isolated, where purification was not possible, or the starting materials were recovered. In route A, AEEA was reacted with NBD first in THF and then a second attempt in MeCN. Purification of **5a-A** was attempted using both normal-phase column chromatography (dichloromethane/methanol) and reverse-phase column chromatography (water/acetonitrile or water/methanol). This resulted in the isolation of a crude product with a 1.2% yield.

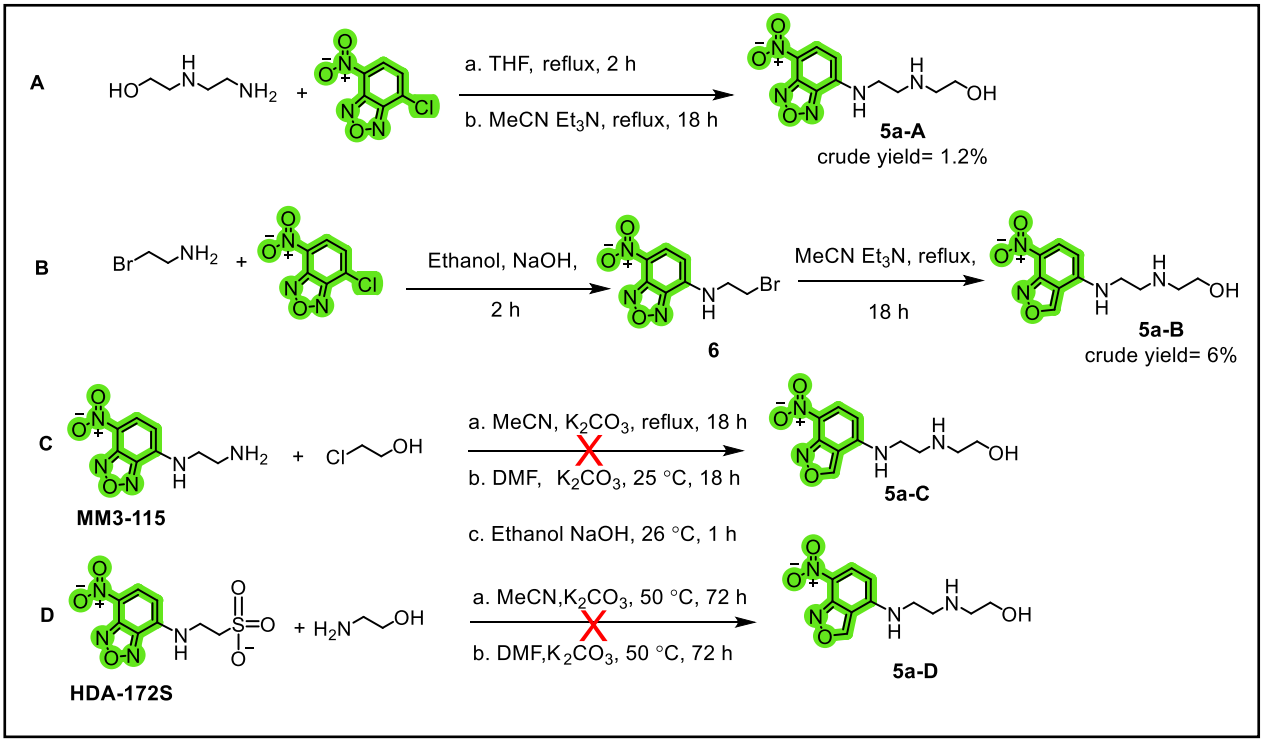

Scheme 2.7. Attempted synthesis of an NBD-containing diamino-ethanol compound **5a** using several reaction routes and conditions (A-D). Conditions a-c represent the different solvents and reagents used within synthetic routes A-D.

As an alternative, route B was explored, in which 2-bromo-ethylamine was reacted with NBD in ethanol to yield compound **6** which was confirmed solely with HPLC-MS. A peak at a retention time of 2.43 min, corresponding to a *m/z* of 289 ($[M+2H]^+$), confirmed the synthesis of compound **6** which has a calculated *m/z* of 287.1. Compound **6** was taken forward without further purification and was reacted with ethyl-ethanolamine to synthesize compound **5a-B**. However, a crude product of **5a-B** was isolated in low yield and could not be purified following several attempts at recrystallization and column chromatography.

Subsequently, routes C and D were attempted using the precursor compounds previously utilized in our laboratory. For each route, more than one set of reaction conditions was attempted, neither of which successfully produced the desired products **5a-C** and **5a-D**. These reaction routes resulted in the recovery of the starting materials.

Due to the difficulty in isolating the NBD analogs, efforts were shifted to exploring dansyl as an alternative fluorophore. Dansyl has an intense absorption band in the near-UV (310 – 350 nm), a strong fluorescence signal in the visible region, and a large Stokes shift.[231] Drug-like compounds tagged with the dansyl fluorophore have also been studied for their cellular localization in *P.falciparum*.[232,233] For the synthesis of the dansyl-labeled probe, dansyl chloride was reacted with *N*-amino-ethyl-ethanolamine in a mixture of THF and MeCN. Compound **7** was reacted with benzoyl isothiocyanate under inert conditions to form intermediate compound **8** which was subsequently reacted with the metal precursor, compound **3a**, to form complex **4a.7** (**Scheme 2.8**).

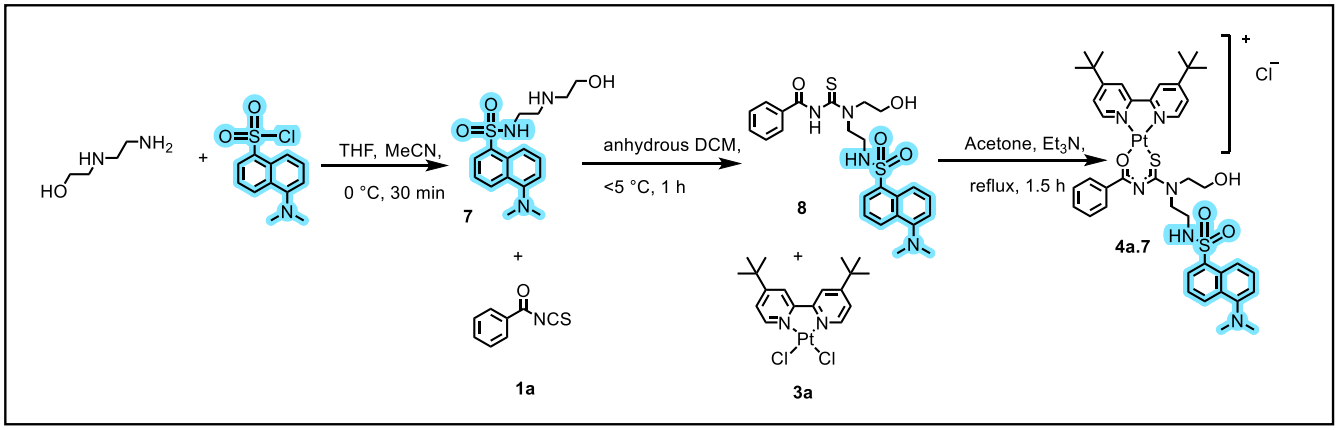

Scheme 2.8. Synthetic scheme for preparing the fluorescent analog **4a.7** containing a dansyl moiety.

The successful synthesis of compound **7** was confirmed by analysis of the ^{1}H-NMR spectrum shown in **Figure 2.24**. The diagnostic peaks are the intense multiplet at 3.3 ppm, integrating for the four aliphatic H-11,11' protons, and the two triplets at 2.5 ppm and 2.4 ppm, each integrating for two of the H-12 and H-12' protons, respectively. The intense singlet at 2.8 ppm integrates for six protons and corresponds to the methyl protons on the dansyl moiety. Each aromatic proton signal, apart from H-3 and H-7 has the expected doublet multiplicity, each integrating for one proton. The signal corresponding to protons H-7 and H-3 appears at a similar chemical shift (7.6 ppm) and overlap being interpreted as a quartet, although these signals are likely to be two doublets each integrating for one proton.

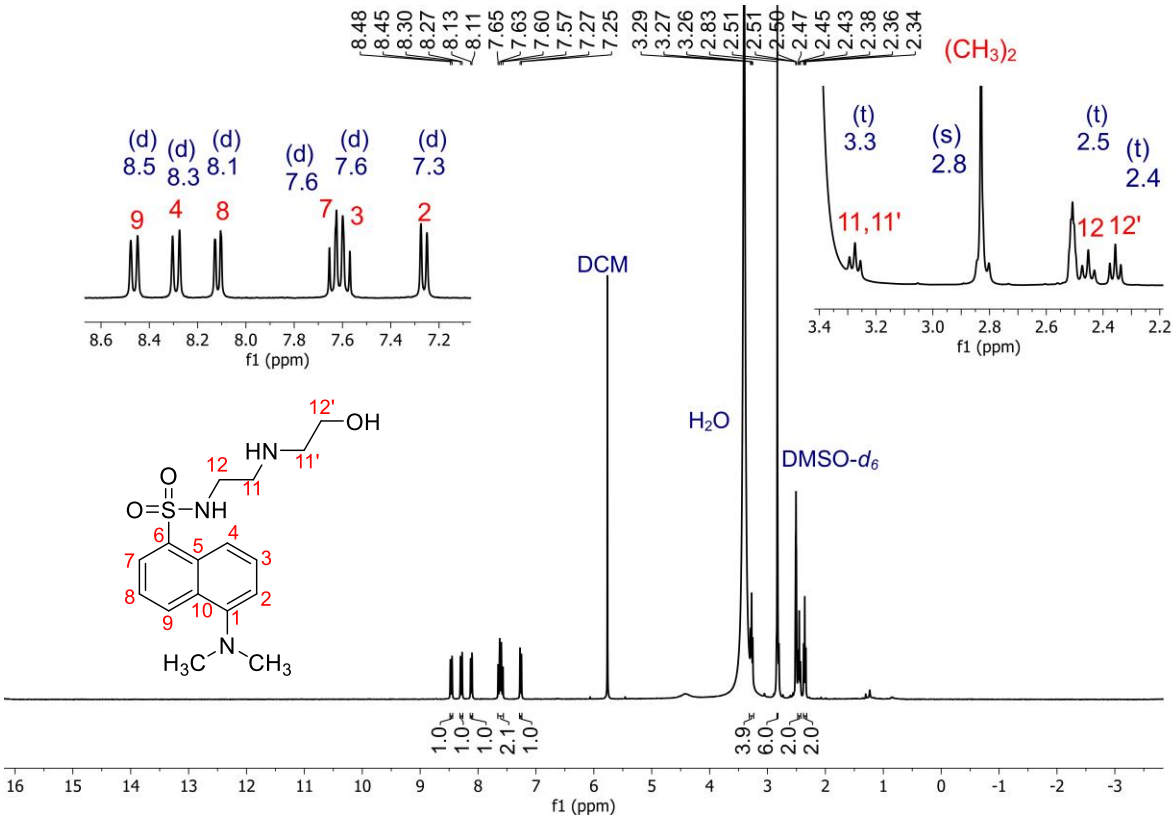

Figure 2.24. The ^{1}H-NMR spectrum of the dansyl-labeled precursor compound **7** in DMSO-d_6. The chemical shifts (in ppm) and peak multiplicities are displayed in blue, the integration values in black, and the proton assignments are displayed in red.

Compound **7** was subsequently reacted with benzoyl isothiocyanate to synthesize **8** via a substitution reaction. In the ^{1}H-NMR spectrum of compound **8** (**Figure 2.25**), the successful reaction between the acyl thiourea and compound **7** is confirmed by the presence of the doublet, multiplet, and triplet corresponding to protons H-16,16', H-18, and H-17,17' at 7.9 ppm, 7.7–7.6 ppm, and 7.5 ppm, respectively. Upon complexation of compound **8** to **3a**, all the proton resonances of **4a.7** shift downfield (**Figure 2.25**), owing to the cationic nature of the platinum metal center. The electron-poor platinum center results in less shielding of the surrounding protons compared to a neutral metal center. In addition to the downfield shift of the proton signals, the two doublets and a multiplet of H-d, H-a,a', and H-d' are seen at 8.6 ppm, 8.3 ppm, and 8.00 ppm, respectively. These signals confirm successful complexation to the [$PtCl_2$(diimine)] precursor complex.

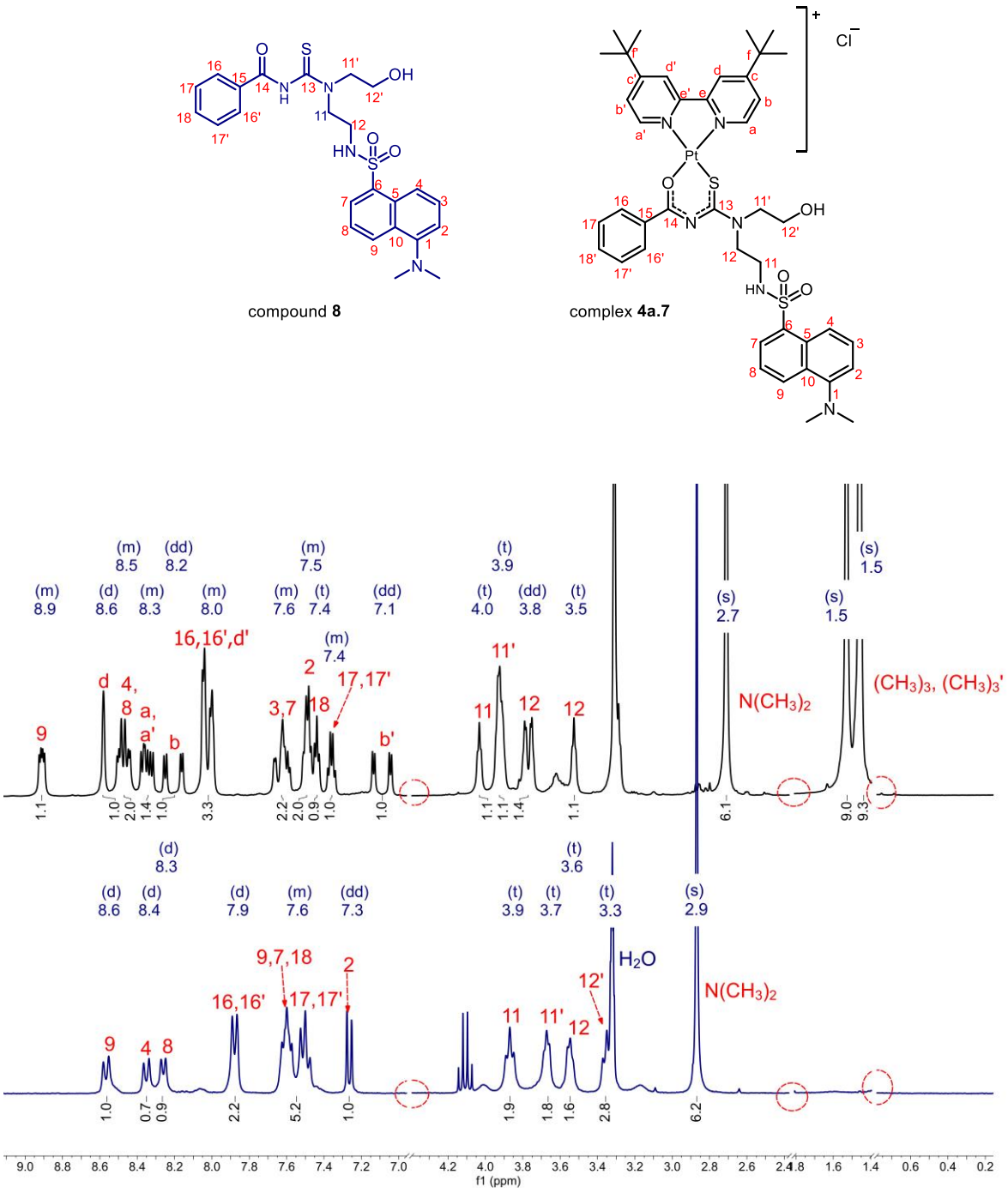

Figure 2.25. Stacked ^{1}H-NMR spectra of compounds **8** (bottom) and **4a.7** (top) and their annotated structures (compound **8**: left, complex **4a.7**: right) in DMSO-d_6. Sections of the x-axis where no proton signals were observed have been cut to make the annotated signals easier to distinguish. Cuts in the spectra are indicated by red circles. The chemical shifts (in ppm) and peak multiplicities are displayed in blue, the integration values in black, and the proton assignments are displayed in red.

The HPLC-MS chromatogram and mass spectrum of complex **4a.7** has a peak corresponding to the parent ion peak $[M\text{-}Cl]^+$ with a *m*/*z* of 963.2 and a calculated molecular weight of 963.11. The data supports the successful synthesis of the dansyl-labeled platinum(II) complex, **4a.7**. It was subsequently used in localization studies as described in **Section 4.8**.

Complex **4a.7** varies from the series 1 complexes in the replacement of one terminal hydroxyl with an amine. This allowed for the synthesis of a derivative with an unlabelled terminal amine (**4a.8a, Figure 2.26**) to determine the SAR of this chemical modification as will be outlined in **Chapter 3**. Furthermore, due to the subsequent limitations of conducting live-cell imaging studies with the dansyl probe (discussed in **Section 4.8**), alternative fluorescent reporters were selected; namely, rhodamine and fluorescein.

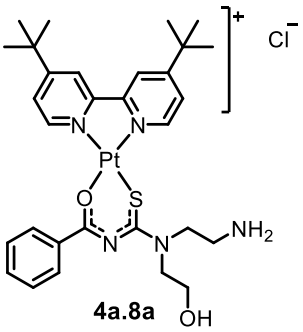

4a.8a

Figure 2.26. The structure of compound **4a.8a** that was synthesized to evaluate the SAR of the chemical modification where one terminal hydroxyl was replaced with an amine moiety. This complex also served as a precursor for subsequent fluorescent probes.

Complex **4a.8a** was used as the starting reagent in these subsequent reactions using rhodamine and fluorescein. Rhodamine 110 chloride was selected based on its photostability,[234] long absorption, and emission wavelengths that extend into the visible light region and a high fluorescent quantum yield.[235] Rhodamine 110 chloride also has a moderate Stokes shift of 17 nm.[236,237] Fluorescein and rhodamine are structurally similar, but fluorescein serves as a more affordable alternative to rhodamine.

To this end, complex **4a.8a** was synthesized via a series of steps shown in **Scheme 2.9**. First, compound **9** was synthesized via a reductive amination reaction between *N*-Boc-2-aminoacetaldehyde and ethanolamine using $NaBH_4$ as the reducing agent (**Scheme 2.9**). Compounds **10** and **4a.8a** were then synthesized using the same reaction conditions previously described in **Schemes 2.1** and **2.4** and was isolated in low yield (3%).

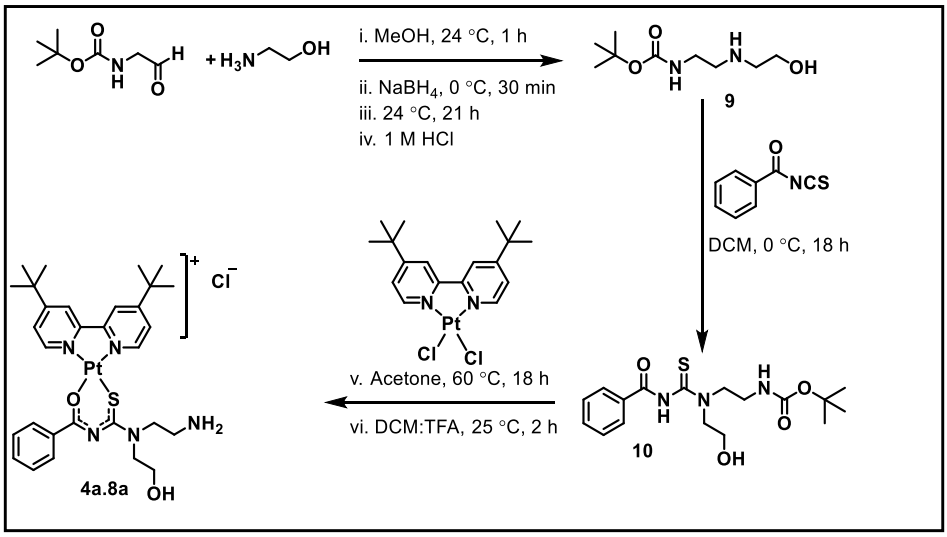

Scheme 2.9. Synthetic scheme for compounds **9**, **10** and complex **4a.8a**. Steps i-iv are indicative of the order in which the reagents were added.

Successful reductive amination is confirmed by the presence of the two amine proton signals, NH-a and NH-b at 3.55 ppm and 2.71 ppm, respectively (**Figure 2.27**). The *N*-Boc *tert*-butyl CH_3 protons appear as an intense singlet at 1.44 ppm, integrating for nine protons.

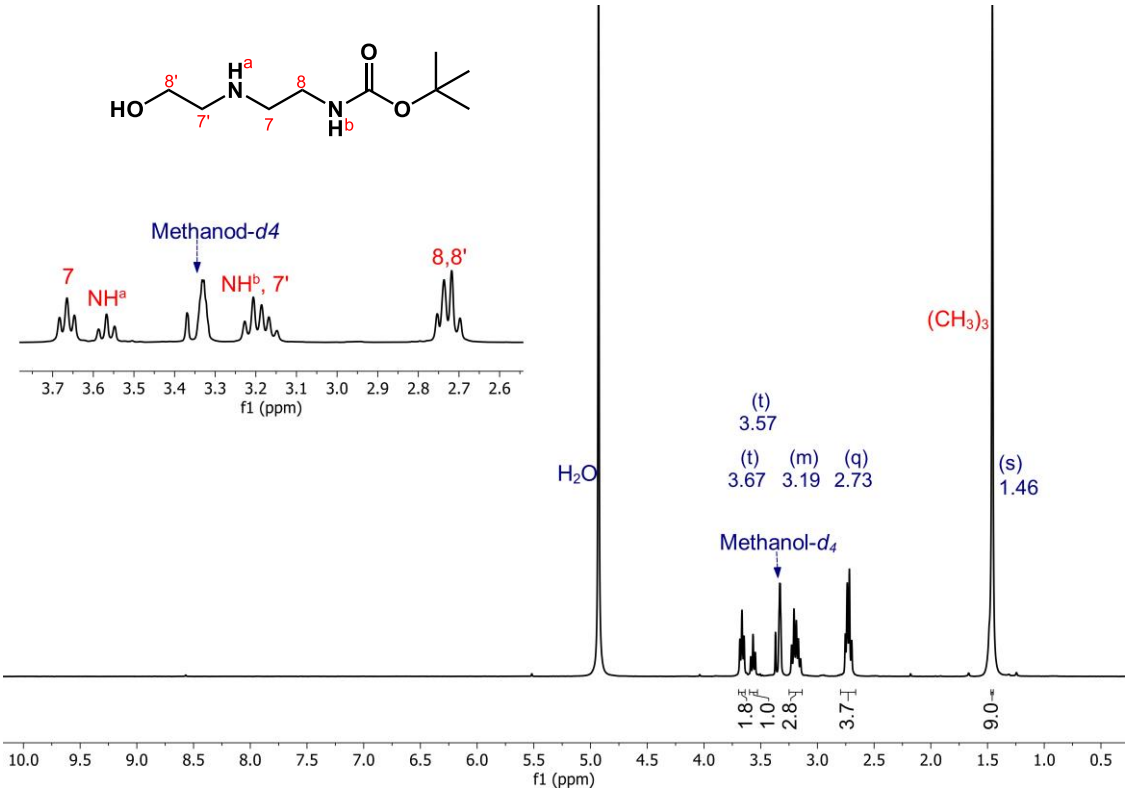

Figure 2.27. The ^{1}H-NMR spectrum of compound **9** in methanol-d_4, showing the proton signals in the aliphatic region. The chemical shifts (in ppm) and peak multiplicities are displayed in blue, the integration values in black, and the proton assignments are displayed in red.

The ^{1}H-NMR spectrum of compound **10** (**Figure 2.28**) has poor resolution, but distinct peaks can be seen and are annotated accordingly. All the aliphatic proton signals are more deshielded relative to those in compound **9**, while the *tert*-butyl CH_3 proton resonance does not shift. To synthesize complex **4a.8a**, compound **10** was reacted with the *tert*-butyl-substituted $PtCl_2$(diimine)] precursor complex in acetone and purified using reverse phase column chromatography and preparative-scale high-performance liquid chromatography. The *N*-Boc group was subsequently removed by stirring the compound in a combination of DCM:TFA (1:0.5). The chemical shifts of the aromatic protons in the ^{1}H-NMR spectrum of

complex **4a.8a** (**Figure 2.29**) appears in the region 8.00-8.66 ppm and for the most part cannot be distinguished. The broad signal at 8.66 ppm integrates for the two H-a,a' protons, and the multiplet between 8.05-5.23 ppm accounts for seven of the aromatic protons. The triplet at 7.86 ppm integrates for the remaining two H-4,4' protons. Similarly, to the *tert*-butyl analogs (**4a.1** and **4a.7**), the CH_3 protons appear as two separate singlets at 2.59 ppm and 2.56 ppm, collectively integrating for the 18 methyl protons. HPLC-MS analysis further confirmed the successful synthesis of complex **4a.8a** with its parent ion peak $[M\text{-}Cl]^+$ having a retention time of 0.904 minutes and *m/z* 730.2 (calculated value 729.83).

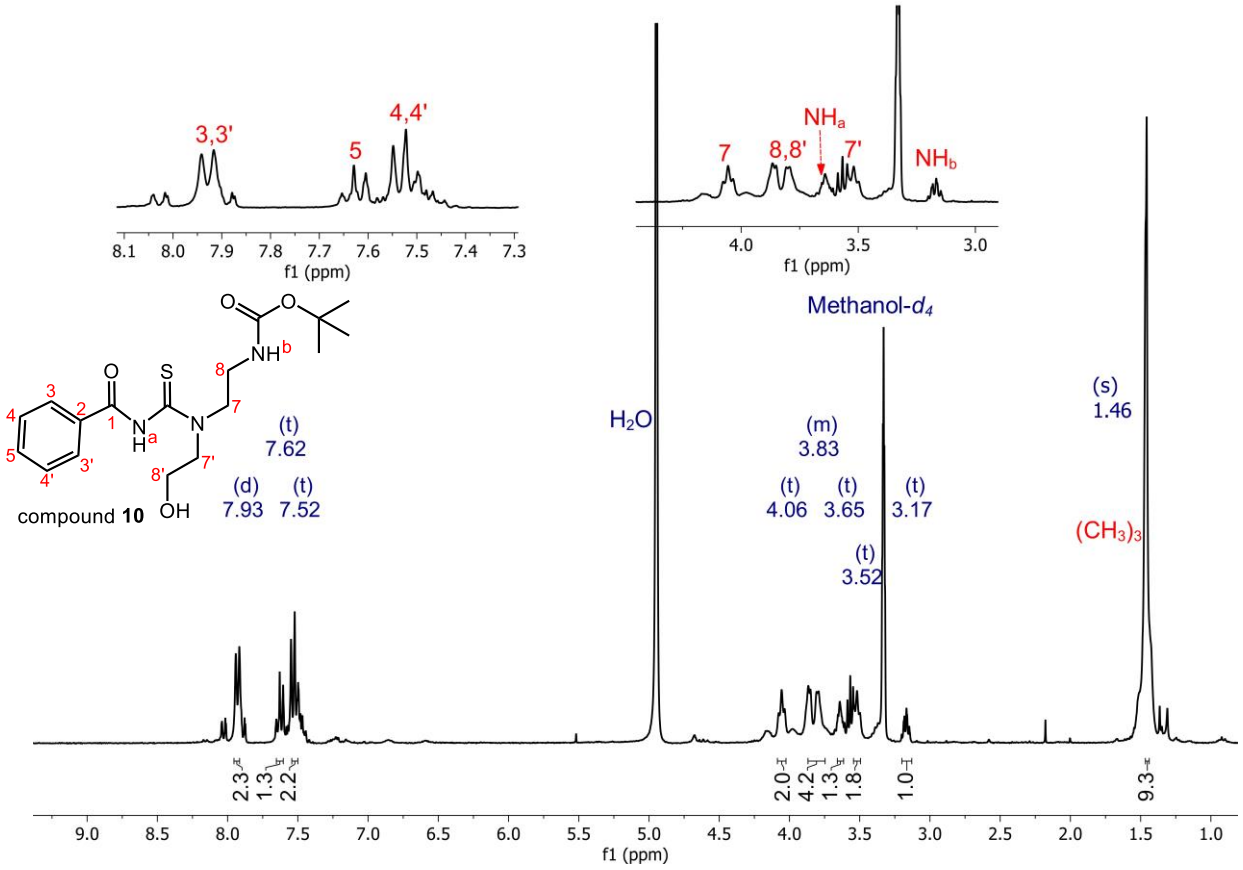

Figure 2.28. The ^{1}H-NMR spectrum of compound **10** in methanol-d_4, that can be compared to that of compound **9** in **Figure 2.27** to highlight the changes in chemical shifts upon bonding to the acyl thiourea ligand. The chemical shifts (in ppm) and peak multiplicities are displayed in blue, the integration values in black, and the proton assignments are displayed in red.

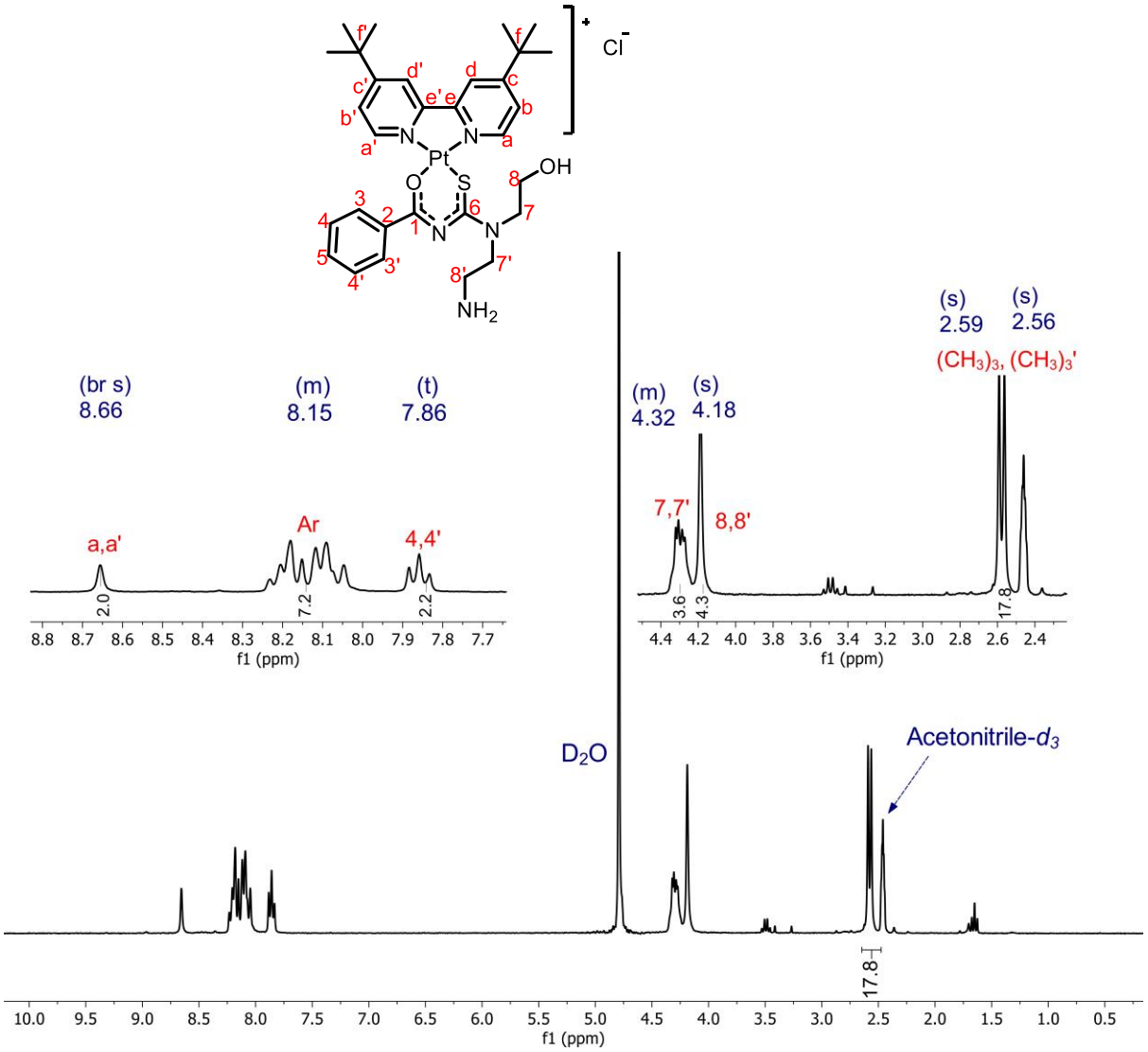

Figure 2.29. ^{1}H-NMR spectrum of complex **4a.8a** in D_2O:acetonitrile-d_3 (1:1), showing a broad signal and triplet at 8.66 ppm and 7.86 ppm, respectively, each integrating for the two H-a,a' and H-4,4' protons, respectively. The indistinguishable multiplet at 8.15 ppm corresponds to the remaining seven aromatic protons. The chemical shifts (in ppm) and peak multiplicities are displayed in blue, the integration values in black, and the proton assignments are displayed in red.

Upon isolation of compound **4a.8a**, it was reacted with either rhodamine or fluorescein under amide coupling conditions (**Scheme 2.10**). However, limiting amounts of rhodamine 110 chloride were available; therefore, the reaction with **4a.8a** was conducted on a small (10 mg) scale. The reaction was monitored by TLC and HPLC-MS over 18 hours, after which there was no evidence of formation of the desired product (**4a.8b**).

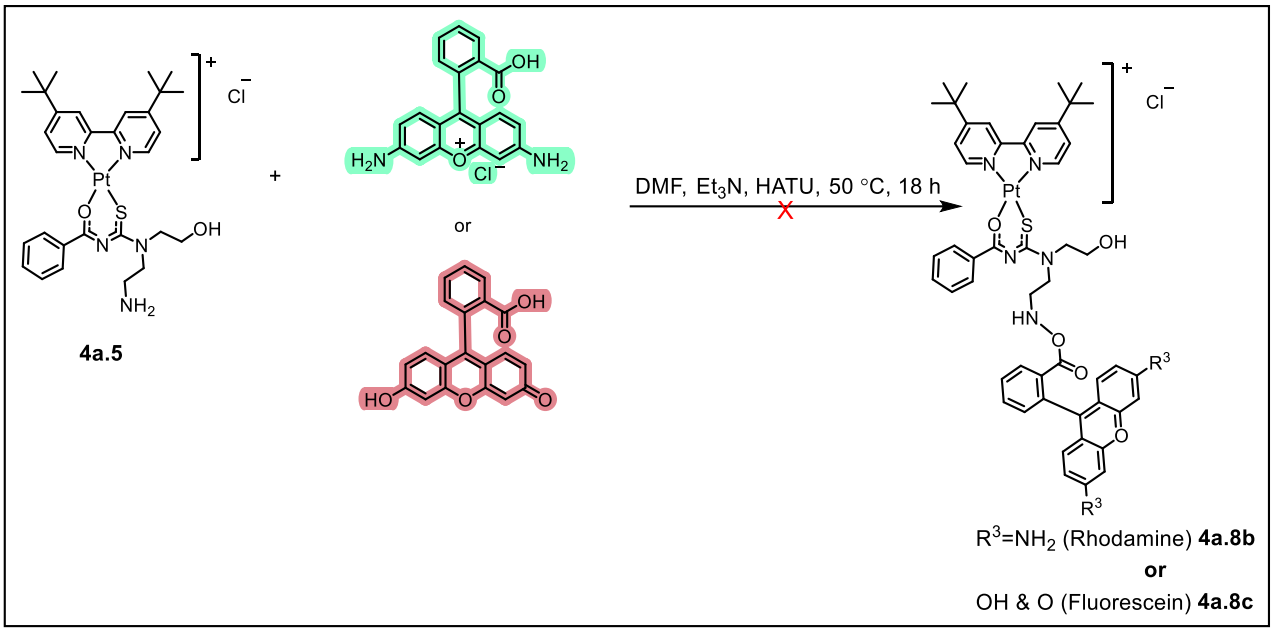

Scheme 2.10. Attempted synthesis of a platinum(II) complex containing either rhodamine or fluorescein.

Isolation of the formed adducts was attempted using preparative-scale HPLC to identify the possible products formed. Only 1-2 mg of each fraction was isolated, and a ^{1}H-NMR spectrum with poor resolution was obtained (**Figure 2.30**). Fractions 5 and 7 show aromatic protons, summing up to nine to eleven protons as opposed to the expected 21 for complex **4a.8b**. Determining the exact number of protons was not possible given the inability to confidently annotate the peaks. Additionally, no distinct aliphatic proton signals are seen in the expected region. Fraction 1 had three distinct aromatic signals suggesting that a small aromatic adduct was isolated; however, each signal integrates for an equivalent number of protons, suggesting that it does not belong to the isothiocyanate moiety. Had this adduct been the isothiocyanate, there would have been two doublets, integrating for two protons and one triplet integrating for one proton. The H^{1}-NMR spectrum of Fraction 1 also had no aliphatic or CH_3 proton signals and therefore is unlikely an unbound bipyridine ligand. The isolated adducts did not ionize on

the HPLC-MS mass spectrum, as it had no parent ion peak. Therefore, without further comprehensive data, the identity of the obtained products could not be determined.

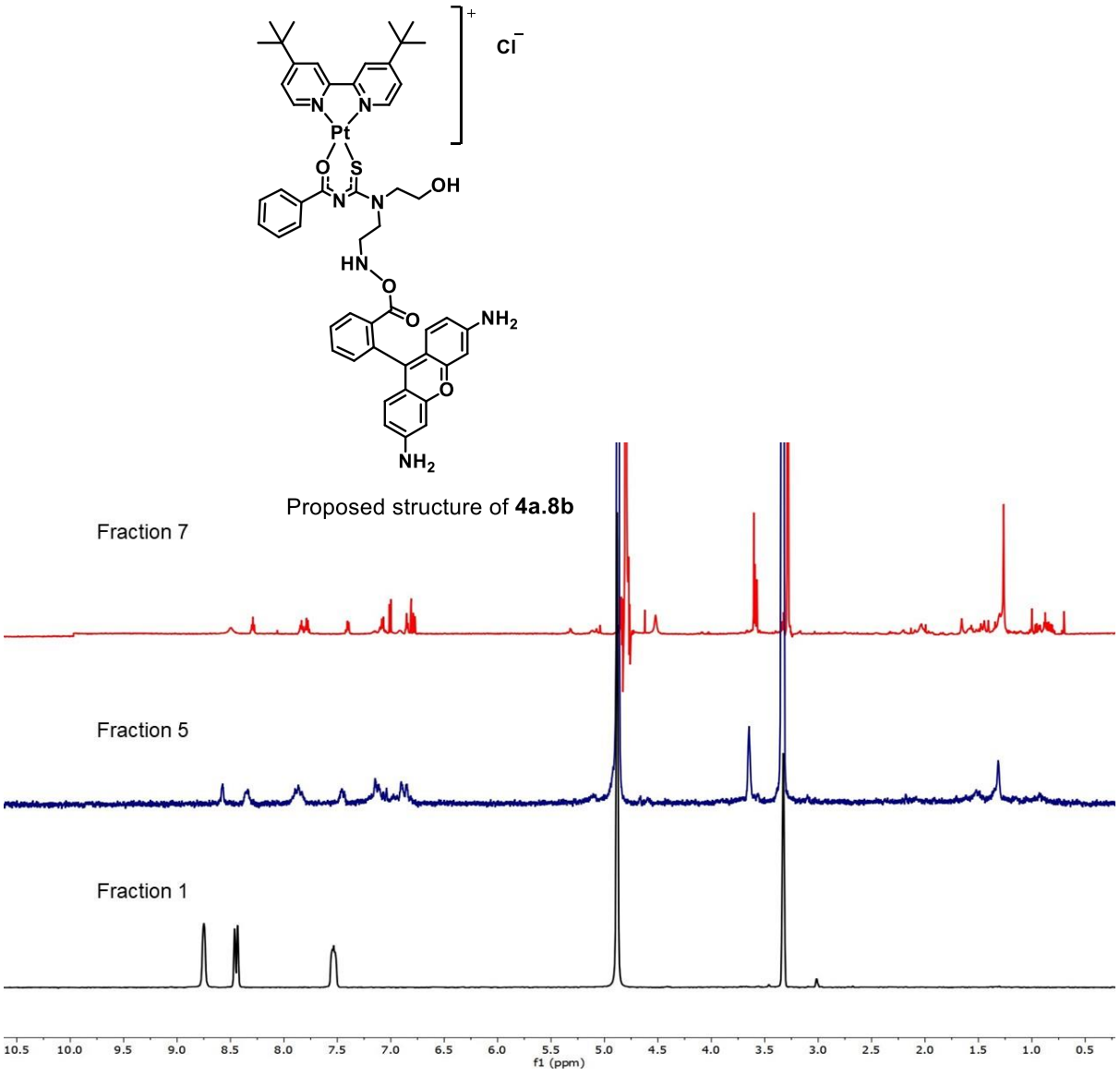

Figure 2.30. Stacked ^{1}H-NMR spectra of fractions obtained from the preparative HPLC purification attempt of complex **4a.8b** in methanol-d_4. The proposed structure of complex **4a.8b** is shown above the ^{1}H-NMR spectra.

Alternatively, a similar reaction was attempted between complex **4a.8a** and fluorescein to synthesize a fluorescein-labeled analog **4a.8c** (**Scheme 2.10**). Complex **4a.8a** was reacted with fluorescein under the same reaction conditions previously mentioned in an attempt to synthesize complex **4a.8c**. As with **4a.8b**, there was no clear evidence to suggest successful amide coupling between the carboxylic acid of the fluorescein moiety and the terminal amine of **4a.8a**. In the aromatic region of the obtained ^{1}H-NMR spectrum of the isolated fractions of compound **4a.8c** (not shown), the signals integrated for a sum of 15 aromatic protons. As discussed for complex **4a.8b**, assigning these proton signals would not be appropriate without HPLC-MS data and the inability to determine the multiplicity of the signals to confirm a proposed compound identity. However, it can be confirmed that the desired fluorescein-containing compound (**4a.8c**) was not synthesized. This was to some extent surprising, given the wealth of fluorescein analogs reported in the literature, including analogs containing a metal center.[238–240] It is noteworthy that due to several reports of fluorescent quenching for fluorescein amines, alternative fluorescent probes such as Bopidy and Oregon Green could also be explored in the future.

2.4. Conclusion

This chapter discussed the rationale for the design of the acyl-thiourea-bipyridine platinum(II) complexes and their precursors. The six chemical modifications to the parent compound **4a.1** were described and selected representative compounds were used for discussing characterization using mainly 1D ^{1}H-NMR, ^{13}C-NMR, and HPLC-MS analysis. Where relevant, 2D NMR experiments including COSY, HSQC, and HMBC spectroscopy were also utilized. ATR-FTIR was used to confirm successful counterion exchanges and the lack of ligated solvent molecules in the gold(III) analog. Although only key intermediates and selected final metal complexes were discussed in this chapter, the full characterization details of the remaining compounds are described in **Chapter 7**. The ^{1}H-NMR data of the intermediates attest to their successful synthesis and the HPLC-MS data of the final complexes were of the high purity (>95%) required for further biological testing, including microscopic studies of the dansyl-labeled analog. The biological evaluation of the complexes is discussed in **Chapter 3** with mechanistic studies discussed in **Chapters 4** and **5**, respectively.

Chapter 3: Pharmacological Evaluation and Structure-Activity/Structure-Property Relationships of [Pt/Au(diimine)L-O,S]$^{+/2+}$ Complexes

3.1. Chapter overview

This chapter describes the pharmacological, physicochemical, and pharmacokinetic properties of the transition metal complexes that were described and synthesized in **Chapter 2**. Herein, the structure-activity relationships (SARs) and structure-property relationships (SPRs) of the six chemical modifications to these complexes were compared within the series to identify the chemical space for improved whole-cell potency, as well as the substituents that resulted in favourable, drug-like properties of the complexes. A screening cascade (**Figure 3.1**) was established and used as a workflow to provide progression criteria to ensure that the most potent compounds were prioritized for downstream assays.

This chapter begins with the comparison of the asexual blood stage (ABS) and gametocyte potencies of the synthesized matched-pair complexes containing rationally designed chemical modifications. The synthesized complexes were tested for their ABS potencies against the drug-sensitive *Pf*-NF54 and multidrug-resistant *Pf*-K1 strains. Compounds with ABS activity below 1 µM, selectivity for activity against the *Pf* parasite relative to mammalian cells (selectivity index above 10), and aqueous solubility above 10 µM, were tested for their microsomal metabolic stability. Finally, the pharmacokinetic (PK) parameters, permeability, and plasma protein binding (PPB) of the frontrunner complex were determined as per the screening cascade (**Figure 3.1**).

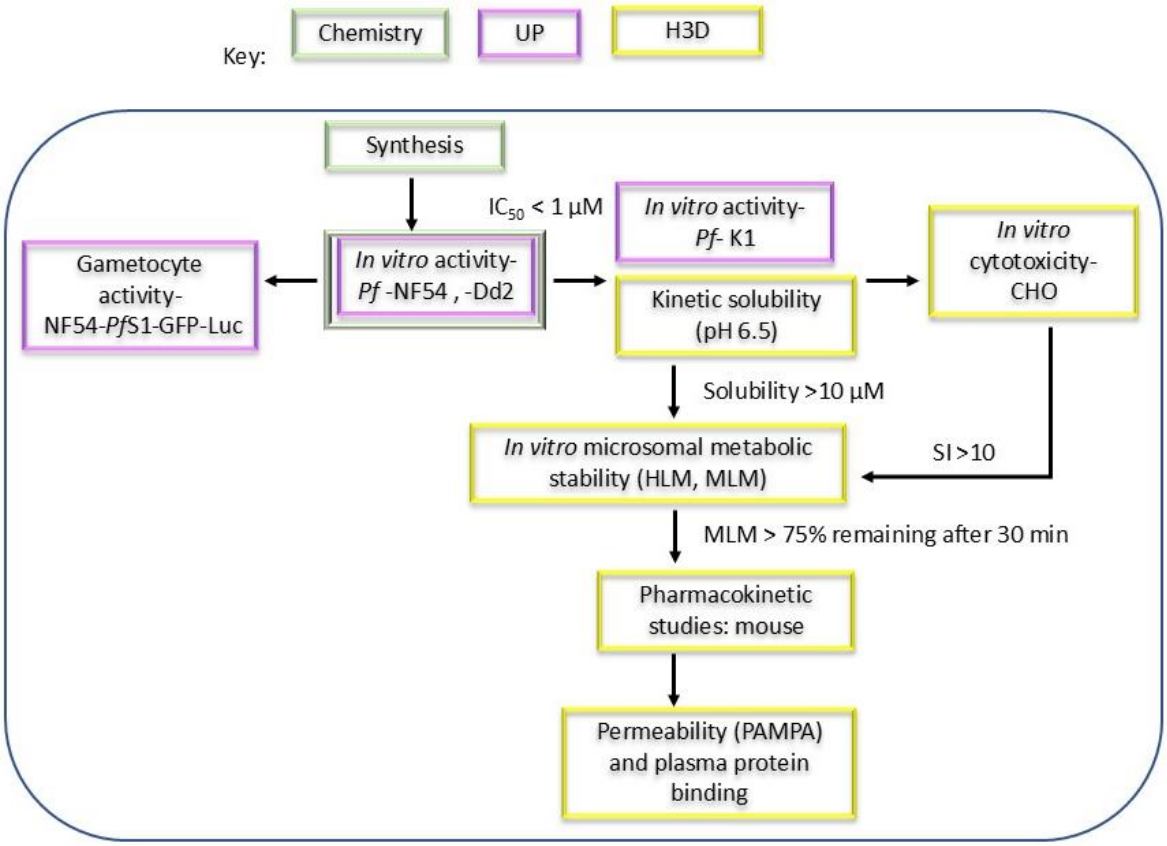

Figure 3.1. The screening cascade which served as a workflow to prioritize the frontrunner complexes for downstream experiments to determine SARs and SPRs. In brief, the project started with the design and synthesis of the complexes. This was followed by *in vitro* antiplasmodium studies in the *Pf*-NF54 and *Pf*-K1 strains, and subsequently by gametocyte activity and cytotoxicity studies. Select complexes were prioritized for aqueous solubility and microsomal metabolic stability studies. One frontrunner complex progressed to PK, permeability, and plasma protein binding studies. The provided key indicates if these assays were run by collaborators at the respective institutes (UP, University of Pretoria; H3D, Holistic Drug Discovery and Development Centre at the University of Cape Town, UCT) or in the UCT synthetic chemistry lab or cell culture lab.

3.2. Antiplasmodium activity of platinum(II) complexes

Many antimalarial drugs that are currently in clinical use act against only the ABS of the parasite life cycle and cannot be used to prevent parasite transmission.[41] Therefore, discovering compounds that act against the sexual stage (gametocytes) of the parasite life cycle is essential for controlling the spread and elimination of the disease,[241] as late-stage gametocytes (LG) are the only form of the parasite that can be transmitted back to the mosquito vector.[242] The spread of drug-resistant strains further supports the importance of screening for compounds with multistage activity. A compound that acts against more than one life cycle stage can elicit its potency through polypharmacology which in turn can assist in preventing the emergence of drug resistance.[243] Furthermore, the selectivity of the complexes for the malaria parasite compared to mammalian cells is important to establish. This is because the cytotoxicity of a compound can flag potential adverse effects that it may have on non-target cells.[244]

To this end, the synthesized [Pt(diimine)L-O,S]$^{+}$ and [Au(diimine)L-O,S]$^{2+}$ complexes (**Sections 2.3.4-2.3.6**) were evaluated for their *in vitro* whole-cell potency against the ABS and gametocyte stages of the *Pf* life cycle. Complexes were screened against both the early-stage (EG) and LG gametocytes. In addition, the selectivity of these complexes for the malaria parasite was determined by testing them against the Chinese hamster ovarian (CHO) cell line. A summary of the six chemical modifications discussed in **Chapter 2** and their respective compound structures are shown in **Figure 3.2**.

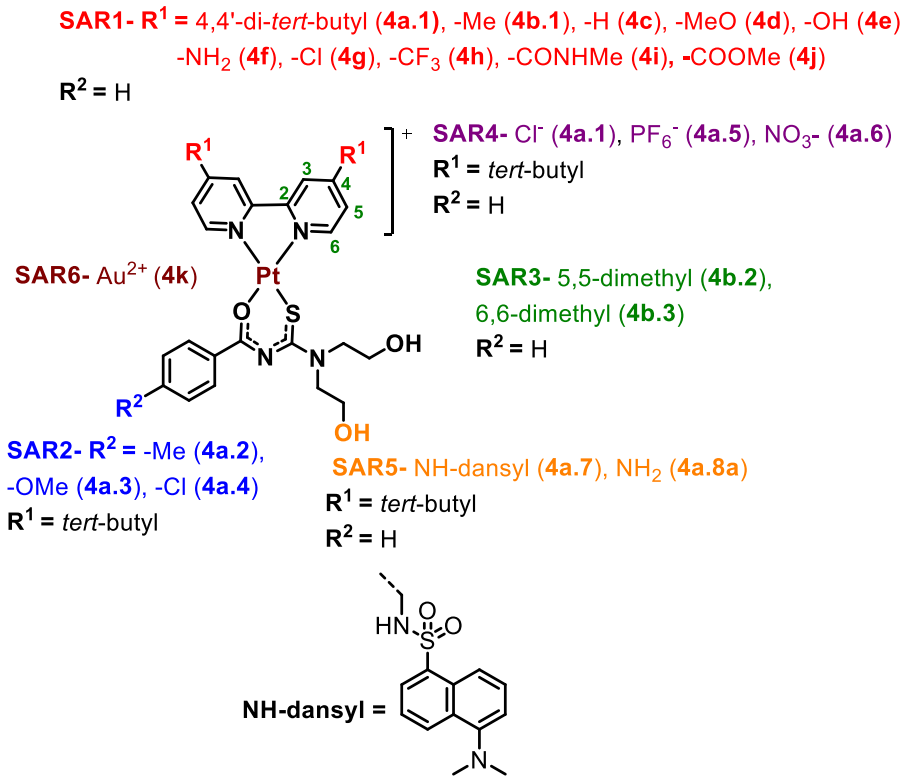

Figure 3.2. The summary of the synthesized metal complexes and their six chemical modifications for SAR and SPR evaluation.

For the evaluation of the ABS activity of the complexes, a SYBR Green I assay was used in which the test compounds were incubated for 96 hours with either the *Pf*-NF54 or *Pf*-K1 strains, with chloroquine (CQ) as the control. The potency of the test compounds against EGs and LGs was determined *in vitro* via a luciferase reporter line-based assay in which the NF54-*Pf*S16-GFP-Luc (transgenic parasite line) was used for the stage-specific assessment of gametocyte activity. Once the parasite enters the sexual stage of its life cycle, it progresses through its five distinct morphological stages over 10-18 days.[5] Thus, EG (stage I-III) experiments were performed on day 5, after parasites enter the sexual stage and LG (stages IV/V) experiments were performed on day 10, with methylene blue (MB) and MMV390048 (MMV048) as positive controls. The SARs for whole-cell ABS and gametocyte potencies are compared and discussed below for each of the six chemical modifications. Where the complexes did not display inhibition of gametocytes in a dual-point assay of >50% at 1 μM and >70% at 5 μM, IC_{50} values were not determined.

3.2.1. Structure-activity relationship of SAR1 [Pt(diimine)L-O,S]$^{+}$ complexes

To evaluate the SAR of compounds from the first series of complexes (**SAR1**, **Figure 3.3**, complexes **4a.1 - 4j**), the substituent in the 4,4'-positions of the bipyridine was varied. At the same time, the acyl-thiourea ligand was unsubstituted in the *para*-position (R^2 = H) and a chloro counterion was maintained. Their whole-cell potencies against the ABS and gametocyte stages of the *Pf* life cycle are listed in **Table 3.1**.

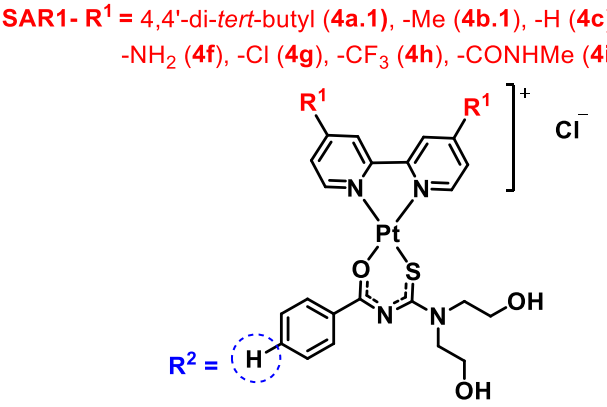

Figure 3.3. The structures of **SAR1** complexes in which the 4,4-position on the bipyridine moiety was substituted with varying substituents from the Craig plot to evaluate their antiplasmodium activities.

Complexes **4a.1** (R^1 = *tert*-butyl), **4c** (R^1 = H), **4d** (R^1 = MeO), and **4f** (R^1 = NH^2) exhibited IC_{50} values below 1 µM against the *Pf*-NF54 strain, with **4f** being the most active within this series (IC_{50} = 36.3 ± 0.6 nM). Complexes **4b.1** and **4d** were slightly more potent against the *Pf*-K1 strain with resistance indices (RIs) below 1. Furthermore, **4a.1**, **4c,** and **4f** were only moderately more active against the drug-susceptible *Pf*-NF54 strain compared with the multidrug-resistant strain *Pf*-K1, with RI values much lower than that of the control drug, CQ. Therefore, the complexes do not show substantial cross-resistance with CQ. Complexes that were substituted with electron-withdrawing moieties at R^1, such as chloro (**4g**), methyl amide (**4i**), methyl ester (**4j**), and trifluoromethyl (**4h**) were inactive up to 5 µM in the *Pf*-NF54 strain and were subsequently not tested against the *Pf*-K1 strain.

Table 3.1. Antiplasmodium activity of **SAR1** complexes as a measure of their IC_{50} values. SEM values are reported in which there were three independent repeats (N) and three technical repeats (n); N, n = 3, 3.

		IC_{50} (nM)			IC_{50} (nM)
Complex	**R^1**	***Pf*-NF54**	***Pf*-K1**	**RI**	**EG/LG**
K_2Cl_4Pt		>5000	ND		
1a		>5000	ND		
3a		>5000	ND		
4a.1	***tert*-butyl**	151 ± 17	433 ± 37	2.9	6362/3539 ± 1639
4b.1	**Me**	1415 ± 276	541 ± 44	0.4	
4c	**H**	142 ± 12	183 ± 22	1.3	
4d	**MeO**	266 ± 29	164 ± 7	0.6	
4e	**OH**	>5000	ND		
4f	**NH_2**	36.3 ± 0.6	102 ± 13	2.8	
4g	**Cl**	>5000	ND		
4h	**CF_3**	>5000	ND		>20000/380 ± 198
4i	**CONHMe**	>5000	ND		
4j	**COOMe**	>5000	ND		
CQ		11 ± 2	143 ± 3	12.7	
MB					190/900
MMV048					215/134

Abbreviations: ND- Not determined, EG- early-stage gametocytes, LG- late-stage gametocytes, RI- resistance index ($\frac{IC_{50}\ K1}{IC_{50}\ NF54}$)

These results suggest that the potency of this series against the *Pf* parasite is favored by the presence of an electron-donating substituent in the 4-4'-positions of the bipyridine ring. However, no trend is observed between the Craig plot π-values of the substituents and the bioactivity of the complexes. Furthermore, to evaluate the pharmacological contribution of each moiety, the antiplasmodium activity of the metal salt (K_2Cl_4Pt), ligand **1a**, and the dichloro-diimine complex **3a** (R^1 = *tert*-butyl) shown in **Figure 3.4**, was also determined. K_2Cl_4Pt, **1a**, and **3a** did not exhibit antiplasmodium activity when tested at a maximum concentration of 5 μM against *Pf*-NF54 (**Table 3.1**), highlighting the structural importance of combining both the acyl-thiourea and platinum-bipyridine moieties to form a pharmacologically active complex.

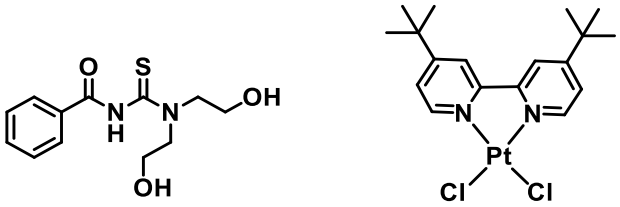

1a **3a**

Figure 3.4. Structures of acyl thiourea ligand (**1a**) and *tert*-butyl diimine platinum(II) precursor complex (**3a**).

Concerning gametocyte activity, the complexes containing the bulkier, more hydrophobic substituents such as *tert*-butyl (**4a.1**) and CF_3 (**4h**) were active against both EG and LG (**4a.1**) or only LG (**4h**) when tested at concentrations up to 20 μM. However, moderate potency was exhibited for complex **4a.1** with complex **4h** having an IC_{50} value below 1 μM against LG. Interestingly, complex **4h** displayed negligible ABS potency at 5 μM but was active against the sexual stage of the life cycle as mentioned above. These results suggest that gametocyte activity for this series may be dependent on the presence of the bulkier tertiary functional groups.

3.2.2. Structure-activity relationship of SAR2 [Pt(diimine)L-O,S]$^{+}$ complexes

For **SAR2**, the substituent on the bipyridine was kept constant (*tert*-butyl) with a chloro counterion and the substituent in the *para*-position of the phenyl ring of the acyl-thiourea ligand was varied (**Figure 3.5**).

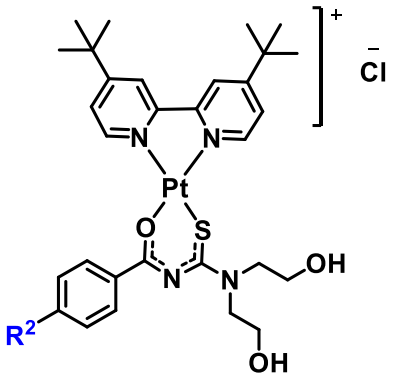

SAR2-R^2 = Me (**4a.2**),OMe (**4a.3**), Cl (**4a.4**)

Figure 3.5. The structures of **SAR2** complexes in which the *para*-position on the phenyl ring of the acyl-thiourea ligand was substituted with a methyl (**4a.2**), methoxy (**4a.3**), and chloride (**4a.4**) substituent while the substituent in the 4,4'-position of the bipyridine moiety remained a *tert*-butyl.

The addition of a methyl (**4a.2**) or methoxy (**4a.3**) functionality in this *para*-position did not further improve whole-cell potency against *Pf*-NF54, compared to the parent complex (**4a.1**), as seen in **Table 3.2**. Interestingly, the addition of an electron-withdrawing substituent in the 4,4'-position of the bipyridine in **SAR1** produced inactive complexes at the tested concentration of 5 µM. However, for **SAR2**, the presence of an electron-withdrawing chloro substituent on the phenyl ring improved whole-cell potency three-fold compared to **4a.1**. Furthermore, the *Pf*-K1 strain was more susceptible to complexes **4a.2** and **4a.3** with resistance indices below 1. Therefore, like the **SAR1** complexes, the **SAR2** series does not exhibit cross-resistance with CQ either. This suggests that substitution in the *para*-position of the phenyl ring could improve the antiplasmodium activity of this chemical series against the drug-resistant *Pf*-K1 strain. Like the observation in **SAR1**, complexes **4a.2** and **4a.3** showed both EG and LG activity with their LG activity below 1 µM with IC_{50} values of 216 ± 56 nM and 405 ± 75 nM, respectively. This further supports the previous statement concerning the essentiality of the *tert*-butyl substituent for gametocyte activity.

Table 3.2. Antiplasmodium activity of **SAR2** complexes as a measure of their IC_{50} values. SEM values are reported where N, n = 3, 3.

		IC_{50} (nM)			IC_{50} (nM)
Complex	**R^2**	***Pf*-NF54**	***Pf*-K1**	**RI**	**EG/LG**
4a.1	**H**	151 ± 17	433 ± 37	2.9	6362/ND
4a.2	**Me**	114 ± 8	29 ± 10	0.3	3030/216 ± 56
4a.3	**OMe**	224 ± 13	13 ± 10	0.1	4610/405 ± 75
4a.4	**Cl**	51 ± 4	251 ± 83	4.9	>20000/>20000
CQ		11 ± 2	143 ± 3	12.7	
MB					190/900
MMV048					215/134

Abbreviation: ND- Not determined, EG- early-stage gametocytes, LG- late-stage gametocytes, RI-resistance index ($\frac{IC_{50}\ K1}{IC_{50}\ NF54}$)

3.2.3. Structure-activity relationship of SAR3 [Pt(diimine)L-O,S]$^+$ complexes

To determine the pharmacological effect of substitution in different positions on the bipyridine (**SAR3**), the methyl substituent was used (**Figure 3.6**). As mentioned in **Section 2.2**, the methyl substituent was selected due to the commercial availability of the necessary synthetic starting materials to evaluate the regiospecificity of the biological activity.

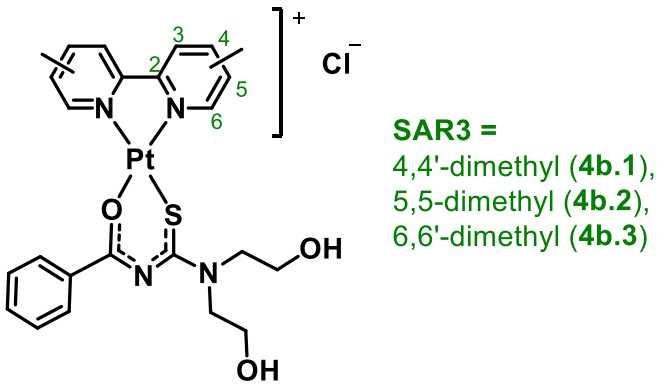

Figure 3.6. The structures of **SAR3** complexes in which the position of the methyl substituent was changed from the 4,4'-position (**4b.1**) to the 5,5'-position (**4b.2**), and 6,6'-position (**4b.3**) on the bipyridine moiety. This was conducted to evaluate the SAR related to this change of position.

Altering the position of the methyl substituent from the 4,4'-position (**4b.1**) to the 5,5'-position (**4b.2**) on the bipyridine moiety improved whole-cell potency against the *Pf*-NF54 strain six-fold whereas changing to the 6,6'-postion (**4b.3**) decreased potency two-fold (**Table 3.3**). For the *Pf*-K1 strain, a similar trend was observed for **4b.3**; changing the position of the methyl substituent to the 6,6'-position decreased potency five-fold. Additionally, changing to the 5,5'-position decreased activity against *Pf*-K1 approximately two-fold. Complexes **4b.1, 4b.2,** and **4b.3**, therefore, showed no cross-resistance with CQ, as their RI values were much lower than CQs. None of the **SAR3** complexes exhibited appreciable potency against the EGs or LGs in the dual-point assays in which they were tested at 1 μM and 5 μM.

Table 3.3. Antiplasmodium activity of **SAR3** complexes as a measure of their IC_{50} values. SEM values are reported where N, n = 3, 3.

		IC_{50} (nM)		
Complex	**R[1]**	***Pf*-NF54**	***Pf*-K1**	**RI**
4b.1	**4,4'-dimethyl**	1415 ± 277	541 ± 44	0.4
4b.2	**5,5'-dimethyl**	241 ± 40	886 ± 59	3.7
4b.3	**6,6'-dimethyl**	2908 ± ND	2764 ± ND	0.9
CQ		11 ± 2	143 ± 3	12.7

Abbreviation: ND- Not determined, EG- early-stage gametocytes, LS- late-stage gametocytes, RI- resistance index ($\frac{IC_{50}\ K1}{IC_{50}\ NF54}$)

3.2.4. Structure-activity relationship of SAR4 [Pt(diimine) L-O,S]$^{+}$ complexes

The pharmacological impact of the counterion was evaluated by exchanging the chloro (Cl^-, **4a.1**) counterion with either hexafluorophosphate (PF_6^-, **4a.5**) or nitrate (NO_3^-, **4a.6**). The scaffold of the parent compound (**4a.1**) was maintained with a *tert*-butyl in the 4,4'-position on the bipyridine ligand and hydrogen in the *para*-position of the phenyl ring on the acyl-thiourea ligand (**Figure 3.7**).

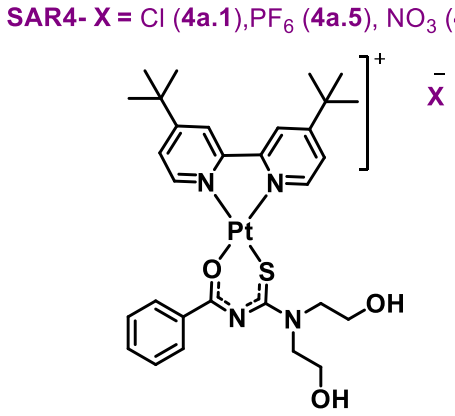

Figure 3.7. Structures of the SAR4 complexes, where the structure-activity relationship between three different counterions: Cl (**4a.1**), PF_6 (**4a.5**), and NO_3 (**4a.6**) was explored. The *tert*-butyl substituent in the 4,4'-position of the bipyridine and hydrogen in the *para*-position of the phenyl ring was maintained.

Comparable *Pf*-NF54 activity was observed between the parent complex **4a.1**, which had an IC_{50} = 151 ± 17 nM, and the hexafluorophosphate analog, **4a.5**, with an IC_{50} = 124 ± 37 nM, as shown in **Table 3.4**. In contrast, the analog with a nitrate counterion, **4a.6**, showed an 11-fold increase in potency against *Pf*-NF54 (IC_{50} = 14 ± 8 nM) compared to **4a.1**. Complexes **4a.5** and **4a.6** were two-fold and three-fold more active than **4a.1** (*Pf*-K1 IC_{50} = 433 ± 37 nM) in the *Pf*-K1 strain with IC_{50} values of 252 ± 94 nM and 135 ± 41 nM, respectively.

Table 3.4. Antiplasmodium activity of **SAR4** complexes as a measure of their IC_{50} values. SEM values are reported where N, n = 3, 3.

		IC_{50} (nM)			IC_{50} (nM)
Complex	**Counterion**	***Pf*-NF54**	***Pf*-K1**	**RI**	**EG/LG**
4a.1	**Cl^-**	151 ± 17	433 ± 37	2.9	6362/ND
4a.5	**PF_6^-**	124 ± 37	252 ± 94	2.0	ND/8922
4a.6	**NO_3^-**	14 ± 8	135 ± 41	9.6	ND/ND
CQ		11 ± 2	143 ± 3	12.7	ND/ND
MB					190/900
MM048					215/134

Abbreviation: ND- Not determined, EG- early-stage gametocytes, LS- late-stage gametocytes, RI-resistance index ($\frac{IC_{50}\ K1}{IC_{50}\ NF54}$)

Furthermore, considering the RI of these complexes, only the nitrate analog, **4a.6**, showed considerable cross-resistance with CQ. Additionally, to the best of our knowledge, there have been no reports on the comparison of the antiplasmodium activity of transition metal complexes containing a nitrate counterion as opposed to other counterions like chloro or hexafluorophosphate.

3.2.5. Structure-activity relationship of SAR5 [Pt(diimine)L-O,S]$^{+}$ complexes

To study the cellular localization of the complexes within the *Pf* parasite, a dansyl-labeled derivative of **4a.1** was synthesized, (**4a.7**, **Section 2.3.7**). Additionally, a derivative with a terminal amine instead of the hydroxyl functionality used in SAR1-4 was also synthesized (**4a.8a**). Complex **4a.8a** served as an unlabeled analog of **4a.7** (**Figure 3.8**), to study the SAR of these chemical modifications.

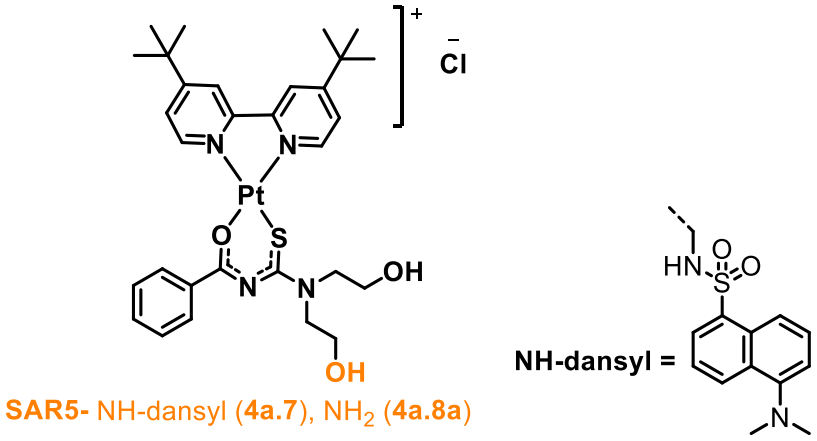

SAR5- NH-dansyl (**4a.7**), NH_2 (**4a.8a**)

Figure 3.8. Structures of the SAR5 complexes, in which the terminal hydroxyl at one end of the diethanolamine chain was replaced with an HN-dansyl reporter (**4a.7**) or terminal amine (**4a.8a**). The *tert*-butyl substituent in the 4,4'-position of the bipyridine and hydrogen in the *para*-position of the phenyl ring was maintained.

Replacing one terminal hydroxyl with an HN-dansyl reporter (**4a.7**) had a negligible effect on its antiplasmodium activity. Despite the bulky size of the dansyl fluorophore, Complex **4a.7** displayed comparable whole-cell potency against the *Pf*-NF54 strain compared to its parent compound, **4a.1**, with an IC_{50} value of 132 ± 16 nM, as shown in **Table 3.5**. The retained potency of **4a.7** compared to the parent compound **4a.1** supported its use as a fluorescent probe for cellular localization studies in **Section 4.8**. Contrastingly, complex **4a.7** (*Pf*-K1-IC_{50} = 209 ± 51 nM) was two-fold more active against the *Pf*-K1 strain compared to **4a.1** (*Pf*-K1-IC_{50} = 433 ± 37 nM) and exhibited negligible cross-resistance with CQ (RI = 1.6). Complex **4a.7** also showed a two-fold increase in potency against the EG of the *Pf* life cycle. Interestingly, replacement of one terminal hydroxyl with an amine (**4a.8a**) resulted in a

decrease in its *Pf*-NF54 potency by eight-fold compared to **4a.1**. However, **4a.8a** was more potent against *Pf*-K1 than *Pf*-NF54 with an IC_{50} of 893 nM and a RI of 0.7.

Table 3.5. Antiplasmodium activity of SAR5 complexes as a measure of their IC_{50} values. SEM values are reported where N, n = 3, 3.

Complex	Terminal attachment	IC_{50} (nM)			IC_{50} (nM)
		***Pf*-NF54**	***Pf*-K1**	**RI**	**EG/LG**
4a.1	OH	151 ± 17	433 ± 37	2.9	6362/ ND
4a.7	HN-dansyl	132 ± 16	209 ± 51	1.6	2897/5075
4a.8a	NH_2	1207 ± ND	893 ± ND	0.7	>20000/>20000
CQ		11 ± 2	143 ± 3	12.7	
MB					190/900
MM048					215/134

Abbreviation: ND- Not determined, EG- early-stage gametocytes, LS- late-stage gametocytes, RI-resistance index ($\frac{IC_{50}\,K1}{IC_{50}\,NF54}$)

3.2.6. Structure-activity relationships of SAR6 platinum(II) and gold(III) complexes

The final chemical modification involved a change of the transition metal and subsequently the oxidation state of the metal center from platinum(II) to gold(III). Gold(III) was selected for this SAR analysis because it forms square planar complexes, maintaining the geometry observed for the platinum analogs. Additionally, gold(I) and gold(III) have been used in cancer studies as alternatives to the potent, but toxic, platinum analogs.[245] Consequently, the charge on the metal center changed from 1+ in the parent platinum complex (**4a.1**) to 2+ in the gold analog (**4k**, **Figure 3.9**). For this chemical modification, the *tert*-butyl substituent was maintained in the 4,4'-position of bipyridine and hydrogen in the *para*-position of the acyl-thiourea ligand. However, complex **4k** was synthesized with two hexafluorophosphate counterions as opposed to the one chloro counterion seen in **4a.1**.

SAR6

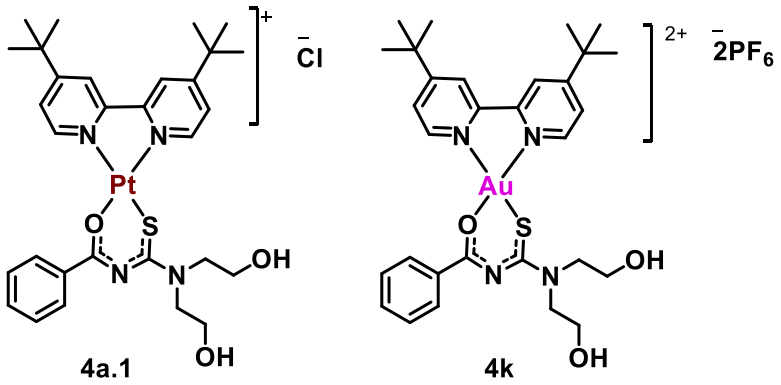

Pf-NF54-IC_{50} = 151 ± 17 nM

Pf-NF54-IC_{50} = 3743 nM

Figure 3.9. Structures of the **SAR6** complexes, in which the transition metal center was changed from platinum(II) (**4a.1**) to gold(III) (**4k**) and subsequently the counterion from chloro to hexafluorophosphate. The *Pf*-NF54-IC_{50} values for the two complexes are provided with SEM where N, n = 3, 3. For the gold analog, the IC_{50} value was calculated from three technical repeats.

The pharmacological effect of this chemical change in the transition metal center was evaluated in the *Pf*-NF54 strain where the gold(III) analog (**4k**, IC_{50} = 3743 nM) was 25-fold less potent than the platinum(II) parent complex (**4a.1**). This high IC_{50} value was not surprising given the micromolar values seen in the literature for other gold(III) complexes containing a thiosemicarbazone ligand.[131] Although there are several reports on gold complexes with appreciable antiplasmodium activity,[131,246,247] the development of gold(III) complexes for chemotherapeutics has been avoided, largely due to low stability under physiological conditions.[131] However, in some instances, the so-called "speciation" of gold (III) analogs from Au^{3+} to Au^{+} in biological systems has been shown to contribute to their potency,[248] although this does not seem to apply to complex **4k** here. Speciation of **4k** was seen in **Section 2.3.6**, where solvent coordination occurred in the presence of H_2O and MeCN, thus potentially altering the bioactive compound. Hence, evaluating the aqueous stability in the growth medium of **4k** in the future will be insightful. Furthermore, the cyclic voltammetry studies discussed in **Chapter 4** also confirm the ability of **4k** to undergo reductions from Au^{3+} to Au^{+}, albeit this redox property does not result in an improvement in its whole-cell potency.

3.3. *In vitro* cytotoxicity against the Chinese hamster ovarian (CHO) cell line

The relatively non-specific action of clinically-used platinum-based drugs such as cisplatin and carboplatin, which cause systemic toxicity, are well known.[249] For this reason, the cytotoxicity of the synthesized platinum(II) complexes were determined using the 3-(4,5-dimethylthiazol-2-yl)-2,5-diphenyltetrazolium bromide (MTT) cell proliferation assay. The growth of the CHO cell line was calorimetrically measured after incubation with the test complexes, shown in **Figure 3.10**.

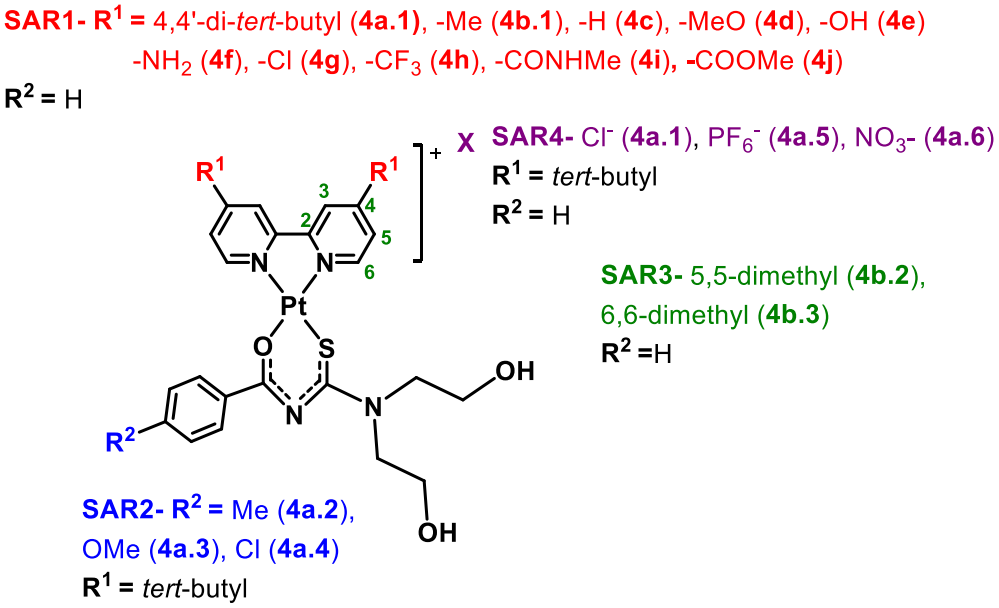

Figure 3.10. Summary of the complexes tested against the CHO cell line to determine their cytotoxicity and selectivity indices.

The selectivity index (SI) was used as a general indication of cytotoxicity and is a ratio between the *Pf*-NF4-IC$_{50}$ and the CHO-IC$_{50}$ and these values are shown in **Table 3.6**. A SI value above 10 was considered desirable and reflects the selectivity of the tested compound to the target species, *Pf*, as opposed to mammalian cells. In general, the **SAR1** complexes exhibited high levels of selectivity to the *Pf* parasite in which definitive CHO-IC$_{50}$ values could not be determined at the tested concentrations of up to 50 µM, except for the *tert*-butyl analog, **4a.1**. Complexes from the **SAR2** series were slightly less selective towards the *Pf* parasite compared to CHO cells with lower SI values compared to **SAR1**, suggesting that substitution in the *para*-position of the phenyl group with Me, MeO and Cl, renders the complex slightly more cytotoxic than a H-substituent. Changing the position of the methyl group on the

bipyridine to 5,5'-substition (**4b.2**) in **SAR3** has a negligible effect on its toxicity while improving whole-cell potency against *Pf*. Contrastingly, the 6,6'-substituted analog, **4b.3** is not only less potent than the parent **4b.1** but also more cytotoxic with a SI of 2.

Table 3.6. Cytotoxicity and selectivity of tested complexes against the CHO cell line. IC_{50} values above 50 μM indicate that the compound was not active against the CHO cell line at a maximum test concentration of 50 μM. The complexes are color-coded according to their SAR: **SAR1**, **SAR2**, **SAR3**, and **SAR4**.

Complex	**4a.1**	**4b.1**	**4c**	**4d**	**4e**	**4f**	**4g**	**4h**	**4i**
CHO IC_{50} (μM)	17	>50	>50	>50	>50	>50	>50	>50	>50
SI	112	>35	>355	>188	>10	>1377	>10	>10	>10
Complex	**4j**	**4a.2**	**4a.3**	**4a.4**	**4b.2**	**4b.3**	**4a.5**	**4a.6**	
CHO IC_{50} (μM)	>50	30	25	23	>50	5	11	16	
SI	>10	90	96	29	>207	2	89	1111	

Abbreviations: CHO-Chinese hamster ovarian cell line, SI- selectivity index: $\frac{\text{CHO IC}_{50}}{Pf-\text{NF54 IC}_{50}}$

Lastly, exchanging the chloro counterion for a hexafluorophosphate (**4a.5**) or nitrate (**4a.6**) in **SAR 4**, resulted in complexes that displayed similar CHO cytotoxicity as its parent, **4a.1**. Most notably, the nitrate analog was far more selective towards the *Pf* parasite than to CHO cells compared to the chloro analog. This further confirms that the 11-fold increase in potency observed for **4a.6** compared to **4a.1** is not a result of a general cytotoxic effect but is specific to its potency against *Pf*.

Following the evaluation of the SARs and cytotoxicity of the compounds within the synthesized series, it was important to investigate their SPRs to determine which analog(s) had the most desirable druglike properties. This began with measuring the complex's kinetic solubilities in an aqueous medium at pH 6.5 as discussed below.

3.4. SPR of [Pt(diimine) L-O,S]+ complexes

3.4.1. Kinetic aqueous solubility at pH 6.5

The solubility of a compound is an important property to investigate during the drug design process. Compounds with poor solubility tend to precipitate out of an aqueous medium during biological testing, decreasing the validity and reproducibility of the results. Poor solubility also affects the bioavailability of the compound and can become a challenge during *in vivo* testing.[250] Furthermore, solubility affects the concentration of the drug in systemic circulation and subsequently plays an important role in the pharmacological response.[251]

For this experiment, an HPLC-based method was used to determine the kinetic solubility of the **SAR1** and **SAR2** transition metal complexes. This allowed for a comparison of solubilities between compounds containing various substituents on the bipyridine compared to those on the phenyl ring. Kinetic solubility differs from thermodynamic solubility in that, for the former, the test compound is introduced into the assay pre-dissolved and the extent to which the compound precipitates out of the aqueous medium is measured. Contrastingly, thermodynamic solubility assays introduce the test compound as a solid and measures the extent to which it dissolves.[252]

Overall, the **SAR1** were highly soluble in aqueous medium at pH 6.5 ($S_{6.5}$) with values ranging between 95 µM and 195 µM as seen in **Table 3.7**.

Table 3.7. Kinetic solubility of compounds in phosphate-buffered saline at pH 6.5, $S_{6.5}$.

	SAR1				
Complex	**4a.1**	**4b.1**	**4c**	**4d**	**4f**
R^1 (R^2 = H)	*tert*-butyl	Me	H	MeO	NH_2
Solubility: $S_{6.5}$ (µM)	95	170	140	195	100
***Pf*-NF54/K1 IC_{50} (nM)**	151/433	1415/541	141/183	266/164	36/102
	SAR2				
Complex	**4a.2**	**4a.3**	**4a.3**		
R^2 (R^1 = *tert*-butyl)	Me	MeO	Cl		
Solubility: $S_{6.5}$ (µM)	<5	<5	150		
***Pf*-NF54/K1 IC_{50} (nM)**	114/29	223/13	52/251		

No trend between Craig plot values (σ: electron-donating/withdrawing properties and π: hydrophobicity) and the solubility of the complexes was observed. The analog containing a water-solubilizing methoxy substituent in the 4,4'-position on the bipyridine (**4d**) was the most soluble (195 μM). Surprisingly, within the **SAR2** series, only the analog with the more hydrophobic electronegative chlorine substituent (**4a.3**) displayed an appreciable solubility of 150 μM. Since no obvious trend was observed between the π values of the substituent and the solubility of the compound, its solubility may be influenced by the dissociation capacity of the anion (Cl^-) and the cationic species which may vary between the analogs.

Furthermore, no correlation between whole-cell potency and solubility was observed as shown by the comparison of the $S_{6.5}$ values and the *Pf*-NF54/K1 IC_{50} values in **Table 3.7**. The most soluble complex in **SAR1** (**4d**, R^1 = MeO) was five-fold less potent than complex **4f** (the most potent analog) which had a solubility half that of **4d** ($S_{6.5}$ = 195 μM). Additionally, complexes **4a.2** and **4a.3** had poor solubilities below 5 μM but were very potent against the *Pf*-K1 strain of the malaria parasite. However, the most soluble **SAR2** analog (**4a.3**, R^2 = Cl) was also the most potent against the *Pf*-NF54 strain.

Following these kinetic aqueous solubility measurements, the microsomal metabolic stabilities of a subset of the synthesized complexes were determined as discussed below.

3.4.2. *In vitro* microsomal metabolic stability

Microsomal metabolic stability is an important parameter in a good drug candidate, as poor metabolic stability can lead to poor oral bioavailability.[253] Microsomal metabolic stability measures the test compounds' susceptibility to undergo biotransformation in the presence of liver microsomes.[253] Liver microsomes are vesicle-like structures found in hepatocytes that contain phase I metabolizing enzymes.[254] The metabolic stability is often expressed as either intrinsic clearance (CL_{int}) or as a percentage (%) of the compound remaining after incubation. Metabolism of various drugs occurs in several organs/tissues, including the lungs,[255] kidneys,[256] intestines,[257] skin,[258] and blood,[259] with the liver being the primary drug metabolizing organ.[260]

Additionally, drug metabolism occurs via different reactions and is categorized as phase I (modification) and phase II (conjugation) metabolism. Phase I metabolism employs the use of cytochrome P450 (CYP450) enzymes and involves reduction, oxidation, and hydrolysis reactions to add or expose polar groups (-OH, -COOH, $-NH_2$, -SH).[261,262] Alternatively, phase II metabolism mainly uses transferase enzymes and involves conjugation reactions such as glucuronidation, sulfation, methylation, acetylation, glutathione, and amino acid

conjugation.[263] Although *in vitro* phase II metabolism can be investigated via a hepatocyte assay, for this study only phase I metabolism was determined for selected complexes.

The microsomal metabolic stability of the test complexes was evaluated in the presence of human (HLM) and mouse liver microsomes (MLM). These two species were selected, as the microsomal metabolic stability of a test compound in the presence of MLM can often correlate to its efficacy and metabolic stability in mice when doing *in vivo* studies.[264] Furthermore, the use of HLM in this study allows for the prediction of possible metabolites that would appear in circulation in humans, should the test compound progress to clinical trials.[265]

For the *in vitro* assay, liver microsomes from either a mouse or human, containing drug-metabolizing enzymes (mainly CYP450) were used. The complexes were incubated with these microsomes for 30 minutes and the percentage of unchanged compounds determined. The microsomal metabolic stability of complexes from **SAR1** and **SAR2** with sub-micromolar potency (IC_{50} <1 μM), low toxicity (SI >10), and favorable solubility ($S_{6.5}$ >10 μM) was determined and is shown in **Figure 3.11**. Complexes with 75% remaining after incubation with either HLM or MLM were considered to be metabolically stable.

Within the series of **SAR1** and **SAR2** complexes, a range of metabolic stabilities were observed. However, the complexes were generally more stable in the presence of MLM compared to HLM. Complexes with a *tert*-butyl in the 4,4-position of bipyridine (**4a.1**, **4a.2**, **4a.3,** and **4a.4**) exhibited moderate to poor microsomal stability with the remaining percentage of the complexes below 51% after 30 minutes of incubation in the presence of microsomes of both species. This was not entirely surprising, given reports in the literature that compounds with *tert*-butyl moieties display poor microsomal metabolic stability.[266] It has been suggested that in the presence of liver microsomes, abstraction of the sp^3 hydrogens from the methyl groups results in oxidative metabolism and the formation of an alcohol metabolite.

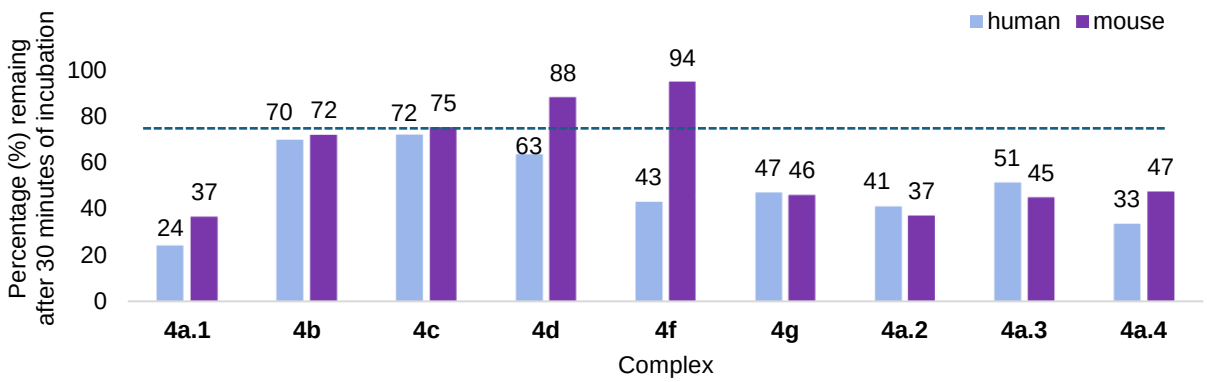

Figure 3.11. Percentage of the complexes remaining after 30 minutes of incubation with human and mouse liver microsomes, indicating their microsomal metabolic stabilities. The dashed line represents the cut-off for microsomal metabolic stability at 75% after 30 minutes of incubation.

Complex **4f** exhibited the highest stability in MLM with 94% remaining after 30 minutes of incubation, but only 43% of **4f** remained after incubation with HLM. Despite the species difference in metabolism, the high stability of **4f** with MLM supports its use in *in vivo* pharmacokinetic (PK) studies. However, poor metabolic stability in the presence of human liver microsomes suggests that further development of the compound would not be viable. Due to its excellent stability in MLM (>75% at 94%), high whole-cell potency <1 μM at 36.2 nM), and good solubility (>10 μM at 100 μM), complex **4f** was selected for an *in vivo* PK study.

3.4.3. *In vivo* pharmacokinetic (PK) profiles of the frontrunner platinum(II) complex, 4f

The pharmacokinetics of a compound summarizes the movement of the test compound throughout the body and ultimately describes how the body acts on the test compound.[267] Understanding the PK profile of a compound is essential in drug development as it assesses important parameters such as adsorption, distribution, metabolism, and excretion (ADME) properties to assist in the planning of dosage regimes.[267] These *in vivo* PK studies are conducted in mice and provide pre-clinical data of the PK parameters of the test compound, such as volume of distribution and clearance. It should therefore be noted that despite the use of a mouse model for these studies, the tested parameters can sometimes differ in humans. During PK evaluation, several parameters are measured, including:

- Half-life ($t_{1/2}$): the time it takes for the drug's concentration to decrease to half of its starting concentration.[268]
- Steady-state volume of distribution (V_{ss}): the ratio of the test compound in the plasma compared to the body of the specimen,[269] and values above 600 mL/kg are considered high.[270]
- Clearance (CL_s): a measure of the volume of drug cleared per a specific time frame.
- Bioavailability (F): measures the rate and ratio of the drug that reaches its target molecule(s) compared to the initial dose,[271,272] and it is highly influenced by the CL_s.[272] Bioavailability values above 20% are often considered desirable.[273,274]

In this regard, three replicates of female Balb/C mice were dosed either intravenously (i.v.) or orally (p.o.) at 3 mg/kg and 10 mg/kg, respectively. Blood was sampled at the respective intervals, shown in **Figure 3.12** over 48 hours. The corresponding PK parameters were calculated using a non-compartmental analysis and are shown in **Table 3.8**. For the oral dosing of complex **4f** at 10 mg/kg, peak total blood concentrations were reached in the first hour (≈0.08 μM). Total blood levels were maintained for the full duration of 48 hours, resulting in a moderately good half-life ($t_{1/2}$) of 12 and 11 hours in the p.o. and i.v. groups, respectively. In the i.v. group, the increase in the total blood concentration of **4f** after eight hours of administration was likely due to enterohepatic recirculation in which the compound was reabsorbed from the mouse intestine into circulation. After eight hours, there was a steady decrease in the total blood concentration in the i.v. group.

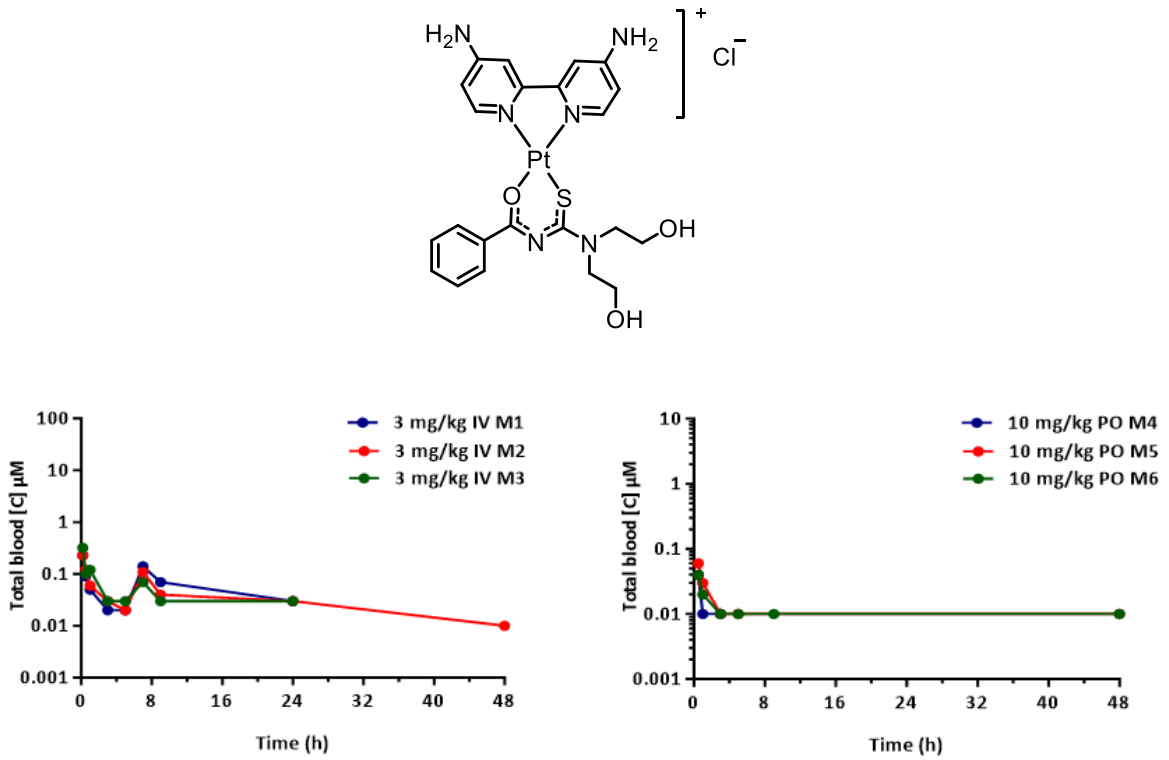

Figure 3.12. Chemical structure of **4f** (top). Pharmacokinetic profiles after oral (right) and intravenous (left) dosing of complex **4f** in Balb/C mice for 48 hours.

Further PK analysis indicated that complex **4f** exhibits a low steady-state volume of distribution (V_{ss} = 45.6 mL/kg (i.v.)), moderate clearance (CL_s = 46.4 mL/min/kg (p.o.)), and low bioavailability (F = 3.8% (p.o.)). The poor bioavailability of compound **4f** can partially be explained by its moderate clearance which results in a lower amount of the test compound in circulation.

Table 3.8. Summary of the pharmacological and pharmacokinetic parameters of complex **4f**. Obtained results were compared against goal criteria either established in the screening cascade or obtained from the literature.

			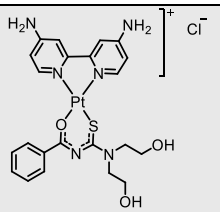
Bioactivity, toxicity, microsomal stability, and solubility		Goal criteria	Complex **4f**
Pf-NF54/Pf-K1 IC_{50} (nM)		<1000	36/102
CHO IC_{50} (µM)		>10	>50
Solubility at pH 6.5 (µM)		>10	100
Microsomal metabolic stability (Mouse/Human)	% after 30 min. incubation	>75 %	94/43
	CL_{int} (µL/min/mg)	< 11.6	<11.6/72.96
Pharmacokinetic parameters (dose= 3 mg/kg (i.v.) or 10 mg/kg (p.o.)			
V_{ss} (mL/kg) i.v.		>600 [275]	45.6
CL_s (mL/min/kg) i.v.		NA	46.4
$T_{1/2}$ (h) p.o./i.v.		14-48 [276]	12/11
F (%) p.o.		>20% [273,274]	3.8

Abbreviations: NA- Not applicable, CHO- Chinese hamster ovarian, V_{ss}- steady state volume of distribution, CL_s-clearance, $T_{1/2}$-drug half-life, F- bioavailability. ()- The references from which goal criteria was obtained.

Since complex **4f** exhibited good solubility and mouse liver microsomal metabolic stability but relatively poor PK properties, it was important to evaluate if factors such as permeability or percentage plasma protein bound (PPB) are the major influencers of the insubstantial PK properties.

3.4.4. Parallel artificial membrane assay (PAMPA) and plasma protein binding (PPB) for complex 4f

The permeability and plasma protein binding parameters of complex **4f** were investigated to rationalize the poor PK properties displayed by **4f**, despite it exhibiting good solubility and microsomal metabolic stability. Permeability refers to the crossing of small molecules through lipid membranes to reach their target site.[277] The permeability of a compound (along with its solubility) contributes significantly to the capacity to which the compound enters and stays in the systemic circulation.[271, 278] Good permeability is therefore crucial for drug distribution to its target(s).[279]

The permeability of **4f** was determined in a PAMPA experiment conducted at pH 6.5. The experiment involved adding the test compound to a donor compartment and evaluating the passive diffusion of a compound across an artificial membrane into an acceptor compartment. The log of the apparent permeability of complex **4f** was measured as -4.68 (P_{app} = 2.1 x 10^{-5}, **Table 3.9**), which is considered highly permeable based on the literature (compounds with P_{app} values above 5 x 10^{-6} are considered highly permeable).[280,281] Therefore the permeability of **4f** does not contribute to its low bioavailability observed in the PK studies. This suggests that other factors such as phase II metabolism in which conjugation reactions, exemplified by acetylation, sulfation and glucuronidation may be responsible for the poor bioavailability of **4f** *in vivo*. However, phase II metabolism of **4f** was not evaluated. Furthermore, efflux transporters found in the membrane of enterocytes in the intestinal tract can also contribute to its low bioavailability as these may prevent the test compound from entering systemic circulation.

Table 3.9. Apparent permeability (represented as a log value) of complex **4f** and its percentage bound and unbound to plasma proteins.

Permeability LogP_{app}	PPB (% bound)	PPB (% unbound)
-4.68	98.89	<5

Additionally, a PPB experiment was conducted using complex **4f** in which pooled human plasma was spiked with the test compound and incubated for four hours. Evaluating the PPB properties of complex **4f** was important, as only free (unbound) fractions of a test compound can leave the vascular compartment to be distributed within the body or excreted.[282] A PPB experiment measures the percentage of the test compound bound to plasma proteins versus

unbound. The PPB percentage was calculated from data obtained from LC-MS/MS analysis. From **Table 3.9**, approximately 99% of complex **4f** was plasma bound with less than 5% being unbound. The PPB results correlate to the low V_{ss} and moderate CL_s and suggest that only a small percentage of the compound can interact with its target to elicit its pharmacological effect.[283]

3.5. Chapter summary

A summary of the most notable SAR is provided in **Figure 3.13**. All the synthesized complexes were tested for their capacity to inhibit the growth of the ABS, as well as early-stage and late-stage gametocytes of the malaria parasite (*Pf*-NF54 and *Pf*-K1 strains). Within **SAR1**, the antiplasmodium activity was positively influenced by the presence of an electron-donating substituent in the 4,4'-position of the bipyridine. The 4,4'-diimine- bipyridine analog (**4f**) exhibited higher potency than the parent complex (**4a.1**) against both *Pf*-NF54 and *Pf*-K1 strains. Contrastingly, for **SAR2**, *para*-substitution with the electron-withdrawing chloro improved potency against *Pf*-NF54 three-fold. Additionally, the highlighting attribute of the **SAR2** complexes was the increased susceptibility of the drug-resistant *Pf*-K1 strain to these complexes compared to the parent complex. For **SAR3**, a change in the position of the 4,4'-dimethyl-substituent (**4b.1**) to the 5,5'-position improved its *Pf*-NF54 activity six-fold but decreased its *Pf*-K1 activity by ~2-fold. In **SAR4**, the SAR between three counterions, chloro (**4a.1**), hexafluorophosphate (**4a.5**) and nitrate (**4a.6**) was explored. These results showed that the nitrate counterion was more favorable than the chloro and hexafluorophosphate counterions with an 11-fold and three-fold increase in *Pf*-NF54 and *Pf*-K1 potency, respectively.

Replacement of one terminal hydroxyl on the acyl-thiourea ligand with a terminal amine (**4a.8a**) decreased potency eight-fold compared to **4a.1**. Contrastingly, the attachment of a dansyl reporter (**4a.7**) had a negligible effect on its activity (IC_{50} values within a three-fold range between analogs), supporting its use as a fluorescently labeled derivative of **4a.1** in the cellular localization studies in **Chapter 4**. Lastly, the platinum(II) analog (**4a.1**) was 25-fold more potent than its gold(III) derivative, **4k**.

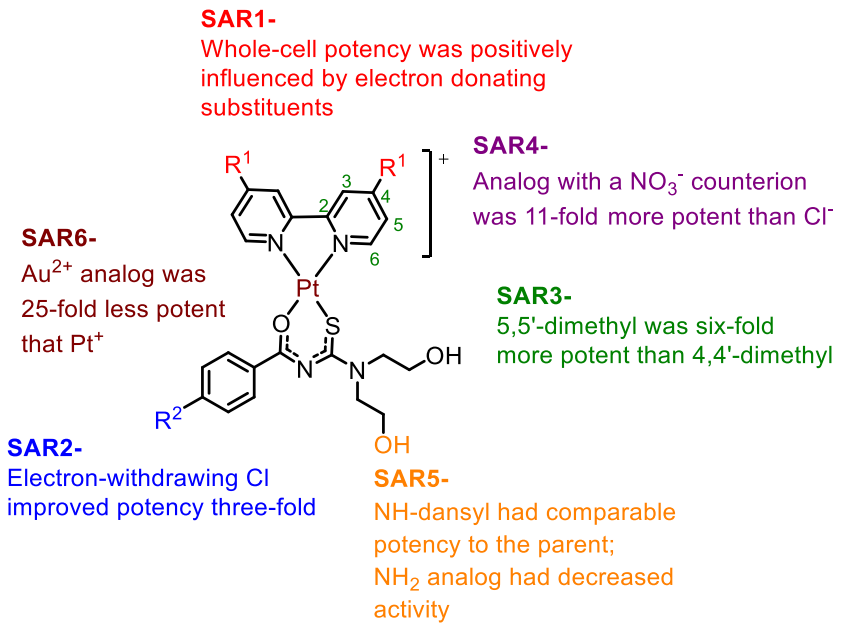

Figure 3.13. Summary of the whole-cell potency results obtained for the mixed-ligand transition metal complexes described in this chapter.

Concerning gametocyte activity, all the complexes were tested for their capacity to inhibit the growth of EGs and LGs in a dual point (1 μM and 5 μM) assay. Complexes with percentage inhibition >50% at 1 μM and >70% at 5 μM were further tested in a full dose-response assay to determine their IC_{50} values. The majority of complexes containing the bulky hydrophobic *tert*-butyl (**4a.1**, **4a.2**, **4a.3**, **4a.5**, **4a.7**) or trifluoromethyl (**4h**) substituent on the bipyridine rings exhibited either early-stage (EG) and/or late-stage (LG) gametocyte activity. Complexes **4a.2** (R^2 = Me), **4a.3** (R^2 = MeO), and **4a.7** (R^2 = H, terminal HN-dansyl) showed improved EG activity compared to the parent complex, **4a.1**. Complexes **4a.2** and **4a.3** also exhibited greater LG activity compared to their EG activity with IC_{50} values below 1 μM. Thus, within this series of compounds, there are at least five complexes with dual-stage activity. Furthermore, despite having a platinum metal center, none of these complexes showed significant toxicity at concentrations up to 50 μM against the Chinese hamster ovarian cell line.

Tested complexes from **SAR1** and **SAR2** showed good solubility above the cut-off criteria of 10 μM at $S_{6.5}$ values above 90 μM, with a range of microsomal metabolic stabilities in the presence of HLM and MLM. As the frontrunner complex, compound **4f** was selected for PK studies. While complex **4f** exhibited appreciable solubility of 100 μM and microsomal metabolic stability of 94% remaining after 30 minutes of incubation with MLM, it displayed poor *in vivo* PK properties. Complex **4f** exhibited a poor steady-state volume of distribution, low bioavailability, moderate clearance, and a relatively good half-life. Further studies showed that

the poor PK properties displayed by **4f** were not related to permeability as it was found to be highly permeable but possibly due to phase II metabolism and its high plasma protein binding of 99%. Following the evaluation of the *in vitro* whole-cell potency and SPRs of the synthesized complexes, their mechanism of action was evaluated, as will be discussed in **Chapter 4**.

Chapter 4: Mechanistic Studies and the Inhibition of Hemozoin Formation of [Pt/Au(diimine)L-O,S]$^{+/2+}$ Complexes

4.1. Introduction

Several chemical and pharmacological features are important for drug candidates to progress to clinical studies. While many of these properties, including solubility and metabolic stability, were discussed in the previous chapter, knowing the biological mechanism of action (MoA) of a compound is also beneficial. Gaining insight into the target, and possible off-target biomolecule(s), of a chemical series facilitates the development of the most efficacious and non-toxic compounds through, for example, the rational design of compounds.[284]

The life cycle of the malaria parasite is described in detail in **Section 1.2.1**, but it should be reiterated that during the asexual blood stage (ABS) of the life cycle, heme released from the degradation of host hemoglobin is incorporated into hemozoin to avoid cytotoxic effects.[285] Hemozoin formation inhibitors such as chloroquine (CQ),[286] prevent heme crystallization via π-π stacking interactions of the quinoline ring system to the fastest growing face of the hemozoin crystal.[287]

Consequently, the proposed square planar geometry of the synthesized platinum(II) and gold(III) metal complexes make them good candidates for π-π stacking interactions with the porphyrin ring of hematin, suggesting that they potentially can act via a similar MoA to that of CQ. To investigate this, a stepwise approach was adopted in which the self-association capacity of the parent complex **4a.1** was first evaluated using a concentration-dependent ^{1}H-NMR spectroscopy study, as described in **Section 4.2**. The self-association assessment was conducted following previous studies by Koch *et al*.,[180] in which similar platinum(II) complexes were found to form aggregates with themselves in solution through intermolecular π-π interactions. Since π-π interactions are crucial for inhibitors of hemozoin formation, it was appropriate to start the MoA studies with experiments to measure self-association.

Following the self-association analysis, the capacity of the compound to inhibit the crystallization of hematin to β-hematin was evaluated in an extracellular β-hematin inhibition (βHI) assay. Finally, prioritized compounds were subjected to an *in vitro* cellular heme fractionation assay, to further validate their inhibition of hemozoin formation.

In addition to the MoA analysis mentioned above, the ability of selected compounds (**4a.1** and **4f**) to accumulate within the parasite's digestive vacuole (DV) was determined via the inoculum effect. This was prompted by the known essentiality of a compound to accumulate in the target organelle or near its target biomolecule for its bioactivity.[288,289] This is exemplified by the many antimalarials, including CQ[290] and artemisinin[291] that target one or more aspects of the DV and therefore accumulate within this organelle to elicit their toxic effects.[292] In essence, the inoculum effect is a phenomenon whereby the observed inhibitory concentration of a compound increases with an increase in the number of organisms being inoculated, i.e. the inoculum size.[293] This generally occurs when the drug accumulates to significant levels in the organism and has been shown to occur in the case of basic compounds accumulating in the parasite's acidic DV via an effect known as 'pH trapping'.[294] The linear relationship between the inoculum size and the measured IC_{50} values can be extrapolated to calculate the cellular accumulation ratio (CAR).[295] The CAR is a measure of the concentration of the drug in the parasitized red blood cells (pRBC) compared to the concentration of the drug outside the cell.[296]

To further probe their MoA, the electrochemical properties of selected complexes were also explored using cyclic voltammetry (CV). This was prompted by reports in which the redox properties and the oxidation state of metal complexes affects their reactivity and consequently their bioactivity.[297] This has been exemplified by reports on the importance of Fe^{2+}/Fe^{3+} redox chemistry of ferrocene derivatives.[298] Depending on their redox chemistry, metal complexes can induce the production of reactive oxygen species (ROS) and therefore act via oxidative stress to kill the parasite.[299]

With the planar geometry of the complexes as the rationale for the MoA investigations, the main aim of this chapter was to determine if the proposed MoA of the platinum(II) complexes is via inhibition of hemozoin formation, analogous to CQ. Furthermore, the objective was to evaluate the electrochemical properties of the gold(III) complex and selected platinum(II) analogs to probe their potential to produce reactive oxygen species (ROS). Additionally, the cellular localization of a dansyl-labeled analog, **4a.7**, was also investigated. This was done to identify the target organelle in which this analog accumulates and elicits its toxicity.

4.2. Concentration-dependent ^{1}H-NMR studies

Complex **4a.1** was selected for the self-association investigation study as Egan *et al*.[179] previously found that it did not exhibit appreciable inhibition of β-hematin (βH) formation. This study was therefore conducted to determine if the negative result obtained in the Egan *et al.* study resulted from the inability of the complex to partake in π-π stacking interactions. Thus, to investigate the self-association capacity of **4a.1**, a concentration-dependent ^{1}H-NMR spectroscopy analysis described by Koch *et al*. and Kotze *et.al.*[180,300] was used.

A downside to using NMR spectroscopy is its limit of detection in which the instrument is not sensitive enough to produce an acceptable signal at low sample concentrations. Preparation of samples at inadequate concentrations often leads to spectra with a low resolution in which peaks cannot be detected, suitably separated, and comprehensively annotated. For this reason, three concentrations were chosen to span a physiologically relevant range that was high enough to produce quality ^{1}H-NMR spectra.

To this end, a stock solution of complex **4a.1** in methanol-d_4 (10 mM) was prepared and diluted to final concentrations of 5.45 mM and 2.69 mM, respectively.^{1}H-NMR spectra were obtained at each concentration of **4a.1** and these are shown in **Figure 4.1**. To facilitate analysis of the proton resonance shifts, the spectra are displayed in a stacked formation. It was observed that as the concentration of the complex in solution decreased from 10 mM to 2.69 mM, the resonances of the aromatic protons shifted downfield, indicative of the self-association of complex **4a.1** in methanol, which is influenced by π-π stacking interactions. The downfield shift in proton resonances results from less aggregation caused by fewer molecules in the solution. Consequently, fewer complexes are present to partake in the π-π stacking interactions and shield adjacent bipyridine moieties.

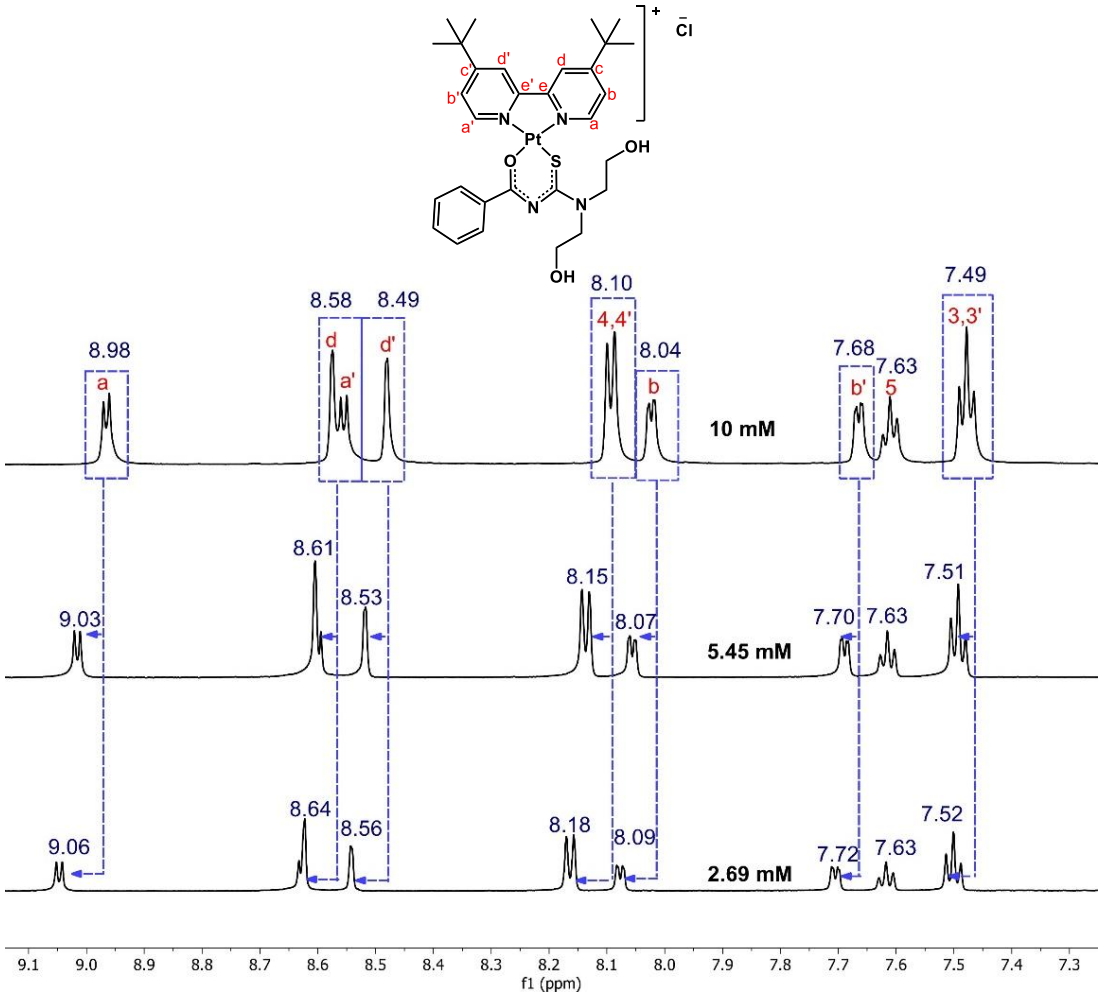

Figure 4.1. Low field range of the stacked ^{1}H-NMR spectra of complex **4a.1** (in methanol-d_4) at concentrations of 10 mM, 5.45 mM, and 2.69 mM, showing that as the concentration decreases, the aromatic proton signals shift downfield, as indicated by the arrows.

In general, the model for π-π stacking as proposed by Hunter *et al*.[301] states that these interactions are driven by net favorable σ-π interactions between the aromatic σ and π framework that overcome π-π repulsions. With respect to the platinum(II) complexes, self-association is proposed to occur via a coplanar stacking arrangement of two complexes such that they point 180° in opposite directions as described by Kock *et al*.[180] Hence two platinum molecules take part in an offset stacked interaction,[302] in which the platinum center of one molecule is located over the center of an adjacent bipyridine as shown in **Figure 4.2**. The offset arrangement of the dimer also contributes to reducing the electrostatic repulsion between the net positive charge of the metal centers, while ensuring favorable π-π interactions and promoting self-aggregation.

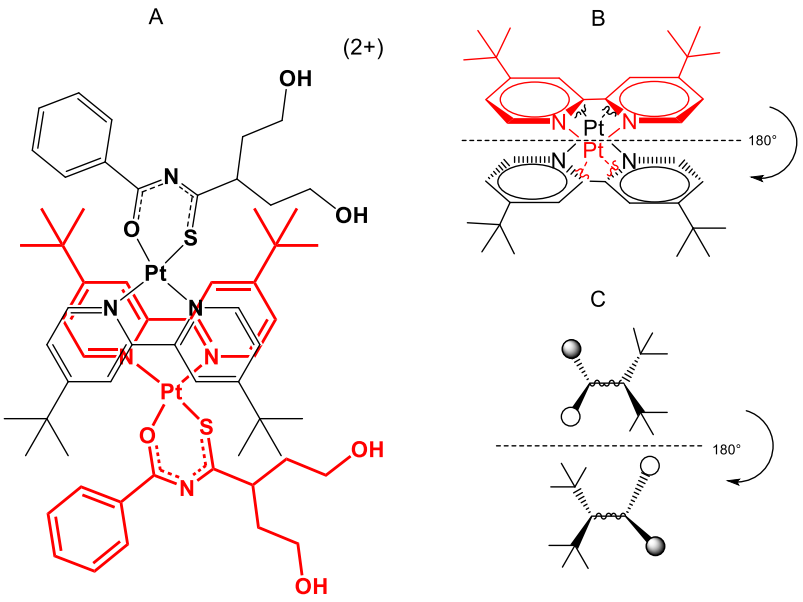

Figure 4.2. Proposed coplanar orientation of complex **4a.1** in solution. **A**: One complex associates with an adjacent molecule via a 180° angle. **B**: Simplified drawing of **A** showing the offset stacked interaction between two platinum(II) molecules. **C**: A schematic drawing that highlights the orientation of the different chemical moieties on one molecule in comparison to those on an adjacent molecule.

The self-association experiment suggested that the negligible inhibition of β-hematin formation activity observed in the Egan *et al*. study for complex **4a.1** (using the less reliable infrared assay as described in **Section 1.6**.) was not a result of the inability of the compound to interact with hematin via a coplanar interaction. This supported the re-evaluation of **4a.1** for its capacity to inhibit β-hematin formation via the more robust βHI assay, as will be discussed below. This pyridine-ferrochrome method developed by Egan and Nkokazi uses NP-40 detergent to mediate the formation of β-hematin, mimicking the endogenous conditions in the DV more closely.

4.3. NP-40 detergent mediated β-hematin inhibition

The βHI assay is valuable in exploring the structure-activity relationships (SARs) of compounds within a chemical series. As such, **SAR1** and **SAR2** complexes (**Figure 4.3**, R^1 on bipyridine and R^2 on phenyl varied, respectively) were prioritized for this study to evaluate their SARs in terms of their capacity to inhibit βH formation. CQ, a known inhibitor of βH formation,[303] was used as a positive control, and pyrimethamine (PM) as a negative control. PM is an antimalarial with known folate biosynthesis inhibition activity,[304] and does not inhibit the formation of βH or hemozoin.[305] The results of the βHI experiments are shown in **Table 4.1** and **Figure 4.4**.

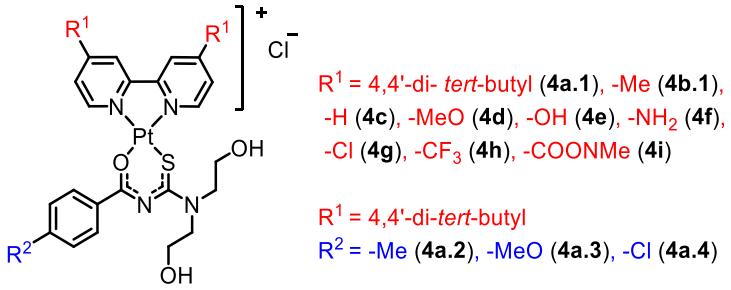

Figure 4.3. Structures of complexes from SAR 1 (red) and SAR 2 (blue) were selected for evaluation as inhibitors of β-hematin formation.

The majority of the SAR1 and SAR2 complexes (excluding where R^1 = H (**4c**) and OH (**4e**)) displayed superior or comparable inhibition of βH formation activity to CQ within their standard errors of the mean (SEM, **Table 4.1**). Interestingly, complexes **4g** (R^1 = Cl) and **4i** (R^1 = CONHMe) exhibited negligible whole-cell antiplasmodium potency, as discussed in **Section 3.2.1**, but showed a 2- and 3-fold increase in inhibition of β-hematin formation activity, respectively, compared to CQ (**Figure 4.4**).

Table 4.1. Inhibition of β-hematin formation activity as a measure of IC_{50} ± SEM values of the [Pt(diimine)(L-O,S)]$^{+}$ complexes belonging to **SAR1** and **SAR2** where R^1 and R^2 was varied. N, n = 3, 2, except for **4g** where N, n = 1, 2.

Complex	**4a.1**	**4b**	**4c**	**4d**	**4e**	**4f**	**4g**	**4i**
IC_{50} (μM)	12 ± 2	9 ± 1	16 ± 1	7.8 ± 0.6	15 ± 1	10 ± 1	5.4	3.6 ± 0.4
Complex	**4a.2**	**4a.3**	**4a.4**	**CQ**	**PM**			
IC_{50} (μM)	6 ± 2	11 ± 2	10 ± 2	10.6 ± 0.1	> 1000			

Meanwhile, complexes **4c** (R^1 = H) and **4e** (R^1 = OH) were tested as suspensions, due to poor solubility in both DMSO and the aqueous buffer solutions. These observed poor solubilities could contribute to their comparably higher βHI-IC_{50} values.

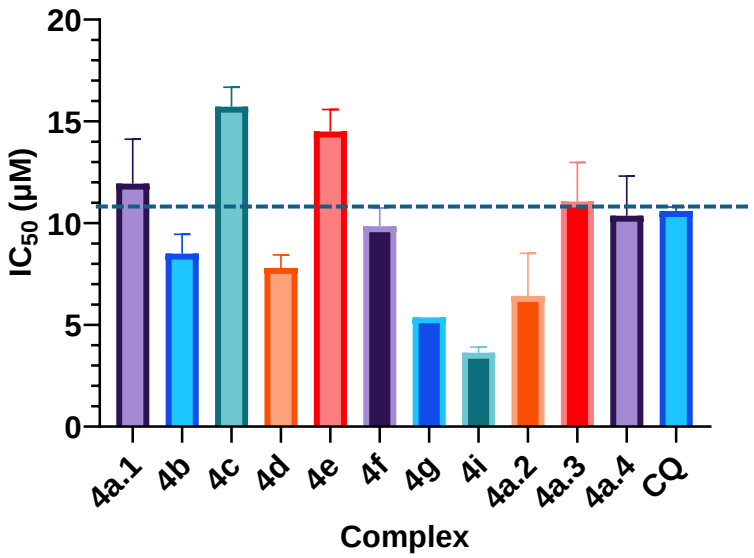

Figure 4.4. The obtained IC_{50} values for the inhibition of β-hematin formation activity of the **SAR1** and **SAR2** [Pt(diimine)(L-O,S)]$^{+}$ complexes show that the majority of the complexes exhibit superior or comparable activity to CQ (indicated). Error bars represent the SEM where N, n = 3, 2 (except for **4g**; N, n = 1, 2). R^1= *tert*-butyl (**4a.1**), Me (**4b**), H (**4c**), MeO (**4d**), OH (**4e**), NH_2 (**4f**), Cl (**4g**), CF_3 (**4h**), CONMe (**4i**). R^1= *tert*-butyl: R^2 = Me (**4a.2**), MeO (**4a.3**), Cl (**4a.4**).

Most notably, the parent complex **4a.1** (R^1 = *tert*-butyl), which showed negligible inhibition of βH formation in the infrared-based study, displayed comparable activity to CQ in this study, with an IC_{50} value of 12 μM. These results highlight the unreliability of the infrared-based analysis of βH formation used in the previous study compared to the more robust NP-40 detergent-mediated assay used here with a colorimetric pyridine-ferrochrome detection method.

Furthermore, while these compounds are inhibitors of βH formation, extracellular inhibition activity does not always mirror activity in the parasite. This is exemplified in a report by Stringer *et al.*,[306] where it was shown that two ferroquine-derived polyamines exhibited inhibition of βH formation activity but did not inhibit hemozoin formation in the intracellular assay. Additionally, this is also shown with the platinum(II) complexes synthesized herein, as is discussed in the next section.

Therefore, to determine whether a subset of the platinum(II) complexes prevented hemozoin formation within parasites, they were subjected to the heme fractionation assay. However, as a pre-requisite for the heme fractionation assay, the complexes of interest were first tested in a pLDH assay to determine the dosing concentrations.

4.4. *Plasmodium* lactate dehydrogenase (pLDH) assay

Compounds **4a.1** and **4f** (**Figure 4.5**) were prioritized for further experiments, including the cellular heme fractionation assay. This selection was guided by their whole-cell potency (discussed in **Chapter 3**), and the fact that their inhibition of βH formation activities were comparable to the remaining complexes. An additional motivation for prioritizing **4a.1** was its dual-stage activity as shown by its ABS and gametocyte activity.

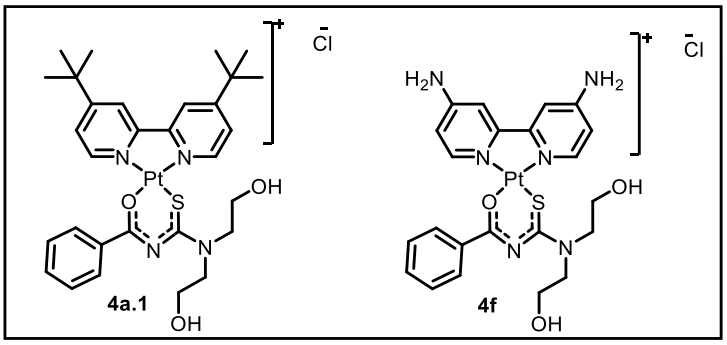

Figure 4.5. Structures of complexes **4a.1** and **4f** that were used in the subsequent whole-cell assays.

As discussed in **Chapter 3**, the whole-cell potency of all the complexes was determined using the SYBR Green I assay. However, for this section, the IC_{50} values of complexes **4a.1** and **4f** were redetermined using the relevant parasite laboratory cell line (*Pf*-NF54) in the *Plasmodium* lactate dehydrogenase (pLDH) assay described by Makler *et al.*[307] From here multiples of the obtained IC_{50} values were used in the subsequent cellular heme fractionation assay.[20]

During both the pLDH and SYBR Green I drug susceptibility assays, parasite survival is measured and its whole-cell potency is reported as a measure of the compounds' IC_{50} values. However, the two assays vary mainly in their detection methods of parasite survival. The SYBR Green I assay relies on the detection of fluorescent SYBR Green I binding to parasitic DNA in which the fluorescence intensity is a measure of the amount of double-stranded DNA. Conversely, the pLDH assay relies on the colorimetric detection of LDH activity in *Plasmodium* ABS parasites at visible wavelengths, which can be more easily recorded using a standard UV-vis plate reader.[308] Additionally, the SYBR Green I assay was conducted over 96 hours, vastly exceeding that of the 32-hour cellular heme fractionation assay by 64 hours. Thus, redetermining the IC_{50} values of **4a.1** and **4f** in a 48-hour pLDH assay was necessary to mimic the cellular heme fractionation conditions more closely. This ensured that the dosing

concentrations used in the heme fractionation were appropriate for the compounds to elicit a dose-dependent effect within 32 hours.

In this study, complexes **4a.1** and **4f** were incubated with the relevant controls in a 96-well plate containing 1% parasitemia and 1% hematocrit for 48 hours before development using Malstat and NBT solutions. The IC_{50} values of complexes **4a.1** and **4f** and the dose-response curves of the tested compounds are shown in **Figure 4.6**, with CQ as a positive control. The IC_{50} values obtained for complexes **4a.1** and **4f** were 117 ± 49 nM and 82 ± 29 nM, respectively, compared to the SYBR Green assay values of 151 ± 17 nM and 36.3 ± 0.6 nM.

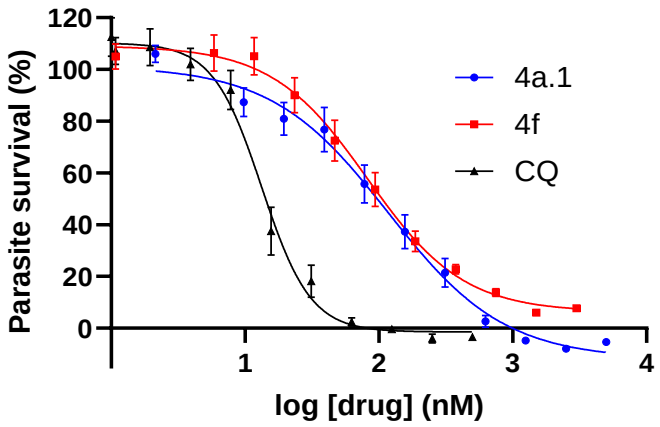

IC_{50} values (nM)		
4a.1	**4f**	**CQ**
117 ± 49	82 ± 29	13 ± 3

Figure 4.6. Dose-response curves (top) evaluating the percentage of *Pf*-NF54 parasite survival after 48 h incubation. Complexes were serially diluted 2-fold from starting concentrations of 5 µM (**4a.1**), 3 µM (**4f**) and 0.5 µM (**CQ**). Error bars represent the SEM where N, n = 3, 3. IC_{50} ± SEM values (bottom) extracted from the dose-response curves.

From these results, the difference in potencies obtained from the two assays is negligible, as the slight variations in the IC_{50} values are within the expected range of biological variation of approximately 3-fold. Variation often occurs as a consequence of differential proliferation rates of biological samples and the large uncertainties associated with the quoted IC_{50}. Nonetheless, discrepancies in these values can also originate from several factors including differences in the starting parasitemia, and incubation period.

Following the established potencies of complexes **4a.1** and **4f** in *Pf*-NF54, the concentrations to be used in the subsequent cellular heme fractionation assay were calculated in multiples of their IC_{50} values as discussed in the next section.

4.5. Cellular heme fractionation assay

Considering the complex's potent inhibition of βH formation activity, their capacity to inhibit the formation of hemozoin was determined intracellularly using the heme fractionation assay. In this assay, the different Fe(III) heme species in whole cells are measured via the detection of the Fe(III)heme-(bis)pyridyl complex.[184] This quantifies the amount of heme iron corresponding to that of hemoglobin, free heme, and hemozoin in the cells. Typically, for a compound that inhibits hemozoin formation, a dose-dependent increase in the amount of free heme, and a subsequent decrease in hemozoin, is observed. This has been shown for multiple antimalarials such as CQ and AQ.[184]

The intracellular heme fractionation assay is conducted over four days with each day comprising several experimental steps as summarized in **Section 7.13**. Briefly, *Pf*-NF54 parasites in the ring phase at 5% parasitemia were incubated with multiples of the IC_{50} value of the test compound. This was followed by saponin-lysis to harvest the trophozoites which were subsequently fractionated through a series of steps using specific reagents and detergents. The hemoglobin, heme, and hemozoin fractions were sequentially isolated and the heme-(bis)pyridyl complex was detected spectrophotometrically. Consequently, spectrophotometric analysis, coupled with flow cytometry, is used to quantify the absolute amounts of each species. First, CQ was tested in the heme fractionation assay and provided a reference for the dose-dependent changes in the amounts of heme and hemozoin that are expected for a hemozoin inhibitor.

As shown in **Figure 4.7**, CQ displays a dose-dependent decrease in hemozoin and a corresponding increase in free heme. This trend is observed in both the percentage and absolute amount of free heme (fg/cell) as the concentration of CQ increases to 3 x IC_{50}.

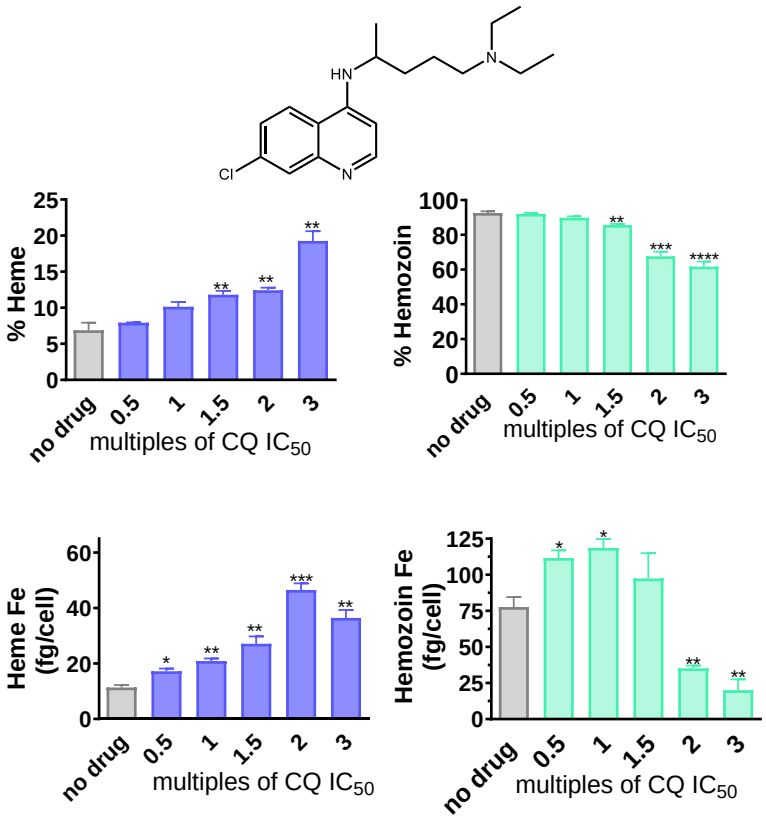

Figure 4.7. Percentage (top panel) and absolute amount (bottom panel) of heme and hemozoin isolated from *Pf*-NF54 trophozoite cells. Cells were incubated with CQ at multiples of the IC_{50} value. The amount of Fe is expressed as femtograms (fg) of heme iron per cell. The no-drug control well contained untreated cells. Statistical significance was calculated from two biological repeats each with four technical repeats (N, n = 2, 4). Statistical significance was determined using a two-tailed *t*-test and error bars show a 95% confidence interval, indicated by the asterisk: *p < 0.05, **p < 0.01, *** p < 0.001, **** p < 0.0001.

After validation of the assay using CQ, the platinum(II) complexes were tested via the same protocol. As shown in **Figure 4.8**, complexes **4a.1** and **4f** did not show a significant dose-response increase in the amount of heme, nor a decrease in the amount of hemozoin, even at concentrations as high as 7 times the IC_{50} for **4a.1**. Notably, the decrease in both the amount of hemozoin and heme at 7 x IC_{50}, for **4a.1** relative to the no-drug control was not statistically significant.

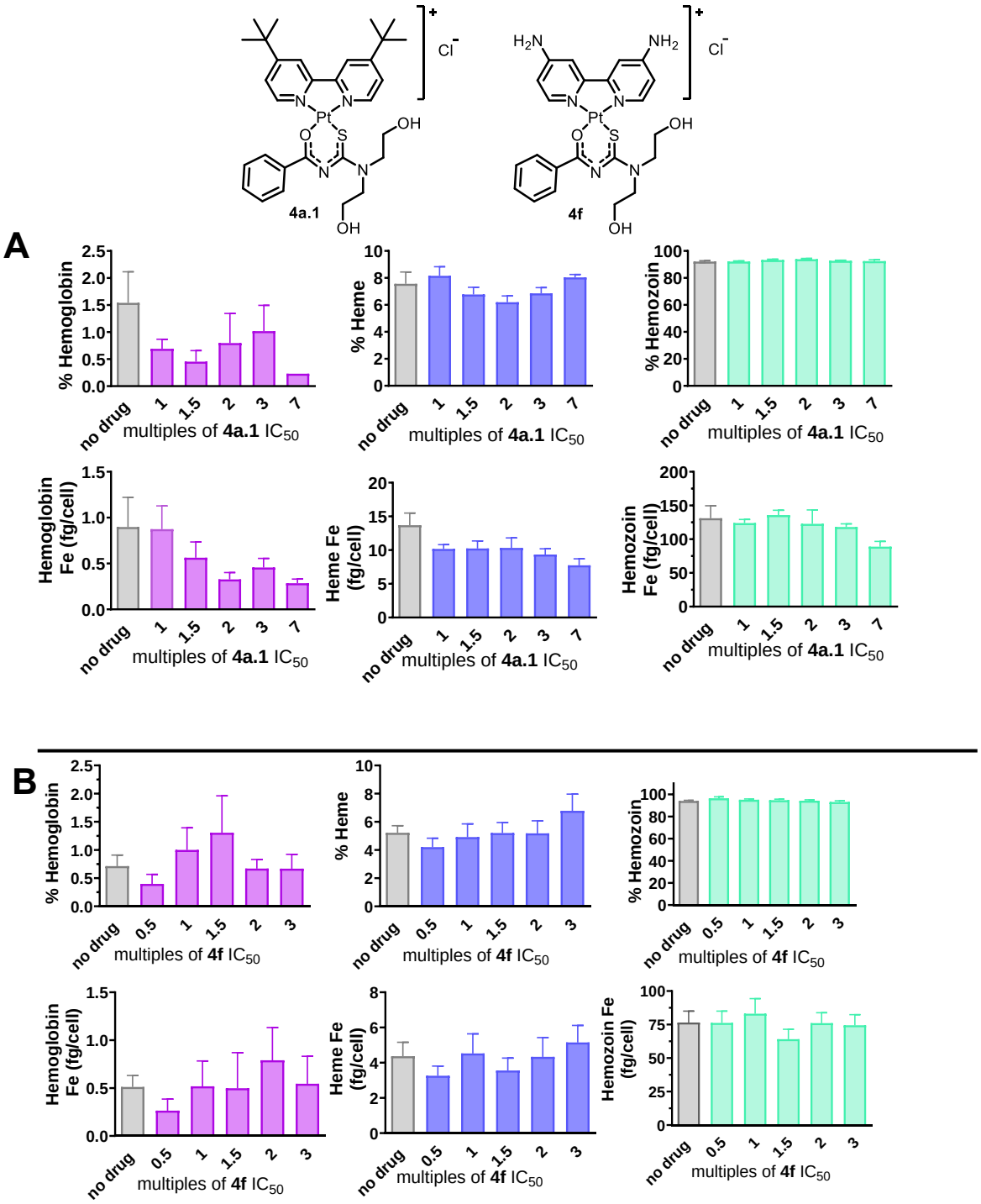

Figure 4.8. Percentage (top panel) and absolute amount (bottom panel) of hemoglobin (Hb), heme, and hemozoin (Hz) isolated from *Pf*-NF54 trophozoite cells. Cells were incubated for 32 hours with **4a.1** (**A**) or **4f** (**B**) at multiples of the IC_{50}. The amount of Fe is expressed as femtograms (fg) heme iron per cell and the no drug control well contained untreated cells. Statistical significance was calculated from two biological repeats, each with three technical repeats (N, n = 2, 3). Statistical significance was determined using a two-tailed *t*-test and error bars show a 95% confidence interval, indicated by the asterisk: *p < 0.05, **p < 0.01, *** p < 0.001, **** p < 0.0001.

The perceived decrease may be explained by the decrease in the total amount of iron (fg/cell) in the DV at high concentrations of the compound, which is likely due to decreased hemoglobin uptake caused by general toxicity and stress to the parasite. The decreased hemoglobin uptake is supported by the dose-dependent decrease in the absolute amount (fg/cell) of hemoglobin seen in **Figure 4.8**, **A**. Since complex **4a.1** has dual-stage activity in the *Pf* malaria parasite, the absence of hemozoin formation inhibition activity is not entirely surprising as hemozoin formation does not occur in gametocytes.

These results were interesting given the original hypothesis that these complexes were likely to inhibit hemozoin formation. This does not necessarily imply that the complexes do not bind or interact with heme at high concentrations, as inhibition of βH formation activity was observed. Rather, they likely possess alternative MoAs within whole-cell parasites at the concentrations tested. This was further investigated using resistance selections as discussed in **Chapter 5**. However, to determine whether the inactivity of the compounds was due to the higher parasitemia used in the cellular fractionation assay, these were subjected to the inoculum effect as described in the next section.

4.6. Inoculum effect assay

Certain antimalarials such as some of the quinolines elicit their whole-cell potency via cellular accumulation in the parasites DV which can be quantified using the inoculum effect. Thus, the inoculum effect is one of the major confounders in the *in vitro* susceptibility tests of CQ and other antiplasmodium agents such as amodiaquine derivatives, mefloquine, and halofantrine.[309]

As mentioned in **Section 4.4**, the IC_{50} values of **4a.1** and **4f** were determined in the pLDH assay at a 1% parasitemia, whereas the heme fractionation assay was conducted using a 5% parasitemia (**Section 4.5**). Therefore, to further validate the heme fractionation results and confirm that the inhibition of hemozoin formation was not affected by the higher parasitemia, the inoculum effect of complexes **4a.1** and **4f** was evaluated. This assay was also utilized to provide insight into the accumulation capacity of these two complexes in the malaria parasite. Briefly, the inoculum effect assay involves varying the parasitemia (inoculum size) between 1% to 6%. The IC_{50} of the test compound is then measured and plotted against its respective inoculum size to calculate its CAR using **Equation 4.1**. This calculation is advantageous as it relays information on drug accumulation without the need for spectroscopic techniques.

$$\mathrm{CAR} = \frac{\mathrm{IC}_{50_{\mathrm{measured}}} - \mathrm{IC}_{50_{\mathrm{absolute}}}}{\mathrm{IC}_{50_{\mathrm{absolute}}} \times \mathrm{V}_{\mathrm{frac.pRBC}}} \quad \mathbf{Eq.4.1}$$

In this equation, the absolute IC_{50} refers to the IC_{50} value at an inoculum size of zero and the fractional volume (V_{frac}) accounts for the volume of parasitized red blood cells (pRBC) which is a product of the parasitemia and hematocrit.

For the assay, stock solutions containing inoculum sizes of 6% and 4% parasitemia (2% hematocrit) in complete media were prepared in falcon tubes. The 4% parasitemia stock was further diluted 2-fold to yield a 2% and subsequently a 1% solution (**Figure 4.9, A**). CQ served as a positive control due to its known accumulation in the DV of the *Plasmodium* parasite. Similar to the pLDH assay, a 96-well plate was used with one compound per plate and two technical repeats of each inoculum size per plate, as illustrated in **Figure 4.9, B**. Three independent biological repeats were conducted to determine the inoculum effect of each complex.

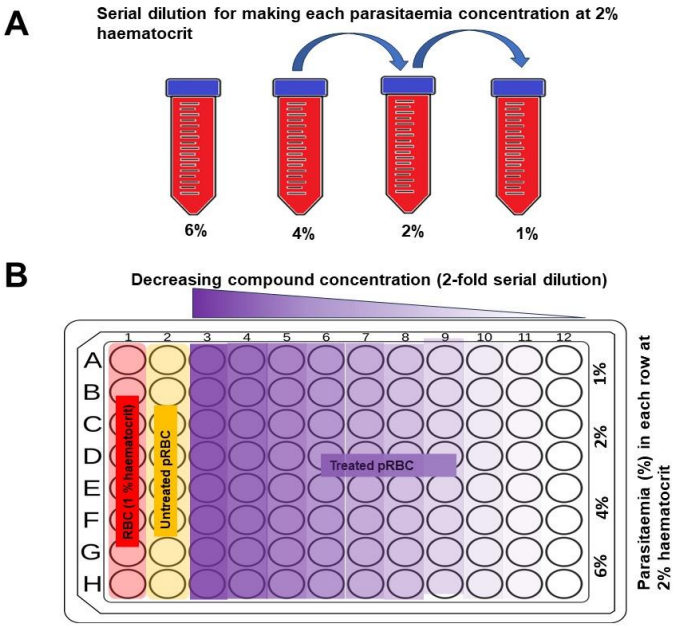

Figure 4.9. Illustration of the serial dilution used for preparing the different *Plasmodium* inoculum sizes (**A**) and the general plate set-up of the inoculum assay (**B**), highlighting that one plate is used per compound.

The dose-response curves in **Figure 4.10** show a shift in the IC_{50} as the inoculum size increases for CQ and complexes **4a.1** and **4f**. This shift is slightly larger for CQ compared to that of the complexes, whereas the fold shift in IC_{50} values is similar between complexes **4a.1** and **4f**. The linear relationship observed between inoculum size and IC_{50} values is indicative of intracellular accumulation.

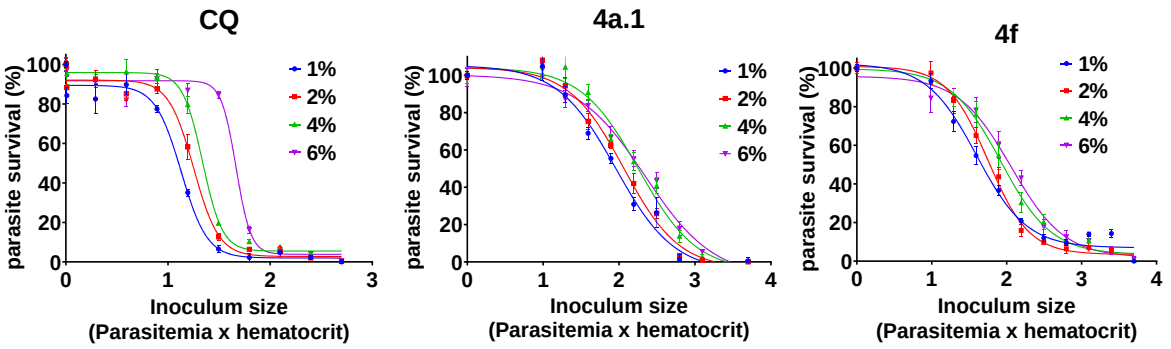

Figure 4.10. Dose-response curves of CQ, complex **4a.1,** and **4f** obtained from the inoculum effect assay using increasing starting % parasitemia values (inoculum sizes). A right shift of the dose-response curves is observed with increasing inoculum size, indicative of cellular accumulation of the compounds. Error bars represent SEM where N, n = 3, 2.

The observed inverse relationship between whole-cell potency and inoculum size (**Table 4.2**) can be justified by the accumulation of the compound in the parasite, resulting in an overall decrease in their concentration in the extracellular medium. Moreover, the IC_{50} values of 260 nM and 113 nM at 6% parasitemia for complexes **4a.1** and **4f**, respectively, confirm that the concentrations of 7 x IC_{50} (7 x 117 i.e. 819 nM) for **4a.1** and 3 x IC_{50} (3 x 82 i.e. 246 nM) for **4f** used in the cellular heme fractionation assay was sufficiently high enough to observe a dose-dependent effect.

Table 4.2. IC_{50} ± SEM values were obtained after 48 hours of incubation of varying inoculum sizes of *Pf*-NF54 with CQ, **4a.1,** and **4f**. SEM values are reported where N, n = 3, 2.

	***Pf*-NF54-IC_{50} (nM)**		
Parasitemia	**CQ**	**4a.1**	**4f**
1%	11 ± 1	91 ± 10	41 ± 6
2%	17 ± 1	119 ± 16	60 ± 10
4%	29 ± 5	193 ± 46	85 ± 8
6%	42 ± 6	260 ± 73	113 ± 13
CAR	14079 ± 112	6369 ± 137	4882 ± 257

Subsequently, the CAR values were obtained using linear regression from the plot of IC_{50} vs inoculum size (**Figure 4.11**) and were calculated from **Equation 4.1** to be 6369 and 4882, for **4a.1** and **4f**, respectively. These values were similar within their SEM values, suggesting that they accumulate to a similar extent. CQ accumulates approximately 2-fold more than the two platinum(II) complexes. However, this is not surprising as CQ and the synthesized platinum(II) complexes have different MoAs.

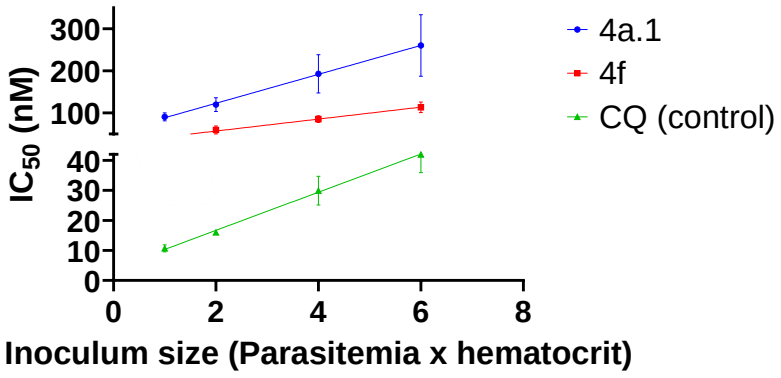

Figure 4.11. Inoculum effect represented by the linear relationship between the IC_{50} value vs inoculum size to illustrate the cellular accumulation of CQ, **4a.1** and **4f** in *P. falciparum*.

4.7. Cyclic voltammetry

Electron transfer reactions are one of the major contributing factors to the reactivity of compounds containing a metal center,[310] and can therefore influence a metal complex's pharmacological properties.[29] In this context, it was worthwhile to determine if the bioactivity of the synthesized gold(III) and a subset of the platinum(II) complexes is influenced by their redox chemistry. Thus, the electrochemistry of the transition metal complexes was evaluated using cyclic voltammetry (CV), which is a tool used to study these reactions.[311] The application of CV has expanded across several disciplines and has been used to study biosynthetic pathways,[312] the electrochemical formation of free radicals,[313] and to evaluate the oxidative/reductive potential of a metal center and its ligands.[314]

CV uses a triangular potential waveform in which the initial potential is scanned in a linear manner causing the chemical species to undergo oxidation or reduction at the surface of an electrode.[315] When the potential reaches an adequate negative or positive potential, an electrochemical current is produced and recorded in the form of a voltammogram. In a CV scan, the potential can be scanned from a negative potential to a positive potential or vice versa.

The CV experiments described herein were performed in either dry MeOH, dry DMF, or dry DMSO that contained tetrabutylammonium chloride (TBACl) as the supporting electrolyte. The working electrode was glassy carbon (GC) with platinum wire as the counter electrode (CE) and Ag/AgCl as the reference. The anodic (E_{pa}) and cathodic (E_{pc}) peak potentials at 0.1 (V/s) and half-wave potentials ($E_{1/2}$) were measured and are shown in **Table 4.3**. Since the potentials of the complexes were determined in either MeOH or DMF based on their solubilities in these solvents, the anodic (E_{pa}) and cathodic (E_{pc}) peak potentials of ferrocene (FC) in each solvent were also obtained so that the $E_{1/2}$ can be corrected for in the different solvents, and the data of each complex can be accurately compared despite the solvent they were run in.

Table 4.3. Cathodic (E_{pc}) and anodic (E_{pa}) peak potentials of complexes when scanned at a speed of 0.1 (V/s) and their half-wave potentials ($E_{1/2}$) corrected to ferrocene (FC) for comparison.

Compound	R	R1	E_{pc1} (V)	E_{pa1} (V)	E_{pc2} (V vs Ag/Ag$^+$)	$E_{1/2}$ (V vs Ag/Ag$^+$)	$E_{1/2}$ (V vs Fe/Fe$^+$)
4a.1 (MeOH)	tb	H	-1.233	-1.127		-1.252	-1.669
4b.1 (DMF)	Me	H	-1.074	-1.016	-1.084	-1.045	-1.585
4c (MeOH)	H	H	-1.210	-1.014		-1.131	-1.530
4d (DMF)	MeO	H	-1.136	-1.064	-1.515	-1.100	-1.640
4f (DMF)	NH_2	H	-1.138	-1.068		-1.103	-1643
4h (MeOH)	CF_3	H	-0.710	-0.607	-1.272	-0.658	-1.076
4a.2 (MeOH	H	Me	-1.239	-1.128		-1.183	-1.601
4a.3 (MeOH)	tb	MeO	-1.247	-1.133		-1.190	-1.608
4a.4 (MeOH)	tb	Cl	-1.233	-1.119		-1.176	-1.594
4k (DMSO)	tb	H	-1.37	0.82			
FC (MeOH)			0.333	0.502		0.418	
FC (DMF)			0.476	0.603		0.540	
FC (DMSO)			0.426	0.558		0.132	

The cyclic voltammograms of the complexes are shown in **Figures 4.12** and **4.13**. As a point of reference, complex **4a.1** is used to describe the results in this section. The red arrow in the cyclic voltammogram indicates the direction the potential was scanned in, initially starting from zero to negative potential (forward scan) after which the scan direction is reversed to the positive potential while measuring the current. The resulting cyclic voltammogram provides crucial information on the number of electrons being transferred during the reduction or oxidation as well as the reversibility of these electron transfers. For complex **4a.1**, the current is swept in the cathodic direction, resulting in a positive peak annotated as E_{pc1} (E = -1.233 V), the sweep is then reversed to the anodic direction resulting in a negative peak annotated as E_{pa1} (E = -1.127 V). From the cyclic voltammogram of **4a.1**, the area under the peaks of the cathodic and anodic sweeps are similar and therefore relatively symmetrical, although they

appear at slightly different potentials. The Pt^{2+}/Pt^{+} reduction that complex **4a.1** undergoes is therefore considered to be reversible.

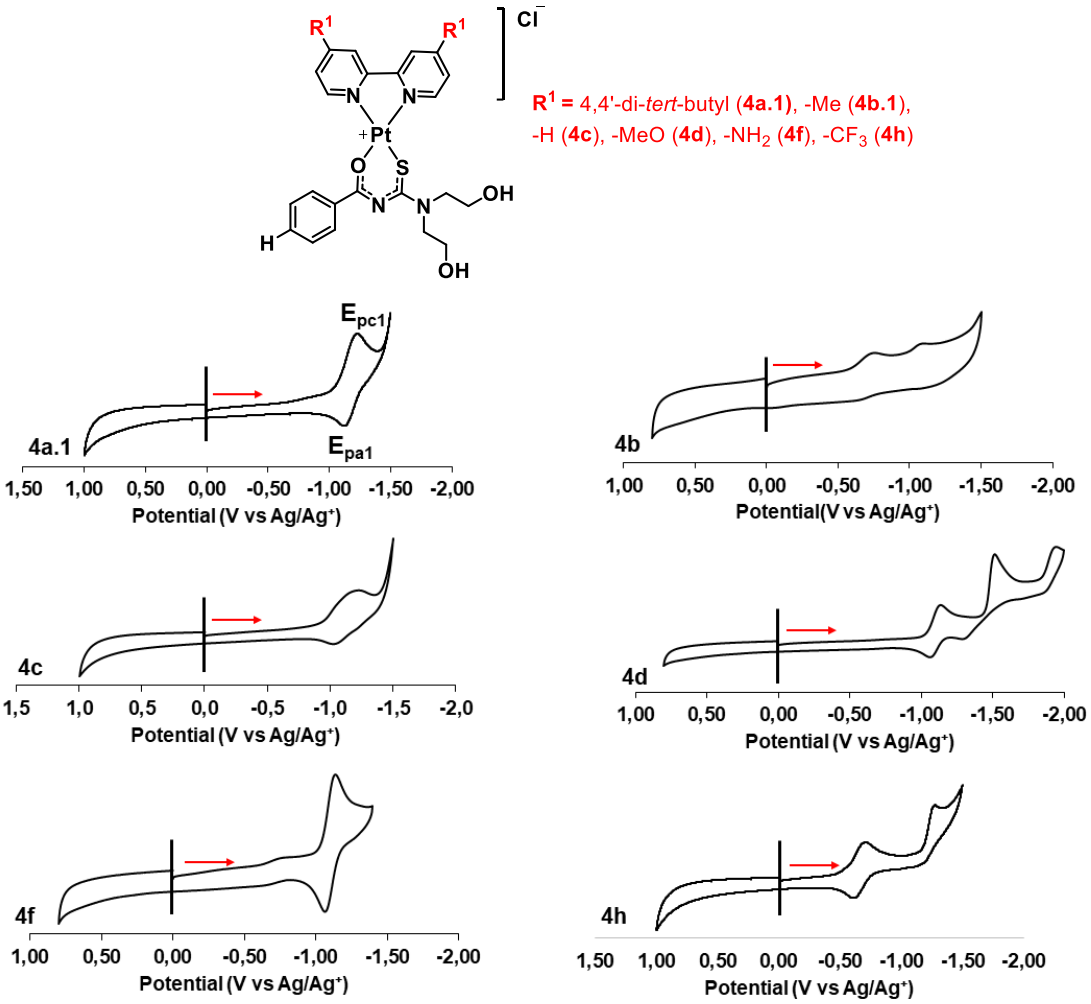

Figure 4.12. Cyclic voltammograms of complexes from SAR1 where the substituent on the bipyridine was varied.

All the platinum(II) complexes undergo reversible one-electron Pt^{2+}/Pt^{+} reductions as shown in **Figures 4.12** and **4.13**. Complexes **4b, 4d,** and **4h** undergo a second non-reversible reduction (E_{pc2}, **Table 4.3**), which is most likely ligand-based and linked to reductions of the substituent on the bipyridine. In general, a more electron-withdrawing substituent reduces the electron density around the metal center making it easier for the metal to be reduced. This trend is seen for SAR2 complexes ($E_{1/2}$ of **4a.4**<**4a.2**<**4a.3**) and for most of the complexes in SAR1, as the $E_{1/2}$ increases from the more electron-withdrawing substituent to less electron-withdrawing substituents ($E_{1/2}$ of **4h**<**4c**<**4b**<**4a.1**). However, there is a slight discrepancy in

this trend when looking at the $E_{1/2}$ potential of complexes **4a.1** and **4d**. Based on the expected trend, $E_{1/2}$ of **4d** should be larger than that of **4a.1**, but their $E_{1/2}$ potentials differ only by 0.03.

Furthermore, a comparison of the $E_{1/2}$ potentials of the complexes and their IC_{50} values does not show a correlation between the ability of the metal center to be reduced and its bioactivity. This is likely because the platinum(II) complexes do not undergo oxidations, and therefore are unlikely to produce ROS as a mechanism of action. The production of ROS is one of the modes of action of ferroquine and ferrocene derivatives,[316] and has been attributed to their oxidation potentials. However, the lack of oxidation is not surprising as other bipyridine platinum (II) complexes reported in literature only undergo reductions as well.[317,318]

Additionally, the electrochemical properties of the gold(III) analog (**4k**) was also determined to compare it to that of the platinum(II) analogs. As seen in **Figure 4.13**, **4k** undergoes a non-reversible $Ag^{3+/}Ag^{+}$ reduction at E_{pc1} = -1.37 V and a non-reversible oxidation at E_{pa1} = 0.82 V. These observed reductions and oxidations correspond to reports in the literature of other gold(III) complexes.[319,320] The electrochemical properties of **4k** differ from the platinum(II) analogs, as it undergoes a non-reversible oxidation and therefore has the potential to form reactive oxygen species (ROS). However, despite this, complex **4k** was 25-fold less potent than its platinum derivative, **4a.1**, as was discussed in **Section 3.2.6**.

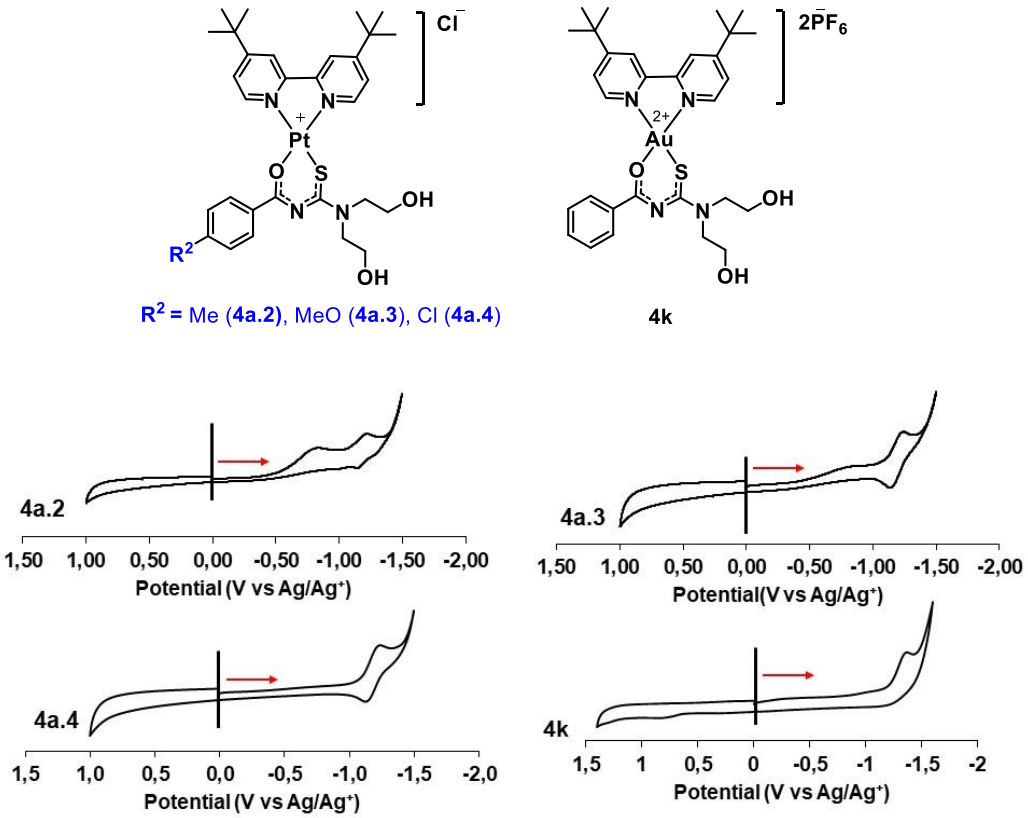

Figure 4.13. Cyclic voltammograms of SAR2 complexes and the gold(III) analog (**4k**). For the SAR2 derivatives, a substituent was added to the *para*-position of the acyl-thiourea ligand.

4.8. Photophysical properties and cellular localization studies of the fluorescently-labeled dansyl analog (4a.7)

As mentioned in **Chapter 2**, the MoA of a compound can be studied by investigating its cellular localization in the parasite. This imparts crucial information on where within the studied organism the compound accumulates and potentially acts, providing insight into the target of the compound. To study the cellular localization, a fluorescent reporter, namely dansyl, was used to synthesize a fluorescent analog of the platinum(II) complexes (**4a.7**) shown in **Figure 4.14**. This was prompted by an analysis of the photophysical properties of the parent complex, **4a.1**, which did not possess intrinsic fluorescence.

Complex **4a.7** retained the basic structure of **4a.1** with a *tert*-butyl in the 4,4'-position of bipyridine and hydrogen in the *para*-position of the acyl-thiourea ligand. Importantly, **4a.7** retained whole-cell potency with a *Pf*-NF54 IC_{50} value of 132 ± 16 nM compared to **4a.1** with

a *Pf*-NF54 IC_{50} of 151 ± 16.8 nM. It should also be noted that the addition of the dansyl reporter in **4a.7** to a scaffold of **4a.1** changes its chemical structure and subsequently can affect its physiochemical properties such as its solubility, permeability, and lipophilicity. While these factors may affect the compartmentalization of the complex, it is proposed that the two analogs should share subcellular localization, given that their core pharmacophore remains the same.

Before the intracellular localization of this complex was investigated, photophysical studies were conducted to characterize its fluorescence. The absorption and fluorescence emission properties of complex **4a.7** were measured in DMSO (**Figure 4.14**). Complex **4a.7** displays two broad bands at ~270 nm and ~365 nm for the intra-ligand charge transfer (ILCT) and the metal-to-ligand charge transfer (MLCT) bands, respectively. The broad, low intensity of the MLCT band is characteristic of metal complexes. The complex exhibits strong fluorescence in solution when excited at a wavelength of 365 nm and has an emission wavelength of 530 nm. The strong fluorescent signal emitted by **4a.7** along with the retained whole-cell potency suggested that it would be a good candidate for its intracellular localization using fluorescence microscopy.

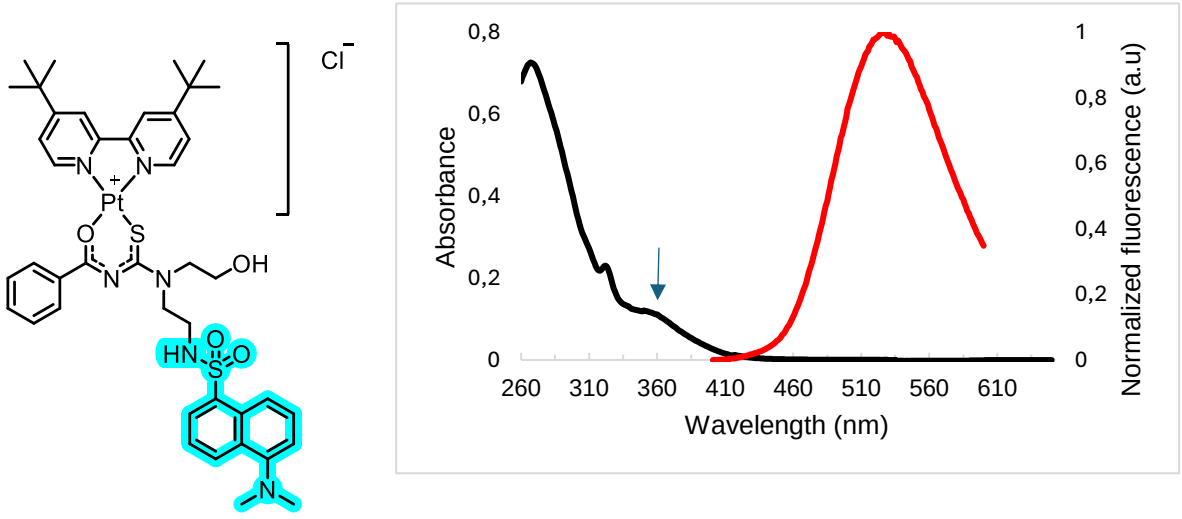

Figure 4.14. Structure of complex **4a.7**, containing the dansyl fluorescent reporter (left) and absorption (**black**) and emission (**red**) spectra of complex **4a.7** (right). The absorption spectrum shows an intra-ligand charge transfer (ILCT) band at 270 nm and a metal-to-ligand charge transfer (MLCT) band at 365 nm. For the fluorescence spectroscopy, a solution of complex **4a.7** (100 µM in DMSO) was excited at 365 nm.

The live-cell images of complex **4a.7** in *Pf*-infected erythrocytes are shown in **Figure 4.15**. These images clearly show the accumulation of the dansyl-labeled analog (**4a.7**) in infected erythrocytes, while no accumulation was observed in the uninfected erythrocytes. The fluorescence signal appears to be distributed throughout the cytoplasm of the parasite. Since DV accumulation is in part influenced by the lipophilicity, basicity, and ability of a compound to bind to heme,[321,322] the compound may accumulate in the DV despite not inhibiting hemozoin formation. However, without further localization analysis, the accumulation of the drug in a particular organelle is unclear. Furthermore, it should be noted that these images were obtained using confocal microscopy which has limitations such as obtaining images from only one optical section of the cell resulting in a long scan time to obtain high resolution images. This results in the cell often being exposed to high intensity light which may cause phototoxicity and photobleaching.

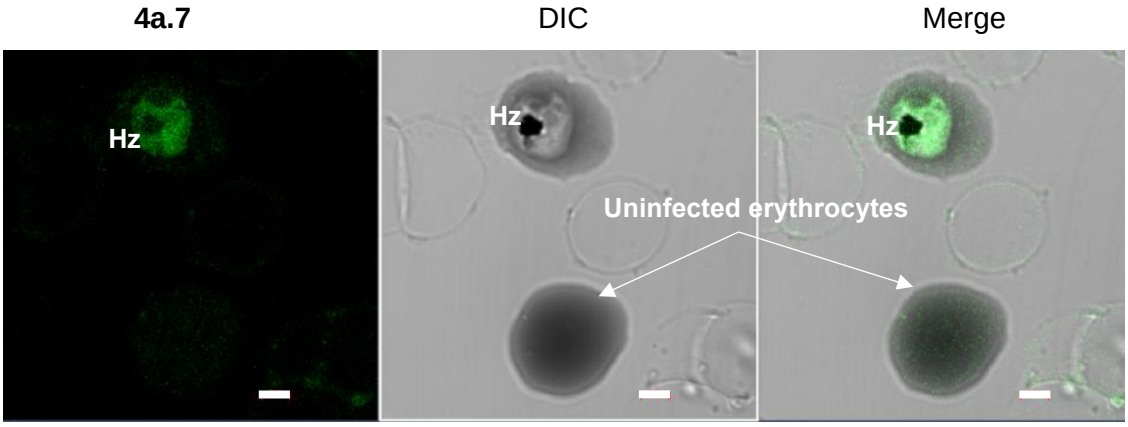

Figure 4.15. Live-cell images of *Pf*-infected erythrocytes incubated with the dansyl-labeled platinum(II) analog (**4a.7**). Scale bar: 2 µm. The image on the left (**4a.7**) shows the fluorescence of the complex. The middle image (DIC) shows an erythrocyte infected with a *Pf* parasite. The image on the right is an overlay of the left and middle images, showing that complex **4a.7** accumulates in the malaria parasite. Uninfected erythrocytes are indicated with arrows. Hemozoin is labeled Hz and appears as a black circle within the parasite DV.

While these live-cell images were a useful tool in visualizing the cellular accumulation of the fluorescently labeled complex, it should be noted that the malaria parasite is exceedingly sensitive to light.[323] It has been established that even modest light exposure for a short period results in acidification of the parasite's cytosol, likely caused by a breakdown of the DV membrane.[323] Despite the substantial fluorescence signal observed for this complex in the spectrofluorometer, the high laser power used to visualize the dansyl-labeled complex (**4a.7**) under the microscope caused visible photo-damage to the parasite thus limiting the utility of

this probe in doing more advanced imaging studies. Furthermore, despite dansyl chloride being a widely used fluorophore, it has drawbacks such as photobleaching (irreversible loss of fluorescence due to excitation using high-intensity light) and pH sensitivity.[324] Therefore, the dansyl-labeled compound was not ideal for live-cell imaging of *Pf*. For this reason, it would be best to synthesize an analog labeled with a fluorescent reporter that requires lower-energy illumination, such as those illuminated in the visible region rather than the ultraviolet region, or by first fixing the cells before incubation with the probe. However, due to synthetic limitations discussed in **Chapter 2**, the use of probes such as NBD and rhodamine which are excited at longer wavelengths was not possible. The synthesis and photophysical analysis of this dansyl-containing reporter was therefore used as a proof of concept to illustrate the accumulation of the compound within the parasite.

4.9. Conclusion

This chapter discussed the assays used to gain mechanistic insights into the synthesized mixed ligand platinum(II) complexes. A stepwise approach was followed, starting with an experiment to determine the capacity of complex **4a.1** to self-associate in solution. Complex **4a.1** exhibited self-association properties in MeOH, likely due to its ability to aggregate through π-π stacking interactions. Since π-π interactions with heme/hematin are a major contributor to compounds that inhibit both β-hematin formation and hemozoin formation, the self-association experiment reinforced testing complex **4a.1** and its derivatives in the subsequent assays. Only **4a.1** was selected for the self-association experiment as it served as a preliminary proof-of-concept experiment and required large amounts of material.

Hence, the complexes from SAR1 and SAR2 were selected for the βHI assay. Most of the tested complexes were able to inhibit the formation of βH with IC_{50} values lower than or similar to the positive control, CQ. The two prioritized complexes **4a.1** and **4f** did, however, not show inhibition of hemozoin formation in the intracellular heme fractionation assay. This was not entirely unexpected for complex **4a.1** as it showed gametocyte activity (**Chapter 3**), a stage of the parasite life cycle where the hemoglobin degradation pathway is irrelevant. Complex **4f**, which only has ABS activity, did not show a dose-dependent inhibition of hemozoin formation either. These results were contrary to the initial hypothesis that suggested that these complexes potentially inhibit hemozoin formation.

The reliabilities of these results were further confirmed using an inoculum effect study which showed that complexes do indeed accumulate in the malaria parasite to a moderate degree. It also confirmed that the concentrations used in the heme fractionation assay were sufficient to elicit an inhibition effect, had this been the MoA. The accumulation of these compounds

within the parasite is further suggested by the intracellular localization images obtained for the dansyl-labeled analog (**4a.7**); however, the high excitation energy required by the probe damaged the parasite and more extensive imaging studies with this probe would have only limited benefit. To further probe the MoA of the complexes, resistance selection studies were performed, and these are discussed in the next chapter.

Chapter 5: A Genomic Approach Towards Probing Mechanisms of Action and Resistance of selected [Pt(diimine)L-O,S]$^+$ Complexes

5.1. Introduction

The first published genomic sequences for chromosomes 2 and 3 of the *Plasmodium falciparum* (*Pf*) parasite[325–327] have been instrumental in enhancing our understanding of malaria parasite biology. This has led to the combined use of resistance selections and whole-genome sequencing (WGS) as techniques to determine the genetic origin of the loss of *Pf* drug susceptibility, in turn aiding the identification of mechanisms of resistance (MoR).[328]

Resistance selection involves culturing the *Pf* parasites at sublethal concentrations of the bioactive compound for a prolonged period to generate mutant parasites that are less susceptible to the selection drug. Monoclonal cells of the recrudesced mutant culture are then isolated, profiled against the selection drug, and their genomes sequenced to identify genetic mutations that are responsible for their resistant phenotype. In some instances, the MoR of a compound corresponds to its mechanism of action (MoA),[329] making resistance selection a potential tool in identifying the target biomolecule(s).

This is possible because the gDNA sequence of recrudesced mutant parasites can be compared to that of the parent strain used in the selection process to identify copy number variations (CNVs) and single nucleotide polymorphisms (SNPs) in the genome. For this experiment, the *Pf*-Dd2 strain is preferentially employed as it rapidly proliferates, is well characterized as a multidrug-resistant strain, and has a higher propensity for mutations compared to other laboratory-adapted strains such as *Pf*-NF54.[330]

As mentioned in **Section 1.8.2**, *in vitro* drug-resistant selections can be conducted either as a single step, stepwise, or using a pulse method as is now described below.

Single-step selection: A large inoculum size is pressured using one drug concentration (3 to 5 x IC_{50}) for up to 60 days. If recrudescence occurs, the resistant mutant can be profiled against the selection drug, and a shift in the IC_{50} value relative to the parental strain calculated. This method is beneficial as it often produces mutant parasites within two months. On the

downside, this method requires the culturing of multiple flasks at once and uses large quantities of growth medium and red blood cells (RBCs).

Stepwise selection: Parasites of a particular inoculum size are incubated at a starting concentration of 1 x IC_{50}, after which the concentration is increased gradually over time. This method is advantageous as smaller culture sizes can be used (5 mL), but the selection period can take months.

Pulse method: For this method, parasites are exposed to the test compound for 1-2 days, after which the compound is washed off and the parasites are allowed to recover.

Since the single-step method produces mutants that maintain their resistant phenotype, it is preferred for MoA/MoR studies and is therefore the method employed in this thesis.

Thus, the main aim of this chapter is to discuss the use of resistance selections and WGS to determine the MoR(s) and the potential MoA(s) or target(s) of the two prioritized platinum(II) complexes, **4f** and **4a.1**.

5.2. *In vitro* resistance selections

To start the resistance selections, the IC_{50} values of complexes **4a.1** and **4f** against *Pf*-Dd2 were first determined, as multiples of these values were used as the selection concentrations for the resistance selections. To this end, a 48-hour *Plasmodium* lactate dehydrogenase (pLDH) assay was employed and the *Pf*-Dd2 IC_{50} values of **4a.1** and **4f** were determined to be 212 nM and 121 nM, respectively.

For the resistance selection, the protocol described by Ng *et al*,[328] was followed with minor modifications where *Pf*-Dd2 cultures were expanded into six 100 mL culture flasks, giving rise to 10^9 parasites per flask (**Figure 5.1**). Dosing with the complexes (three flasks per analog) started at 4% parasitemia (in the ring phase) with a 3% hematocrit. The selections were performed using initial concentrations of 3x, 5x, and 7x the IC_{50} of **4f** in flasks Fl1-Fl3 and with 3x, 4x, and 5x the IC_{50} of **4a.1** in flasks Fl4-Fl6, respectively. These concentrations were guided by the dose-response profiles of each compound which ensured that an appropriate range was used to promote optimal chances of recrudescence, following clearance of the sensitive parasites from the cultures.

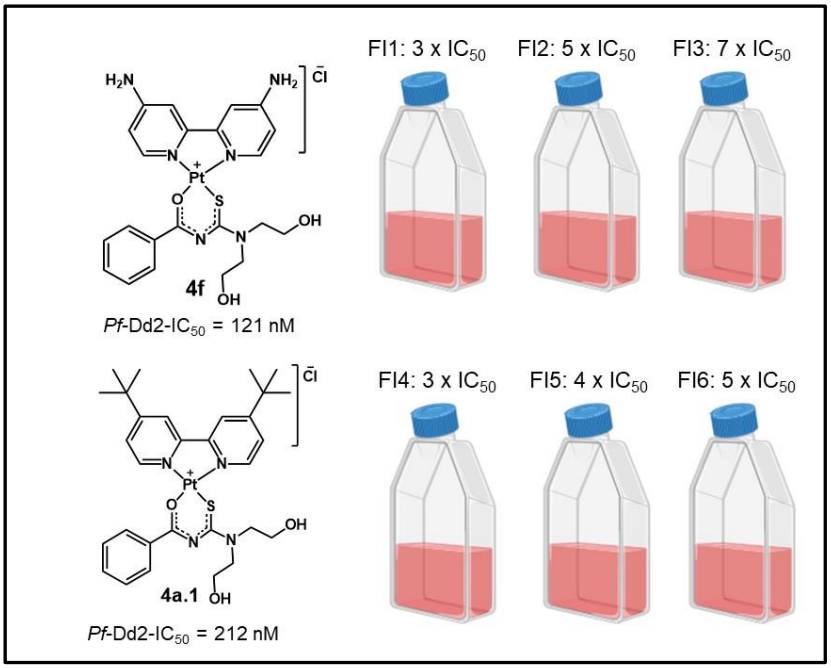

Figure 5.1. Pictorial representation of resistance selection culture flasks each containing 10^9 parasites, illustrating their allocated flask number and the selection concentrations of the respective compound (**4a.1** or **4f**) in multiples of their IC_{50} values.

Dosing with the relevant selection concentrations of each complex in their allocated flask began on day 0 (**Figure 5.2**) with monitoring of each flask every day for seven days and then every second to third day for the remaining period. Images of the culture smears stained with Giemsa (**Figure 5.2**) were obtained to visualize the daily morphological changes that occurred during the resistance selections. Following incubation under drug pressure for 24 hours, the parasites in all six flasks proliferated normally and progressed from rings to trophozoites on the first day of monitoring. A decrease in parasitemia and a halt in their life cycle was observed across all six flasks after 48 hours on day 2, indicative of the parasite's susceptibility to complexes **4a.1** and **4f**. On day 3, after ~72 hours of drug pressure, trophozoites at a low parasitemia and no progression to rings were still seen in flask Fl1, which was under the lowest pressure from complex **4f** (3 x IC_{50}). However, also on day 3, parasitic debris was observed in flasks Fl2-Fl6, with no healthy parasites (rings or trophozoites) seen. Furthermore, all healthy trophozoites and rings were cleared from Fl1-Fl6 by Day 15, as seen in **Figure 5.2**.

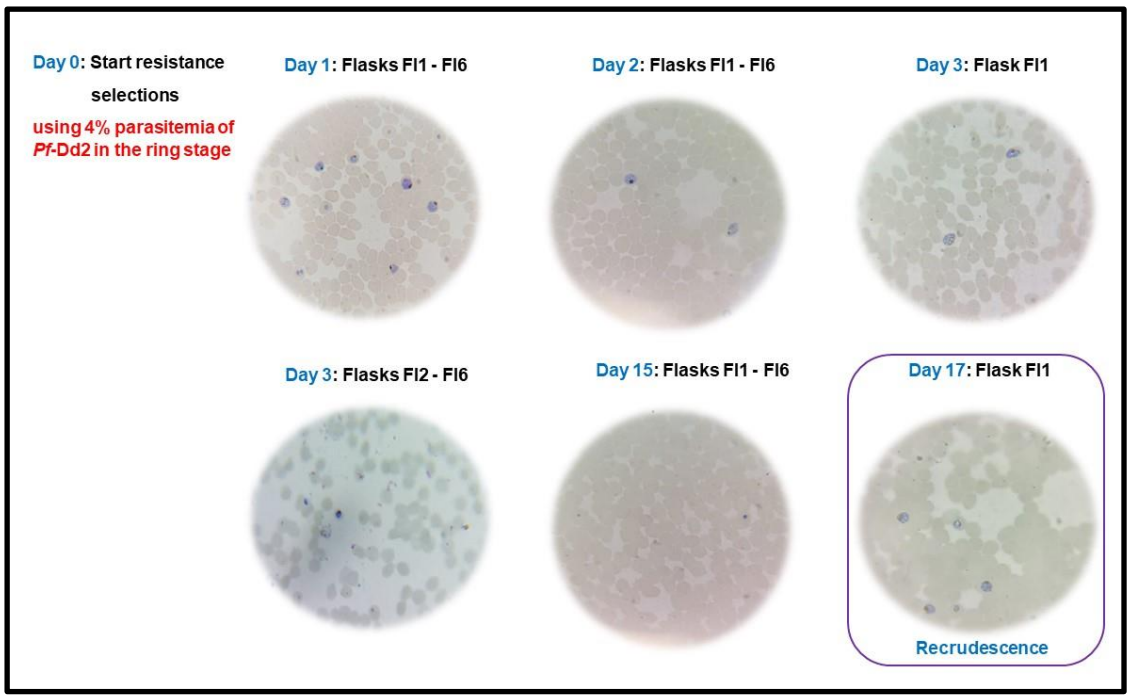

Figure 5.2. Microscope images of Giemsa-stained smears of the contents in flasks Fl1-Fl6 on indicated days. Resistance selection began on day 0 (image not provided) using a culture of synchronous rings.

Following the clearance of all healthy parasites by day 15, Fl1 and Fl4 were removed from drug pressure to prompt the growth of mutant parasites, as shown in **Figure 5.3**. Consequently, recrudescence occurred in flask Fl1 on day 17, after two days of culturing under no drug pressure (NDP). The selection concentration in Fl1 was subsequently increased to 5 x IC_{50} of **4f** for approximately two weeks before being profiled. This was to ensure that a resistant phenotype would be maintained during the culturing period. Furthermore, flask Fl4 was kept under NDP, and the remaining four flasks (Fl2, Fl3, Fl5, and Fl6) were continuously pressured with their respective selection concentrations over the entire 60-day period, with no recrudescence occurring in any of the flasks (Fl2-Fl6).

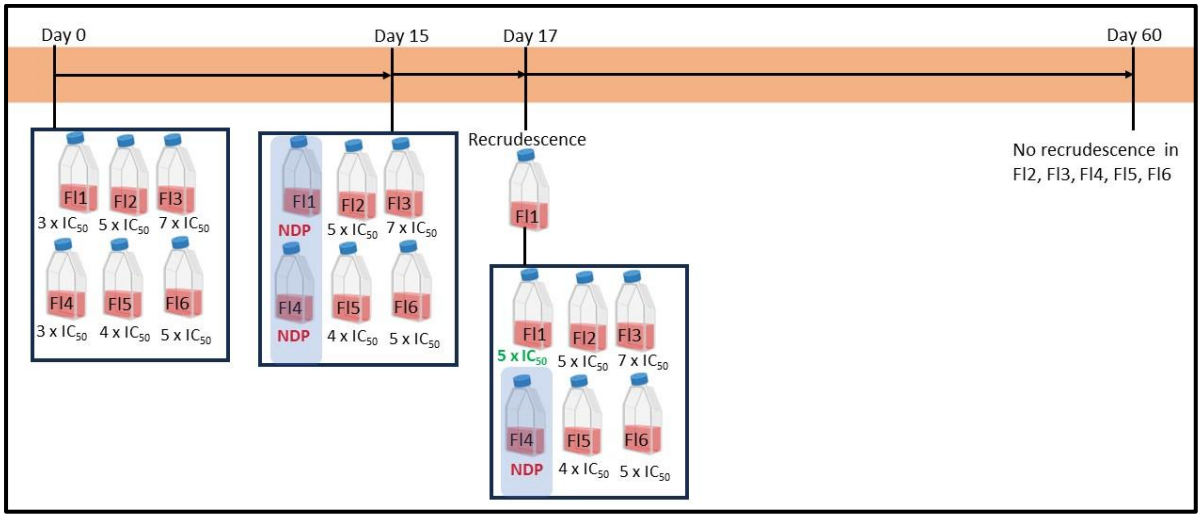

Figure 5.3. Timeline showing the selection concentrations of compounds **4f** (Fl1-Fl3) or **4a.1** (Fl4-Fl6) in each flask on the respective days. On day 15, flasks Fl1 and Fl4 were removed from drug pressure, as indicated by NDP (no drug pressure). On day 17, following recrudescence in flask Fl1, it was cultured under 5 x IC_{50} of **4f** until day 60. Flask Fl4 was cultured under NDP for the remaining duration of the experiment with no recrudescence occurring in either Fl2, Fl3, Fl4, Fl5, or Fl6 within the 60-day selection period.

Upon the observation of recrudesced parasites from Fl1 on day 17, the drug susceptibility of these bulk mutants to **4f** was subsequently determined and compared to that of the *Pf*-Dd2 parent to confirm that resistant mutants were successfully raised. These drug susceptibility assays were conducted while flask Fl1 was not under drug pressure. For this, the growth inhibition pLDH assay was performed with a 48-hour incubation period. **Figure 5.4, A** represents the 96-well plate post-incubation of *Pf*-Dd2 and the bulk mutant culture with either complex **4f** or the control drug, chloroquine (CQ). **Figure 5.4, A** shows that despite treatment with **4f** at concentrations up to 5 µM, high parasite survival occurred in all wells with the inability to obtain an IC_{50} value at this concentration. This is emphasized by the continuous intense purple color (indicative of high parasite survival) across the 96-well plate, even at the maximum concentration. This is further shown in **Figure 5.4, B** where a clear shift in the dose-response curve is observed for the bulk mutant culture, confirming that it is indeed resistant to **4f**.

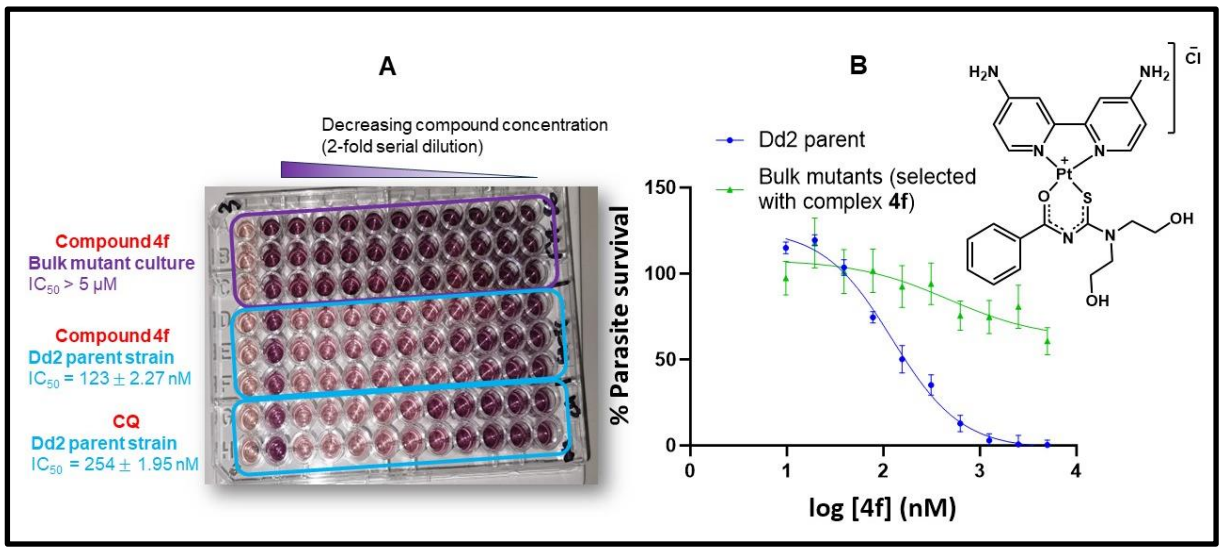

Figure 5.4. **A**: The Malstat- and NBT-developed 96-well plate post 48-hour incubation of the *Pf*-Dd2 parent and the bulk-resistant culture with either complex **4f** or CQ. Column 1 contained unparasitized red blood cells (RBCs) and column 2, untreated parasitized RBCs, each at 1% parasitemia and 1% hematocrit. Compound **4f** or CQ was added to column 3 and diluted 2-fold down to column 12. Resistance of the bulk mutant culture to **4f** is indicated by a high parasite survival emphasized by the intense purple color. **B**: The dose-response curves of complex **4f** in the Dd2 parent strain (blue) compared to the Fl1 bulk mutant culture (green), highlighting the significant shift in IC_{50} value, which could not be obtained at the maximum concentration of 5 µM.

5.3. Isolating 4f-mutant clones by limiting dilution

Successful resistance selections generate a polyclonal mass of cells, referred to above as the bulk recrudesced culture. Thus, several mutant parasites with their unique set of genetic polymorphisms and phenotypes can exist within this bulk culture. To isolate a monoclonal cell population(s), cloning by limiting dilution, described by Macedo-Silva *et al.*,[331] was used with minor modifications. Cloning by limiting dilution is based on a Poisson distribution which calculates the theoretical probability of a countable outcome.[193,332] Here, the **4f** bulk mutants from Fl1 were cultured in a 96-well plate at dilutions starting below one parasite per well to prevent the growth and isolation of more than one clone per aliquot. **Figure 5.5** illustrates these dilutions, calculated from **Equation 5.1**, to obtain the overall equivalent of ¼ or ½ a parasite per well across the plate (200 µL per well). The plates were incubated for 17 days, with changes to the growth medium and replenishment of 0.4% RBCs every 7 days.

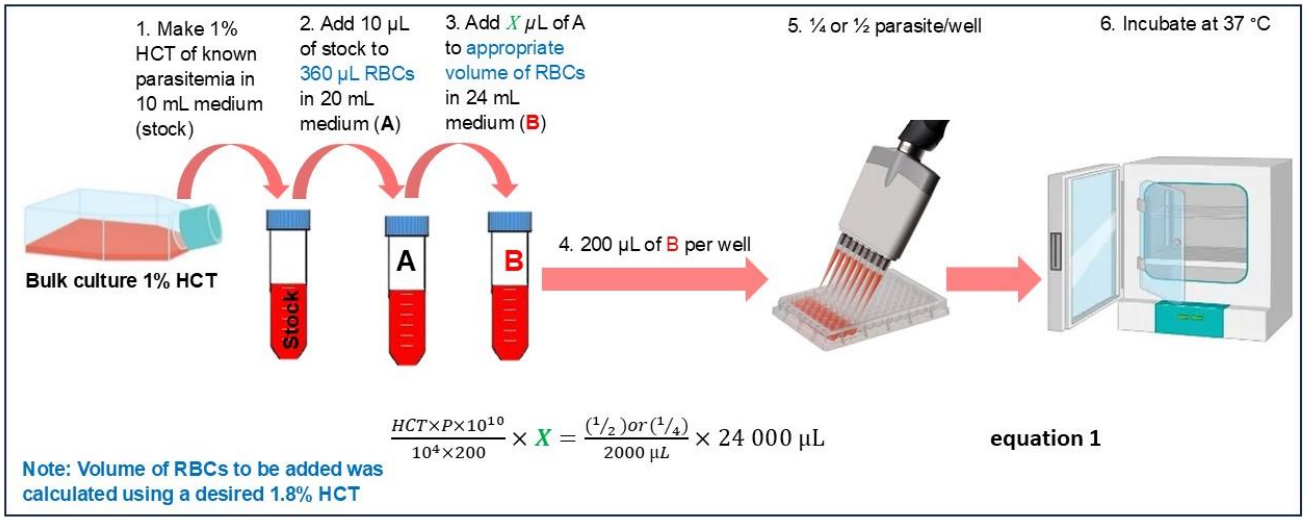

Figure 5.5. Graphical representation of the cloning by limiting dilution protocol to initially start with either ¼ or ½ parasite per well in a 96-well plate. X µL of the contents in tube B was transferred to 200 µL of growth medium containing 1% HCT in each well and incubated for 17 days at 37 °C. Abbreviations: HCT-hematocrit; P-parasitemia.

Parasite growth was evaluated on day 18 using flow cytometry where wells containing unparasitized RBCs served as a reference (**Figure 5.6, A**). Flow cytometry is a technique used to quantify and distinguish between populations of cells where each distinct cell type appears in its own region on the dot map, referred to as a gated population. Therefore, unparasitized RBCs appear in a different region to those containing parasites (asynchronous trophozoites and rings) as shown in **Figure 5.6, A** and **B**. The cells were recorded as the number of "events" per the injection volume (40 µL) and were quantified as a percentage of cells within the gated population region.

Thus **Figure 5.6, A** shows 99.6% of unparasitized RBCs with approximately 0.05% of the counted events in 40 µL likely corresponding to background noise. **Figure 5.6, B** corresponds to wells containing an asynchronous culture which was recorded as 9.31% of parasites within the gated population.

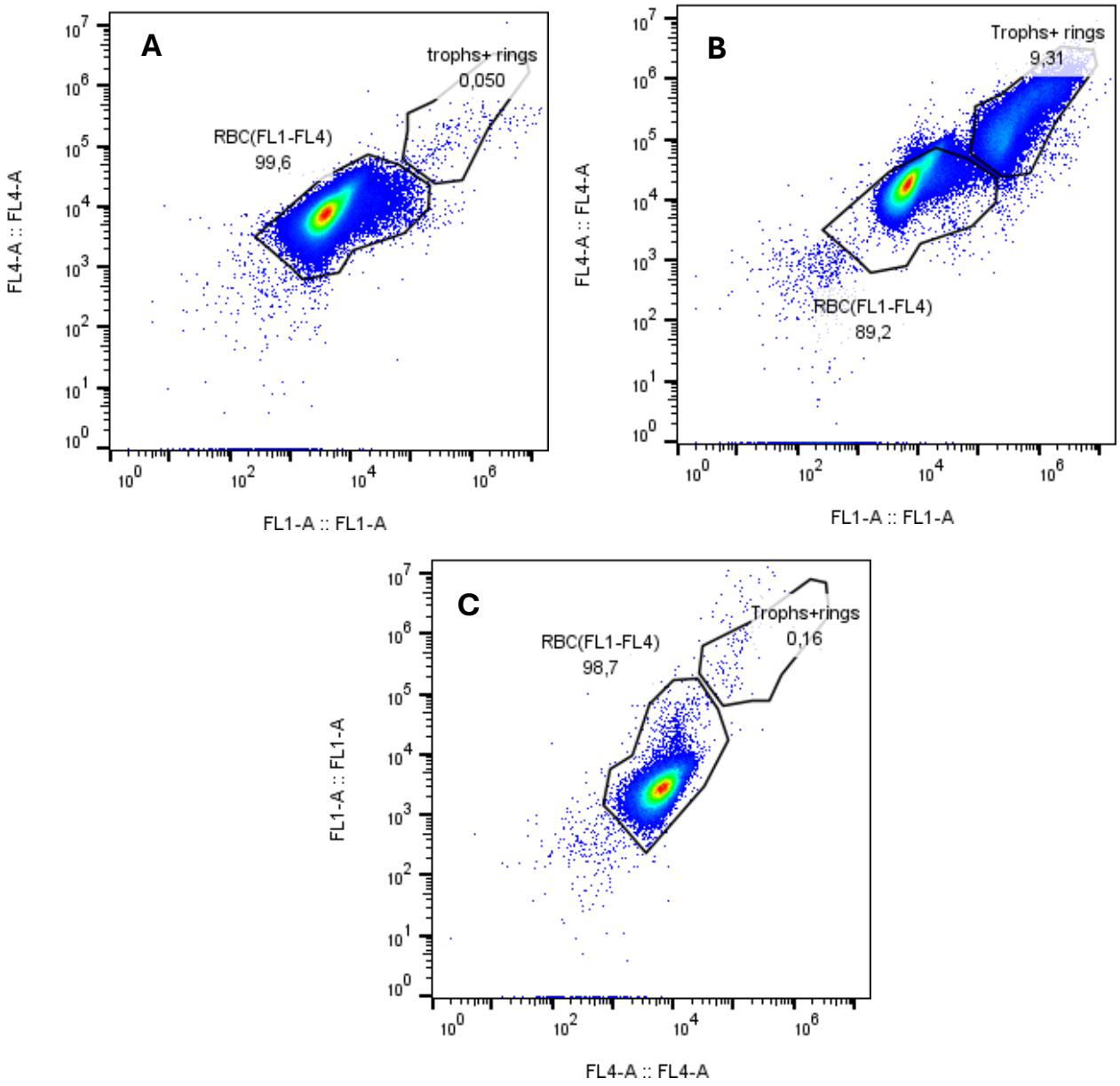

Figure 5.6. Dot plots obtained from flow cytometry showing the distribution of gated populations in wells containing **A**: Unparasitized RBCs, illustrating that 0.05% of the parasite-gated population corresponds to background noise and should not be considered as parasite growth; **B**: An asynchronous culture of *Pf* parasites illustrating the population distribution of parasitized RBC as a recorded percentage of 9.3%. **C**: Representative well for positive parasite growth with >0.1% parasitized RBCs. These dot plots are represented using a log scale, where the populations are quantified as a percentage.

Based on the percentages represented by these reference wells, those containing a minimum of 0.1% in the rings + trophozoite gated population were considered to have parasite growth and these aliquots were expanded into a 24-well plate. A representative of a selected well (**Figure 5.6, C**) shows 0.16% in the parasite-gated population on the dot map. Ultimately, a total of 12 wells from the 96-well plates were expanded into the 24-well plate and cultured under no drug pressure while their growth was monitored. Consequently, three wells from the plate incubated with "½" parasite per well (**B3**, **C2**, **E11**) and one from the plate incubated with "¼" parasite per well (**G7**) were further expanded into 50 mL culture flasks for profiling against complexes **4a.1** and **4f**.

5.4. Profiling of clones using the pLDH assay

The four individual clones selected and expanded from the cloning plate, as mentioned in the previous section were annotated as follows: Dd2-**4f**-Fl1-**B3**, Dd2-**4f**-Fl1-**C2**, Dd2-**4f**-Fl1-**G7,** and Dd2-**4f**-Fl1-**E11**. Subsequently, a drug susceptibility (pLDH) assay was employed to evaluate if the clones had unique phenotypes and resistant profiles to complex **4f**, compared to Dd2. The dose-response curves of clones **B3**, **C2**, and **E11**, shown in **Figure 5.7**, follow a similar sigmoidal shape to that of the Dd2 parent when treated with **4f**, with clone **C2** having the lowest fold-shift in IC_{50} relative to Dd2. The dose-response profile of clone **G7** diverges slightly from the other three clones, highlighting its higher level of resistance to **4f**, further verified by the significant 21-fold shift in IC_{50} compared to Dd2 (**Table 5.1**).

Furthermore, to assess the potential of cross-resistance between other analogs in this chemical series and **4f**, the whole-cell potency of **4a.1** was also evaluated against the isolated clones as shown in **Figure 5.7**. The sigmoidal dose-response profiles of all the clones treated with **4a.1** resemble those of the Dd2 parent. However, the fold-shift in IC_{50} values spans a lower range than what was observed for **4f**, varying from 1.2-fold to 6.5-fold for **4a.1** (**Table 5.1**).

From this, a degree of cross-resistance is observed for **4a.1**, in all tested clones except for **C2** where an IC_{50} fold-shift of 1.2 is observed. Overall, the clones exhibit higher levels of resistance to the compound used for their selection (**4f**), but these results do allude to a possible shared MoA between complexes **4a.1** and **4f**.

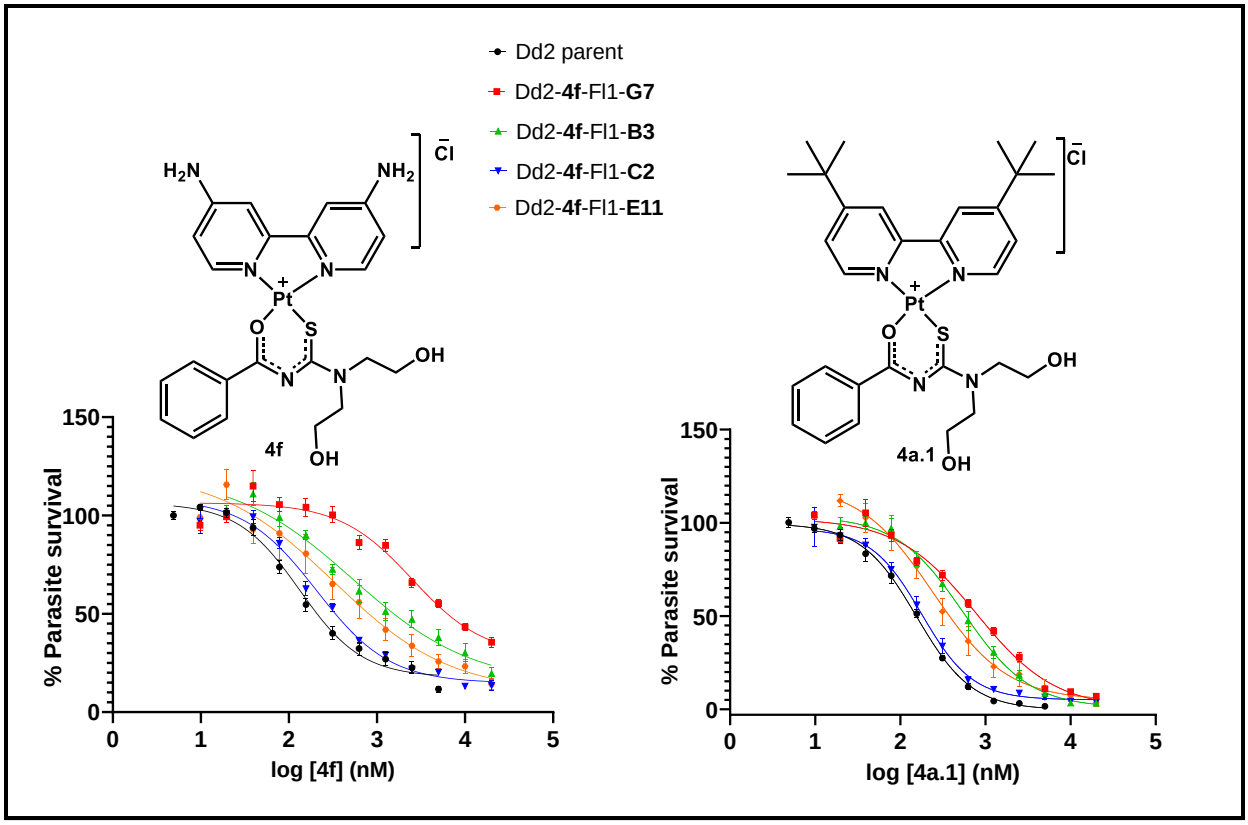

Figure 5.7. Dose-response curves of mutant clones, **B3**, **C2**, **G7**, and **E11** selected with **4f** and the Dd2 parent that was profiled against complexes **4f** and analog **4a.1.** Error bars represent the SEM values, where N, n = 3, 3.

Table 5.1. IC_{50} values obtained from the profiling of the **4f**-mutant clones against complexes **4f** and **4a.1**. SEM values are included where N, n = 3, 3. RI = resistance index, indicating the fold shift of the clone IC_{50} compared to the Dd2 IC_{50}.

	IC_{50} ± SEM (nM)		RI (clone IC_{50}/Dd2 IC_{50})	
Strain	**4f**	**4a.1**	**4f**	**4a.1**
Dd2	135 ± 21	144 ± 19	-	-
Dd2-4f-Fl1-G7	2778 ± 378	938 ± 208	21	6.5
Dd2-4f-Fl1-B3	566 ± 171	533 ± 207	4.2	3.7
Dd2-4f-Fl1-C2	180 ± 54	179 ± 49	1.3	1.2
Dd2-4f-Fl1-E11	1172 ± 942	445 ± 334	8.7	3.1

Based on the different phenotypes of each clone, all four were selected for whole-genome sequencing. To determine the polymorphisms responsible for their resistant phenotypes, gDNA from harvested trophozoites of each clone was extracted. For this, cultures of each clone containing approximately 10% trophozoites were lysed with saponin, freeing them from the RBCs. The gDNA was subsequently extracted using a QIAamp DNA Blood Midi Kit of which the purity was verified on a NanoDrop1000 spectrophotometer. Subsequently, the extracted gDNA was submitted for whole-genome sequencing.

5.5. Illumina-Based Whole Genome Sequencing of 4f- mutant clones

Illumina-based WGS was employed to obtain the genomic profiles of the isolated clones which were compared to that of the Dd2 parent. Several CNVs in genes on chromosome 5, common to clones **B3**, **C2**, and **E11**, were observed (**Table 5.2**). Additionally, deletions in the copy numbers of genes on chromosome 8, unique to clone **C2**, were also identified. Of note, clones **B3**, **C2**, and **E11** showed amplifications in the gene encoding for the *Pf*-multidrug resistance-1 (PfMDR1) protein. An increase in the copy number of the *Plasmodium falciparum* multidrug resistance-1 (*pfmdr1*) gene, which encodes for a transmembrane drug transporter protein on the digestive vacuole (DV),[333] has long been associated with multidrug resistance in malaria.[334] Although the molecular mechanism of the PfMDR1 transporter remains largely unknown, amplification of the *pfmdr1* gene has been associated with resistance to several clinical antimalarials such as mefloquine, lumefantrine, halofantrine, quinine, and artemisinin derivatives.[335,336–339]

The amplifications of the *pfmdr1* gene observed for three of the clones suggest that the susceptibility of the parasite to **4f** is likely influenced by the transportation of the compound between the cytosol and DV by PfMDR1. Amplifications in the *Pfmdr1* gene have been associated with increased transportation of the drug into the DV, particularly when its target resides in the cytosol.[340] In addition to this and the cellular localization studies which showed approximately even distribution of the fluorescent analog within the parasite, the target of **4f** likely resides in the cytoplasm of the parasite.

Table 5.2. Results from the WGS of the Dd2-**4f**-Fl1 clones show the single nucleotide polymorphisms (SNPs) and copy number variations (CNVs) that occurred to render these clones resistant to complex **4f**. Illumina-based WGS was used, and the clones' genomes were compared to that of the Dd2 parent. Amplifications in the gene encoding for the MDR1 protein and an SNP in the gene encoding for kinesin-13 are in red to highlight that this CNV and SNP are likely driving resistance in the **4f** clones B3, C2 and E11 or in clone G7, respectively.

CNVs: The factor refers to the number of amplifications or deletions in the copy number of the designated gene. NA refers to no amplification in the copy number of the gene compared to the Dd2 parent. The count is the number of times the gene was read during the analysis process.

Gene ID	chromosome	Annotation	count	Fl1-B3 factor	Fl1-C2 factor	Fl1-E11 factor	Mean factor
PF3D7_0521900	Pf3D7_05_v3	conserved Plasmodium protein, unknown function	3	1,875	2,423	1,790	2,029
PF3D7_0522000	Pf3D7_05_v3	conserved Plasmodium protein, unknown function	3	1,875	2,423	1,790	2,029
PF3D7_0522100	Pf3D7_05_v3	conserved Plasmodium protein, unknown function	3	1,875	2,423	1,790	2,029
PF3D7_0522200	Pf3D7_05_v3	transcription initiation factor TFIID subunit 10, putative	3	1,875	1,371	1,790	1,679
PF3D7_0522300	Pf3D7_05_v3	18S rRNA (guanine-N(7))-methyltransferase, putative	3	1,875	1,371	1,790	1,679
PF3D7_0522400	Pf3D7_05_v3	conserved Plasmodium protein, unknown function	3	1,875	2,912	1,790	2,192
PF3D7_0522500	Pf3D7_05_v3	50S ribosomal protein L17, apicoplast, putative	3	1,875	2,055	1,790	1,907
PF3D7_0522600	Pf3D7_05_v3	magnesium transporter NIPA, putative	3	1,875	2,055	1,790	1,907
PF3D7_0522700	Pf3D7_05_v3	iron-sulfur cluster assembly protein SufA	3	1,875	2,055	1,790	1,907
PF3D7_0522800	Pf3D7_05_v3	pre-mRNA-splicing factor BUD31, putative	3	1,875	2,055	1,790	1,907
PF3D7_0522900	Pf3D7_05_v3	zinc finger protein, putative	3	1,875	2,055	1,790	1,907
PF3D7_0523000	Pf3D7_05_v3	multidrug resistance protein 1	3	1,875	2,577	1,790	2,081
PF3D7_0523100	Pf3D7_05_v3	mitochondrial-processing peptidase subunit alpha, putative	3	1,875	2,577	1,790	2,081
PF3D7_0523200	Pf3D7_05_v3	heptatricopeptide repeat-containing protein, putative	3	1,875	2,577	1,790	2,081
PF3D7_0813800	Pf3D7_08_v3	GDP-mannose 4,6-dehydratase	1	NA	-2,099	NA	-2,099
PF3D7_0813900	Pf3D7_08_v3	40S ribosomal protein S16, putative	1	NA	-2,099	NA	-2,099
PF3D7_0814000	Pf3D7_08_v3	60S ribosomal protein L13-2, putative	1	NA	-2,099	NA	-2,099
PF3D7_0814100	Pf3D7_08_v3	conserved Plasmodium protein, unknown function	1	NA	-2,099	NA	-2,099
PF3D7_0814200	Pf3D7_08_v3	DNA/RNA-binding protein Alba 1	1	NA	-2,099	NA	-2,099
PF3D7_0826100	Pf3D7_08_v3	HECT-like E3 ubiquitin ligase, putative	1	NA	1,424	NA	1,424

SNPs:

Chromosome	POS	REF	ALT	Mutation in	Gene name	Exon ID	Amino acid change	Codon Change	Effect	Description
Pf3D7_03_v3	205372	A	C	F1-E11	PF3D7_0304100	1	E277D	gaA/gaC	NON_SYNONYMOUS_CODING	inner membrane complex protein 1e, putative
Pf3D7_07_v3	855291	C	A	F1-C2	PF3D7_0719500	2	W371L	tGg/ tTg	NON_SYNONYMOUS_CODING	LEM3/CDC50 family protein, putative
Pf3D7_09_v3	394113	C	A	F1-G7	PF3D7_0908500	16	E601*	Gag/ Tag	STOP_GAINED	conserved *Plasmodium* protein, unknown function
Pf3D7_12_v3	1886953	AATAATAATGTTGATAATAATGTTGATAATAATG	AATAATAATGTTGATAATAATG	F1-G7	PF3D7_1245100	2	VDNND1092D	gttgataataatgat/gat	CODON_CHANGE_PLUS_CODON_DELETION	kinesin-13, putative
Pf3D7_14_v3	901122	A	T	F1-G7	PF3D7_1422400	1	N246I	aAt/aTt	NON_SYNONYMOUS_CODING	conserved *Plasmodium* protein, unknown function

Furthermore, single nucleotide polymorphisms (SNPs) were observed on chromosomes 3 and 7 in clones **E11** and **C2**, respectively. For clone **E11**, the nucleotide adenine was replaced with cytosine in the gene coding for a putative inner membrane complex (IMC) protein 1e. The IMC class of proteins are found in the motile stages of apicomplexan parasites like *Pf* and are essential for their gliding and invasion of host cells.[341] The IMC proteins also contribute to the shape and rigidity of the cell during cell division.[342] In the **C2** clone, an SNP in the gene encoding for a putative LEM3/CDC50 family protein was observed. There are three putative *Pf*-CDC50 proteins, annotated as CDC50**A** (PF3D7_0719500), CDC50**B** (PF3D7_1133300), or CDC50**C** (PF3D7_1029400). A previous study conducted in the *Plasmodium yoelii* mouse model showed that the binding of the CDC50**A** orthologue to guanylyl cyclase beta (Gcβ, important for the conversion of ATP and GTP to other important proteins) is essential for the motility of ookinetes in the mosquito vector and consequently for the transmission of the parasite.[343]

However, for clone **G7**, three independent SNPs were observed, two of which occurred in a conserved *Plasmodium* protein of unknown function and the third in the gene encoding for kinesin-13. The kinesin-13 SNP was particularly interesting as there have been no reported MoRs involving kinesin-13 in the literature. Kinesins are a class of motor proteins, locally based on microtubules (MT) in kinetochores (**Figure 5.8**), and play an important role in cell division, motility, organization of cell polarity, and intracellular transport.[344]

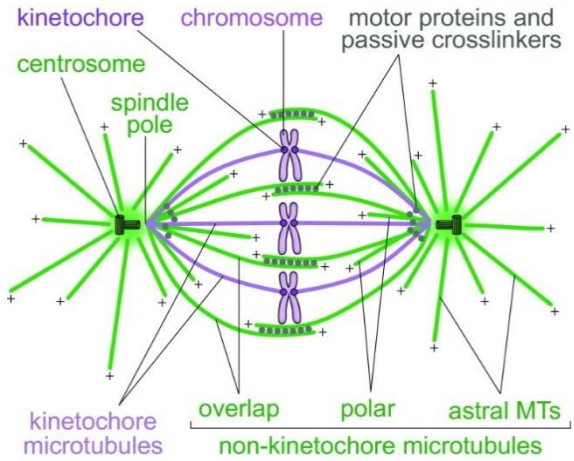

Figure 5.8. Image showing the kinetochore microtubules and the orientation of motor proteins on these microtubules. Republished from Tolić *et al*. under the Creative Commons Attribution license (CC BY), Copyright (2024).[345]

Kinesin-13 is a sub-family of this class of proteins and is important for the depolymerization of the MT during mitotic cell division. Contrary to other kinesin sub-families like kinesin-8, kinesin-13 diffuses to both ends of the MT for its depolymerization action.[346] In a recent study, nine kinesins were phylogenetically identified and functionally characterized in *P. bergei*.[344] Eight of those kinesins were found to be essential during the transmission (gametocyte) stage of the parasite life cycle, with only kinesin-13 being essential during the schizogony stage, as shown in **Figure 5.9**.[344]

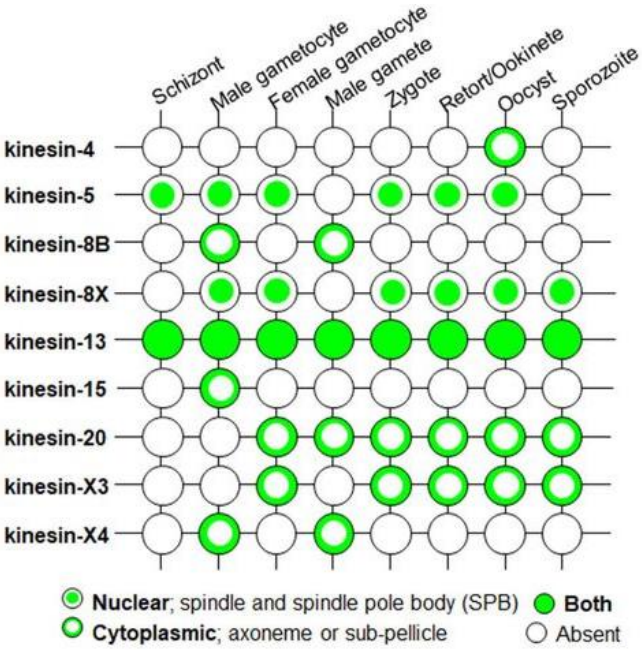

Figure 5.9. A summary of the expression location of each of the nine kinesins during the different life cycle stages of the *P. berghei* parasite as reported by Zeeshan *et al*. Republished under the Creative Commons CC0 public domain dedication.[344]

Interestingly, clone **G7** varies quite significantly from the other three clones, with the MoR likely being driven by *mdr1* for clones **B3**, **C2,** and **E11** and the MoR potentially being driven by kinesin-13 for **G7**. These studies have thus presented a novel MoR and suggest that kinesin-13 can be probed as a new pathway for resistance and as a potential antiplasmodium drug target. This is further motivated by studies of kinesin inhibitors in the cancer field, where filanesib, an inhibitor of the kinesin spindle protein (KSP), successfully made it into phase I clinical trials.[347] Several other kinesin inhibitors have also been investigated as cancer therapeutics, showing the potential and importance of kinesins as a therapeutic target.[348–350]

5.6. Chapter Summary

Designing compounds that target novel biomolecules has been aided by breakthroughs in *Pf* genomic research. These genetic advances have fuelled the use of resistance selections and WGS to identify the molecular markers responsible for reduced drug susceptibility. In this chapter, these tools were employed to investigate the MoR of two synthesized platinum(II) complexes, to provide insight into their MoA. Culturing of the Dd2 parent under a concentration of 3x the IC_{50} of complex **4f** resulted in the recrudescence of resistant parasites in Fl1, while culturing at higher concentrations of **4f** or **4a.1** did not yield mutants after 60 days. This suggests that these complexes have a high minimum inoculum of resistance (low frequency of recrudescence), which is a favourable property for antimalarial drugs. Monoclonal populations from the Fl1 bulk culture were isolated using cloning by limiting dilution, producing four clones with IC_{50} fold shifts up to 21 (clone **G7**) compared to Dd2 when treated with **4f**. Furthermore, cross-resistance was observed between clones **B3**, **G7**, **E11**, and Dd2 when tested with complex **4a.1**.

Whole-genome sequencing identified several CNVs and SNPs involved in the resistant phenotypes of the clones with the most noticeable CNV corresponding to the well-known *pfmdr1* gene, encoding for a membrane transport protein. The amplification of *pfmdr1* likely allows for the complex to be transported away from the target protein, decreasing parasite susceptibility to the complex. A SNP in the kinesin-13 gene was unique to the most resistant clone, **G7**, suggesting that its MoR is likely driven by this mutation. Although not conclusive in identifying the MoA of the herein synthesized platinum(II) complexes, these genomic results imply that these complexes may have a novel target or act via polypharmacology, possibly involving kinesin-13, and this should be investigated further in the future.

Chapter 6: Conclusions and Future Work

6.1. Conclusions

Despite enormous efforts to eradicate malaria, the emergence of resistance to the majority of the clinical antimalarial drugs has slowed progress. Thus, the rationale behind this work was to synthesis and investigate a series of novel compounds with dual-stage antiplasmodium activity, that can potentially circumvent resistance.

The first aim of this thesis work was to resynthesize the metal complexes reported in the previous study by Egan *et al.*[179] and further explore their chemical space with additional chemical modifications. This was done to evaluate structure-activity relationship (SAR) and structure-property relationship (SPR) trends. The second objective was to probe the mechanism of action (MoA) of these complexes. This included using assays such as the detergent-mediated β-hematin inhibition and cellular heme fractionation assays as well as attempts to identify the target biomolecule(s) and mechanism(s) of resistance (MoR) using a genomic approach involving resistance selections followed by whole-genome sequencing (WGS). Within this thesis, a range of whole-cell potencies, physiochemical properties, and microsomal metabolic stabilities were measured for the complexes.

6.1.1. SAR and SPR of mixed-ligand platinum(II) and gold(III) complexes

Asexual blood stage (ABS) whole-cell potency

The whole-cell potencies of complexes from the six discussed chemical modifications against *Plasmodium falciparum* (*Pf)* are summarized in **Figure 6.1**. The 4,4'-di-*tert*-butyl analog (**4a.1**) was considered the parent complex within this series, to which the whole-cell potency of the other derivatives was compared. For **SAR1**, whole-cell potency was increased by the presence of an electron-donating substituent in the 4,4'-position of the bipyridine. Additionally, replacing the bulky hydrophobic *tert*-butyl substituent with an amine substituent improved whole-cell potency four-fold against both the *Pf*-NF54 and *Pf*-K1 strains.

The main attribute of the **SAR2** complexes was the increased susceptibility of the multidrug-resistant *Pf*-K1 strain to complexes with a methyl and methoxy substituent in the *para*-position of the phenyl ring. These potencies suggest that the electron properties of the attached

substituent, as opposed to hydrophobicity, may be driving bioactivity within these two series of platinum(II) complexes.

For **SAR3**, whole-cell potency against *Pf*-NF54 and *Pf*-K1 was favored when the position of the methyl substituent on bipyridine was switched from 4,4'-substitution to 5,5'-substitution. This is possibly due to its interaction and binding with its target biomolecule which may be influenced by the position of the substituent.

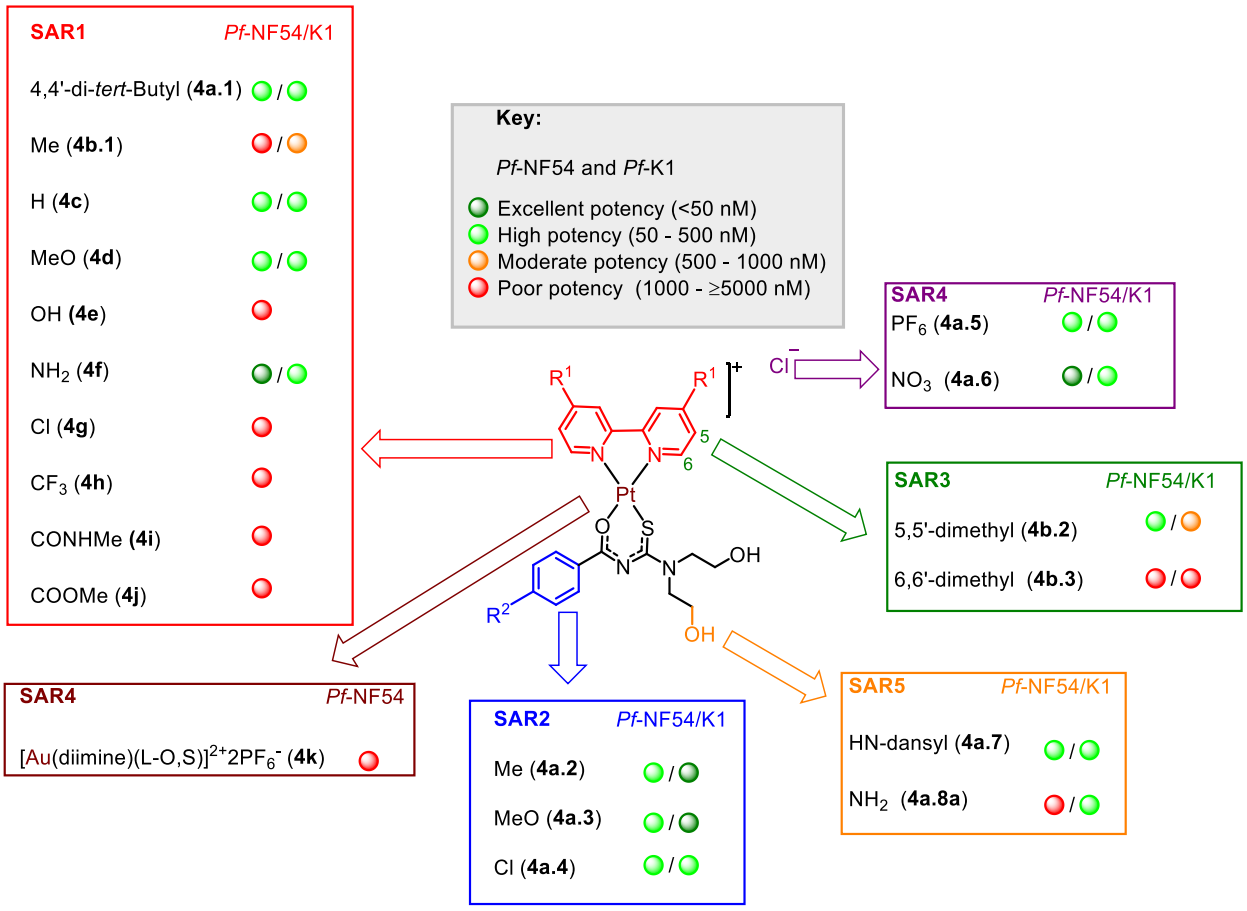

Figure 6.1. A pictorial representation summarizing the whole-cell potency of the synthesized transition metal complexes against *Pf*-NF54 and *Pf*-K1 strains. The provided key is used as a scale to gauge potency according to their IC_{50} values.

The exchange of the chloro counterion (**4a.1**) for a nitrate counterion (**4a.6**) in **SAR4** was also highly favored against the *Pf*-NF54 and *Pf*-K1 strains for the *tert*-butyl analog. There are no reports comparing the antiplasmodium potency between transition metal complexes with a

chloro and nitrate counterion in the literature, but factors such as lipophilicity can affect its potency.

From the SAR5, the hydroxy group (**4a.1**) is more beneficial on the terminal end of the ethylamine chains than an amino (**4a.8a**) functionality, as **4a.8a** is less potent than **4a.1** against both tested strains.

The final chemical modification involved replacing the platinum(II) center with gold(III) (**4k**). The change in transition metal ultimately resulted in the formation of a gold(III) species with a 2+ charge that was 25-fold less potent than the platinum(II) species. However, the speciation of the gold(III) analog in water (discussed in **Chapter 2**, **Section 2.3.6**) may also result in the lower whole-cell potency that was exhibited by **4k**, as the whole-cell assay is conducted in aqueous medium.

Gametocyte activity

Potency against gametocytes was highly dependent on the presence of the bulkier more hydrophobic *tert*-butyl or trifluoromethane substituent on the bipyridine ligand. Thus, within the series, seven complexes exhibited early-stage and/or late-stage gametocyte activity. Additionally, six of the seven complexes displayed dual-stage activity, although only the SAR2 complexes **4a.2** (R^2 = Me) and **4a.3** (R^2 = MeO) exhibited sub-micromolar potency against late-stage gametocytes.

Cytotoxicity and aqueous solubility

Platinum complexes such as cisplatin and carboplatin are known for their cytotoxicity.[351,352] To confirm that the whole-cell potency of the synthesized platinum(II) complexes was not a consequence of a general cytotoxic effect exhibited by the compounds, their cytotoxicity was evaluated against the Chinese hamster ovarian (CHO) cell line. In summary, there were subtle differences in cytotoxicity between the six series but in general, most of the complexes were selective to the *Pf* parasite with selectivity indices (SI) above 50.

In general, the SAR1 complexes were also highly soluble with aqueous solubilities at pH 6.5 above 95 µM. Furthermore, no obvious trends were seen between the substituents and their solubilities. SAR2 complexes with a Me (**4a.2**) and MeO (**4a.3**) as R^2 were very potent against *Pf*-K1 but showed negligible solubility below 5 µM, despite being very potent against *Pf*-K1. Interestingly, the addition of the electron-withdrawing Cl substituent (**4a.4**) in the *para*-position

resulted in improved whole-cell potency (three-fold) and improved solubility of 150 μM compared to **4a.1**.

Microsomal metabolic stability

A range of microsomal metabolic stabilities was observed for the tested compounds in the presence of human liver microsomes (HLM) and mouse liver microsomes (MLM) as shown in **Figure 6.2**. All analogs with a *tert*-butyl substituent on the bipyridine ligand displayed poor microsomal metabolic stabilities in the presence of microsomes from both species with the percentage of compound remaining after 30 minutes of incubation ≤51%. Overall, none of the complexes displayed metabolic stability above 75% (preferred cut-off) in the presence of HLMs.

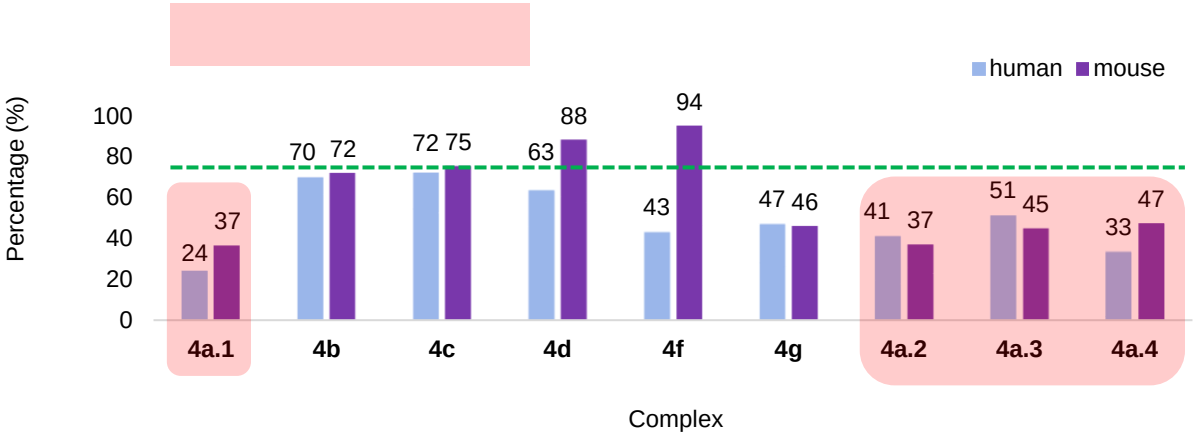

Figure 6.2. Bar graph showing a summary of the microsomal metabolic stabilities of tested complexes as a measure of the percentage of compound remaining after 30 minutes of incubation in human or mouse liver microsomes. The dashed line represents the 75% cut-off and the compounds highlighted in red contained a tert-butyl substituent on the bipyridine.

Pharmacokinetics (PK), permeability and plasma protein binding (PPB) of frontrunner complex, 4f

The *in vivo* PK analysis of **4f** (R^1 = NH_2) indicated that the complex had a low volume of distribution, moderate clearance, and low bioavailability, as seen in **Figure 6.3**. Further analysis of **4f** showed that these poor PK properties may correlate with high PPB (99%) which corresponds with its low volume of distribution and moderate clearance. Additionally, the complex was highly permeable and soluble, suggesting that the poor bioavailability is likely a result of the high PPB and phase II metabolism.

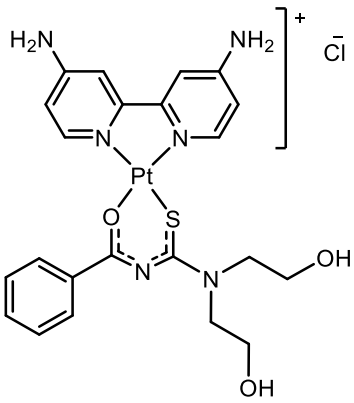

Pharmakonetics parameters

V_{ss} (mL/kg) i.v.	= 45.6
CL_s (mL/min/kg) i.v.	= 46.4
$t_{1/2}$ (h) p.o./i.v.	= 12.0/10.8
Bioavalability (%) p.o.	= 3.8

Figure 6.3. Structure of complex **4f** and summary of its PK parameters.

6.1.2. Mechanistic studies

To gain mechanistic insights into the synthesized complexes, several experiments were conducted as discussed in **Chapter 4**. Comparable to compounds of a similar structure reported in the literature,[180] complexes **4a.1** displayed the ability to self-associate in MeOH as was shown by the concentration-dependent ^{1}H-NMR spectroscopy experiment in **Chapter 4**, **Section 4.2**. This self-association was proposed to result from the intermolecular aggregation of the platinum(II) compounds with each other through π-π stacking interactions.

Subsequently, the inhibition of β-hematin formation activities of the complexes were evaluated in the extracellular NP-40 detergent-mediated assay. In general, the inhibition of β-hematin formation activities of the complexes were comparable or superior to those of the positive control drug, chloroquine (CQ). Additionally, no correlation was observed between their whole-cell potencies, kinetic solubilities, and inhibition of β-hematin formation activities. These results contrasted with the original Egan *et al.* study, in which the parent complex was determined not to inhibit β-hematin formation (possibly as a result of the different detection methodology used). Furthermore, the two selected complexes did not exhibit a dose-dependent inhibition

of hemozoin formation within the parasite; thus, contrary to the initial hypothesis, they do not share the MoA of quinolines, despite their ability to partake in π-π stacking interactions.

Genomic approach

Resistance selection experiments using the *tert*-butyl (**4a.1**) or amine (**4f**) analogs and the *Pf*-Dd2 strain resulted in a low frequency of resistance in which recrudescence only occurred in one flask (3 x IC_{50} of **4f**) out of the six that were being pressured. This suggests a lower likelihood of resistance occurring for this scaffold, given that recrudescence also only occurred for one of the two compounds. Furthermore, cloning by limiting dilution isolated four monoclonal populations with the most resistant clone (**G7**) having a resistance index of 21 and 6.5 against complexes **4f** and **4a.1**, respectively.

WGS identified several copy number variations (CNVs) and single-nucleotide polymorphisms (SNPs) which were likely responsible for the clones' resistant phenotypes. The most noticeable CNV corresponded to the amplification of the well-known *pfmdr1* gene. For the most resistant clone, **G7**, a SNP in the kinesin-13 gene was unique to this clone and is thus likely responsible for its MoR.

Since the amplification in the *pfmdr1* gene was common to three of the four clones and the kinesin-13 SNP only occurred in one clone, they could not be conclusively linked to the MoA. This does not necessarily indicate that kinesin-13 is not a molecular target, but further target identification and validation experiments are necessary. It is also possible that these complexes target a novel biomolecule(s) or act via polypharmacology that could include kinesin-13.

6.2. Overall conclusions

A range of whole-cell potencies was displayed in which an amine in the 4,4'-position of the bipyridine resulted in favorable potency and drug-like properties. Furthermore, the exchange of a chloro counterion to a nitrate in the *tert*-butyl analog had the most significant positive influence on potency against *Pf*-NF54. Overall, the **SAR2** complexes exhibited the most favorable whole-cell potencies as their IC_{50} values against the multidrug-resistant *Pf* -K1 strain were in the low nanomolar range (below 30 nM) and their late-stage gametocyte activity was below 500 nM. Therefore, these complexes had the most ideal dual-stage potencies within all six series. However, they did exhibit low solubility (below 5 μM) and poor microsomal metabolic stabilities in MLM and HLM (below 51%). Furthermore, these complexes did not act via the hypothesized pathway of inhibiting hemozoin formation but with the assistance of resistance selections and whole-genome sequencing, a possible novel target (kinesin-13) was identified.

6.3. Future work

6.3.1. Synthesis

For this thesis, efforts were made to explore the chemical space of these metal complexes by varying substitutions at various attachment points, but further modifications can also be explored. A summary of further proposed chemical modifications is shown in **Figure 6.4**. Replacing a *tert*-butyl substituent with a trifluoromethyl-cyclopropyl substituent has been shown to improve microsomal metabolic stability in the literature.[266] This would therefore be an appropriate start to synthesizing a complex with improved metabolic stability (**Figure 6.5**, **C**) as many of the *tert*-butyl analogs displayed low IC_{50} values with dual-stage activity, such as those from **SAR2** (R^2 = Me, MeO, and Cl). Additionally, concerning the **SAR2** complexes, inserting a water-solubilizing substituent (e.g. MeO, amine, carboxylic acid) in the R^1 position with a MeO and Me in the R^2 position (**Figure 6.5**, **B**) can be explored to improve the aqueous solubility of these complexes. Furthermore, considering the SAR3 analog (5,5-dimethyl) the synthesis of derivatives with an NH_2 or *tert*-butyl substituent in the 5,5'-position of the bipyridine should be explored.

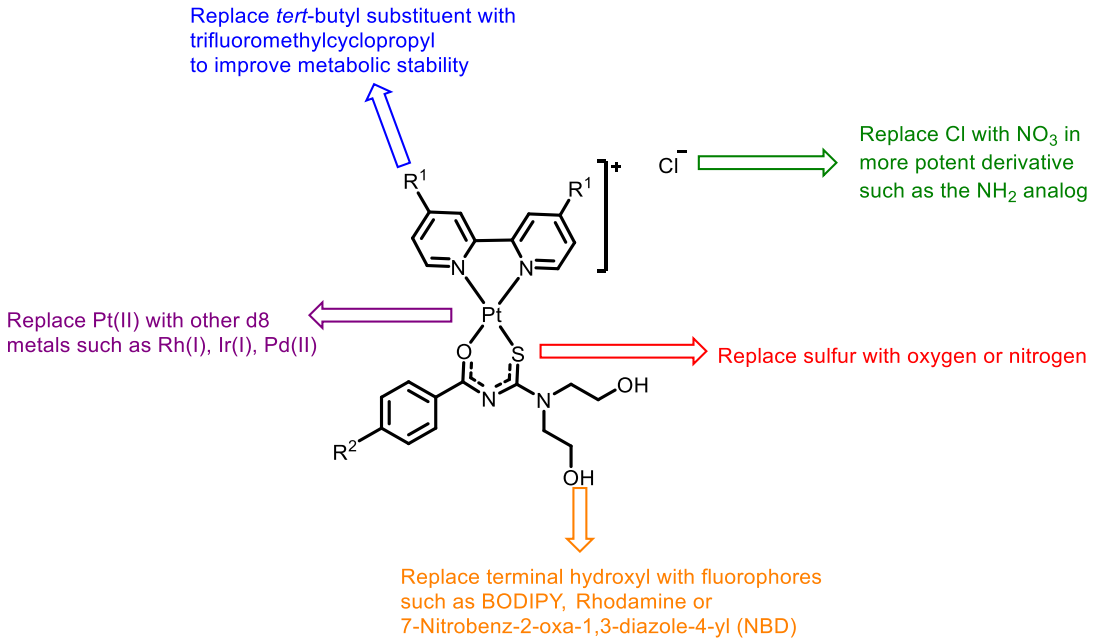

Figure 6.4. Summary of the proposed future chemical modifications to further explore the SAR of the reported series of complexes.

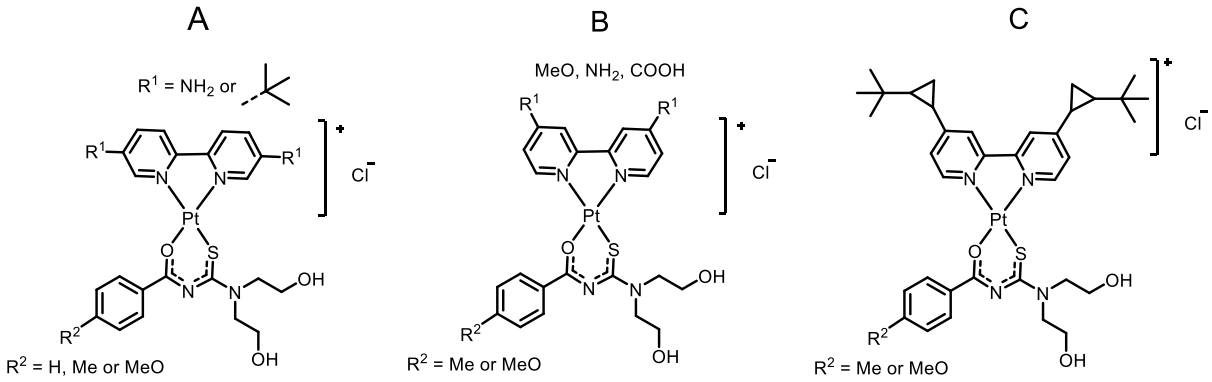

Figure 6.5. Proposed derivatives of the most potent analogs to be synthesized in future to improve whole-cell potency and drug-like properties.

Conducting counterion exchanges between chloride and nitrate for the more potent amine analog and the other derivatives could be insightful in identifying the role of the nitrate counterion. This may also be interesting as there are no reports on the biological role of these counterions in the literature.

Since the gold(III) derivative **4k** maintained the square platinum geometry of the platinum(II) parent but displayed a significant decrease in whole-cell potency, additional d^8 metal centers

can be explored. These would include iridium(I), rhodium(I), and palladium(II), which would still maintain the square planar geometry around the metal center but may contribute favorably to the whole-cell potency through varying electronic, physicochemical, and stability (metabolic and aqueous) properties.

Additionally, replacing the sulfur in the acyl thiourea ligand with either oxygen or nitrogen is another change worth exploring. These subtle changes could affect the overall properties of the formed metal species as they affect the metal-ligand interactions and therefore possible ligand exchange reactions.[353]

Lastly, further attempts can be made to synthesize a fluorescent probe to study the intracellular localization of this chemical series. This could include attempting the synthesis of a Bodipy-containing derivative or reattempting the synthesis of an NBD- or rhodamine-containing derivative. For the NBD and rhodamine derivatives, alternative synthetic routes that are reported in the literature[354–358] could be attempted as shown in **Figure 6.6**. These methods mainly include changing the base and/or the solvent used in the reaction compared to those attempted in **Chapter 2**, **Section 2.3.7**.

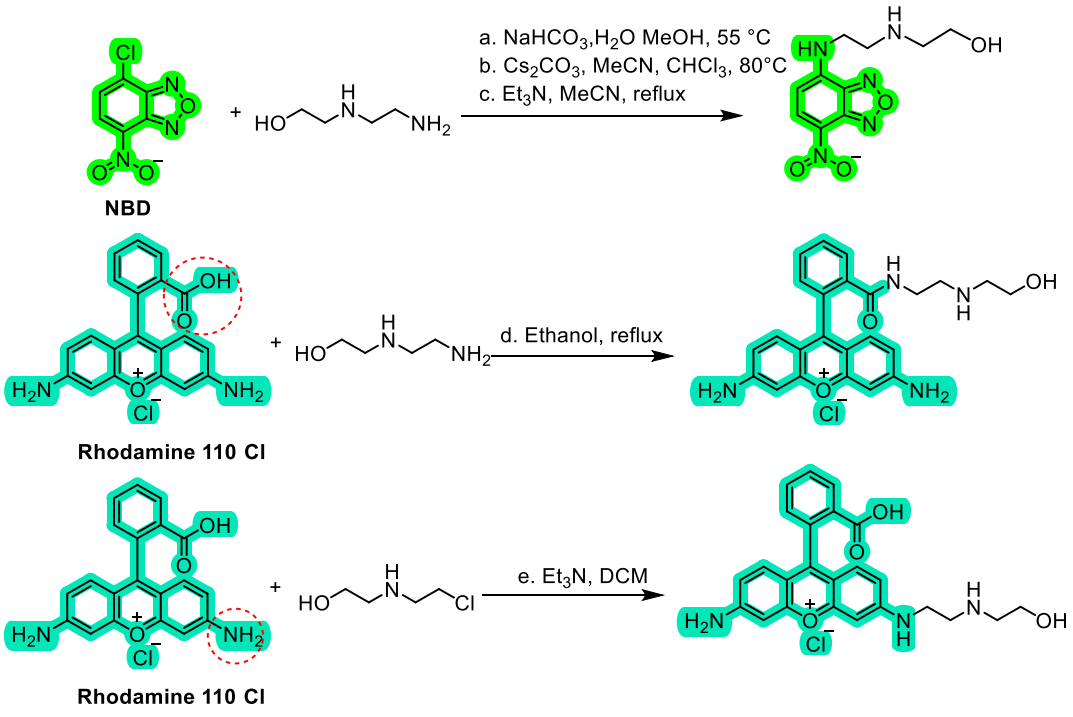

Figure 6.6. Alternative reaction conditions to attempt the synthesis of NBD or rhodamine-containing fluorescent probes. The red circles on rhodamine indicate the reacting group.

Additionally, NBD, rhodamine, and BODIPY can be excited at a less photodamaging wavelength (lower energy of 480 nm to 511 nm) than the dansyl reporter discussed in **Chapter 4**. Determining the cellular localization of the synthesized series can assist in identifying the target organelles and/or biomolecule(s) of these complexes. For example, should these complexes partially act via the inhibition of heme synthesis in the mitochondrion, they would be expected to accumulate there.

To further evaluate the factors that contribute to the whole-cell potency displayed by the synthesized series, several additional experiments can also be conducted. These include evaluating the lipophilicity of all the synthesized complexes using a shake-flask method involving water and octanol. This will assist in determining if lipophilicity influences whole-cell potency of the analogs with different counterions. Additionally, the permeability of the other analogs (only the permeability of **4f** is reported here), including those with a hexafluorophosphate and nitrate counterion, can be determined. This can be used to evaluate if permeability contributes to the significant increase in whole-cell potency exhibited by the nitrate *tert*-butyl analog compared to the chloro *tert*-butyl parent. Lastly, following the microsomal metabolic stability studies, metabolites can be identified. This will highlight the metabolic hot spots and compounds can then rationally be designed to block the sites of metabolism.

6.3.2. Mechanistic studies

Despite the original hypothesis that these complexes should inhibit hemozoin formation, they were found not to do so. Thus, additional assays and experiments are required to probe their MoA. Based on the MoA of other square planar platinum complexes such as cisplatin, DNA binding experiments can be conducted for the complexes synthesized herein. Additionally, protein pull-down experiments coupled with mass spectrometry to identify possible protein targets can be conducted. Since kinesin-13 was shown to be a MoR in the resistance selection studies, it can be evaluated as a possible target by conducting biochemical assays or screening against kinesin-13 conditional knockdown lines that investigate the capacity of the complexes to inhibit kinesin-13 *in vitro*.

Furthermore, based on the capacity of these complexes to inhibit βH formation extracellularly, it may be worthwhile to determine the extent of hematin (free heme, ferriprotoporphyrin IX (Fe(III)PPIX)) association. The binding strengths of the complexes to Fe(III)PPIX can be compared using their binding constants. This is important as there have been reports that the heme needed by the parasite for metabolic function is synthesized in its mitochondrion instead

of sourced from host hemoglobin.[359] As a future experiment, it may be interesting to further investigate the intracellular localization of these complexes and determine if they accumulate in the parasite mitochondrion, interfering with the heme biosynthesis pathway.

Additionally cell morphology studies can be conducted in which the parasites can be treated with a platinum(II) analog at the ring stage and the effect on morphology can be observed using Giemsa stained smears observed under a microscope. This experiment can be informative with regards to the stage specificity of the tested complex.

Following the resistance selection studies, several additional experiments can also be conducted using the isolated clones and several of the other platinum(II) analogs. These include profiling the remaining platinum(II) analogs against the isolated **G7** clone to determine if they share cross-resistance which could suggest a shared MoR amongst the analogs. The fitness cost of the **4f**-resistant mutants can be determined using a competitive growth assay. A MIR (minimum inoculum of resistance) study can also be conducted using compound **4f** to determine the risk of resistance.

Furthermore, to validate kinesin-13 as a possible molecular target for future drug design, genomic editing could be attempted using the CRISPR/Cas9 editing tools in which the kinesin-13 resistant mutation can be introduced. If successful, the transfectant *Plasmodium* parasites could be selected for using the compound WR99210, a known antagonist of the *Pf* folate pathway. It is now widely used for the selection of *Plasmodium* transfectants, as it selectively targets the *Plasmodium* dihydrofolate reductase thymidine synthase bifunctional enzyme (DHFR-TS) over the human one. Additionally, untransformed species of *Plasmodium* are sensitive to low doses of WR99210 allowing for the selection of transfectant lines.[360] Subsequently, the whole-cell potency of the test compounds (**4f** and derivatives) can be determined against the edited and control parasite lines to evaluate if kinesin-13 is primarily responsible for the resistance phenotype.

Towards addressing the devasting impact that malaria has had on the African continent, and for which drug resistance has been the major inhibiting factor to the extensive efforts made to control and eradicate the disease, this thesis emphasizes the advantages of metal complexes as novel chemotherapeutic agents. This thesis brings to light the potential of metal complexes to meet the main objectives of contemporary antimalarial drug discovery, i.e. combating resistance, finding compounds with multi-stage activity, and identifying those that act against novel targets. In this work, several compounds were identified with dual-stage activity that act against the *Pf*-K1 strain with potency in the low nanomolar range. Mechanistic studies coupled with resistance selection experiments suggest that these complexes may act via a novel MoA.

Chapter 7: Experimental Procedures

7.1. Chapter overview

In this chapter, the synthetic methods and protocols for biological assays used in this thesis are described. This chapter lists the synthetic reaction conditions, characterization data, and biological assay conditions that support the data provided in the preceding chapters. First, a full description of the reagents and reaction conditions for each synthesized compound is outlined, followed by their spectroscopic characterization data. This is followed by the biological assay protocols, including culture conditions, microscopy, and resistance selections, and the protocols of the physiochemical assays used to determine the solubility, metabolic microsomal stability, pharmacokinetic, permeability, and plasma protein binding parameters of the compounds. Culturing of and assays involving Plasmodium parasites were carried out according to safety protocols defined by UCT's Science Faculty & Institutional Biosafety Committees and the Faculty of Health Science Human Research Ethics Committee protocol HREC 890/2019

7.2. Chemistry

7.2.1. Reagents and solvents

All commercially available reagents were purchased from Merck (South Africa, SA), FluoroChem (UK), and Combi-Blocks (USA). Anhydrous solvents such as dimethylformamide (DMF), tetrahydrofuran (THF), and acetonitrile (MeCN) were purchased from Merck (SA). The analytical reagents (AR grade) solvents such as absolute ethanol (EtOH), methanol (MeOH), ethyl acetate (EtOAc), *n*-hexane, *n*-pentane, dichloromethane (DCM), and acetone were purchased from either Protea Chemicals Pty Ltd (SA) and or KIMIX. All high-performance liquid chromatography (HPLC) grade solvents (ammonium acetate, DMSO, MeCN, and MeOH) were also purchased from Merck (SA) and/or Microsep.

7.2.2. Spectroscopic and analytical methods

All reactions were either monitored via thin-layer chromatography (TLC) in which aluminium backed, precoated silica-gel 60 F254 plates (Merck) was used, or it was monitored via HPLC-MS. TLC plates were observed under ultraviolet light at 254 nm. All synthesized compounds were dried under a high vacuum. All solvents used for NMR spectroscopy analysis were deuterated and were purchased from Merck. Where purification was carried out via reverse-

phase column chromatography, it was done so using a C-18 (10g or 25g cartridge) Biotage column. Nuclear magnetic resonance (NMR) spectra were recorded on Bruker Topsin GmbH 600 MHz (^{1}H at 600.22 MHz; ^{13}C at 100.65 MHz) or Varian Mercury 300 (^{1}H at 300.08 MHz at ^{13}C at 75.46 MHz) spectrometers, equipped with a Bruker Biospin GmbH casing and sample injector at 30 °C. Chemical shifts and *J*-coupling constants are reported in ppm and Hz, respectively. NMR spectra were recorded using either deuterated dimethyl sulfoxide (DMSO-d_6), deuterated dichloromethane (CD_2Cl_2), deuterated methanol (MeOD-d_4), or a mixture of deuterium oxide (D_2O) and deuterated acetonitrile (CD_3CN). Where ^{1}H-NMR and ^{13}C-NMR spectral data are not provided, compounds were not soluble at appropriate concentrations to obtain a spectrum of representable resolution. Where compounds were intermediates, they were taken forward to subsequent reactions without further characterization, and where possible, HPLC-MS data are provided to attest to the identity and purity of the compounds.

7.2.3. Synthesis and characterization

7.2.3.1. General procedure for the synthesis of acyl thiourea ligands 1a-1d[179]

To a 50-mL round bottom flask (RBF) equipped with a magnetic stirrer and septum with a needle connected to a balloon containing nitrogen, the relevant benzoyl isothiocyanate (1 eq.) followed by anhydrous DCM (2 mL) was added. The mixture was cooled in an ice-water bath to 0 °C. Diethanolamine (1 eq.) in anhydrous DCM (2 mL) was added slowly over 15 minutes. The ice-water bath was removed, and the reaction mixture was allowed to stir under nitrogen for 4-20 hours. The resulting precipitate was collected using suction filtration and washed with cold DCM.

N-(bis(2-hydroxyethyl)carbamothioyl)benzamide (1a)

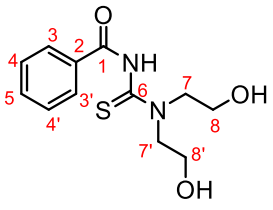

Chemical Formula: $C_{12}H_{16}N_2O_3S$
Exact Mass: 268.09
Molecular Weight: 268.33

Benzoyl isothiocyanate (1.00 mL, 7.44 mmol, 1 eq.) and diethanolamine (1.10 mL, 7.44 mmol, 1 eq.) were stirred at ambient temperature (25 °C) for 20 hours. Refer to the general procedure in **Section 7.2.3.1** for the reaction conditions. Compound **1a** was isolated as a beige solid. Yield: 1.66 g, 83%; ^{1}H-NMR (600 MHz, MeOD-d_4) δ 7.88 (d, *J* = 8.5 Hz, 2H, H-3,3'), 7.57 (t, *J* = 8.1 Hz, 1H, H-5), 7.47 (t, *J* = 7.9 Hz, 2H, H-4,4') 4.06 (t, *J* = 6.0 Hz, 2H, H-7), 3.96 (t, *J* = 6.0 Hz, 2H, H-7'), 3.84 (br s, 4H, H-8,8'); HPLC-MS (ESI): Purity = 98%, t_R = 0.387 min, *m/z* $[M-H]^+$ = 267.0, calculated mass $[M-H]^+$ = 267.3.

_N_-(bis(2-hydroxyethyl)carbamothioyl)-4-methylbenzamide (1b)

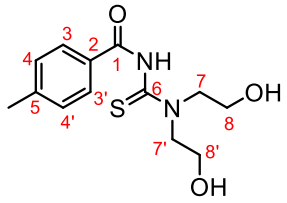

Chemical Formula: $C_{13}H_{18}N_2O_3S$
Exact Mass: 282.10
Molecular Weight: 282.36

4-Methylbenzoyl isothiocyanate (0.100 mL, 0.654 mmol, 1 eq.) and diethanolamine (1.100 mL, 0.654 mmol, 1 eq.) were stirred at ambient temperature (25 °C) for 20 hours. Refer to the general procedure in **Section 7.2.3.1** for the reaction conditions. Compound **1b** was isolated as a beige solid. Yield: 139 mg, 75%; ^{1}H-NMR (300 MHz, MeOD-d_4) δ 7.89 (d, J = 8.3 Hz, 2H, H-3,3'), 7.03 (d, J = 7.9 Hz, 2H, H-4,4'), 4.07 (t, J = 5.8 Hz, 2H, H-7), 3.99 (t, J = 5.6 Hz, 2H, H-7'), 3.88 (s, 7H, H-8,8', C$\underline{H}_3$). HPLC-MS (ESI): Purity = 98%, t_R = 0.702 min, m/z $[M+H]^+$ = 283.1, calculated mass $[M+H]^+$ = 283.4.

N-(bis(2-hydroxyethyl)carbamothioyl)-4-methoxybenzamide (1c)

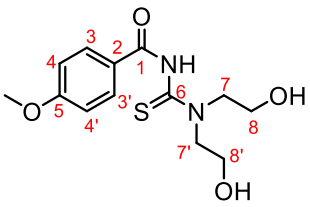

Chemical Formula: $C_{13}H_{18}N_2O_4S$
Exact Mass: 298.10
Molecular Weight: 298.36

4-Methoxybenzoyl isothiocyanate (0.100 mL, 0.641 mmol, 1 eq.) and diethanolamine (0.060 mL, 0.641 mmol, 1 eq.) were stirred at ambient temperature (25 °C) for 20 hours. Refer to the general procedure in **Section 7.2.3.1** for the reaction conditions. Compound **1c** was isolated as an off-white solid. Yield: 136 mg, 76%; ^{1}H-NMR (300 MHz, MeOD-d_4) δ 7.81 (d, J = 9.0 Hz, 2H, H-3,3'), 7.33 (d, J = 9.0 Hz, 2H, H-4,4'), 4.08 (t, J = 5.7 Hz, 2H, H-7), 4.00 (t, J = 5.6 Hz, 2H, H-7'), 3.87 (br s, 4H, H-8,8') 2.42 (s, 3H, C$\underline{H}_3$O). HPLC-MS (ESI): Purity = 97%, t_R = 0.654 min, m/z $[M+H]^+$ = 299.1, calculated mass $[M+H]^+$ = 299.4.

N-(bis(2-hydroxyethyl)carbamothioyl)-4-chlorobenzamide (1d)

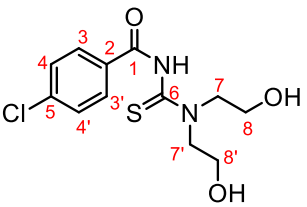

Chemical Formula: $C_{12}H_{15}ClN_2O_3S$
Exact Mass: 302.05
Molecular Weight: 302.77

4-Chlorobenzoyl isothiocyanate (204 mg, 1.03 mmol, 1 eq.) and diethanolamine (0.100 mL, 1.03 mmol, 1 eq.) were stirred at ambient temperature (25 °C) for 4 hours. Refer to general procedure in **Section 7.2.3.1** for reaction conditions. Compound **1d** was isolated as an off-white solid (289 mg, 92%). Crude yield: 279 mg, 89%.

7.2.3.2. Condensation reactions of [2,2'-bipyridine]-4,4'-dicarboxylic acid

*N*4,*N*4'-dimethyl-[2,2'-bipyridine]-4,4'-dicarboxamide (2a)

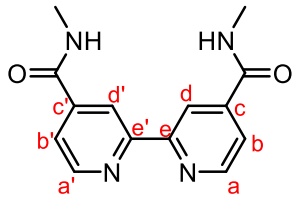

Chemical Formula: $C_{14}H_{14}N_4O_2$
Exact Mass: 270.11
Molecular Weight: 270.29

Triethylamine (51.7 µL, 3.71 mmol, 4 eq.) was added to a solution of [2,2'-bipyridine]-4,4'-dicarboxylic acid (226 mg, 0.928 mmol, 1 eq.) in DMF (5 mL). The solution was stirred for 15 minutes before adding HATU (1.41 g, 3.71 mmol, 4 eq.). The solution was allowed to stir for a further 30 minutes. Methylamine in THF (2 M, 1.86 mL, 3.71 mmol, 4 eq.) was added and the reaction mixture was stirred at ambient temperature (25 °C) for 2 hours. The DMF was reduced using rotary evaporation after which MeOH (~5 mL) was added. Compound **2a** was collected using suction filtration and washed with MeOH. Compound **2a** was isolated as an off-white solid. Yield: 225 mg, 90%; ^{1}H-NMR (400 MHz, DMSO-*d*$_6$) δ 8.90 (d, *J* = 4.8 Hz, 2H, NH), 8.87 (d, *J* = 5.0 Hz, 2H, H-a,a'), 8.79 (s, 2H, H-d,d'), 7.85 (dd, *J* = 1.8 Hz, 5.0 Hz, 2H, H-b,b'), 2.85 (d, *J* = 4.5 Hz, 6H, CH_3). HPLC-MS (ESI): Purity = 99%, t_R = 0.598 min, *m*/*z* $[M+H]^+$ = 271.1, calculated mass $[M+H]^+$ = 271.3.

Dimethyl [2,2'-bipyridine]-4,4'-dicarboxylate (2b)

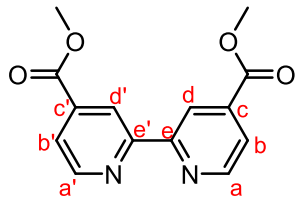

Chemical Formula: $C_{14}H_{12}N_2O_4$
Exact Mass: 272.08
Molecular Weight: 272.26

Triethylamine (34.7 µL, 2.49 mmol, 4 eq.) was added to a solution of [2,2'-bipyridine]-4,4'-dicarboxylic acid (304 mg, 1.24 mmol, 1 eq.) in MeOH (5 mL). The solution was stirred for 15 minutes before adding HATU (1.89 g, 2.49 mmol, 4 eq.). The reaction mixture was stirred at 50 °C for 24 hours. The resulting precipitate was collected using suction filtration. Compound **2b** was isolated as a white solid. Yield: 283 mg, 84%; ^{1}H-NMR (300 MHz, DMSO-*d*$_6$) δ 8.93 (d, *J* = 4.9 Hz, 2H, H-a,a'), 8.86 (s, 2H, H-d,d'), 7.92 (dd, *J* = 1.6 Hz, 5.0 Hz, 2H, H-b,b'), 3.31 (s, 6H, CH_3). HPLC-MS (ESI): Purity = 97%, t_R = 1.003 min, *m*/*z* $[M+H]^+$ = 273.1, calculated mass $[M+H]^+$ = 273.3.

7.2.3.3. General synthesis of [$PtCl_2$(diimine)] complexes (3a-3j)[203]

To a stirring solution of potassium tetrachloroplatinate (1 eq.) dissolved in H_2O (2 mL), the appropriate diimine (1 eq.) was added. The solution was either left unchanged or acidified with HCl (1 mL, 4 M). The mixture was allowed to reflux for either 2 hours or 18 hours and the resulting powder was collected via suction filtration. The product was washed with water and dried under a vacuum. Where the crude product was isolated, no spectral analysis was done, and the crude product was used in the next step (**3f** and **3j**). Where the product was insoluble in the available deuterated solvents (**3c**), the compound was also taken forward to the next synthetic step. These [$PtCl_2$(diimine)] complexes did not ionize on the HPLC-MS and therefore their purity and ionization mass data are not provided, hence their yields are reported as crude (**3b.1-3j**).

4,4'-Di-*tert*-butyl-2,2'-bipyridyldichloroplatinum(II) (3a)

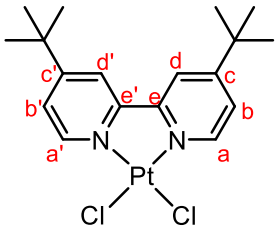

Chemical Formula: $C_{18}H_{24}Cl_2N_2Pt$
Exact Mass: 533.10
Molecular Weight: 534.39

4,4'-Di-*tert*-butyl-2,2'-dipyridyl (70.2 mg, 0.259 mmol, 1 eq.) was added to a stirring solution of potassium tetrachloroplatinate (108 mg, 0.259 mmol, 1 eq). Refer to the general procedure in **Section 7.2.3.3** for the reaction conditions. Crude yield: 65 mg, 47%; ^{1}H-NMR (600 MHz, CD_2Cl_2) δ 9.51 (d, *J* = 6.2 Hz, 2H, H-a,a'), 7.91 (d, *J* = 2.2 Hz, 2H, H-d,d'), 7.56 (dd, *J* = 6.3 Hz, 2.2 Hz, 1H, H-b,b'), 1.45 (s, 18H, $(CH_3)_3$); HR-ESI MS: (*m/z*) $[M+Cl]^+$ = 569.06, calculated mass $[M+Cl]^+$ = 569.84.

4,4'-Dimethyl-2,2'-bipyridyldichloroplatinum(II) (3b.1)

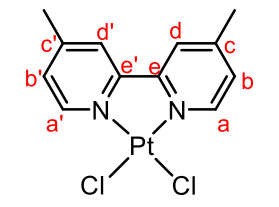

Chemical Formula: $C_{12}H_{12}Cl_2N_2Pt$
Exact Mass: 449.00
Molecular Weight: 450.23

4,4'-Dimethyl-2,2'-bipyridine (166 mg, 0.900 mmol, 1 eq.) was added to a stirring solution of potassium tetrachloroplatinate (374 mg, 0.900 mmol, 1 eq.). Refer to the general procedure in **Section 7.2.3.3** for the reaction conditions. Crude yield: 256 mg, 63%;^{1}H-NMR (300 MHz, DMSO-d_6) δ 9.22 (d, *J* = 6.2 Hz, 2H, H-a,a'), 8.43 (s, 2H, H-d,d'), 2.55 (d, *J* = 6.0 Hz, 2H, H-b,b').

5,5'-Dimethyl-2,2'-bipyridyldichloroplatinum(II) (3b.2)

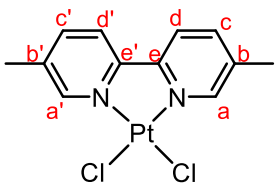

Chemical Formula: $C_{12}H_{12}Cl_2N_2Pt$
Exact Mass: 449.00
Molecular Weight: 450.23

5,5'-Dimethyl-2,2'-bipyridine (79.7 mg, 0.433 mmol, 1 eq.) was added to a stirring solution of potassium tetrachloroplatinate (180 mg, 0.433 mmol, 1 eq.). Refer to the general procedure in **Section 7.2.3.3** for the reaction conditions. Crude yield: 105 mg, 54%; ^{1}H-NMR (300 MHz, DMSO-d_6) δ 9.24 (d, J = 2.1 Hz, 2H, H-a,a'), 8.41 (d, J = 8.3 Hz, 2H, H-d,d'), 8.22 (dd, J = 2.0 Hz, 8.3 Hz, 2H, H-c,c'), 2.55 (s, 6H, CH_3).

6,6'-Dimethyl-2,2'-bipyridyldichloroplatinum(II) (3b.3)

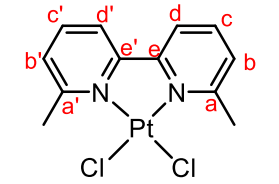

Chemical Formula: $C_{12}H_{12}Cl_2N_2Pt$
Exact Mass: 449.00
Molecular Weight: 450.23

6,6'-Dimethyl-2,2'-bipyridine (84.1 mg, 0.456 mmol, 1 eq.) was added to a stirring solution of potassium tetrachloroplatinate (189 mg, 0.456 mmol, 1 eq.). Refer to the general procedure in **Section 7.2.3.3** for .the reaction conditions. Crude yield: 143 mg, 69%; ^{1}H-NMR (300 MHz, DMSO-d_6) δ 8.17 (d, J = 7.9 Hz, 2H, H-b,b'), 7.80 (t, J = 7.7 Hz, 2H. H-c,c'), 7.29 (d, J = 7.6 Hz, 2H, H-d,d'), 2.55 (s, 6H, CH_3).

2,2'-Bipyridyldichloroplatinum(II) (3c)

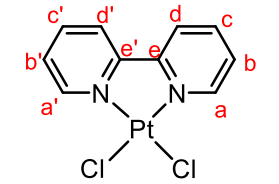

Chemical Formula: $C_{10}H_8Cl_2N_2Pt$
Exact Mass: 420.97
Molecular Weight: 422.17

2,2'-Bipyridine (339 mg, 2.17 mmol, 1 eq.) was added to a stirring solution of potassium tetrachloroplatinate (905 mg, 2.17 mmol, 1 eq). Refer to the general procedure in **Section 7.2.3.3** for the reaction conditions. Crude yield: 846 mg, 92%.

4,4'-Dimethoxy-2,2'-bipyridyldichloroplatinum(II) (3d)

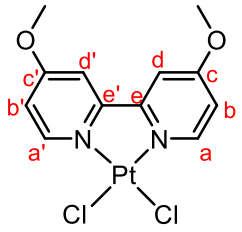

Chemical Formula: $C_{12}H_{12}Cl_2N_2O_2Pt$
Exact Mass: 480.99
Molecular Weight: 482.22

4,4'-Dimethoxy-2,2'-bipyridine (81.2 mg, 0.371 mmol, 1 eq.) was added to a stirring solution of potassium tetrachloroplatinate (154 mg, 0.371 mmol, 1 eq.). Refer to the general procedure in **Section 7.2.3.3** for the reaction conditions. Crude yield: 150 mg, 84%; ^{1}H-NMR (400 MHz, DMSO-d_6) δ 9.14 (d, J = 6.8 Hz, 2H, H-a,a'), 8.19 (d, J = 2.9 Hz, 2H, H-d,d'), 7.41 (dd, J = 2.8 Hz, 7.1 Hz, 2H, H-b,b'), 4.06 (s, 6H, CH_3).

4,4'-Dihydroxy-2,2'-bipyridyldichloroplatinum(II) (3e)

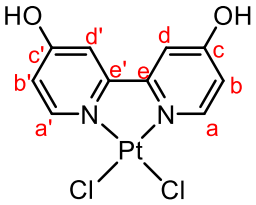

Chemical Formula: $C_{10}H_8Cl_2N_2O_2Pt$
Exact Mass: 452.96
Molecular Weight: 454.17

4,4'-Dihydroxy-2,2'-bipyridine (114 mg, 0.605 mmol, 1 eq.) was added to a stirring solution of potassium tetrachloroplatinate (251 mg, 0. 605 mmol, 1 eq). Refer to the general procedure in **Section 7.2.3.3** for the reaction conditions. Crude yield: 245 mg, 89%; ^{1}H-NMR (400 MHz, DMSO-d_6) δ 9.04 (d, J = 7.1 Hz, 2H, H-a,a'), 7.75 (d, J = 3.5 Hz, 2H, H-d,d'), 7.12 (dd, J = 3.5 Hz, 8.0 Hz, 1H, H-b,b').

4,4'-Diamino-2,2'-bipyridyldichloroplatinum(II) (3f)

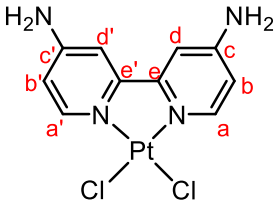

Chemical Formula: $C_{10}H_{10}Cl_2N_4Pt$
Exact Mass: 450.99
Molecular Weight: 452.20

4,4'-Diamino-2,2'-bipyridine (96 mg, 0.515 mmol, 1 eq.) was added to a stirring solution of potassium tetrachloroplatinate (214 mg, 0. 515 mmol, 1 eq). Refer to the general procedure in **Section 7.2.3.3** for the reaction conditions. Crude yield: 123 mg, 53%.

4,4'-Dichloro-2,2'-bipyridyldichloroplatinum(II) (3g)

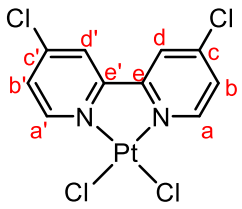

Chemical Formula: $C_{10}H_6Cl_4N_2Pt$
Exact Mass: 488.89
Molecular Weight: 491.06

4,4'-Dichloro-2,2'-bipyridine (105 mg, 0.466 mmol, 1 eq.) was added to a stirring solution of potassium tetrachloroplatinate (194 mg, 0.466 mmol, 1 eq). Refer to the general procedure in **Section 7.2.3.3** for the reaction conditions. Crude yield: 201 mg, 88%; ^{1}H-NMR (600 MHz, DMSO-d_6) δ 9.42 (d, J = 6.3 Hz, 2H, H-a,a'), 8.92 (d, J = 2.4 Hz, 2H, H-d,d'), 8.02 (dd, J = 2.4 Hz, 6.4 Hz, 2H, H-b,b').

4,4'-bis(trifluoromethyl)-2,2'-bipyridyldichloroplatinum(II) (3h)

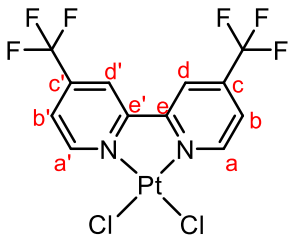

Chemical Formula: $C_{12}H_6Cl_2F_6N_2Pt$
Exact Mass: 556.95
Molecular Weight: 558.17

4,4'-bis(trifluoromethyl) -2,2'-bipyridine (115 mg, 0.395 mmol, 1 eq.) was added to a stirring solution of potassium tetrachloroplatinate (164 mg, 0.395 mmol, 1 eq). Refer to the general procedure in **Section 7.2.3.3** for the reaction conditions. Crude yield: 124 mg, 56%; ^{1}H-NMR (600 MHz, DMSO-d_6) δ 9.78 (d, J = 6.1 Hz, 2H, H-a,a'), 8.29 (d, J = 1.92 Hz, 2H, H-d,d'), 8.28 (dd, J = 1.9 Hz, 6.3 Hz, 2H, H-b,b').

***N*4,*N*4'-dimethyl-[2,2'-bipyridine]-4,4'-dicarboxamide dichloroplatinum(II) (3i)**

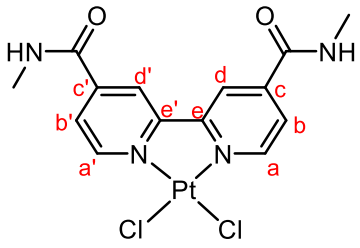

Chemical Formula: $C_{14}H_{14}Cl_2N_4O_2Pt$
Exact Mass: 535.01
Molecular Weight: 536.28

dimethyl-[2,2'-bipyridine]-4,4'-dicarboxamide, (**2a**, 96 mg, 0.516 mmol, 1 eq.) was added to a stirring solution of potassium tetrachloroplatinate (214 mg, 0.516 mmol, 1 eq). Refer to the general procedure in **Section 7.2.3.3** for the reaction conditions. Crude yield: 208 mg, 75%; ^{1}H-NMR (400 MHz, DMSO-d_6) δ 9.62 (d, J = 6.1 Hz, 2H, H-a,a'), 9.13 (q, J = 4.6 Hz, 2H, NH), 8.89 (d, J = 2.0 Hz, 2H, H-d,d'), 8.18 (dd, J = 6.1 Hz, 2.0 Hz, 1H, H-b,b'), 2.89 (d, J = 4.5 Hz, 6H, CH_3).

dimethyl-[2,2'-bipyridine]-4,4'-dicarboxylate dichloroplatinum(II) (3j)

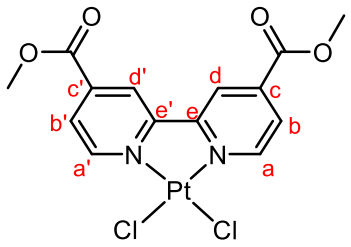

Chemical Formula: $C_{14}H_{12}Cl_2N_2O_4Pt$
Exact Mass: 536.98
Molecular Weight: 538.24

Dimethyl-[2,2'-bipyridine]-4,4'-dicarboxylate (**2b**, 101 mg, 0.371 mmol, 1 eq.) was added to a stirring solution of potassium tetrachloroplatinate (154 mg, 0.371 mmol, 1 eq). Refer to the general procedure in **Section 7.2.3.3** for the reaction conditions. Crude yield: 132 mg, 66%; ^{1}H-NMR (300 MHz, DMSO-d_6) δ 9.74 (d, J = 6.1 Hz, 2H, H-a,a'), 9.10 (d, J = 1.8 Hz, 2H, H-d,d'), 8.96 (d, J = 5.0 Hz, 1H, H-a,a'), 8.86 (d, J = 2.6 Hz, 1H, H-d,d'), 8.27 (dd, J = 1.8 Hz, 6.1 Hz, 2H, H-b,b'), 7.96 (dd, J = 5.0 Hz, 1.7 Hz, 1H, Hb'), 4.01 (s, 3H, CH_3), 3.97 (s, 3H, CH_3). Proton signals indicated in blue belong to the residual starting material (compound **2b**).

7.2.3.4. Synthesis of [Pt(diimine)(L-O,S)]$^+$ complexes

General procedure[179]

The respective acyl-thiourea ligands (**1a**/**1b**/**1c**/**1d**) (1.1 eq.) and triethylamine (1.1 eq.) in acetone/dry DMF/MeCN (1 mL) were added dropwise to a stirring solution of the respective precursor [$PtCl_2$(diimine)] complexes **3a-3j** (1 eq.) in acetone/dry DMF/MeCN (1 mL). The mixture was refluxed either at 60 °C or 80 °C for 4 hours (**4a.1**-**4d**) or 24 hours (**4e**-**4j**) and then allowed to cool. The precipitate was collected via suction filtration while being washed with acetone. Where the complex was collected as a crude product, it was purified using reverse phase column chromatography using either MeOH:H_2O or MeCN:H_2O as the mobile phase.

(*N*-Benzoyl-*N'*,*N'*-di(2-hydroxyethylthioureato)-*S*,*O*)(4,4'-di-*tert*-butyl-2,2'-bipyridyl)platinum(II) chloride (4a.1)

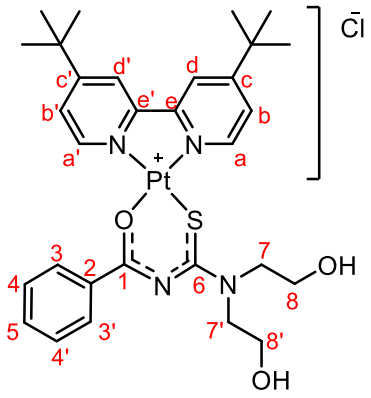

Chemical Formula: $[C_{30}H_{39}N_4O_3PtS]^+Cl^-$
Exact Mass: 765.21
Molecular Weight: 766.26

Compound **1a** and triethylamine (0.033 mL, 0.259 mmol, 1.1 eq.) in acetone were added to a solution of compound **3a** (0.126 g, 0.236 mmol 1 eq.) in acetone. Refer to the general procedure in **Section 7.2.3.4** for the reaction conditions. Compound **4a.1** was isolated as a yellow solid. Yield: 88.8 mg, 49%; ^{1}H-NMR (600 MHz, MeOD-d_4) δ 8.92 (d, *J* = 6.0 Hz, 1H, H-a), 8.55 (d, *J* = 2.1 Hz, 1H, H-d), 8.52 (d, *J* = 6.2 Hz, 1H, H-a'), 8.45 (d, *J* = 2.2 Hz, 1H, H-d'), 8.05 (d, *J* = 6.0 Hz, 2H, H-3,3'), 7.99 (dd, *J* = 6.0 Hz, 2.0 Hz, 1H, H-b), 7.64 (dd, *J* = 6.2 Hz, 2.2 Hz, 1H, H-b'), 7.60 (t, *J* = 6.0 Hz, 1H, H-5), 7.46 (t, *J* = 6.0 Hz, 2H, H-4,4'), 4.11 (t, *J* = 5.9 Hz, 2H, H-7), 4.05 – 4.02 (m, 4H, H-8,8'), 3.84 (t, *J* = 5.9 Hz, 2H, H-7'), 1.59 (s, 9H, CH_3), 1.53 (s, 9H, CH_3); ^{13}C-NMR (151 MHz, MeOD-d_4) δ 171.13, 168.59, 168.13, 168.04, 159.00, 156.08, 149.45, 145.19, 136.44, 133.87, 130.51 (2C), 129.87 (2C), 126.11, 123.24, 122.71, 60.80 (2C), 60.10 (2C), 57.95, 56.46, 37.21, 30.38 (6C); HPLC-MS (ESI): Purity = 97%, t_R = 17.370 min HR-ESI MS: (*m/z*) $[M-Cl]^+$ = 730.2451, calculated mass $[M-Cl]^+$ = 730.8; IR (ATR, cm^{-1}): 3325 (broad, weak, OH), 2957 (sharp, weak, N=C=S), 2866 (sharp, weak, N=C=S), 1614 (sharp, weak, C=N), 1500 (sharp, strong, C=C), 1411 (sharp, strong, C-H).

(*N*-Benzoyl-*N'*,*N'*-di(2-hydroxyethylthioureato)-*S*,*O*)(4,4'-dimethyl-2,2'-bipyridyl)platinum(II) chloride (4b.1)

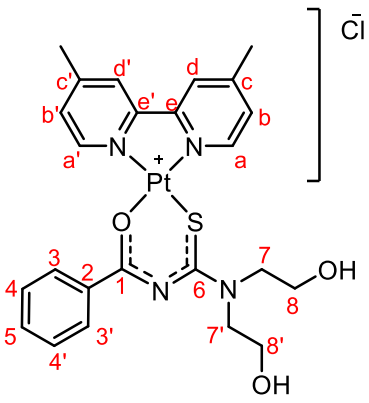

Chemical Formula: $[C_{24}H_{27}N_4O_3PtS]^+Cl^-$
Exact Mass: 681.11
Molecular Weight: 682.10

Compound **1a** (78.9 mg, 0.294 mmol, 1.1 eq.) and triethylamine (40 µL, 0.294 mmol, 1.1 eq.) in dry DMF were added to compound **3b.1** (119 mg, 0.267 mmol, 1 eq.) in dry DMF. Refer to the general procedure in **Section 7.2.3.4** for the reaction conditions. Complex **4b.1** was isolated as a yellow solid: Yield: 148 mg, 81%; ^{1}H-NMR (600 MHz, D_2O/CD_3CN) δ 8.47 (d, *J* = 5.9 Hz, 1H, H-a), 8.27 (d, *J* = 5.9 Hz, 1H, H-a'), 8.07 (t, *J* = 7.2 Hz, 1H, H-5), 8.02 – 7.92 (m, 3H, H-d',3,3'), 7.90 (brs, 1H, H-d'), 7.82 (t, *J* = 7.2 Hz, 2H, H-4,4'), 7.70 (d, *J* = 6.0 Hz, 1H, H-b), 7.49 (d, *J* = 6.0 Hz, 1H, H-b'), 4.28 (t, *J* = 6.1 Hz, 2H, H-7), 4.17 (t, *J* = 6.0 Hz, 2H, H-7'), 4.13 (s, 4H, H-8,8'), 2.67 (s, 3H, CH_3), 2.60 (s, 3H, CH_3); ^{13}C-NMR (151 MHz, D_2O) δ 167.78, 165.24, 155.85, 153.70, 153.13, 146.55, 142.47, 133.55 (2C), 132.75 (2C), 128.78, 128.48, 127.92, 124.45, 123.91, 58.84 (2C), 57.84 (2C), 55.70, 54.20, 20.62, 20.30; HPLC-MS (ESI): Purity = 98%, t_R = 2.31 min, (*m/z*) $[M\text{-}Cl]^+$ = 646.1, calculated mass $[M\text{-}Cl]^+$ = 646.7.

(*N*-Benzoyl-*N'*,*N'*-di(2-hydroxyethylthioureato)-*S*,*O*)(2,2'-bipyridyl)platinum(II) chloride (4c)

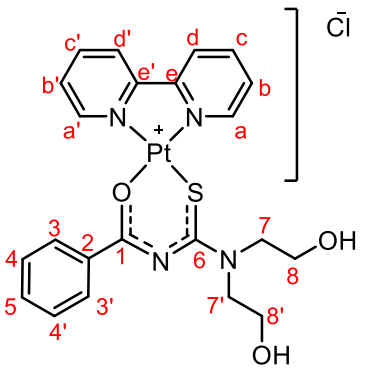

Chemical Formula: $[C_{22}H_{23}N_4O_3PtS]^+Cl^-$
Exact Mass: 653.08
Molecular Weight: 654.05

Compound **1a** (166 mg, 0.518 mmol, 1.1 eq.) and triethylamine (86 µL, 0.518 mmol, 1.1 eq.) in DMF were added to compound **3c** (237 mg, 0.561 mmol, 1 eq.). Refer to the general procedure in **Section 7.2.3.4** for the reaction conditions. Compound **4c** was isolated as a yellow solid. Yield: 333 mg, 91%; ^{1}H-NMR (600 MHz, DMSO-d_6) δ 9.01 (d, *J* = 6.0 Hz, 1H, H-a), 8.69 (d, *J* = 8.0 Hz, 1H, H-d), 8.65 (d, *J* = 6.0 Hz, 1H, H-a'), 8.62 (d, *J* = 8.2 Hz, 1H, H-d'), 8.48 (t, *J* =7.7 Hz, 1H, H-c), 8.39 (t, *J* = 7.8 Hz, 1H, H-c'), 8.12 (d, *J* = 6.0 Hz, 2H, H-3,3'), 8.08 (t, *J* = 6.0 Hz, 1H, H-b), 7.75 (t, *J* = 6.0 Hz, 1H, H-b'), 7.65 (d, *J* = 6.0 Hz, 1H, H-5), 7.56 (t, *J* = 6.0 Hz, 2H, H-4,4'), 5.15 (t, *J* = 5.4 Hz, 1H, OH), 5.02 (t, *J* = 5.4 Hz, 1H, OH), 4.03 (t, *J* = 5.8 Hz, 2H, H-7), 4.00 (t, *J* =

5.9 Hz, 2H, H-7'), 3.86 – 3.84 (m, 2H, H-8), 3.71 – 3.69 (m, 2H, H-8'). ^{13}C NMR (151 MHz, DMSO-d_6) δ 169.43, 166.47, 157.87, 154.84, 148.98, 144.74, 142.18, 142.09, 135.00, 133.23, 129.78 (2C), 129.33 (2C), 128.90, 128.75, 125.51, 124.95, 59.26, 58.49, 56.92, 55.44; HPLC-MS (ESI): Purity = 99%, t_R = 2.40 min, (*m/z*) $[M\text{-}Cl]^+$ = 618.1, calculated mass $[M\text{-}Cl]^+$ = 618.6.

(*N*-Benzoyl-*N'*,*N'*-di(2-hydroxyethylthioureato)-*S*,*O*)(4,4'-dimethoxyl-2,2'-bipyridyl)platinum(II) chloride (4d)

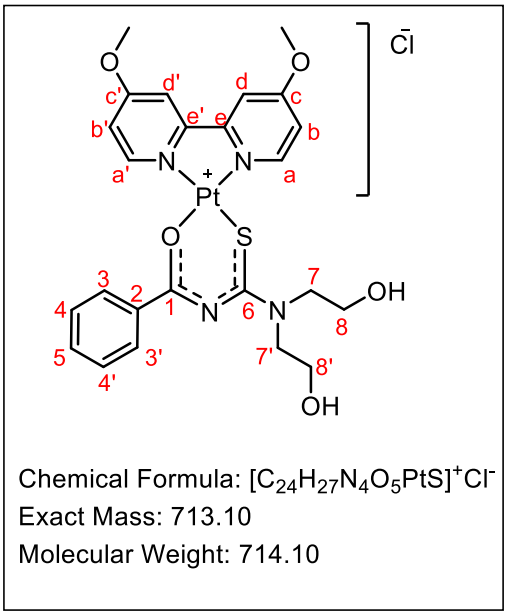

Chemical Formula: $[C_{24}H_{27}N_4O_5PtS]^+Cl^-$
Exact Mass: 713.10
Molecular Weight: 714.10

Compound **1a** (86.2 mg, 0.321 mmol, 1.1 eq.) and triethylamine (44 µL, 0.321 mmol, 1.1 eq.) in acetone were added to compound **3d** (140 mg, 0.292 mmol, 1 eq.). Refer to the general procedure in **Section 7.2.3.4** for the reaction conditions. Compound **4d** was isolated as a yellow solid. Yield: 177 mg, 86%; ^{1}H-NMR (600 MHz, DMSO-d_6) δ 8.55 (d, *J* = 6.2 Hz, 1H, H-a), 8.18 (d, *J* = 6.0 Hz, 1H, H-a'), 8.12 (d, *J* = 1.9 Hz, 2H, H-d,3), 7.98 (d, *J* = 1.9 Hz, 2H, H-d',3'), 7.66 (t, *J* = 6.0 Hz, 1H, H-5), 7.54 (dd, *J* = 2.2 Hz, 6.4 Hz, 1H, H-b), 7.50 (t, *J* = 6.0 Hz, 2H, H-4,4'), 7.18 (dd, *J* = 2.2 Hz, 6.4 Hz, 1H, H-b'), 5.23 (t, *J* = 5.3 Hz, 1H, OH), 5.10 (t, *J* = 5.2 Hz, 1H, OH), 4.01 (s, 3H, CH_3O), 3.94 (s, 7H, CH_3O, H-7,7'), 3.85 – 3.83 (m, 2H, H-8), 3.72 –3.70 (m, Hz, 2H, H-8'). ^{13}C-NMR (151 MHz, DMSO-d_6) δ 168.85 (d, *J* = 11.8 Hz), 166.20, 158.81, 156.08, 149.26, 145.41, 135.07, 133.05, 129.56 (2C), 129.21 (2C), 113.99, 113.77, 111.94, 111.39, 59.18 (2C), 58.33 (2C), 57.87 (2C), 56.77, 55.33; HPLC-MS (ESI): Purity = 98%, t_R = 2.41 min, (*m/z*) $[M\text{-}Cl]^+$ = 678.1, calculated mass $[M\text{-}Cl]^+$ = 678.6.

(*N*-Benzoyl-*N'*,*N'*-di(2-hydroxyethylthioureato)-*S*,*O*)(4,4'-dihydroxy-2,2'-bipyridyl)platinum(II) chloride (4e)

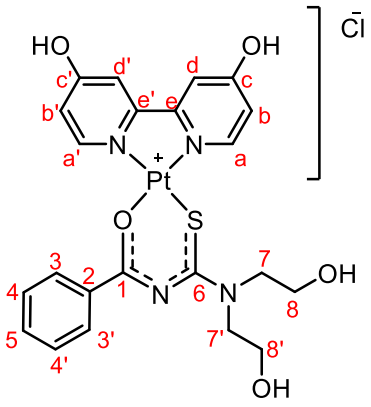

Chemical Formula: $[C_{22}H_{23}N_4O_5PtS]^+Cl^-$
Exact Mass: 685.07
Molecular Weight: 686.04

Compound **1a** (67.2 mg, 0.500 mmol, 1.1 eq.) and triethylamine (34.9 µL, 0.250 mmol, 1.1 eq.) in acetone were added to compound **3e** (102 mg, 0.228 mmol, 1 eq.). Refer to the general procedure in **Section 7.2.3.4** for the reaction conditions. Compound **4e** was isolated as a brown solid. Yield: 118 mg, 75%; ^{1}H-NMR (600 MHz, DMSO-d_6) δ 8.65 (d, *J* = 6.0 Hz, 1H, H-a), 8.20 (d, *J* = 6.0 Hz, 1H, H-a'), 8.12 (d, *J* = 8.3 Hz, 2H, H-3,3'), 7.88 (br s, 1H, H-d), 7.81 (br s, 1H, H-d'), 7.71 (br s, 1H, Ar-OH), 7.63 (t, *J* = 6.0 Hz, 1H, H-5), 7.51 (t, *J* = 6.0 Hz, 2H, H-4,4'), 7.40 (dd, *J* = 2.3 Hz, 6.0 Hz, 1H, H-b), 7.11 (dd, *J* = 2.3 Hz, 6.0 Hz, 1H, H-b') 7.09 (br s, 1H, OH), 5.05 (br s, 1H, OH), 4.95 (s, 1H, OH), 4.00 – 3.98 (m, 4H, H-8,8'), 3.84 (t, *J* = 6.0 Hz, 2H, H-7), 3.70 (t, *J* = 6.0 Hz, 2H, H-7'); HPLC-MS (ESI): Purity = 95%, t_R = 2.48 min, (*m/z*) $[M+H]^+$ = 687.0, calculated mass $[M+H]^+$ = 687.0. HR-ESI MS: (*m/z*) $[M-2OH-Cl+H]^+$ = 653.21 calculated mass $[M+Cl]^+$ = 653.03.

(*N*-Benzoyl-*N'*,*N'*-di(2-hydroxyethylthioureato)-*S*,*O*)(4,4'-diamino-2,2-bipyridyl)platinum(II) chloride (4f)

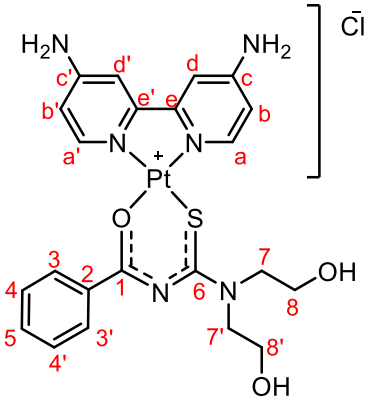

Chemical Formula: $[C_{22}H_{25}N_4O_3PtS]^+Cl^-$
Exact Mass: 683.10
Molecular Weight: 684.08

Compound **1a** (67.9 mg, 0.253 mmol, 1.1 eq.) and triethylamine (35 µL, 253 mmol, 1.1 eq.) in acetone were added to compound **3f** (103 mg, 0.230 mmol, 1 eq.). Compound **4f** was purified using reverse-phase column chromatography and isolated as a brown solid. Refer to the general procedure in **Section 7.2.3.4** for the reaction conditions. Yield: 28.8 mg, 18%; ^{1}H-NMR (300 MHz, CD_3CN) δ 7.79 (d, *J* = 6.0 Hz, 1H, H-a), 7.70 (d, *J* = 6.0 Hz, 2H, H-d,d'), 7.54 (t, *J* = 6.1 Hz, 1H, H-5), 7.32 (t, *J* = 6.1 Hz, 2H, H-4,4'), 7.24 (d, *J* = 6.7 Hz, 1H, H-a'), 6.59 (d, *J* =6.0 Hz, 2H, H-3,3'), 6.44 (dd, *J* = 3 Hz, 6.0 Hz, 1H, H-b), 6.23 (dd, *J* = 3 Hz, 6.0 Hz, 1H, H-b'), 3.80 (t, *J* = 5.6 Hz, 2H, H-7), 3.70 (br s, 6H, H-7', 8, 8'); HPLC-MS (ESI): Purity = 97%, t_R = 0.87

min, (*m/z*) $[M\text{-}Cl]^+$ = 648.1, HR-ESI MS: (*m/z*) $[M\text{-}Cl]^+$ = 648.25, calculated mass $[M\text{-}Cl]^+$ = 648.6.

(*N*-Benzoyl-*N'*,*N'*-di(2-hydroxyethylthioureato)-*S*,*O*)(4,4'-dichloro-2,2'-bipyridyl)platinum(II) chloride (4g)

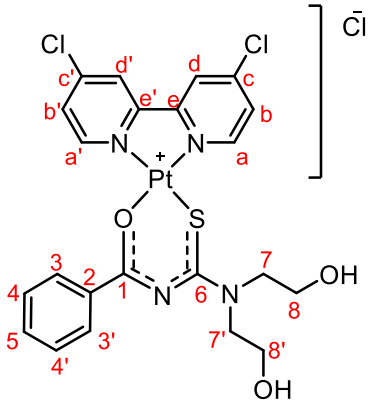

Chemical Formula: $[C_{22}H_{21}Cl_2N_4O_3PtS]^+Cl^-$
Exact Mass: 721.00
Molecular Weight: 722.93

Compound **1a** (61.7 mg, 0.229 mmol, 1.1 eq.) and triethylamine (32 µL, 0.229 mmol, 1.1 eq.) in acetone were added to compound **3g** (102 mg, 0.209 mmol, 1 eq.). Compound **4g** was purified using reverse-phase column chromatography and isolated as a yellow solid. Refer to the general procedure in **Section 7.2.3.4** for the reaction conditions. Yield: 133 mg, 88%; ^{1}H-NMR (600 MHz, MeOD-d_4) δ 9.07 (d, *J* = 6.0 Hz, 1H, H-a), 8.79 (d, *J* = 2.1 Hz, 1H, H-d), 8.75 – 8.68 (m, 2H, H-a',d'), 8.15 (d, *J* = 6.0 Hz, 1H, H-b), 8.13 (d, *J* = 6.0 Hz, 2H, H-3,3'), 7.79 (d, *J* = 6.3 Hz, 1H, H-b), 7.62 (t, *J* = 6.0 Hz, 1H, H-5), 7.53 (t, *J* = 6.6 Hz, 2H, H-4,4'), 4.15 (t, *J* = 5.9 Hz, 2H, H-7), 4.12 (t, *J* = 5.8 Hz, 2H, H-7'), 4.04 (t, *J* = 5.7 Hz, 2H, H-8), 3.92 (t, *J* = 5.8 Hz, 2H, H-8'). ^{13}C-NMR (151 MHz, DMSO-d_6) δ 160.77, 160.05, 159.79, 158.34, 150.44, 147.96, 140.84, 137.01, 126.81, 124.44, 121.12 (2C), 120.73 (2C), 106.78, 106.51, 104.47, 103.50, 50.69, 49.92, 48.27, 46.85.; HPLC-MS (ESI): Purity = 99%, t_R = 2.39 min, (*m/z*) $[M\text{-}Cl]^+$ = 687.1, calculated mass $[M\text{-}Cl]^+$ = 687.5.

(*N*-Benzoyl-*N'*,*N'*-di(2-hydroxyethylthioureato)-*S*,*O*)(bis(trifluoromethyl)-2,2'-bipyridyl)platinum(II) chloride (4h)

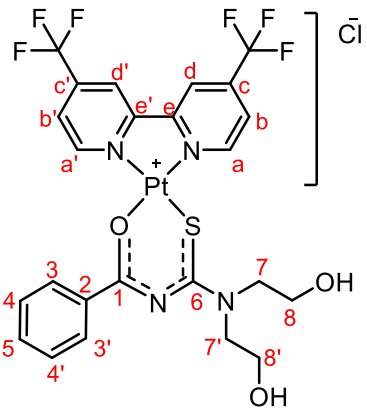

Chemical Formula: $[C_{24}H_{21}F_6N_4O_3PtS]^+Cl^-$
Exact Mass: 789.06
Molecular Weight: 790.04

Compound **1a** (98.4 mg, 0.334 mmol, 1.1 eq.) and triethylamine (51 µL, 0.367 mmol, 1.1 eq.) in acetone were added to compound **3h** (186 mg, 0.334 mmol, 1 eq.). Compound **4h** was purified using reverse-phase column chromatography and isolated as a yellow solid. Refer to the general procedure in **Section 7.2.3.4** for the reaction conditions. Yield: 112 mg, 42%; ^{1}H-NMR (600 MHz, MeOD-d_4) δ 9.49 (d, *J* = 5.9 Hz, 1H, H-a), 9.26 (d, *J* = 6.0 Hz, 1H, H-d), 9.18 (d, *J* = 6.0 Hz, 1H, H-d'), 9.14 (d, *J* = 6.0 Hz, 1H, H-a'), 8.47 (dd, *J* = 2.1 Hz, 6.1 Hz, 1H, H-b), 8.22 (d, *J* = 6.1 Hz, 1H, H-3), 8.21 (d, *J* = 6.0 Hz, 1H, H-3'), 8.09 (dd, *J* = 2.0 Hz, 6.1 Hz, 1H, H-b'), 7.63 (t, *J* = 6.0 Hz, 1H, H-5), 7.53 (t, *J* = 6.3 Hz, 2H, H-4,4'), 4.22 (t, *J* =, 5.8 Hz, 2H, H-7), 4.17 (t, *J* = 5.8 Hz, 2H, H-7'), 4.06 (t, *J* = 5.7 Hz, 2H, H-8), 3.91 (t, *J* = 5.8 Hz, 2H, H-8'). ; HPLC-MS (ESI): Purity = 96%, t_R = 0.95 min, (*m/z*) $[M-Cl]^+$ = 754.1, calculated mass $[M-Cl]^+$ = 754.6.

(*N*-Benzoyl-*N'*,*N'*-di(2-hydroxyethylthioureato)-*S*,*O*)((*N*4,*N*4'-dimethyl-2,2'-bipyridyl)-4,4'-dicarboxamide)platinum(II) chloride (4i)

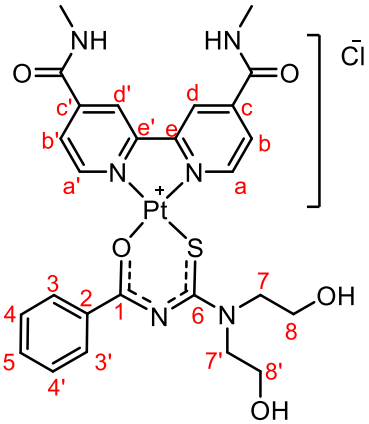

Chemical Formula: $[C_{26}H_{29}N_6O_5PtS]^+Cl^-$
Exact Mass: 767.13
Molecular Weight: 768.15

Compound **1a** (32.6 mg, 0.122 mmol, 1.1 eq.) and triethylamine (17 µL, 0.122 mmol, 1.1 eq.) in MeCN were added to compound **3i** (59.3 mg, 0.111 mmol, 1 eq.). Compound **4i** was washed with copious amounts of acetone and isolated as a yellow solid. Refer to the general procedure in **Section 7.2.3.4** for the reaction conditions. Yield: 65.8 mg, 77%; ^{1}H-NMR (400 MHz, DMSO-d_6) δ 9.24 (d, *J* = 5.9 Hz, 3H, H-a, a',d), 9.14 (d, *J* = 5.9 Hz, 2H, H-d',b), 8.81 (d, *J* = 6.1 Hz, 1H, H-b), 8.48 (d, *J* = 5.7 Hz, 1H, NH), 8.15 (d, *J* = 7.7 Hz, 2H, H-3,3'), 8.10 (d, *J* = 5.9 Hz, 1H, NH), 7.69 (t, *J* = 7.6 Hz, 1H, H-5), 7.54 (t, *J* = 7.6 Hz, 2H, H-4,4'), 5.18 (t, *J* = 5.4 Hz, 1H, OH), 5.04 (t, *J* = 5.3 Hz, 1H, OH), 4.11 – 4.06 (m, 4H, H-7,7'), 3.92 – 3.90 (m, 2H, H-8), 3.76 – 3.74 (m,

2H, H-8'), 2.92 (d, *J* = 4.4 Hz, 3H, CH_3), 2.88 (d, *J* = 4.4 Hz, 3H, CH_3); HPLC-MS (ESI): Purity = 98%, t_R = 0.81 min, (*m/z*) $[M\text{-}Cl]^+$ = 732.1, HR-ESI MS: (*m/z*) $[M\text{-}Cl]^+$ = 732.27, calculated mass $[M\text{-}Cl]^+$ = 732.7.

(*N*-Benzoyl-*N'*,*N'*-di(2-hydroxyethylthioureato)-*S*,*O*)(dimethyl-[2,2'-bipyridine]-4,4'-dicarboxylate)platinum(II) chloride (4j)

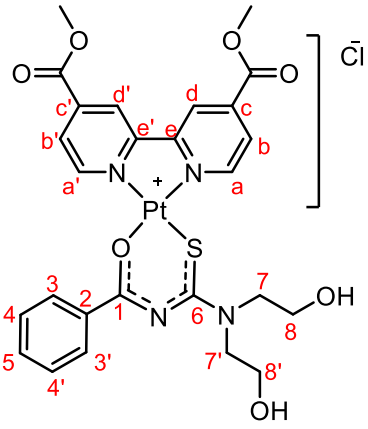

Chemical Formula: $[C_{26}H_{27}N_4O_7PtS]^+Cl^-$
Exact Mass: 769.09
Molecular Weight: 770.12

Compound **1** (98.9 mg, 0.369 mmol, 1.1 eq.) and triethylamine (51.3 µL, 0. 369 mmol, 1.1 eq.) in acetone were added to compound **3j** (180 mg, 0.335 mmol, 1 eq.). Compound **4j** was purified using reverse-phase column chromatography and preparative HPLC and was isolated as a brown solid. Refer to the general procedure in **Section 7.2.3.4** for the reaction conditions. The compound was not appropriately soluble in any of the available deuterated solvents; therefore, no NMR spectroscopy data was provided. Yield: 9.2 mg, 3.5%; HPLC-MS (ESI): Purity = 95%, t_R = 0.9 min, (*m/z*) $[M\text{-}Cl]^+$ = 734.1, calculated mass $[M\text{-}Cl]^+$ = 734.7.

_N_-(4-methyl-Benzoyl-_N'_,_N'_-di(2-hydroxyethylthioureato)-_S_,_O_)(4,4'-di-_tert_-butyl-2,2'-bipyridyl)platinum(II) chloride (4a.2)

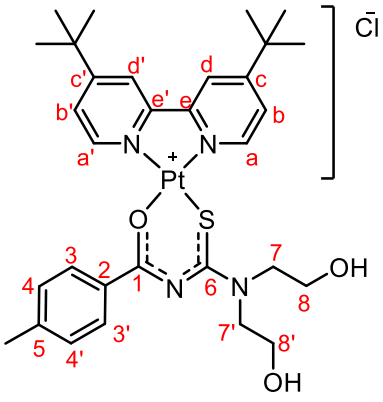

Chemical Formula: $[C_{31}H_{41}N_4O_3PtS]^+Cl^-$
Exact Mass: 779.22
Molecular Weight: 780.29

Compound **1b** (70.6 mg, 0.250 mmol, 1.1 eq.) and triethylamine (35 µL, 0.250 mmol, 1.1 eq.) in acetone were added to a solution of compound **3a** (0.121 g, 0.227 mmol 1 eq.) in acetone. Compound **4a.2** was isolated as a yellow solid. Refer to the general procedure in **Section 7.2.3.4** for the reaction conditions. Yield: 146 mg, 81%; ^{1}H-NMR (300 MHz, MeOD-d_4) δ 8.83 (d, J = 6.1 Hz, 1H, H-a), 8.50 (d, J = 2.0 Hz, 1H, H-d), 8.44 (d, J = 6.3 Hz, 1H, H-a'), 8.40 (d, J = 2.1 Hz, 1H, H-d'), 7.92 (dd, J = 2.0 Hz, 6.1 Hz, 1H, H-b'), 7.87 (d, J = 8.2 Hz, 2H, H-3,3'), 7.57 (dd, J = 2.2 Hz, 6.3 Hz, 1H, H-b'), 7.20 (d, J = 8.0 Hz, 2H, H-4,4'), 4.02 (t, J = 4.7 Hz, 2H, H-7), 3.95 – 3.93 (m, 4H, H-8,8'), 3.76 (t, J = 5.7 Hz, 2H, H-7'), 2.33 (s, 3H, phenyl-CH_3), 1.44 (s, 9H, $(CH_3)_3$), 1.37 (s, 9H, $(CH_3)_3$'); HPLC-MS (ESI): Purity = 97%, t_R = 1.12 min, (*m/z*) $[M\text{-}Cl]^+$ = 744.2,HR-ESI MS: (*m/z*) $[M+Cl]^+$ = 744.38, calculated mass $[M\text{-}Cl]^+$ = 744.8.

_N_-(4-methoxy-Benzoyl-_N'_,_N'_-di(2-hydroxyethylthioureato)-_S_,_O_)(4,4'-di-_tert_-butyl-2,2'-bipyridyl)platinum(II) chloride (4a.3)

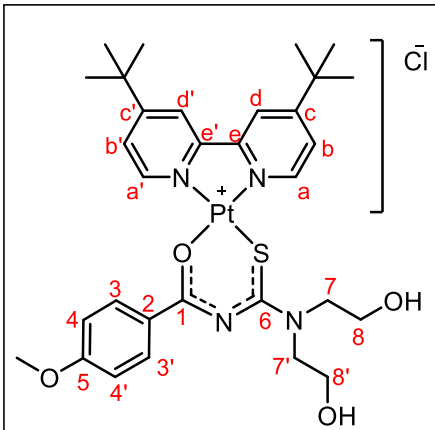

Chemical Formula: $[C_{31}H_{41}N_4O_4PtS]^+Cl^-$
Exact Mass: 795.22
Molecular Weight: 796.29

Compound **1c** (63.6 mg, 0.213 mmol, 1.1 eq.) and triethylamine (30 µL, 0.213 mmol, 1.1 eq.) in acetone were added to a solution of compound **3a** (103 mg, 0.193 mmol 1 eq.) in acetone. Compound **4a.3** was isolated as a yellow solid. Refer to the general procedure in **Section 7.2.3.4** for the reaction conditions. Yield: 142 mg, 92%; ^{1}H-NMR (300 MHz, DMSO-d_6) δ 8.85 (d, J = 6.1 Hz, 1H, H-a), 8.78 (d, J = 2.0 Hz, 1H, H-d), 8.67 (d, J = 2.1 Hz, 1H, H-d'), 8.48 (d, J = 6.3 Hz, 1H, H-a), 8.09 – 8.03 (m, 3H, H-b,3,3'), 7.72 (dd, J = 2.1 Hz, 6.3 Hz, 1H, H-b), 7.04 (d, J = 8.9 Hz, 2H, H-4,4'), 5.24 (t, J = 5.2 Hz, 1H, OH), 5.06 (t, J = 5.3 Hz, 1H, OH), 4.01 (t, J = 5.8 Hz, 2H, H-7), 3.94 (t, J = 6.0 Hz, 2H, H-7'), 3.88 (br s, 5H, H-8, CH_3O), 3.70 – 3.66 (m, 2H, H-8'), 1.48 (s, 9H, CH_3), 1.41 (s, 9H, CH_3); HPLC-MS (ESI): Purity = 98%, t_R =

1.12 min, (*m/z*) $[M\text{-}Cl]^+$ = 760.2,HR-ESI MS: (*m/z*) $[M\text{-}Cl]^+$ = 760.37, calculated mass $[M\text{-}Cl]^+$ = 760.8.

N-(4-chloro-Benzoyl-*N*',*N*'-di(2-hydroxyethylthioureato)-*S*,*O*)(4,4'-di-*tert*-butyl-2,2'-bipyridyl)platinum(II) chloride (4a.4)

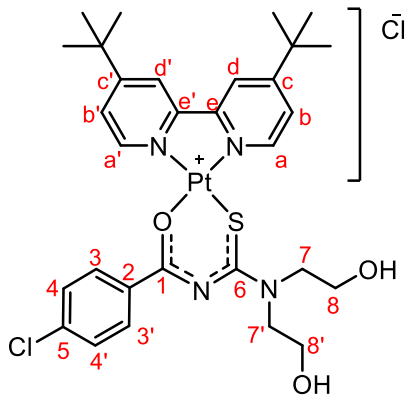

Chemical Formula: $[C_{30}H_{38}ClN_4O_3PtS]^+Cl^-$
Exact Mass: 799.17
Molecular Weight: 800.70

Compound **1d** (79.9 mg, 0.264 mmol, 1.1 eq.) and triethylamine (37 µL, 0.264 mmol, 1.1 eq.) in acetone were added to a solution of compound **3a** (0.128 g, 0.239 mmol 1 eq.) in acetone. Compound **4a.4** was isolated as a yellow solid. Refer to the general procedure in **Section 7.2.3.4** for the reaction conditions. Yield: 139 mg, 73%; ^{1}H-NMR (300 MHz, DMSO-d_6) δ 8.83 (d, *J* = 6.1 Hz, 1H, H-a), 8.80 (d, *J* = 2.0 Hz, 1H, H-d), 8.68 (d, *J* = 2.1 Hz, 1H, H-d), 8.51 (d, *J* = 6.3 Hz, 1H, H-a), 8.13 – 8.00 (m, 3H, H-3,3'), 7.74 (dd, *J* = 2.1 Hz, 6.3 Hz, 1H, H-b), 7.54 (d, *J* = 8.7 Hz, 2H, H-4,4'), 5.28 (t, *J* = 5.2 Hz, 1H, OH), 5.09 (t, *J* = 5.3 Hz, 1H, OH), 4.03 (t, *J* =5.3 Hz, 2H, H-7), 3.96 (t, *J* = 5.3 Hz, 2H, H-7'), 3.92 – 3.87 (m, 2 H, H-8') 3.70 – 3.66 (m, 2H, H-8'), 1.49 (s, 9H, $(CH_3)_3$), 1.41 (s, 9H, $(CH_3)_3$); HPLC-MS (ESI): Purity = 99%, t_R = 1.13 min, (*m/z*) $[M\text{-}Cl]^+$ = 765.2, HR-ESI MS: (*m/z*) $[M\text{-}Cl]^+$ = 765.33, calculated $[M\text{-}Cl]^+$ = 765.2.

(*N*-Benzoyl-*N'*,*N'*-di(2-hydroxyethylthioureato)-*S*,*O*)(5,5'-dimethyl-2,2'-bipyridyl)platinum(II) chloride (4b.2)

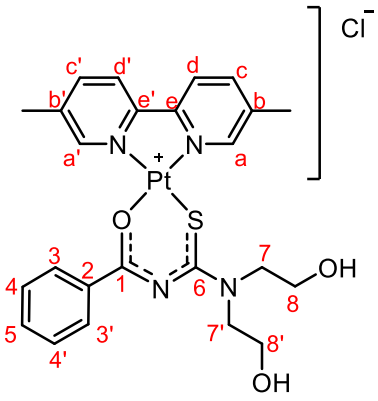

Chemical Formula: $[C_{24}H_{27}N_4O_3PtS]^+Cl^-$
Exact Mass: 681.11
Molecular Weight: 682.10

Compound **1a** (78.4 mg, 0.292 mmol, 1.1 eq.) and triethylamine (41 µL, 0.292 mmol, 1.1 eq.) in dry DMF was added to compound **3b.2** (119 mg, 0.266 mmol, 1 eq.) in dry DMF. Compound **4b.2** was isolated as a yellow solid. Refer to the general procedure in **Section 7.2.3.4** for the reaction conditions. Yield: 148 mg, 82%; ^{1}H NMR (300 MHz, D_2O/CD_3CN) δ 8.30 – 8.04 (m, 9H, Ar), 7.91 (t, *J* = 7.6 Hz, 2H, Ar), 4.40 – 4.29 (m, 4H, H-7,7'), 4.23 (br s, 4H, H-8,8'), 2.62 (d, *J* = 8.6 Hz, 6H, CH_3); HPLC-MS (ESI): Purity = 98%, t_R = 2.33 min, (*m/z*) $[M-Cl]^+$ = 646.1, HR-ESI MS: (*m/z*) $[M-Cl]^+$ = 646.25, calculated mass $[M-Cl]^+$ = 646.1.

(*N*-Benzoyl-*N'*,*N'*-di(2-hydroxyethylthioureato)-*S*,*O*)(6,6'-dimethyl-2,2'-bipyridyl)platinum(II) chloride (4b.3)

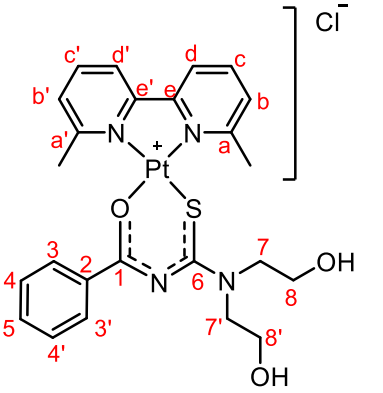

Chemical Formula: $[C_{24}H_{27}N_4O_3PtS]^+Cl^-$
Exact Mass: 681.11
Molecular Weight: 682.10

Compound **1a** (78.4 mg, 0.292 mmol, 1.1 eq.) and triethylamine (41 µL, 0.292 mmol, 1.1 eq.) in dry DMF was added to compound **3b.3** (119 mg, 0.266 mmol, 1 eq.) in dry DMF. Compound **3b.3** was isolated as a yellow solid. Refer to the general procedure in **Section 7.2.3.4** for the reaction conditions. Yield: 82.3 mg (45%); ^{1}H-NMR (300 MHz, DMSO-d_6) δ 8.15 – 7.98 (m, 5H, Ar), 7.63 – 7.43 (m, 5H, Ar), 6.92 (d, *J* = 8.5 Hz, 1H, Ar), 5.05 (s, 1H, OH), 4.95 (s, 1H, OH), 4.05 – 3.96 (m, 4H, H-7,7'), 3.89 – 3.85 (m, 2H, H-8), 3.75 – 3.71 (t, *J* = 5.4 Hz, 2H, H-8'), 3.02 (s, 3H, CH_3), 2.40 (s, 1H, CH_3). ^{13}C-NMR (151 MHz, DMSO-d_6) δ 168.31, 167.53, 162.71, 162.37, 160.70, 152.41, 139.14, 138.12, 131.53, (2C) 128.93, 128.46 (2C), 126.57, 125.48, 122.89, 118.10, 58.93 (2C), 58.20 (2C), 55.38, 54.47, 23.37. HPLC-MS: Purity = 98%, t_R = 2.69 min, (*m/z*) $[M-Cl]^+$ = 646.1, calculated mass $[M-Cl]^+$ = 646.1.

7.2.3.5. Counterion exchange via salt metathesis reactions

(*N*-Benzoyl-*N*',*N*'-di(2-hydroxyethylthioureato)-*S*,*O*)(4,4'-di-*tert*-butyl-2,2'-bipyridyl)platinum(II) hexafluorophosphate (4a.5)

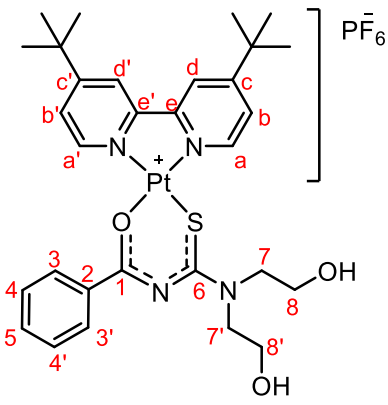

Chemical Formula: $[C_{30}H_{39}N_4O_3PtS]^+PF_6^-$
Exact Mass: 875.20
Molecular Weight: 875.78

NH_4PF_6 (6.78 mg, 0.042 mmol, 1.1 eq.) was added to Compound **4a.1** (29.1 mg, 0.038 mmol, 1 eq.) in dry DCM:EtOH (1:1). The reaction mixture was allowed to stir under argon at room temperature (27 °C) for 1 hour. The resulting precipitate was collected via suction filtration. Compound **4a.5** was isolated as a yellow solid. Yield: 29.4 mg, 88%; ^{1}H-NMR (300 MHz, DMSO-d_6) δ 8.88 (d, J = 6.1 Hz, 1H, H-a), 8.77 (d, J = 2.1 Hz, 1H, H-d), 8.66 (d, J = 2.4 Hz, 1H, H-d'), 8.51 (d, J = 6.3 Hz, 1H, H-a'), 8.14 – 8.06 (m, 3H, H-3,3',b), 7.75 – 7.7.66 (m, 2H, H-b',5), 7.55 (t, J = 7.6 Hz, 2H, H-4,4'), 5.19 (t, J = 6.0 Hz, 1H, OH), 5.05 (t, J = 6.0 Hz, 1H, OH), 4.08 – 3.95 (m, 4H, H-7,7'), 3.92 – 3.88 (m, 2H, H-8), 3.72 – 3.68 (m, 2H, H-8'). HPLC-MS (ESI): Purity = 95%, t_R = 1.074 min, (*m/z*) $[M\text{-}PF_6]^+$ = 730.1, HR-ESI MS: (*m/z*) $[M\text{-}PF_6]^+$ = 730.36, calculated mass $[M\text{-}PF_6]^+$ = 730.8; IR (ATR, cm^{-1}): 3601 (broad, weak, OH), 2960 (sharp, weak, N=C=S), 2874 (sharp, weak, N=C=S), 1619 (sharp, weak, C=N), 1496 (sharp, strong, C=C), 1411 (sharp, strong, C-H), 833 (sharp, strong, PF_6).

(*N*-Benzoyl-*N'*,*N'*-di(2-hydroxyethylthioureato)-*S*,*O*)(4,4'-di-*tert*-butyl-2,2'-bipyridyl)platinum(II) nitrate (4a.6)

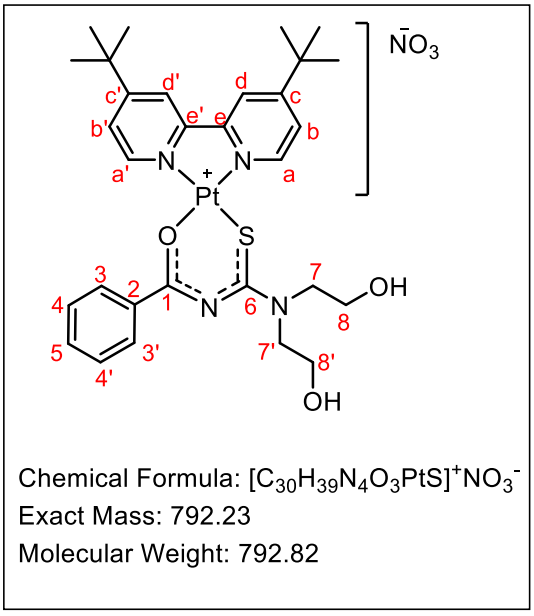

Chemical Formula: $[C_{30}H_{39}N_4O_3PtS]^+NO_3^-$
Exact Mass: 792.23
Molecular Weight: 792.82

$AgNO_3$ (7.80 mg, 0.046 mmol, 1.1 eq.) was added to Compound **4a.1** (32.1 mg, 0.042 mmol, 1 eq.) in dry MeOH (2 mL). The reaction mixture was allowed to stir in the dark under argon at room temperature (25 °C) for 3 hours. The resulting precipitate was collected *via* suction filtration. **4a.6** was collected as a yellow solid Yield: 5.00 mg, 15%; ^{1}H-NMR (300 MHz, DMSO-d_6) δ 8.93 (d, *J* = 6.2 Hz, 1H, H-a), 8.80 (brs, 1H, H-d), 8.69 (brs, 1H, H-d'), 8.55 (d, *J* = 6.2 Hz, 1H, H-a'), 8.19 –8.08 (m, 3H, H-3,3',b), 7.77 (dd, *J* = 6.3 Hz, 1H, H-b'), 7.71 (t, *J* = 7.2 Hz 1H, H-5), 7.56 (t, *J* = 7.5 Hz, 2H, H-4,4'), 5.17 (t, *J* = 5.7 Hz, 1H, OH), 5.03 (t, *J* = 5.6 Hz, 1H, OH), 4.10 – 4.00 (m, 4H, H-7,7'), 3.94 – 3.88 (m, 2H, H-8), 3.77 – 3.70 (m, 2H, H-8'); ^{13}C-NMR (151 MHz, DMSO-d_6) δ 168.85, 166.10, 165.78, 157.02, 154.10, 148.09, 143.89, 134.61, 132.73, 129.23 (2C), 128.82 (2C), 124.93, 122.49, 121.93, 58.77 (2C), 58.01 (2C), 56.43, 55.02, 36.19, 36.00, 29.86 (6 C). HPLC-MS (ESI): Purity = 97%, t_R = 1.074 min, (*m/z*) $[M\text{-}NO_3]^+$ = 730.1, HR-ESI MS: (*m/z*) $[M\text{-}NO_3]^+$ = 730.36, calculated mass $[M\text{-}NO_3]^+$ = 730.1; IR (ATR, cm^{-1}): 3392 (broad, weak, OH), 2965 (sharp, weak, N=C=S), 2872 (sharp, weak, N=C=S), 1621 (sharp, weak, C=N), 1494 (sharp, strong, C=C), 1808 (sharp, strong, C-H), 1396 (broad, strong, NO_3).

7.2.3.6. Synthesis and characterization of the [Au(diimine)(L-O,S)]$^{2+}$ analog

(4,4'-Di-*tert*-butyl-2,2'-bipyridyldichloroaurate(III)) hexafluorophosphate (3k)[361]

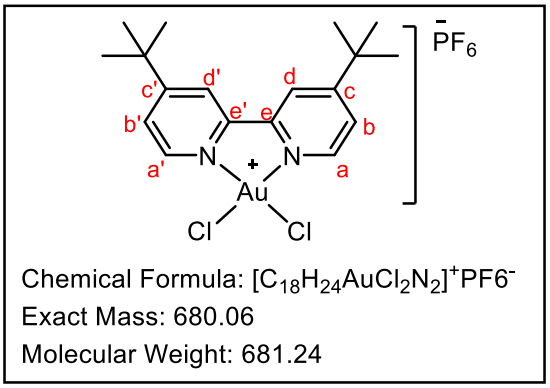

Chemical Formula: $[C_{18}H_{24}AuCl_2N_2]^+PF6^-$
Exact Mass: 680.06
Molecular Weight: 681.24

4,4'-Di-*tert*-butyl-2,2'-dipyridyl (228 mg, 0.844 mmol, 1 eq.) was added to a stirring solution of potassium tetrachloroaurate (320 mg, 0.844 mmol, 1 eq) in H_2O/MeOH (1:1). Potassium hexafluorophosphate was added (62.4 mg, 0.391 mmol, 4 eq.). The reaction mixture was allowed to stir at room temperature (25 °C) for 18 hours. The resulting yellow precipitate was isolated via suction filtration. Crude yield: 300 mg, 52%; ^{1}H-NMR (300 MHz, DMSO-d_6) δ 9.26 (d, *J* = 6.4

Hz, 2H, H-a, a'), 8.92 (d, *J* = 6.0 Hz, 2H, H-d,d'), 8.10 (dd, *J* = 6.4 Hz, 2.2 Hz, 1H, H-b,b'), 1.47 (s, 18H, $(CH_3)_3$).

(*N*-Benzoyl-*N*',*N*'-di(2-hydroxyethylthioureato)-*S*,*O*)(4,4'-di-*tert*-butyl-2,2'-bipyridyl)aurate(III) hexafluorophosphate (4K)

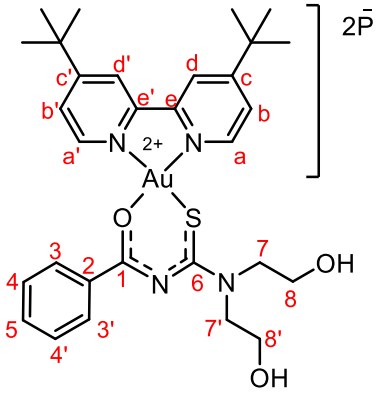

Chemical Formula: $[C_{30}H_{39}N_4O_3AuS]^{2+}2PF_6^-$
Exact Mass: 1020.16
Molecular Weight: 1020.73

Cesium carbonate (48.9 mg, 0.152 mmol, 1.1 eq) was added to compound **1a** (40.9 mg, 0.152 mmol, 1.1 eq) in MeCN (1 mL). The **1a** mixture was added dropwise to a stirring solution of **3k** (94.4 g, 0.139 mmol 1 eq.) in MeCN (1 mL). Lastly, hexafluorophosphate (50.9 mg, 0.277 mmol, 2 eq) was added and the reaction mixture was allowed to stir at room temperature (25 °C) for 18 hours. Complex **4k** was purified using normal phase column chromatography (DCM/MeOH). Complex **4k** was isolated as a purple solid. Yield: 67 mg, 47 %); ^{1}H-NMR (600 MHz, DMSO-d_6) δ 8.74 (d, *J* = 6.0 Hz, 2H, H-a), 8.58 (d, *J* = 1.9 Hz, 2H, H-d,d'), 8.04 (d, *J* = 6.6 Hz, 2H, H-3,3') 7.77 (dd, *J* = 5.6 Hz, 1.9 Hz, 2H, H-b,b'), 7.56 (t, *J* = 5.7 Hz, 2H, H-5), 7.48 (t, *J* = 5.8 Hz, 2H, H-4,4'), 4.14 (t, *J* = 5.8 Hz, 2H, H-7), 3.95 (t, *J* = 6.0 Hz, 2H, H-7'), 3.83 (t, *J* = 6.0 Hz, 2H, H-8), 3.80 (t, *J* = 5.6 Hz, 2H, H-8'), 1.41 (s, 18H, $(CH_3)_3$, $(CH_3)_3$'); ^{13}C-NMR (151 MHz, DMSO-d_6) δ 176.23, 175.95, 165.39, 150.51, 147.56 (2C), 134.52, 132.59, 129.43 (3C), 128.86 (3C), 123.38 (2C), 120.15 (2C), 66.01, 58.80, 57.82, 50.72, 35.89 (2C), 30.37. HPLC-MS (ESI): t_R = 0.885 min and 1.02 min, (*m/z*) $[M\text{-}2PF_6\text{+}4H_2O]^+$ = 804.7 and (*m/z*) $[M\text{-}2PF_6\text{+}2H_2O + CH_3CN]^+$ = 809.0, calculated mass $[M\text{-}2PF_6\text{+}4H_2O]^+$ = 804.8 and $[M\text{-}2PF_6\text{+}2H_2O\text{+}CH_3CN]^+$ = 809.8. IR (ATR, cm^{-1}): 3415 (broad, weak, OH), 2958 (sharp, strong, N=C=O), 2868 (sharp, weak, N=C=S), 1632 (sharp, weak, C=N), 1585 (sharp, strong, C=C), 826 (sharp, strong, PF_6).

7.2.3.7. Synthesis of a fluorescent probe and its precursors

5-(dimethylamino)-*N*-(2-((2-hydroxyethyl)amino)ethyl)naphthalene-1-sulfonamide (7)[362]

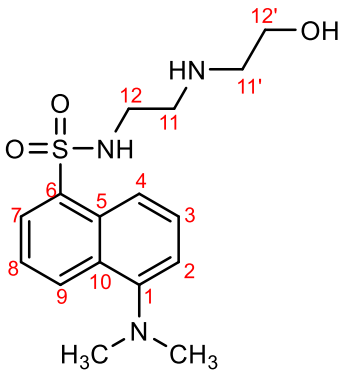

Chemical Formula: $C_{16}H_{23}N_3O_3S$
Exact Mass: 337.15
Molecular Weight: 337.44

N-(2-Aminoethyl)ethanolamine (1.91 mL, 18.8 mol, 5 eq.) was added to a 250 mL round-bottom flask equipped with a stirrer bar. Dansyl chloride (1.01 g, 3.76 mol, 1 eq.) in THF/MeCN (60 mL/30 mL) was added dropwise. After the completion of the reaction, the solvent was removed, and the crude product was purified using column chromatography (petroleum ether/ethyl acetate). Compound **7** was isolated as a green oil. Yield: 412 mg, 33%; ^{1}H-NMR (300 MHz, DMSO-d_6) δ 8.46 (d, J = 8.4 Hz, 1H, H-9), 8.29 (d, J = 6.0 Hz, 1H, H-4), 8.12 (d, J = 6.0 Hz, 1H, H-8), 7.64 (d, J = 7.2 Hz, 1H, H-7), 7.58 (d, J= 6.0 Hz, 1H, H-3), 7.26 (d, J = 7.2 Hz, 1H, H-2), 3.27 (t, J = 5.8 Hz, 1H, H-11,11), 2.79 (s, 6H, N-(C$\underline{H}_3$)$_2$), 2.45 (t, J = 6.5 Hz, 2H, H-12), 2.45 (t, J = 6.5 Hz, 2H, H-12'); HPLC-MS (ESI): Purity = 98%, t_R = 2.36 min, (*m/z*) $[M+H]^+$ = 338.20, calculated mass $[M+H]^+$ = 338.4.

***N*-((2-((5-(dimethylamino)naphthalene)-1-sulfonamido)ethyl)(2-hydroxyethyl)carbamothioyl) benzamide (8)**

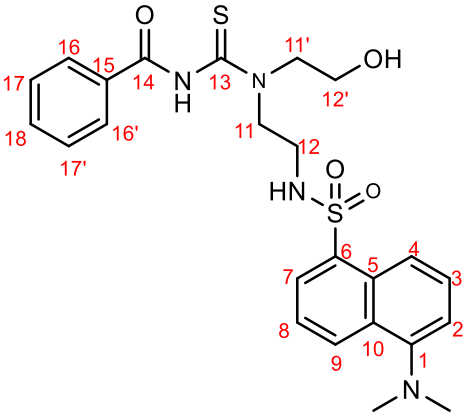

Chemical Formula: $C_{24}H_{28}N_4O_4S_2$
Exact Mass: 500.16
Molecular Weight: 500.63

Benzoyl isothiocyanate (47 µL, 0.35 mmol, 1 eq.) and dry DCM (3 mL) were added to a 10-mL RBF equipped with a magnetic stirrer and septum with a needle connected to a balloon containing nitrogen. The mixture was cooled in an ice-water bath to a temperature of 0 °C. Compound **7** (57.0 mg, 0.35 mmol, 1 eq.) in dry DCM (2 mL) was added dropwise. The reaction mixture was allowed to stir at room temperature (23 °C) for 1 hour. The crude product was purified using column chromatography with a mobile phase of petroleum ether and ethyl acetate. Compound **8** was isolated as a green oil. Yield: 144 mg, 82%; ^{1}H-NMR (300 MHz, MeOD-d_4) δ 8.57 (d, J = 8.6 Hz, 1H, H-9), 8.35 (d, J = 8.6 Hz, 1H, H-4), 8.26 (d, J = 7.2 Hz, 1H, H-8), 7.88 (d, J = 7.6 Hz, 2H, H-16,16'), 7.66 – 7.44 (m, 5H, H-9,7,18,17,17'), 7.26 (dd, J = 0.9 Hz, 7.6 Hz, 1H, H-2), 3.87 (t, J = 6.5 Hz, 2H,

H-11), 3.67 (t, *J* = 6.5 Hz, 2H, H-11'), 3.55 (t, *J* = 6.6 Hz, 2H, H-12), 3.33 (t, *J* = 6.6 Hz, 2H, H-12'), 2.87 (s, 6H, N-($C\underline{H}_3$)$_2$).HPLC-MS (ESI): Purity = 96%, t_R = 2.49 min, *m/z* $[M+H]^+$ = 501.20, calculated mass $[M+H]^+$ = 501.6.

(*N*-Benzoyl-*N'*,*N'*-di(2-hydroxyethylthioureato)-*S*,*O*)(5-(dimethylamino)-*N*-(2-((2-hydroxyethyl)amino)ethyl)naphthalene-1-sulfonamido)(4,4'-di-*tert*-butyl-2,2'-bipyridyl)platinum(II) chloride (4a.7)

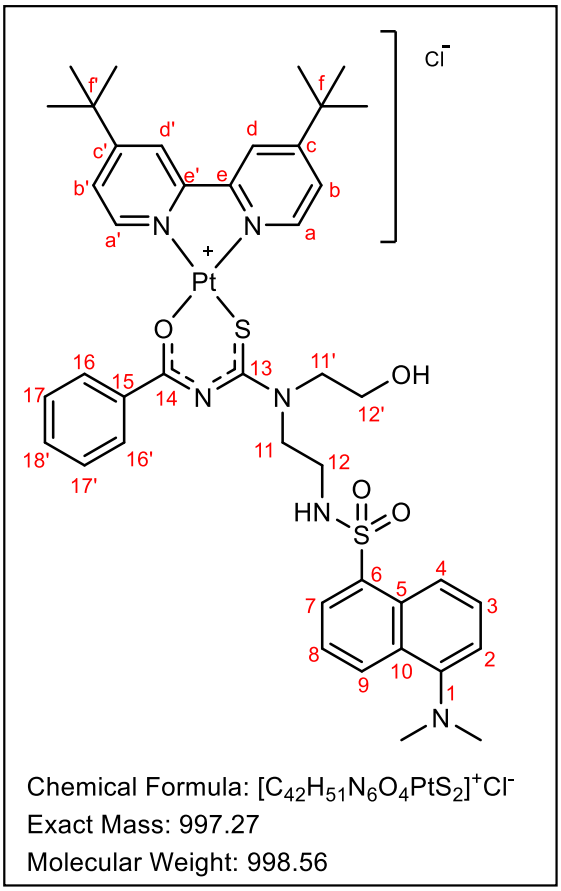

Compound **8** (61.9 mg, 0.124 mmol, 1.1 eq) and triethylamine (17 µL, 0.124 mmol) in acetone (1 mL) were added dropwise to compound **3a** (60.1 mg, 0.112 mmol, 1 eq.) in acetone (1 mL). The reaction mixture was allowed to reflux for 1.5 hours. The resulting precipitate was filtered off by gravity and the filtrate was purified using reverse-phase column chromatography with H_2O/MeCN as the mobile phase. Compound **4a.7** was isolated as a yellow solid. Yield: 41.5 mg, 37%; ^{1}H-NMR (600 MHz, MeOD-d_4) δ 8.94 – 9.88 (m, 1H, H-9), 8.58 (d, *J* = 1.8 Hz 1H, H-d), 8.5 – 8.43 (m, 2H, H-4,8), 8.40 – 8.29 (m, 1H, H-a,a'), 8.21 (dd, *J* = 8.8 Hz, 1.6 Hz, 1H, H-b), 8.04 – 8.00 (m, 3H,H-16,16', d'), 7.69 – 7.57 (m, 2H, H-3,7), 7.52 – 7.47 (m, 1H, H-2), 7.44 (t, *J* = 5.9 Hz, 1H, H-18), 7.39 – 7.33 (m, 2H, H-17,17'), 7.09 (dd, *J* = 8.8 Hz, 1.6 Hz,1, H, H-b'), 4.03 (t, *J* = 6.4 Hz, 2H, H-11), 3.93 (t, *J* = 5.3 Hz, 2H, H-11'), 3.78 (dd, *J* = 6.0 Hz, 18 Hz, H-12), 3.53 (t, *J* = 6.4 Hz, 1H, H-12'), 2.71 (d, *J* = 3.9 Hz, 6H, N-($C\underline{H}_3$)$_2$), 1.53 (s, 9H, ($C\underline{H}_3$)$_3$), 1.46 (s, 9H, ($C\underline{H}_3$)$_3$'). HPLC-MS (ESI): Purity = 98%, t_R = 1.12 min, *m/z* $[M-Cl]^+$ = 963.2, calculated mass *m/z* $[M-Cl]^+$ = 963.1.

***tert*-butyl (2-((2-hydroxyethyl)amino)ethyl)carbamate (9)**[363]

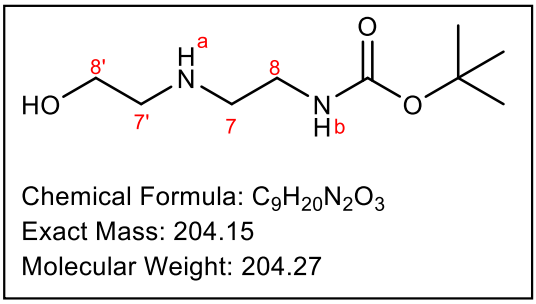

Chemical Formula: $C_9H_{20}N_2O_3$
Exact Mass: 204.15
Molecular Weight: 204.27

N-Boc-2-aminoacetaldehyde (956 mg, 6.00 mmol, 1.5 eq.) and ethanolamine (245, 4.00 mmol, 1 eq.) in MeOH (50 mL) were allowed to stir at room temperature (25 °C) for 2 hours. The reaction mixture was put on ice and $NaBH_4$ (309 mg, 8.19 mol, 5 eq.) was added slowly over 20 minutes. The reaction mixture was allowed to stir at room temperature for 18 hours. 1 M HCl (~15 mL) was added until the mixture had a pH of 6. The solvent was removed via rotary evaporation and DCM (5 mL) was added. The resulting precipitate was removed using gravity filtration and the filtrate was purified using reverse-phase column chromatography with H_2O/MeOH as the mobile phase. Compound **9** was isolated as a yellow oil. Crude yield: 110 mg, 13%; ^{1}H-NMR (300 MHz, MeOD-d_4) δ 3.67 (t, J = 6.0 Hz, 2H, H-7), 3.57 (t, J = 6.3 Hz 1H, NH^a), 3.25 – 3.11 (m, 3H, NH^b, H-7), 2.75 – 2.69 (m, 4H, H-8,8'), 1.46 (s, 9H, $(CH_3)_3$).

***tert*-butyl (2-(3-benzoyl-1-(2-hydroxyethyl)thioureido)ethyl)carbamate (10)**

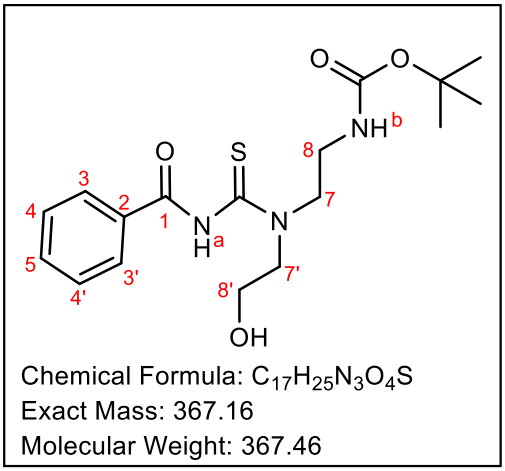

Chemical Formula: $C_{17}H_{25}N_3O_4S$
Exact Mass: 367.16
Molecular Weight: 367.46

Benzoyl isothiocyanate (34.6 µL, 0.258 mmol, 1 eq.) and dry DCM (1 mL) were added to a 10 mL RBF purged with argon. The contents of the RBF were cooled on ice to 0 ˚C. Compound **9** (52.6 mg, 0.258 mmol, 1 eq.) in dry DCM (3 mL) was added dropwise and the reaction mixture was allowed to stir at room temperature for 18 hours. Compound **10** was purified *via* column chromatography using DCM/MeOH as the mobile phase. Compound **10** was isolated as a yellow oil. Yield: 41.2 mg, 43%; ^{1}H-NMR (300 MHz, MeOD-d_4) δ 7.93 (d, J = 6.0 Hz, 2H, H-3,3'), 7.62 (t, J = 6.0 Hz, 1H, H-5), 7.52 (t, J = 7.0 Hz, 2H, H-4,4'), 4.06 (t, J = 6.6 Hz, 2H, H-7), 3.89 – 3.73 (m, 4H, H-8,8'), 3.65 (t, J = 5.2 Hz, 1H, NH^a), 3.52 (t, J = 6.5 Hz, 2H, H-7'), 3.17 (t, J = 5.2 Hz, 1H, NH^b) , 1.46 (s, 9H, $(CH_3)_3$). HPLC-MS (ESI): Purity = 98 %, t_R = 0.941 min, *m/z* $[M+H]^+$ = 368.2.

(*N*-Benzoyl-*N'*,*N'*-((2-aminoethyl)(2-hydroxyethylthioureato)-*S*,*O*)(4,4'-di-*tert*-butyl-2,2'-bipyridyl)platinum(II) chloride (4a.8a)

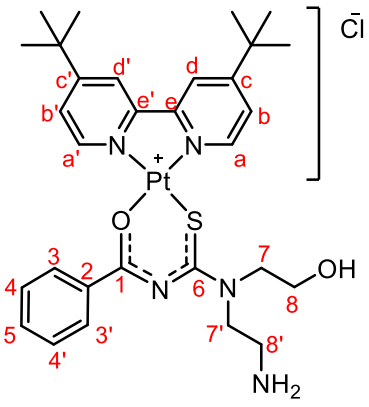

Chemical Formula: $[C_{30}H_{40}N_2O_2PtS]^+Cl^-$
Exact Mass: 764.22
Molecular Weight: 765.28

Compound **10** (42.8 mg, 0.116 mmol, 1.1 eq) and triethylamine (16 µL, 0.116 mmol, 1.1 eq.) in acetone (1 mL) was added dropwise to compound **3a** (56.6 mg, 0.106 mmol, 1 eq) in acetone (1 mL). The reaction mixture was allowed to reflux for 2 hours. The resulting precipitate was filtered off by gravity and the filtrate was purified using reverse-phase column chromatography with 0.1% formic acid in H_2O/ 0.1% formic acid in MeCN as the mobile phase. The solvent was removed via rotary evaporation and DCM (1 mL) and trifluoroacetic acid (TFA, 0.5 mL) were added to the residue. The mixture was allowed to stir for 2 hours after which the solvent and TFA were removed using rotary evaporation. MeOH (5 mL) was added to quench the residual TFA and the solvent was removed using rotary evaporation. Compound **4a.8a** was isolated as a yellow solid. Yield: 2.3 mg, 3%; ^{1}H-NMR (300 MHz, D_2O) δ 8.66 (br s, 2H, H-a,a'), 8.23 – 8.05 (m, 7H, Ar), 7.86 (t, *J* = 7.7 Hz, 2H, H-4,4'), 4.36 – 4.23 (m, 4H, H-7,7'), 4.18 (s, 4H, H-8,8'), 2.59 (s, 3H, $(CH_3)_3$), 2.56 (s, 3H, $(CH_3)_3$'). HPLC-MS (ESI): Purity = 99%, t_R = 0.904, (*m/z*) $[M-Cl]^+$ = 729.2, calculated mass $[M-Cl]^+$ = 729.8.

7.3. Cultivation of *Plasmodium falciparum* parasites

Pf-NF54 (drug-sensitive), *Pf*-K1 (multidrug-resistant), and *Pf*-Dd2 (multidrug-resistant) strains were used to investigate the *in vitro* antiplasmodium efficacy of the mixed-ligand platinum(II) complexes. The parasites were maintained at 2% hematocrit (HCT) in B+ or O+ human red blood cells in a growth medium containing RPMI-1640; 4.2% sodium bicarbonate; 1 mL/L gentamycin; 6 g/L HEPES; glucose 4 g/L; hypoxanthine 0.088 g/L and 5 g/L Albumax. The parasites were incubated at 37 °C in an atmosphere of 5% CO_2, 5% O_2 and 90% N_2. Synchronous cultures of the ring stage were obtained with 5% (w/v) D-sorbitol treatment.[364] During the synchronization step, 5x the volume of D-sorbitol was added to the pellet and the culture was incubated at 37 °C for 10 minutes. Post incubation, the culture was spun at 750 rcf for 5 minutes and the supernatant was removed with an aspirator. The morphology and development of the parasites were monitored using Giemsa-stained smears under a microscope.

7.4. *In vitro* assessment of the test complexes' antiplasmodium activity using the SYBR Green I and pLDH assays

7.4.1. SYBR Green I assay

This assay was conducted by collaborators, Professor Lyn-Marie Birkholtz and her team from the Institute for Sustainable Malaria Control at the University of Pretoria, South Africa.

The *in vitro* activities of the test platinum(II) complexes were evaluated against the asexual blood stages of *Pf* (NF54 and K1) using the Malaria SYBR Green I-based fluorescence assay.[175] Compounds were dissolved in DMSO and diluted accordingly to make either a 2 µM or 10 µM solution which was added to and serially diluted down a 96-well plate. Each compound was tested with three technical repeats as well as one to three independent biological repeats. The ring stage of *Pf* (2% parasitemia (P), 2% HCT) was added to each well and the plates were incubated at 37 °C for 96 hours. Subsequently, SYBR Green I lysis buffer (100 µL) which consists of: 0.2 µL/mL of 10 000x SYBR Green I (Invitrogen); 20 mM Tris (pH 7.5); 5 mM EDTA; 0.008% (w/v) saponin and 0.08% (v/v) Triton X-100 was added to the parasite suspension. The plates were incubated in the dark at ambient temperature for 1 hour. The fluorescence was determined on a microplate reader at an excitation of 485 nm and an emission of 538 nm. Dose-response curves were generated using Sigma Plot 11.0, from which the IC_{50} was determined.

7.4.2. pLDH assay

The *in vitro* asexual blood stage activity of the selected test compounds against *Pf*-Dd2 was determined using the pLDH assay. A 10 mM stock of the test compounds in DMSO was diluted to 10 µM using a complete growth medium. Complete growth medium (100 µL) was added to all wells in columns 1 – 2 and 4 – 12. The test compounds in a complete growth medium (200 µL) were added in triplicate to well 3 of a 96-well plate and serially diluted two-fold down the plate (from wells 3 – 12). Unparasitized RBCs (100 µL) at 2% HCT were added to all wells in column 1. A trophozoite stage *Pf-Dd2* culture (2% P, 2% HCT) was added to each well in columns 2 – 12 and the plates were incubated at 37 °C for 48 hours after which they were frozen to lyse the cells. A Malstat solution (100 µL) was added to a new 96-well plate (developing plate), followed by 20 µL of the thawed and lysed cell suspension and 25 µL of nitroblue tetrazolium (NBT). The Malstat consisted of Triton X-100 (339 µM), L-lactate (92 mM), Tris buffer (54 mM) and 3-acetyl pyridine adenine dinucleotide (APAD, 166 µM) in milli-Q water. The pH of the solution was then adjusted to 9. The NBT solution contained NBT (2 µM) and phenazine ethosulphate (261 µM) in milli-Q water. The plates were incubated in the

dark at ambient temperature (20 – 25 °C) for 30 minutes after which the absorbance values were read on a microplate reader (Thermo scientific Multiskan GO) at a wavelength of 620 nm. Dose-response curves and IC_{50} values were generated as per the SYBR Green I assay, using GraphPad Prism 10.

7.5. In vitro activity against gametocyte stages

This assay was conducted by collaborators, Professor Lyn-Marie Birkholtz and her team from the Institute for Sustainable Malaria Control at the University of Pretoria, South Africa.

Pf-NF54 gametocytes were prepared and isolated according to the method reported by Reader *et al*.[365,366] Briefly, gametocytogenesis was induced from a culture of synchronous rings using nutrient starvation (growth medium without glucose) in combination with a reduction in hematocrit. The *in vitro* gametocyte activities of the synthesized complexes were determined using a luciferase reporter line-based assay. In each instance, assays were set up using three technical repeats and one to three independent biological repeats. Methylene blue (MB) was used as a positive control in this assay. NF54-*Pf*S16-GFP-Luc (transgenic parasite line) was used for the stage-specific assessment of gametocyte activity. Early-stage (ES) gametocyte (stages I-III) experiments were performed on day 5 (representing >90% of early-stage GAM) and late-stage (LS) gametocyte (stages IV/V) experiments were performed on day 10. In each experiment, 2 – 3% gametocytaemia at 1.5% hematocrit was used for each assay. The treated cultures were incubated for 48 hours at 37 °C in a gas chamber (90% N_2, 5% O_2, and 5% CO_2). Luciferin substrate (30 µL) (Promega Luciferase Assay System) was added to parasite lysates (30 µL). The luciferase activity was determined by reading the resulting bioluminescence at an integration constant of 10 s which was detected using the GloMax®-Multi+ Detection System with Instinct® Software.

7.6. In vitro cytotoxicity assay using the Chinese hamster ovarian (CHO) cell line

This assay was conducted by the pharmacology team at the Holistic Drug Discovery and Development (H3D) Centre, Division of Clinical Pharmacology, Department of Medicine, University of Cape Town.

Cultivation of the CHO cell-line

CHO cells were donated from S. Schwager, Department of Medical Biochemistry, University of Cape Town, South Africa. These cells were originally obtained from the ATCC (American Type Culture Collection) in 2001.

To maintain the CHO-cell line in culture, the medium is removed from the flask using aspiration and the cells are rinsed twice with 10 ml PBS. 10% Trypsin (5 mL, heated to 37ºC) was added after which complete medium is added (5 mL) and the suspension was centrifuged at 750 rpm for 5 minutes. The supernatant was removed via aspiration and the pellet was resuspended in complete medium (5 mL). Approximately 1 ml of the cell suspension was transferred to a new culture flask containing a complete medium (9 mL). This flask was kept under gas (5% CO2) at 37 °C for 48 hours or until needed for the MTT assay.

MTT assay

A 3-(4,5-dimethylthiazol-2-yl)-2,5-diphenyltetrazoliumbromide (MTT) assay was used to screen the metal complexes against the mammalian Chinese hamster ovarian (CHO) cell line. A stock solution of each test compound (2 mg/mL) in DMSO was prepared and kept at -20 °C until needed. Emetine was used as a reference drug for this assay. A starting concentration of 100 µg/mL was serially diluted ten-fold in a complete medium, resulting in a final concentration of 0.001 µg/mL (6 dilutions). The assay plates with treated CHO cells were incubated for 48 hours. Sterile MTT (Thermo Fisher Scientific) (25 µL) was added to the treated cell suspensions in each well, followed by 4 hours incubation in the dark at room temperature (20 – 25 °C). This was followed by centrifugation and removal of the supernatant via aspiration. DMSO (100 µL) was then added to assist the solubilization of the formed crystals. The absorbance of each well was determined at a wavelength of 540 nm. The full dose-response curves were plotted using a non-linear dose-response curve fitting analysis via GraphPad Prism v.4.0 software. The IC_{50} values of each compound were determined from their dose-response curves and converted from µg/mL to µM.

7.7. Kinetic solubility by HPLC (pH 6.5)[367]

This assay was conducted by the DMPK team at the H3D Centre.

Solubility was measured at pH 6.5 using an adapted miniaturized shake-flask method, in 96-well plate format. Briefly, 4 µL of a 10 mM stock in DMSO was added to a 96-well plate and evaporated using a GeneVac system. Phosphate buffer pH 6.5 (196 µL) was then added to the wells and the plate was incubated for 24 h at 25 °C with shaking. At the end of this incubation, the samples were centrifuged at 3500 g for 15 min and then transferred to an analysis plate. A calibration curve in DMSO for each sample between 10 – 220 µM was prepared and included in the analysis plate. Analysis was then performed by HPLC-DAD and the solubility of each sample was determined from the corresponding calibration curve.

Reserpine (solubility <5 µM) and hydrocortisone (solubility >180 µM) were used as controls and gave data that compared well to historical data in our laboratory.

7.8. *In vitro* hepatic microsomal metabolic stability studies

This assay was conducted by the DMPK team at the H3D Centre.

Preparation of liver microsomes

Thaw microsomes (XenoTech) at 37 °C and dilute to 0.4 mg/mL using 0.1 M phosphate buffer.

Assay

In vitro microsomal metabolic stability studies were conducted in duplicate in a 96-well microtiter plate, following previously reported methods.[368] Briefly, a solution of the test compounds (1 µM, in phosphate buffer (pH 7.4)) was incubated at 37 °C in the presence of either mouse or pooled human liver microsomes (0.5 mg/mL) for 30 minutes. Incubation was conducted in both the presence and absence of the cofactor NADPH regeneration system (1 mM). Carbamazepine, 0.0236 µg/mL (internal standard) in ice-cold acetonitrile was used to quench the reaction. The samples were centrifuged (4200 rpm) for 20 minutes (20 °C). The supernatant was diluted by half the concentration with water and then filtered. Analysis was conducted using HPLC-MS/MS (Agilent Rapid Resolution HPLC, AB SCIEX 4500 MS). The percentage (%) of the parent compound that remained after 30 minutes of incubation was calculated using **Equation 7.1**. This was used to calculate the degradation half-life ($t_{1/2}$, **Equation 7.1**) and *in vitro* intrinsic clearance (CL_{int}, **Equation 7.2**) value.

$$\%\ \text{parent remaining} = \frac{\text{peak area or height at time point}}{\text{peak area or height at t} = 0} \times 100 \quad \mathbf{Eq.\ 7.1}$$

$$t_{1/2} = \frac{-\ln 2}{\lambda} \quad \mathbf{Eq.\ 7.2} \quad (\text{where } \lambda \text{ is the slope of Ln \% remaing vs. time})$$

$$Cl_{int} = \frac{\ln 2 \times \text{volume of incubation (µL)}}{t_{1/2} \times \text{mass of microsomes per incubation (mg)}} \quad \mathbf{Eq.\ 7.3}$$

7.9. Determination of pharmacokinetic parameters

This assay was conducted by Dr Liezl Gibhard and her team at the H3D Centre.

Triplicates of male Balb/C mice were used for the determination of *in vivo* pharmacokinetic parameters. This work was conducted under the University of Cape Town's ethics policies

using protocols that have been approved by the research ethics committee (AEC017/026). Compounds were administered either intravenously as a bolus solution (DMA/PEG/PPG/H_2O:5/15/30/50) or orally as a solution containing 0.5% (w/v) HPMC with 0.2% Tween 80 to male Balb/C mice. Mice were not fasted overnight and were allowed to eat and access water freely.

To determine the PK parameters, blood samples were collected from the tail vein of the mice into heparinized microcentrifugation tubes at distinct sampling times (0.17, 0.5, 1, 3, 5, 7, 9, 24, and 48 hours for intravenous dosing; 0.5, 1, 3, 5, 7, 9, 24 and 48 hours for oral dosing). All samples were stored at -80 °C until extraction.

For the bioanalysis, frozen whole blood was thawed at room temperature and 20 µL of each sample was extracted by protein precipitation (using 100 µL of acetonitrile containing 10 ng/ml of the internal standard, MMV394902). The sample was centrifuged. Supernatants of each sample were injected into the LC-MS/MS column for analysis. The analytical limit of quantitation (LOQ) was 2 ng/mL. The pharmacokinetic parameters were calculated using noncompartmental analysis using PK Solutions 2.0 (Summit Research Services, Montrose, CO, USA) and a curve stripping-based method.

7.10. *In vitro* parallel artificial membrane permeability assay (PAMPA) for permeability determination

This assay was conducted by the ADME team at the H3D Centre.

In preparation for the assay, the required membrane filters were precoated with hexadecane (5%) in hexane and were allowed to dry. The assay was performed with three technical repeats in 96-well MultiScreen filter plates (Millipore, 0.4 µm PCTE membrane). Lucifer yellow was added to the apical wells of the precoated MultiScreen donor plate and served as an integrity marker for the membrane. Phosphate buffer (pH 7.4) was added to the 96-well acceptor plate followed by relevant amounts of the 10 mM stock of the test compound. The donor plate was slotted into an acceptor plate and incubated at room temperature for 4 hours with gentle shaking. Post incubation, aliquots of the samples from the acceptor plates were transferred to the analysis plate, and the matrix was matched with a blank donor buffer. Carbamazepine (0.0236 ng/mL) in acetonitrile was added to all samples as an internal standard. The samples were analyzed using LCMS/MS (Agilent rapid resolution HPLC, AB SCIEX 4500 MS). The permeability (P_{app}) was calculated by using the normalized (analyte/internal standard) peak areas. Membrane integrity was calculated from the P_{app} of Lucifer yellow (acceptable values < 50nm/s) using a Modulus microplate reader.

7.11. Plasma protein binding (PPB)

This assay was conducted by the ADME team at the H3D Centre.

To determine the percentage of test compound bound to plasma, ultracentrifugation was used. The test compound (5 µM of a 10 mM DMSO stock) was used to spike pooled human plasma. An aliquot of the spiked solution was removed immediately and quenched with carbamazepine, 0.0236 µg/mL in ice-cold acetonitrile. The aliquot was frozen and served as the total concentration sample to be referenced against later. Samples were pre-incubated for 1 hour at 37 °C. Following pre-incubation, aliquots of the spiked plasma were taken in duplicate and were transferred to ultra-centrifugation tubes. The samples were ultracentrifuged for 4 hours at 37 °C (42000 rpm, Beckman Optima L-80XP). This was followed by analysis using LCMS/MS (Agilent Rapid Resolution HPLC, AB SCIEX 4500 QTRAP MS). The percentage of the test compound bound to plasma protein was calculated by comparison of the analyte: peak ratios of the ultracentrifuged sample to that of the total concentration sample.

7.12. NP40-detergent-mediated β-hematin inhibition assay

The β-hematin inhibition assay was followed according to the method outlined by Carter *et al*.[28] A 305.5 µM stock solution of NP-40 detergent was prepared. The test compounds were dissolved in the relevant volumes of DMSO to produce stock solutions (20 mM). Milli-Q water (140 µL), NP-40 detergent (40 µL, 305.5 µM), and the stock solution of the test compounds (20 µL) were added to column 12 of a 96-well plate. A mixture of milli-Q water, NP-40 (305.5 µM), and DMSO (v/v ratio of 7/2/1) was added to all wells in columns 1-11. The contents of column 12 were serially diluted (2-fold) to well 2, discarding 100 µL from column 2. Therefore, column 1 served as a no-drug blank. A pre-read of each of the well's absorbance values was obtained at 405 nm on a plate reader. Hematin (16.3 g) in 1 mL of DMSO was prepared to produce a 25 mM stock. A 178 µL aliquot of this stock solution was added to the acetate buffer (1 M, pH 4.8, 20 mL). The suspension (100 µL) of hematin in acetate buffer was added to each well. The plates were covered with plate covers and incubated for 5 hours at 37 °C. Finally, an analysis of the β-hematin inhibition activities of the test compounds was carried out using the pyridine-ferrichrome method developed by Ncokazi and Egan.[182] A prepared solution of pyridine/H_2O/acetone/HEPES buffer (2 M, pH 7.4) in a v/v ratio of 5/2/2/1 (32 µL), and acetone (60 µL) were added to each well of the original assay plate. The contents of each well were thoroughly mixed by agitation and the UV/vis absorbance was recorded on a SpectraMax P340 plate reader at 405 nm. Sigmoidal dose-response curves were obtained using the absorbance values using GraphPad Prism v.10 software.

7.13. Cellular heme fractionation assay

The cellular heme fractionation assay was carried out following the method described by Combrinck *et al*. [369] without modification.

Day 1: *Pf*-NF54 parasites in the ring stage (5% P and 2% HCT) were synchronized with sorbitol and added to a 24-well plate containing varying multiples of the test compounds IC_{50}. No drug controls were included and there were four technical repeats of each concentration of the test compound per a plate. Two independent biological repeats were included for each test compound. The plates were incubated at 37 °C for 32 hours. After 32 hours, the rings mature into trophozoites and these trophozoites were harvested on day 2.

Day 2: The RBCs were lysed with saponin (5%), liberating the matured trophozoites. PBS (100 µL) was added to each well and mixed before being transferred to a 500 µL 96-well round bottom plate (Axygen Scientific), called the stock plate. Separately, a SYBR Green I-based cell counting (FACS) solution was made by adding 0.125% (v/v) of glutaraldehyde and 0.5% (v/v) DNase to PBS (pH 7.5). In a separate flat-bottom 96-well plate (counting plate), 10 µL of resuspended trophozoites and 190 µL FACS solution were added. The stock plate was stored at -20 °C until day 4 and the counting plate at 3 °C overnight (~ 16 hours).

Day 3: Cells were counted using a flow cytometer (Becton Dickinson (BD) AccuriTM C6 Plus system with SSC/FL1530 nm) using BD AccuriTM C6 Plus software. In preparation for the flow cytometry analysis, 160 µL of SYBR Green I (2 µL, 10 000x in DMSO, Invitrogen Thermo Fisher Scientific) in PBS (20 mL) solution was added to a 96-well round bottom plate. An aliquot of resuspended cells (20 µL) from the counting plate and 20 µL of a Trucount bead solution (in 1 mL PBS) were transferred into the same 96-well flat-bottom plate. This plate was covered with aluminum foil to prevent exposure to light and incubated at 37 °C for 30 minutes. The contents of each well were mixed thoroughly before reading on the flow cytometer. The number of events in a 40 µL solution was counted for each sample. FlowJo software (V10) was used to analyze the data.

Day 4: A series of cellular fraction steps were performed to quantify the amount of hemoglobin, heme, and hemozoin in the cells post-incubation with the test compounds. The stock plate was thawed at room temperature. 100 µL of water was added to each well and the plate was sonicated for 5 minutes. 50 µL of HEPES buffer (0.02 M, pH 7.5) was added, and the sample was centrifuged at 3600 rpm for 20 minutes. The supernatant (hemoglobin fraction) was transferred to an adjacent set of wells on the same plate. The three different heme species

were then fractionated via the stepwise addition of several pre-made salt solutions and buffers. The stepwise protocol can be seen in **Table 7.1**.

From here the absorbance maximum of the Fe(III)heme-pyridine complex was recorded on a multi-well plate reader and was used to calculate the percentage of each heme species. The amount of total heme was calculated from the flow cytometry counting method developed by Combrinck *et al*.[369] Briefly, the concentration of cells in each well was used to determine the amount of total heme (fg/cell). This was done using **Equation 7.4** below where $C_{flowcytometry}$ refers to the concentration of cells in 1 mL as determined by flow cytometry. T is the gated parasite cells, B is the number of gated Trucount beads and $C_{trucount\ beads}$ is the concentration of Trucount beads, as specified by the supplier.

$$C_{\text{flowcytometry}} \frac{T}{B} \times C_{\text{Trucount beads}} \quad \textbf{Eq. 7.4}$$

Subsequently, the percentage of each fraction was determined from the absorbance maxima where the absorbance of a particular fraction (Frac.) was divided by the sum of the absorbances of all three fractions and converted to a percentage using **Equation 7.5**. The fractions are either heme, hemoglobin, or hemozoin and the total absorbance refers to the sum of the absorbances of all three fractions.

$$\%\ \text{Frac.} = \frac{\text{absorbance of frac.}}{\text{Total absorbance}} \times 100 \quad \textbf{Eq. 7.5}$$

After that, the total heme Fe was divided by the number of cells calculated for a particular concentration of test compound to determine the total amount of heme Fe per cell (fg/cell). Therefore, the amount of heme Fe (fg/cell) for each fraction was determined using **Equation 7.6**, where V is a 0.2 normalizing constant and corresponds to the amount of Fe in 200 µL of sample volume and the fraction (frac.) refers to either heme, hemoglobin, or hemozoin.

$$\text{Frac. Fe}\left(\frac{\text{fg}}{\text{cell}}\right) = \text{frac.}\,\% \times \text{total Fe}\left(\frac{\text{fg}}{\text{cell}}\right) \times \text{V} \quad \textbf{Eq. 7.6}$$

Table 7.1. Steps for the fractionation of the three heme species. Numbered steps were conducted in parallel, and the reagents were added to both the hemoglobin and heme fractions.

	To the supernatant (hemoglobin)	**To the pellet (heme)**
1.	Add 50 µL 4% SDS	Add 50 µL 4% SDS
2.	N/A	Add 50 µL milliQ water
3.	N/A	Re-suspend
4.	Sonicate 5 min	Sonicate for 5 min
5.	Incubate at rt for 30 min	Incubate at rt for 30 min
6.	N/A	Add 50 µL HEPES (0.2 M, pH 7.5)
7.	Add 50 µL NaCl (0.3 M)	Add 50 µL NaCl (0.3 M)
8.	Add 50 µL 25% pyridine (1 M in HEPES)	Add 50 µL 25% pyridine (1 M in HEPES)
9.	Re-suspend and transfer 200 µL to a flat bottom 96-well reading plate	N/A
10.	N/A	Spin @ 3600 rpm for 20 min
11.	N/A	Transfer supernatant to adjacent wells on the same plate
12.	N/A	Add 150 µL of milli-Q to supernatant
13.	N/A	Resuspend and transfer 200 µL to reading
	To the second pellet (hemozoin)	
14.	Add 50 µL milli-Q	N/A
15.	Add 50 µL 0f 0.3 M NaOH	N/A
16.	Sonicate for 15 min	N/A
17.	Incubate for 30 min @ rt	N/A
18.	Add 50 µL HEPES (0.2 M, Ph 7.5)	N/A
19.	Add 50 µL HCl	N/A
20.	Add 50 µL 25% pyridine	N/A
21.	Add 150 µL milli-Q water	N/A
22.	Mix and transfer 200 µL to the reading plate	N/A

Abbreviation: N/A- Not applicable

7.14. Cyclic voltammetry

The general experimental set-up used to collect CV data is shown in **Figure 7.1** and is called an electrochemical cell. For this, the electrochemical cell, comprised of the three electrodes, is placed in an electrolyte solution containing the test compound. As electrons are transferred from the electrode to the analyte, ions move in solution, compensating for the charge produced by the chemical species and closing the circuit.[310] This electrolyte solution is a mixture of a salt and an appropriate solvent. Common electrolyte solutions include potassium chloride in water and tetrabutylammonium perchlorate in acetonitrile.

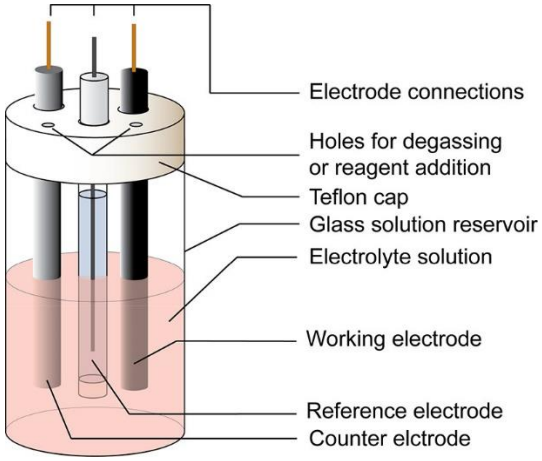

Figure 7.1. Schematic representation of an electrochemical cell used for CV experiments republished from Elgrishi *et al*. under the standard ACS Author Choice/Editors Choices' usage agreement.[310]

As shown in **Figure 7.1**, there are three electrodes: namely, the working electrode, a reference electrode, and a counter electrode. The electrochemical reaction is carried out by the working electrode as it is redox inert. The electrochemical cell is attached to a potentiostat which linearly sweeps the potential between the working and reference electrodes. When the potentiostat reaches the pre-set limit, it will sweep back in the opposite direction. When a potential is applied to the working electrode, oxidation/reduction of the analyte occurs and current starts to flow. This current is recorded and reported as the flow of electrons between the working electrode and the counter electrode, producing the voltammogram.

For the experiment a solution of the test compound (1×10^{-3}) in DMSO (3 mL) is added to the electrolyte solution (0.1 M tetrabutylammonium chloride (TBACl) in DMSO). The electrochemical measurements were then obtained using a Basi Epsilon Eclipse

Electrochemical Analyzer Potentiostat and the CV graphs generated using Excel. The working electrode was glassy carbon (GC) with platinum wire as the counter electrode (CE) and Ag/AgCl as the reference.

7.15. Fluorescence Live-Cell Microscopy

This section of work was conducted at the University of Cape Town's Confocal and Light Microscope Imaging Facility by Dr John Woodland.

7.15.1. General Methods

Nunc Lab-Tek II eight-well chamber slides were coated with a 0.01% (w/v) poly-L-lysine solution (150 µL). After 10 minutes, the solution was removed, and the slides were allowed to air dry. For imaging, Ringer's solution was used to maintain the parasite cell out of culture and to avoid the intrinsic fluorescence of phenol red which is typically present in standard culture media. The Ringer's solution was prepared as previously described by Kuhn *et al*.[370] Harvested parasites (5 µL, trophozoites, ~5% P, 2% HCT) were added to the Ringer's solution and gently vortexed to prevent the cells from forming clusters. The cell suspension (150 µL) was added to the imaging chamber slide and the slide was incubated for 30 minutes. Excess Ringer's solution was removed post-incubation, removing all loose cells. The previous step was repeated twice. The fluorescent compound in Ringer's solution (150 µL) was added to the cells and the chamber slide was incubated for 30 minutes before imaging.

The ringer's solution contained: NaCl (122.5 mM); KCl (5.4 mM), CaCl2 (1.2 mM), MgCl2 (0.8 mM), D-glucose (11 mM), Hepes (25 mM) and NaH2PO4 (1 mM) in milli-Q water. The pH of the solution was then corrected to 7.4.

7.15.2. Live-Cell Confocal Microscopy

Confocal images were obtained using a Zeiss Axiovert 200 M LSM 150-META confocal microscope. The ojective lens used for imaging was a Plan-Apochromat 63x/1.40 Oil DIC M27, and the cells were incubated at 37 °C. Images were captured and processed using the software on ZEN 2011 (Carl Zeiss Microscopy GmbH). To minimize cell phototoxicity, the laser transmission was kept as low as possible. For the dansyl-linked probe, a 405 nm laser was used with collection wavelengths spanning 465 nm to 600 nm. To maximize the collected signal, a concentration of 20 µM of the probe was used. (Lower concentrations did not yield sufficient signal for the detector.)

7.16. *In vitro* resistance selection and cloning

The resistance selection assay was carried out following the method described by Ng *et al.*[328] Briefly, three flasks containing *Pf*-Dd2 parasites at 4% parasitemia (3 % HCT in 100 mL of culture media) were cultured under 3x, 4x, 5x, or 7x the IC_{50} of either complex **4a.1** or **4f**, as shown in **Table 7.2**.

Table 7.2. The multiples of complexes **4a.1** and **4f** IC_{50} values were used for the dosing in the resistance selections.

	Complex	
	4a.1	**4f**
Pf-Dd2 IC_{50} (nM)	212	121
Multiple of IC_{50} (flask #)	3x (Fl1), 4x (Fl2), 5x (Fl3)	3x (Fl4), 5x (Fl5), 7x (Fl6)

The growth medium was replaced daily for seven days with the dosing of the test compound at the relevant concentrations. The morphological changes of parasites in each flask were monitored using culture smears stained with Giemsa. After seven days, monitoring of each flask occurred every second or third day in which media was replaced and fresh aliquots of the test compound were added. Fresh RBCs (1% HCT) were added to each flask once a week and the total culture volume decreased to 50 mL by the third week of culturing.

The bulk mutant culture of recrudesced parasites that resulted from selection with 3 x IC_{50} of **4f** was profiled against the test compound (**4f**) using the standard pLDH assay to confirm their resistance. Monoclonal cells of the recrudesced parasites were then isolated using cloning via the limiting dilution method described by Macedo-Silva *et al.*[331] with minor modifications. The stock solution of bulk parasites was diluted using **Equation 7.7** so that each well in a 96-well plate contained either 0.25 or 0.5 parasites per well.

$$\frac{\mathrm{HCT}\times\mathrm{P}\times10^{10}}{10^{4}\times200}\times\mathbf{X}=\frac{(1/2)\mathrm{or}(1/4)}{200\ \mu\mathrm{L}}\times24\,000\ \mu\mathrm{L}\quad\textbf{Eq. 7.7}$$

The plates were incubated for 17 days, with changes to the growth medium and replenishment of 0.4% RBCs every 7 days. The plates were screened for viable parasites on day 18 using flow cytometry.

For the flow cytometry experiment, a 1:1 (0.5 µL:0.5 µL) ratio of MitoTracker Deep Red Thermo Fisher Scientific):SYBR Green I (Invitrogen Thermo Fisher Scientific) was added to PBS (5 mL). The staining solution (40 µL) was added to a new 96-well plate followed by 5 µL of resuspended cells. The plates were incubated at 37 °C for 20 minutes before being read on an Accuri BD C6 flow cytometer. Positive wells were expanded into a 24-well plate and further expanded into 50 mL culture flasks for phenotypic profiling. Isolate clones were expanded into larger culture flasks (100 mL) for harvesting of the resistant trophozoite cells.

7.17. Harvesting clone trophozoites to extract gDNA

A 100 mL culture at 3% hematocrit and approximately 10% parasitemia was divided into two 50 mL falcon tubes and spun down in a centrifuge at 1500 rpm for 3 minutes. The pellet was washed with PBS (20 mL), spun down and the supernatant removed. Saponin lysis was performed by resuspending the pellet in PBS (50 mL) containing 0.1% saponin. The suspension was incubated on ice for 10 min. The solution was spun down at 4000 rpm for 10 minutes with a slow break setting (break 2) on the centrifuge. The supernatant was removed with an aspirator and the pellet resuspended in 10 mL PBS containing 0.1% saponin and incubated on ice for 5 minutes. The solution was once again spun down at 4000 rpm for 5 minutes with a slow break setting (break 2) and the supernatant was removed. PBS (1 mL) was added to the tube and the pellet was resuspended and then transferred to an Eppendorf and frozen in 3x aliquots at -20 °C until needed for gDNA extraction.

The clone and Dd2 parent gDNA were extracted from harvested cells using a Qiagen QIAamp DNA blood mini kit after which its purity was verified using a NanoDrop1000 spectrophotometer.

7.18. Whole genome sequencing (WGS) of harvested gDNA

WSG was performed via collaborators at the Columbia University Medical Center, New York (Fidock group).

For the WGS of the extracted gDNA from parental *Pf*-Dd2 and clones isolated from the resistant selection of complex **4f**, an Illumina TruSeqDNA PCR-Free library preparation protocol and a MiSeq sequencing platform were used. Briefly, gDNA (2 mg) was cut so that there was an average length of 256 containing 550 bp. These were then end-repaired, adenylated on their 3’ ends, and ligated to indexed adaptors. Sequencing of pooled samples were conducted on Illumina MiSeq flow cells to obtain end reads of 300 bp pairs. Sequence data were compared to that of the *Pf*-Dd2 (PlasmoDB version 48) using BWA (Burrow-

Wheeler Alignment). Reads that did not correlate to the reference genome and PCR duplicates were removed using Samtools and Picard. GATK Realigner Target Creator was used to realign reads around indels while GATK Table-Recalibration was used to recalibrate the quality scores. Variants were filtered using quality scores (as a function of depth QD > 1.5, mapping quality > 40) and read depth (depth of reading > 5) on GATK HaplotypeCaller (version 4.1.8; Min Base quality score ≥ 20). This was done to obtain qualitative single nucleotide polymorphisms (SNPs) which were annotated using snpEFF. SNPs of the **4f**-resistant clones were compared with those of *Pf*-Dd2 to identify homozygous SNPs exclusive to the resistant clones. The SNPs were then confirmed with IGV. Copy number variants (CNVs) in the gDNA sequence of the **4f**-resistant clones were identified using BicSeq which used the *Pf*-Dd2 parent as a reference.

References

(1) Carter, R.; Mendis, K. N. Evolutionary and Historical Aspects of the Burden of Malaria. *Clin Microbiol Rev* 2002, 15 (4), 564–594. https://doi.org/10.1128/CMR.15.4.564-594.2002.

(2) Gelband, H.; Panosian, C. B.; Arrow, K. J. Saving Lives, Buying Time; Economics of Malaria Drugs in an age of Resistance, Eds.; *National Academies Press*: Washington, D.C., 2004. https://doi.org/10.17226/11017.

(3) Sherman, I. W. Biochemistry of *Plasmodium* (Malarial Parasites). *Microbiol Rev* 1979, 43 (4), 453–495. https://doi.org/10.1128/mr.43.4.453-495.1979.

(4) Martinsen, E. S.; Perkins, S. L.; Schall, J. J. A Three-Genome Phylogeny of Malaria Parasites (*Plasmodium* and Closely Related Genera): Evolution of Life-History Traits and Host Switches. *Mol Phylogenet Evol* 2008, 47 (1), 261–273. https://doi.org/10.1016/j.ympev.2007.11.012.

(5) Sato, S. *Plasmodium*—a Brief Introduction to the Parasites Causing Human Malaria and Their Basic Biology. *J Physiol Anthropol* 2021, 40 (1), 1. https://doi.org/10.1186/s40101-020-00251-9.

(6) Tilley, L.; Dixon, M. W. A.; Kirk, K. The *Plasmodium falciparum*-Infected Red Blood Cell. *Int J Biochem and Cell Biol* 2011, 43 (6), 839–842. https://doi.org/10.1016/j.biocel.2011.03.012.

(7) Howes, R. E.; Battle, K. E.; Mendis, K. N.; Smith, D. L.; Cibulskis, R. E.; Baird, J. K.; Hay, S. I. Global Epidemiology of *Plasmodium* Vivax. *Am J Trop Med Hyg* 2016, 95 (6 Suppl), 15–34. https://doi.org/10.4269/ajtmh.16-0141.

(8) Bruce-Chwatt, L. J. Alphonse Laveran's Discovery 100 Years Ago and Today's Global Fight against Malaria. *J R Soc Med* 1981, 74 (7), 531–536. https://doi.org/10.1177/014107688107400715

(9) Cox, F. E. History of the Discovery of the Malaria Parasites and Their Vectors. *Parasit Vectors* 2010, 3 (1), 1–9. https://doi.org/10.1186/1756-3305-3-5.

(10) Shortt, H. E.; Garnham, P. C. C. Demonstration of a Persisting Exo-Erythrocytic Cycle in *Plasmodium cynomolgi* and Its Bearing on the Production of Relapses. *Br Med J* 1948, 1 (4564), 1225–1228. https://doi.org/10.1136/bmj.1.4564.1225.

(11) Sinden, R.; Talman, A.; Marques, S.; Wass, M.; Sternberg, M. The Flagellum in Malarial Parasites. *Curr Opin Microbiol* 2010, 13 (4), 491–500. https://doi.org/10.1016/j.mib.2010.05.016.

(12) *World Health Organization*. World Malaria Report 2023; Geneva, 2023.

(13) Vale, N.; Aguiar, L.; Gomes, P. Antimicrobial Peptides: A New Class of Antimalarial Drugs? *Front Pharmacol* 2014, 5 (Dec), 275. https://doi.org/10.3389/fphar.2014.00275.

(14) Bousema, T.; Drakeley, C. Epidemiology and Infectivity of *Plasmodium falciparum* and *Plasmodium vivax* Gametocytes in Relation to Malaria Control and Elimination. *Clin Microbiol Rev* 2011, 24 (2), 377–410. https://doi.org/10.1128/CMR.00051-10.

(15) van Dijk, M. R.; Janse, C. J.; Thompson, J.; Waters, A. P.; Braks, J. A. M.; Dodemont, H. J.; Stunnenberg, H. G.; van Gemert, G.-J.; Sauerwein, R. W.; Eling, W. A Central Role for P48/45 in Malaria Parasite Male Gamete Fertility. Cell 2001, 104 (1), 153–164. https://doi.org/10.1016/S0092-8674(01)00199-4.

(16) Valenciano, A. L.; Gomez-Lorenzo, M. G.; Vega-Rodríguez, J.; Adams, J. H.; Roth, A. In Vitro Models for Human Malaria: Targeting the Liver Stage. *Trends Parasitol* 2022, 38 (9), 758–774. https://doi.org/10.1016/j.pt.2022.05.014.

(17) Kinsinger, L. S.; Oignone, M.; Nelson, H. D. *Health Promotion and Disease Prevention in Clinical Practice*, second edition.; Woolf, S. H., Jonas, S., Kaplan-Liss, E., Eds.; Lippincott Williams & Wilkins: USA, 2008.

(18) Dorjsuren, D.; Eastman, R. T.; Wicht, K. J.; Jansen, D.; Talley, D. C.; Sigmon, B. A.; Zakharov, A. V; Roncal, N.; Girvin, A. T.; Antonova-Koch, Y.; Will, P. M.; Shah, P.; Sun, H.; Klumpp-Thomas, C.; Mok, S.; Yeo, T.; Meister, S.; Marugan, J. J.; Ross, L. S.; Xu, X.; Maloney, D. J.; Jadhav, A.; Mott, B. T.; Sciotti, R. J.; Winzeler, E. A.; Waters, N. C.; Campbell, R. F.; Huang, W.; Simeonov, A.; Fidock, D. A. Chemoprotective Antimalarials Identified through Quantitative High-Throughput Screening of *Plasmodium* Blood and Liver Stage Parasites. *Sci Rep* 2021, 11 (1), 2121. https://doi.org/10.1038/s41598-021-81486-z.

(19) Watson, J. A.; Commons, R. J.; Tarning, J.; Simpson, J. A.; Llanos Cuentas, A.; Lacerda, M. V. G.; Green, J. A.; Koh, G. C. K. W.; Chu, C. S.; Nosten, F. H.; Price, R. N.; Day, N. P. J.; White, N. J. The Clinical Pharmacology of Tafenoquine in the Radical Cure of *Plasmodium* Vivax Malaria: An Individual Patient Data Meta-Analysis. *Elife* 2022, 11. https://doi.org/10.7554/eLife.83433.

(20) Camarda, G.; Jirawatcharadech, P.; Priestley, R. S.; Saif, A.; March, S.; Wong, M. H. L.; Leung, S.; Miller, A. B.; Baker, D. A.; Alano, P.; Paine, M. J. I.; Bhatia, S. N.; O'Neill, P. M.; Ward, S. A.; Biagini, G. A. Antimalarial Activity of Primaquine Operates via a Two-Step Biochemical Relay. *Nat Commun* 2019, 10 (1), 3226. https://doi.org/10.1038/s41467-019-11239-0.

(21) Vera, I. M.; Grilo Ruivo, M. T.; Lemos Rocha, L. F.; Marques, S.; Bhatia, S. N.; Mota, M. M.; Mancio-Silva, L. Targeting Liver Stage Malaria with Metformin. *JCI Insight* 2019, 4 (24). https://doi.org/10.1172/jci.insight.127441.

(22) Ruivo, M. T. G.; Vera, I. M.; Sales-Dias, J.; Meireles, P.; Gural, N.; Bhatia, S. N.; Mota, M. M.; Mancio-Silva, L. Host AMPK Is a Modulator of *Plasmodium* Liver Infection. *Cell Rep* 2016, 16 (10), 2539–2545. https://doi.org/10.1016/j.celrep.2016.08.001.

(23) Stanway, R. R.; Bushell, E.; Chiappino-Pepe, A.; Roques, M.; Sanderson, T.; Franke-Fayard, B.; Caldelari, R.; Golomingi, M.; Nyonda, M.; Pandey, V.; Schwach, F.; Chevalley, S.; Ramesar, J.; Metcalf, T.; Herd, C.; Burda, P.-C.; Rayner, J. C.; Soldati-Favre, D.; Janse, C. J.; Hatzimanikatis, V.; Billker, O.; Heussler, V. T. Genome-Scale Identification of Essential Metabolic Processes for Targeting the *Plasmodium* Liver Stage. *Cell* 2019, 179 (5), 1112-1128.e26. https://doi.org/10.1016/j.cell.2019.10.030.

(24) Shibeshi, M. A.; Kifle, Z. D.; Atnafie, S. A. Antimalarial Drug Resistance and Novel Targets for Antimalarial Drug Discovery. *Infect Drug Resist* 2020, 13, 4047–4060. https://doi.org/10.2147/IDR.S279433.

(25) Fong, K. Y.; Wright, D. W. Hemozoin and Antimalarial Drug Discovery. *Future Med Chem* 2013, 5 (12), 1437–1450. https://doi.org/10.4155/fmc.13.113.

(26) Egan, T. J. Haemozoin Formation. *Mol Biochem Parasitol* 2008, 157 (2), 127–136. https://doi.org/10.1016/j.molbiopara.2007.11.005.

(27) Kumar, S.; Guha, M.; Choubey, V.; Maity, P.; Bandyopadhyay, U. Antimalarial Drugs Inhibiting Hemozoin (β -Hematin) Formation : A Mechanistic Update. *Life Sci* 2007, 80, 813–828. https://doi.org/10.1016/j.lfs.2006.11.008.

(28) Carter, M.; Phelan, V.; Sandlin, R.; Bachmann, B.; Wright, D. Lipophilic Mediated Assays for β-Hematin Inhibitors. *Comb Chem High Throughput Screen* 2010, 13 (3), 285–292. https://doi.org/10.2174/138620710790980496.

(29) Egan, T. J. Pigment Biocrystallization in *Plasmodium falciparum* Biocrystallization in *Plasmodium*. *Trends Parasitol* 2002, 18 (February), 10–11. https://doi.org/10.1016/S1471-4922(01)02146-8.

(30) Bendrat, K.; Berger, B. J.; Cerami, A. Haem Polymerization in Malaria. *Nature* 1995, 378 (6553), 138–138. https://doi.org/10.1038/378138a0.

(31) Coronado, L. M.; Nadovich, C. T.; Spadafora, C. Malarial Hemozoin: From Target to Tool. *Biochim Biophys Acta Gen Subj* 2014, 1840 (6), 2032–2041. https://doi.org/10.1016/j.bbagen.2014.02.009.

(32) Messina, V.; Valtieri, M.; Rubio, M.; Falchi, M.; Mancini, F.; Mayor, A.; Alano, P.; Silvestrini, F. Gametocytes of the Malaria Parasite *Plasmodium falciparum* Interact With and Stimulate Bone Marrow Mesenchymal Cells to Secrete Angiogenetic Factors. *Front Cell Infect Microbiol* 2018, 8. https://doi.org/10.3389/fcimb.2018.00050.

(33) Demanga, C. G.; Eng, J. W. L.; Gardiner, D. L.; Roth, A.; Butterworth, A.; Adams, J. H.; Trenholme, K. R.; Dalton, J. P. The Development of Sexual Stage Malaria Gametocytes in a Wave Bioreactor. *Parasit Vectors* 2017, 10 (1), 216. https://doi.org/10.1186/s13071-017-2155-z.

(34) Ngwa, C. J.; Rosa, T. F. de A.; Pradel, G. The Biology of Malaria Gametocytes. In Current Topics in Malaria; *InTech*, 2016; pp 117–145. https://doi.org/10.5772/65464.

(35) Kongkasuriyachai, D.; Fujioka, H.; Kumar, N. Functional Analysis of *Plasmodium falciparum* Parasitophorous Vacuole Membrane Protein (Pfs16) during Gametocytogenesis and Gametogenesis by Targeted Gene Disruption. *Mol Biochem Parasitol* 2004, 133 (2), 275–285. https://doi.org/10.1016/j.molbiopara.2003.10.014.

(36) Furuya, T.; Mu, J.; Hayton, K.; Liu, A.; Duan, J.; Nkrumah, L.; Joy, D. A.; Fidock, D. A.; Fujioka, H.; Vaidya, A. B.; Wellems, T. E.; Su, X. Disruption of a *Plasmodium falciparum* Gene Linked to Male Sexual Development Causes Early Arrest in Gametocytogenesis. *Proc Natl Acad Sci* 2005, 102 (46), 16813–16818. https://doi.org/10.1073/pnas.0501858102.

(37) Abugri, J.; Ayariga, J.; Sunwiale, S. S.; Wezena, C. A.; Gyamfi, J. A.; Adu-Frimpong, M.; Agongo, G.; Dongdem, J. T.; Abugri, D.; Dinko, B. Targeting the *Plasmodium falciparum* Proteome and Organelles for Potential Antimalarial Drug Candidates. *Heliyon* 2022, 8 (8), e10390. https://doi.org/10.1016/j.heliyon.2022.e10390.

(38) Hitz, E.; Grüninger, O.; Passecker, A.; Wyss, M.; Scheurer, C.; Wittlin, S.; Beck, H.-P.; Brancucci, N. M. B.; Voss, T. S. The Catalytic Subunit of *Plasmodium falciparum* Casein Kinase 2 Is Essential for Gametocytogenesis. *Commun Biol* 2021, 4 (1), 336. https://doi.org/10.1038/s42003-021-01873-0.

(39) Baker, D. A.; Stewart, L. B.; Large, J. M.; Bowyer, P. W.; Ansell, K. H.; Jiménez-Díaz, M. B.; El Bakkouri, M.; Birchall, K.; Dechering, K. J.; Bouloc, N. S.; Coombs, P. J.; Whalley, D.; Harding, D. J.; Smiljanic-Hurley, E.; Wheldon, M. C.; Walker, E. M.; Dessens, J. T.; Lafuente, M. J.; Sanz, L. M.; Gamo, F.-J.; Ferrer, S. B.; Hui, R.; Bousema, T.; Angulo-Barturén, I.; Merritt, A. T.; Croft, S. L.; Gutteridge, W. E.; Kettleborough, C. A.; Osborne, S. A. A Potent Series Targeting the Malarial CGMP-Dependent Protein Kinase Clears Infection and Blocks Transmission. *Nat Commun* 2017, 8 (1), 430. https://doi.org/10.1038/s41467-017-00572-x.

(40) Munro, B. A.; McMorran, B. J. Antimalarial Drug Strategies to Target *Plasmodium* Gametocytes. *Parasitologia* 2022, 2 (2), 101–124. https://doi.org/10.3390/parasitologia2020011.

(41) Reader, J.; van der Watt, M. E.; Taylor, D.; Le Manach, C.; Mittal, N.; Ottilie, S.; Theron, A.; Moyo, P.; Erlank, E.; Nardini, L.; Venter, N.; Lauterbach, S.; Bezuidenhout, B.; Horatscheck, A.; van Heerden, A.; Spillman, N. J.; Cowell, A. N.; Connacher, J.; Opperman, D.; Orchard, L. M.; Llinás, M.; Istvan, E. S.; Goldberg, D. E.; Boyle, G. A.; Calvo, D.; Mancama, D.; Coetzer, T. L.; Winzeler, E. A.; Duffy, J.; Koekemoer, L. L.; Basarab, G.; Chibale, K.; Birkholtz, L. M. Multistage and Transmission-Blocking Targeted Antimalarials Discovered from the Open-Source MMV Pandemic Response Box. *Nat Commun* 2021, 12 (1). https://doi.org/10.1038/s41467-020-20629-8.

(42) Malebo, H. M.; D'Alessandro, S.; Ebstie, Y. A.; Sorè, H.; Tenoh Guedoung, A. R.; Katani, S. J.; Parapini, S.; Taramelli, D.; Habluetzel, A. In Vitro Multistage Malaria Transmission Blocking Activity of Selected Malaria Box Compounds. *Drug Des Devel Ther* 2020, 14, 1593–1607. https://doi.org/10.2147/DDDT.S242883.

(43) Plouffe, D. M.; Wree, M.; Du, A. Y.; Meister, S.; Li, F.; Patra, K.; Lubar, A.; Okitsu, S. L.; Flannery, E. L.; Kato, N.; Tanaseichuk, O.; Comer, E.; Zhou, B.; Kuhen, K.; Zhou, Y.; Leroy, D.; Schreiber, S. L.; Scherer, C. A.; Vinetz, J.; Winzeler, E. A. High-Throughput Assay and Discovery of Small Molecules That Interrupt Malaria Transmission. *Cell Host Microbe* 2016, 19 (1), 114–126. https://doi.org/10.1016/j.chom.2015.12.001.

(44) Sanders, N. G.; Sullivan, D. J.; Mlambo, G.; Dimopoulos, G.; Tripathi, A. K. Gametocytocidal Screen Identifies Novel Chemical Classes with *Plasmodium falciparum* Transmission Blocking Activity. *PLoS One* 2014, 9 (8), e105817. https://doi.org/10.1371/journal.pone.0105817.

(45) Pryce, J.; Richardson, M.; Lengeler, C. Insecticide-Treated Nets for Preventing Malaria. Cochrane Database Sys Rev 2018. https://doi.org/10.1002/14651858.CD000363.pub3.

(46) Pryce, J.; Medley, N.; Choi, L. Indoor Residual Spraying for Preventing Malaria in Communities Using Insecticide-Treated Nets. *Cochrane Database of Systematic Reviews* 2022, *2022* (1). https://doi.org/10.1002/14651858.CD012688.pub3.

(47) Lindsay, S. W.; Thomas, M. B.; Kleinschmidt, I. Threats to the Effectiveness of Insecticide-Treated Bednets for Malaria Control: Thinking beyond Insecticide Resistance. *Lancet Glob Health* 2021, 9 (9), e1325–e1331. https://doi.org/10.1016/S2214-109X(21)00216-3.

(48) Killeen, G. F.; Smith, T. A.; Ferguson, H. M.; Mshinda, H.; Abdulla, S.; Lengeler, C.; Kachur, S. P. Preventing Childhood Malaria in Africa by Protecting Adults from Mosquitoes with Insecticide-Treated Nets. *PLoS Med* 2007, 4 (7), e229. https://doi.org/10.1371/journal.pmed.0040229.

(49) Govella, N. J.; Okumu, F. O.; Killeen, G. F. Insecticide-Treated Nets Can Reduce Malaria Transmission by Mosquitoes Which Feed Outdoors. *Am J Trop Med* Hyg 2010, 82 (3), 415–419. https://doi.org/10.4269/ajtmh.2010.09-0579.

(50) Nussenzweig, R. S.; Vanderberg, J.; Most, H.; Orton, C. Protective Immunity Produced by the Injection of X-Irradiated Sporozoites of *Plasmodium berghei*. *Nature* 1967, 216 (5111), 160–162. https://doi.org/10.1038/216160a0.

(51) Datoo, M. S.; Dicko, A.; Tinto, H.; Ouédraogo, J.-B.; Hamaluba, M.; Olotu, A.; Beaumont, E.; Ramos Lopez, F.; Natama, H. M.; Weston, S.; Chemba, M.; Compaore, Y. D.; Issiaka, D.; Salou, D.; Some, A. M.; Omenda, S.; Lawrie, A.; Bejon, P.; Rao, H.; Chandramohan, D.; Roberts, R.; Bharati, S.; Stockdale, L.; Gairola, S.; Greenwood, B. M.; Ewer, K. J.; Bradley, J.; Kulkarni, P. S.; Shaligram, U.; Hill, A. V. S.; Mahamar, A.; Sanogo, K.; Sidibe, Y.; Diarra, K.; Samassekou, M.; Attaher, O.; Tapily, A.; Diallo, M.; Dicko, O. M.; Kaya, M.; Maguiraga, S. O.; Sankare, Y.; Yalcouye, H.; Diarra, S.; Niambele, S. M.; Thera, I.; Sagara, I.; Sylla, M.; Dolo, A.; Misidai, N.; Simando, S.; Msami, H.; Juma, O.; Gutapaka, N.; Paul, R.; Mswata, S.; Sasamalo, I.; Johaness, K.; Sultan, M.; Alexander, A.; Kimaro, I.; Lwanga, K.; Mtungwe, M.; Khamis, K.;

Rugarabam, L.; Kalinga, W.; Mohammed, M.; Kamange, J.; Msangi, J.; Mwaijande, B.; Mtaka, I.; Mhapa, M.; Mlaganile, T.; Mbaga, T.; Yerbanga, R. S.; Samtouma, W.; Sienou, A. A.; Kabre, Z.; Ouedraogo, W. J. M.; Yarbanga, G. A. B.; Zongo, I.; Savadogo, H.; Sanon, J.; Compaore, J.; Kere, I.; Yoni, F. L.; Sanre, T. M.; Ouattara, S. B.; Provstgaard-Morys, S.; Woods, D.; Snow, R. W.; Amek, N.; Ngetsa, C. J.; Ochola-Oyier, L. I.; Musyoki, J.; Munene, M.; Mumba, N.; Adetifa, U. J.; Muiruri, C. M.; Mwawaka, J. S.; Mwaganyuma, M. H.; Ndichu, M. N.; Weya, J. O.; Njogu, K.; Grant, J.; Webster, J.; Lakhkar, A.; Ido, N. F. A.; Traore, O.; Tahita, M. C.; Bonko, M. dit A.; Rouamba, T.; Ouedraogo, D. F.; Soma, R.; Millogo, A.; Ouedraogo, E.; Sorgho, F.; Konate, F.; Valea, I. Safety and Efficacy of Malaria Vaccine Candidate R21/Matrix-M in African Children: A Multicentre, Double-Blind, Randomised, Phase 3 Trial. *The Lancet* 2024, 403 (10426), 533–544. https://doi.org/10.1016/S0140-6736(23)02511-4.

(52) Björkman, A.; Benn, C. S.; Aaby, P.; Schapira, A. RTS,S/AS01 Malaria Vaccine—Proven Safe and Effective? *Lancet Infect Dis* 2023, 23 (8), e318–e322. https://doi.org/10.1016/S1473-3099(23)00126-3.

(53) Genton, B. R21/Matrix-MTM Malaria Vaccine: A New Tool to Achieve WHO's Goal to Eliminate Malaria in 30 Countries by 2030? *J Travel Med* 2023, 30 (8). https://doi.org/10.1093/jtm/taad140.

(54) Nnaji, C. A.; Amaechi, U. A.; Wiysonge, C. S. R21/Matrix-M Vaccine: Optimising Supply, Maximising Impact. *The Lancet* 2024, 403 (10426), 525. https://doi.org/10.1016/S0140-6736(23)02716-2.

(55) Greenwood, B.; Cairns, M.; Chaponda, M.; Chico, R. M.; Dicko, A.; Ouedraogo, J.-B.; Phiri, K. S.; ter Kuile, F. O.; Chandramohan, D. Combining Malaria Vaccination with Chemoprevention: A Promising New Approach to Malaria Control. *Malar J* 2021, 20 (1), 361. https://doi.org/10.1186/s12936-021-03888-8.

(56) Achan, J.; Talisuna, A. O.; Erhart, A.; Yeka, A.; Tibenderana, J. K.; Baliraine, F. N.; Rosenthal, P. J.; D'Alessandro, U. Quinine, an Old Anti-Malarial Drug in a Modern World: Role in the Treatment of Malaria. *Malar J* 2011, 10 (1), 144. https://doi.org/10.1186/1475-2875-10-144.

(57) Kaufman, T. S.; Rúveda, E. A. The Quest for Quinine: Those Who Won the Battles and Those Who Won the War. *Angew Chem Int* Ed 2005, 44 (6), 854–885. https://doi.org/10.1002/anie.200400663.

(58) van Schalkwyk, D. A. History of Antimalarial Agents. In *Encyclopedia of Life Sciences*; Wiley, 2015; pp 1–5. https://doi.org/10.1002/9780470015902.a0003624.pub3.

(59) Guttmann P; Ehrlich P. Uber Die Wirkung Des Methylenblau Bei Malaria. *Berl Klin Wochenschr* 1891, 28(1), 953–956.

(60) Atamna, H.; Krugliak, M.; Shalmiev, G.; Deharo, E.; Pescarmona, G.; Ginsburg, H. Mode of Antimalarial Effect of Methylene Blue and Some of Its Analogues on *Plasmodium falciparum* in Culture and Their Inhibition of P. Vinckei Petteri and P. Yoelii Nigeriensis in Vivo. *Biochem Pharmacol* 1996, 51 (5), 693–700. https://doi.org/10.1016/S0006-2952(95)02258-9.

(61) Myint, H. Y.; Berman, J.; Walker, L.; Pybus, B.; Melendez, V.; Baird, J. K.; Ohrt, C. Review: Improving the Therapeutic Index of 8-Aminoquinolines by the Use of Drug Combinations: Review of the Literature and Proposal for Future Investigations. *Am J Trop Med Hyg* 2011, 85 (6), 1010–1014. https://doi.org/10.4269/ajtmh.2011.11-0498.

(62) Foley, M.; Tilley, L. Quinoline Antimalarials Mechanisms of Action and Resistance and Prospects for New Agents. *Pharmacol Ther* 1998, 79 (1), 55–87. https://doi.org/10.1016/S0163-7258(98)00012-6.

(63) Vidal, D.; Altés, J.; Smandia, J. A. Yellow Skin Discoloration Induced by Quinacrine in a Patient with Cutaneous Lupus Erythematosus. *Actas Dermosifiliogr* 2013, 104 (1), 89–90. https://doi.org/10.1016/j.ad.2011.12.025.

(64) Pou, S.; Winter, R. W.; Nilsen, A.; Kelly, J. X.; Li, Y.; Doggett, J. S.; Riscoe, E. W.; Wegmann, K. W.; Hinrichs, D. J.; Riscoe, M. K. Sontochin as a Guide to the Development of Drugs against Chloroquine-Resistant Malaria. *Antimicrob Agents Chemother* 2012, 56 (7), 3475–3480. https://doi.org/10.1128/AAC.00100-12.

(65) Al-Bari, Md. A. A. Chloroquine Analogues in Drug Discovery: New Directions of Uses, Mechanisms of Actions and Toxic Manifestations from Malaria to Multifarious Diseases. *J Antimicrob Chemother* 2015, 70 (6), 1608–1621. https://doi.org/10.1093/jac/dkv018.

(66) Coatney, G. R. Pitfalls in a Discovery: The Chronicle of Chloroquine. *Am J Trop Med* Hyg 1963, 12, 121–128. https://doi.org/10.4269/ajtmh.1963.12.121.

(67) Wellems, T. E.; Plowe, C. V. Chloroquine-Resistant Malaria. *J Infect Dis* 2001, 184 (6), 770–776. https://doi.org/10.1086/322858.

(68) Kaur, K.; Jain, M.; Reddy, R. P.; Jain, R. Quinolines and Structurally Related Heterocycles as Antimalarials. *Eur J Med Chem* 2010, 45 (8), 3245–3264. https://doi.org/10.1016/j.ejmech.2010.04.011.

(69) Pillat, M. M.; Krüger, A.; Guimarães, L. M. F.; Lameu, C.; de Souza, E. E.; Wrenger, C.; Ulrich, H. Insights in Chloroquine Action: Perspectives and Implications in Malaria and COVID-19. *Cytom Part A* 2020, 97 (9), 872–881. https://doi.org/10.1002/cyto.a.24190.

(70) Martin, R. E.; Marchetti, R. V.; Cowan, A. I.; Howitt, S. M.; Bröer, S.; Kirk, K. Chloroquine Transport via the Malaria Parasite's Chloroquine Resistance Transporter. *Science* (1979) 2009, 325 (5948), 1680–1682. https://doi.org/10.1126/science.1175667.

(71) Kuter, D.; Benjamin, S. J.; Egan, T. J. Multiple Spectroscopic and Magnetic Techniques Show That Chloroquine Induces Formation of the μ-Oxo Dimer of Ferriprotoporphyrin IX. *J Inorg Biochem* 2014, 133, 40–49. https://doi.org/10.1016/j.jinorgbio.2014.01.002.

(72) de Villiers, K. A.; Egan, T. J. Heme Detoxification in the Malaria Parasite: A Target for Antimalarial Drug Development. *Acc Chem Res* 2021, 54 (11), 2649–2659. https://doi.org/10.1021/acs.accounts.1c00154.

(73) Herraiz, T.; Guillén, H.; González-Peña, D.; Arán, V. J. Antimalarial Quinoline Drugs Inhibit β-Hematin and Increase Free Hemin Catalyzing Peroxidative Reactions and Inhibition of Cysteine Proteases. *Sci Rep* 2019, 9 (1), 15398. https://doi.org/10.1038/s41598-019-51604-z.

(74) Acosta, M. E.; Gotopo, L.; Gamboa, N.; Rodrigues, J. R.; Henriques, G. C.; Cabrera, G.; Romero, A. H. Antimalarial Activity of Highly Coordinative Fused Heterocycles Targeting β-Hematin Crystallization. *ACS Omega* 2022, 7 (9), 7499–7514. https://doi.org/10.1021/acsomega.1c05393.

(75) Hyde, J. E. Exploring the Folate Pathway in *Plasmodium falciparum*. *Acta Trop* 2005, 94 (3), 191–206. https://doi.org/10.1016/j.actatropica.2005.04.002.

(76) Nzila, A. The Past, Present and Future of Antifolates in the Treatment of *Plasmodium falciparum* Infection. *J Antimicrob Chemother* 2006, 57 (6), 1043–1054. https://doi.org/10.1093/jac/dkl104.

(77) Tse, E. G.; Korsik, M.; Todd, M. H. The Past, Present and Future of Anti-Malarial Medicines. *Malar J* 2019, 18 (1), 93. https://doi.org/10.1186/s12936-019-2724-z.

(78) Carrington, H. C.; Crowther, A. F.; Davey, D. G.; Levi, A. A.; Rose, F. L. A Metabolite of 'Paludrine' with High Antimalarial Activity. *Nature* 1951, 168 (4286), 1080–1080. https://doi.org/10.1038/1681080a0.

(79) Falco, E. A.; Goodwin, L. G.; Hitching, G. H.; Rollo, I. M.; Russell, P. B. 2:4-Diaminopyrimidines- a New Series of Antimalarials. *Br J Pharmacol Chemother* 1951, 6 (2), 185–200. https://doi.org/10.1111/j.1476-5381.1951.tb00634.x.

(80) Wattanagoon, Y.; Taylor, R.; Moody, R.; Ochekpe, N.; Looareesuwan, S.; White, N. Single Dose Pharmacokinetics of Proguanil and Its Metabolites in Healthy Subjects. *Br J Clin Pharmacol* 1987, 24 (6), 775–780. https://doi.org/10.1111/j.1365-2125.1987.tb03245.x.

(81) Baggish, A. L.; Hill, D. R. Antiparasitic Agent Atovaquone. *Antimicrob Agents Chemother* 2002, 46 (5), 1163–1173. https://doi.org/10.1128/AAC.46.5.1163-1173.2002.

(82) Wang, J.; Xu, C.; Wong, Y. K.; Li, Y.; Liao, F.; Jiang, T.; Tu, Y. Artemisinin, the Magic Drug Discovered from Traditional Chinese Medicine. *Engineering* 2019, 5 (1), 32–39. https://doi.org/10.1016/j.eng.2018.11.011.

(83) Krishna, S.; Bustamante, L.; Haynes, R. K.; Staines, H. M. Artemisinins: Their Growing Importance in Medicine. *Trends Pharmacol Sci* 2008, 29 (10), 520–527. https://doi.org/10.1016/j.tips.2008.07.004.

(84) Faurant, C. From Bark to Weed: The History of Artemisinin. *Parasite* 2011, 18 (3), 215–218. https://doi.org/10.1051/parasite/2011183215.

(85) McIntosh, H. M.; Olliaro, P. Artemisinin Derivatives for Treating Uncomplicated Malaria. *Cochrane Database Syst Rev* 2000, 1999 (2), CD000256. https://doi.org/10.1002/14651858.CD000256.

(86) Tilley, L.; Straimer, J.; Gnädig, N. F.; Ralph, S. A.; Fidock, D. A. Artemisinin Action and Resistance in *Plasmodium falciparum*. *Trends Parasitol* 2016, 32 (9), 682–696. https://doi.org/10.1016/j.pt.2016.05.010.

(87) Siqueira-Neto, J. L.; Wicht, K. J.; Chibale, K.; Burrows, J. N.; Fidock, D. A.; Winzeler, E. A. Antimalarial Drug Discovery: Progress and Approaches. *Nat Rev Drug Discov* 2023, 22 (10), 807–826. https://doi.org/10.1038/s41573-023-00772-9.

(88) Zhu, P.; Zhou, B. The Antagonizing Role of Heme in the Antimalarial Function of Artemisinin: Elevating Intracellular Free Heme Negatively Impacts Artemisinin Activity in *Plasmodium falciparum*. *Molecules* 2022, 27 (6), 1755. https://doi.org/10.3390/molecules27061755.

(89) Meshnick, S. R. Artemisinin Antimalarials: Mechanisms of Action and Resistance. *Med Trop (Mars)* 1998, 58 (3 Suppl), 13–17.

(90) Ma, W.; Balta, V. A.; West, R.; Newlin, K. N.; Miljanić, O. Š.; Sullivan, D. J.; Vekilov, P. G.; Rimer, J. D. A Second Mechanism Employed by Artemisinins to Suppress *Plasmodium falciparum* Hinges on Inhibition of Hematin Crystallization. *J Biol Chem* 2021, 296, 100123. https://doi.org/10.1074/jbc.RA120.016115.

(91) White, N. J. Antimalarial Drug Resistance. *J Clin Invest* 2004, 113 (8), 1084–1092. https://doi.org/10.1172/JCI21682.

(92) Hutchinson, D. B.; Viravan, C.; Kyle, D. E.; Looareesuwan, S.; Canfield, C. J.; Webster, H. K. Clinical Studies of Atovaquone, Alone or in Combination with Other Antimalarial Drugs, for Treatment of Acute Uncomplicated Malaria in Thailand. *Am J Trop Med Hyg* 1996, 54 (1), 62–66. https://doi.org/10.4269/ajtmh.1996.54.62.

(93) Antony, H. A.; Parija, S. C. Antimalarial Drug Resistance: An Overview. *Trop Parasitol* 2016, 6 (1), 30–41. https://doi.org/10.4103/2229-5070.175081.

(94) Klein, E. Y. Antimalarial Drug Resistance: A Review of the Biology and Strategies to Delay Emergence and Spread. *Int J Antimicrob Agents* 2013, 41 (4), 311–317. https://doi.org/10.1016/j.ijantimicag.2012.12.007.

(95) Krogstad, D. J.; Gluzman, I. Y.; Herwaldt, B. L.; Schlesinger, P. H.; Wellems, T. E. Energy Dependence of Chloroquine Accumulation and Chloroquine Efflux in *Plasmodium falciparum*. *Biochem Pharmacol* 1992, 43 (1), 57–62. https://doi.org/10.1016/0006-2952(92)90661-2.

(96) Andrea Ecker, Adele M. Lehane, Jérôme Clain, and D. A. F. PfCRT and Its Role in Antimalarial Drug Resistance. *Trends Parasitol* 2012, 4, 504–514. https://doi.org/10.1016/j.pt.2012.08.002.PfCRT.

(97) Tarama, C. W.; Soré, H.; Siribié, M.; Débé, S.; Kinda, R.; Ganou, A.; Nonkani, W. G.; Tiendrebeogo, F.; Bantango, W.; Yira, K.; Sagnon, A.; Ilboudo, S.; Hien, E. Y.; Guelbéogo, M. W.; Sagnon, Nf.; Traoré, Y.; Ménard, D.; Gansané, A. *Plasmodium falciparum* Drug Resistance-Associated Mutations in Isolates from Children Living in Endemic Areas of Burkina Faso. *Malar J* 2023, 22 (1), 213. https://doi.org/10.1186/s12936-023-04645-9.

(98) Nagesha, H. S.; Din-Syafruddin; Casey, G. J.; Susanti, A. I.; Fryauff, D. J.; Reeder, J. C.; Cowman, A. F. Mutations in the Pfmdr1, Dhfr and Dhps Genes of *Plasmodium falciparum* Are Associated with in-Vivo Drug Resistance in West Papua, Indonesia. Trans R Soc Trop *Med Hyg* 2001, 95 (1), 43–49. https://doi.org/10.1016/S0035-9203(01)90329-3.

(99) Triglia, T.; Cowman, A. F. Primary Structure and Expression of the Dihydropteroate Synthetase Gene of *Plasmodium falciparum*. *Proc Natl Acad Sci USA* 1994, 91 (15), 7149–7153. https://doi.org/10.1073/pnas.91.15.7149.

(100) Noedl, H.; Se, Y.; Sriwichai, S.; Schaecher, K.; Teja-Isavadharm, P.; Smith, B.; Rutvisuttinunt, W.; Bethell, D.; Surasri, S.; Fukuda, M. M.; Socheat, D.; Chan Thap, L. Artemisinin Resistance in Cambodia: A Clinical Trial Designed to Address an Emerging Problem in Southeast Asia. *Clin Infect Dis* 2010, 51 (11), e82-9. https://doi.org/10.1086/657120.

(101) Hanboonkunupakarn, B.; Tarning, J.; Pukrittayakamee, S.; Chotivanich, K. Artemisinin Resistance and Malaria Elimination: Where Are We Now? *Front Pharmacol* 2022, 13, 876282. https://doi.org/10.3389/fphar.2022.876282.

(102) Chotivanich, K.; Tripura, R.; Das, D.; Yi, P.; Day, N. P. J.; Pukrittayakamee, S.; Chuor, C. M.; Socheat, D.; Dondorp, A. M.; White, N. J. Laboratory Detection of Artemisinin-Resistant *Plasmodium falciparum*. *Antimicrob Agents Chemother* 2014, 58 (6), 3157–3161. https://doi.org/10.1128/AAC.01924-13.

(103) Zhu, L.; van der Pluijm, R. W.; Kucharski, M.; Nayak, S.; Tripathi, J.; White, N. J.; Day, N. P. J.; Faiz, A.; Phyo, A. P.; Amaratunga, C.; Lek, D.; Ashley, E. A.; Nosten, F.; Smithuis, F.; Ginsburg, H.; von Seidlein, L.; Lin, K.; Imwong, M.; Chotivanich, K.; Mayxay, M.; Dhorda, M.; Nguyen, H. C.; Nguyen, T. N. T.; Miotto, O.; Newton, P. N.; Jittamala, P.; Tripura, R.; Pukrittayakamee, S.; Peto, T. J.; Hien, T. T.; Dondorp, A. M.; Bozdech, Z. Artemisinin Resistance in the Malaria Parasite, *Plasmodium falciparum*, Originates from Its Initial Transcriptional Response. *Commun Biol* 2022, 5 (1), 274. https://doi.org/10.1038/s42003-022-03215-0.

(104) Blasco, B.; Leroy, Di.; Fidock, D. A. Antimalarial Drug Resistance: Linking *Plasmodium falciparum* Parasite Biology to the Clinic. *Nat Med*. Nature Publishing Group August 4, 2017, pp 917–928. https://doi.org/10.1038/nm.4381.

(105) Wicht, K. J.; Mok, S.; Fidock, D. A. Molecular Mechanisms of Drug Resistance in Plasmodium Falciparum Malaria. Annu Rev Microbiol 2020, 74, 431–454. https://doi.org/10.1146/annurev-micro-020518-115546.

(106) Birnbaum, J.; Scharf, S.; Schmidt, S.; Jonscher, E.; Hoeijmakers, W. A. M.; Flemming, S.; Toenhake, C. G.; Schmitt, M.; Sabitzki, R.; Bergmann, B.; Fröhlke, U.; Mesén-Ramírez, P.; Blancke Soares, A.; Herrmann, H.; Bártfai, R.; Spielmann, T. A Kelch13-

Defined Endocytosis Pathway Mediates Artemisinin Resistance in Malaria Parasites. Science (1979) 2020, 367 (6473), 51–59. https://doi.org/10.1126/science.aax4735.

(107) Shibeshi, M. A.; Kifle, Z. D.; Atnafie, S. A. Antimalarial Drug Resistance and Novel Targets for Antimalarial Drug Discovery. *Infect Drug Resist* 2020, 13, 4047–4060. https://doi.org/10.2147/IDR.S279433.

(108) Toczek, J.; Sadłocha, M.; Major, K.; Stojko, R. Benefit of Silver and Gold Nanoparticles in Wound Healing Process after Endometrial Cancer Protocol. *Biomedicines* 2022, 10 (3). https://doi.org/10.3390/biomedicines10030679.

(109) Galib; Barve, M.; Mashru, M.; Jagtap, C.; Patgiri, B. J.; Prajapati, P. K. Therapeutic Potentials of Metals in Ancient India: A Review through Charaka Samhita. *J Ayurveda Integr Med* 2011, 2 (2), 55–63. https://doi.org/10.4103/0975-9476.82523.

(110) Medici, S.; Peana, M.; Marina, V.; Lachowicz, J. I.; Crisponi, G.; Antonietta, M. Noble Metals in Medicine : Latest Advances. *Coord Chem Rev* 2015, 284, 329–350. https://doi.org/10.1016/j.ccr.2014.08.002.

(111) Monneret, C. Platinum Anticancer Drugs. From Serendipity to Rational Design. *Ann Pharm Fr* 2011, 69 (6), 286–295. https://doi.org/10.1016/j.pharma.2011.10.001.

(112) Gómez-Ruiz, S.; Maksimović-Ivanić, D.; Mijatović, S.; Kaluđerović, G. N. On the Discovery, Biological Effects, and Use of Cisplatin and Metallocenes in Anticancer Chemotherapy. *Bioinorg Chem Appl* 2012, 2012, 140284. https://doi.org/10.1155/2012/140284.

(113) Kelland, L. The Resurgence of Platinum-Based Cancer Chemotherapy. *Nat Rev Cancer* 2007, 7 (8), 573–584. https://doi.org/10.1038/nrc2167.

(114) Pricker, S. P. Medical Uses of Gold Compounds: Past, Present and Future. *Gold Bull* 1996, 29 (2), 53–60. https://doi.org/10.1007/BF03215464.

(115) Finkelstein, A. E.; Walz, D. T.; Batista, V.; Mizraji, M.; Roisman, F.; Misher, A. Auranofin. New Oral Gold Compound for Treatment of Rheumatoid Arthritis. *Ann Rheum Dis* 1976, 35 (3), 251–257. https://doi.org/10.1136/ard.35.3.251.

(116) Sutton, B. M.; McGusty, E.; Walz, D. T.; DiMartino, M. J. Oral Gold. Antiarthritic Properties of Alkylphosphinegold Coordination Complexes. *J Med Chem* 1972, 15 (11), 1095–1098. https://doi.org/10.1021/jm00281a001.

(117) Abdalbari, F. H.; Telleria, C. M. The Gold Complex Auranofin: New Perspectives for Cancer Therapy. *Discov Oncol* 2021, 12 (1), 42. https://doi.org/10.1007/s12672-021-00439-0.

(118) Azam, A.; Raza, M. A.; Sumrra, S. H. Therapeutic Application of Zinc and Vanadium Complexes against Diabetes Mellitus a Coronary Disease: A Review. *Open Chem* 2018, 16 (1), 1153–1165. https://doi.org/10.1515/chem-2018-0118.

(119) Sharma, B.; Shukla, S.; Rattan, R.; Fatima, M.; Goel, M.; Bhat, M.; Dutta, S.; Ranjan, R. K.; Sharma, M. Antimicrobial Agents Based on Metal Complexes: Present Situation and Future Prospects. *Int J Biomater* 2022, 2022, 1–21. https://doi.org/10.1155/2022/6819080.

(120) Szczepaniak, A.; Fichna, J. Organometallic Compounds and Metal Complexes in Current and Future Treatments of Inflammatory Bowel Disease and Colorectal Cancer-a Critical Review. *Biomolecules* 2019, 9 (9). https://doi.org/10.3390/biom9090398.

(121) Mjos, K. D.; Orvig, C. Metallodrugs in Medicinal Inorganic Chemistry. *Chem Rev* 2014, 114(8), 4540–4563. https://doi.org/10.1021/cr400460s.

(122) Portes, M. C.; Ribeiro, G. A.; Sabino, G. L.; De Couto, R. A. A.; Vieira, L. Q.; Alves, M. J. M.; Da Costa Ferreira, A. M. Antiparasitic Activity of Oxindolimine–Metal Complexes against Chagas Disease. *Inorganics (Basel)* 2023, 11 (11), 420. https://doi.org/10.3390/inorganics11110420.

(123) Adams, M.; de Kock, C.; Smith, P. J.; Land, K. M.; Liu, N.; Hopper, M.; Hsiao, A.; Burgoyne, A. R.; Stringer, T.; Meyer, M.; Wiesner, L.; Chibale, K.; Smith, G. S. Improved Antiparasitic Activity by Incorporation of Organosilane Entities into Half-Sandwich Ruthenium(II) and Rhodium(III) Thiosemicarbazone Complexes. *Dalt Trans* 2015, 44 (5), 2456–2468. https://doi.org/10.1039/C4DT03234A.

(124) Colina-Vegas, L.; da Cruz B. Silva, M.; de Souza Pereira, C.; Isis Barros, A.; Araújo Nobrega, J.; Navarro, M.; Rottmann, M.; D'Alessandro, S.; Basilico, N.; Azevedo Batista, A.; Moreira, D. R. M. Antimalarial Agents Derived from Metal-Amodiaquine

Complexes with Activity in Multiple Stages of the *Plasmodium* Life Cycle. *Chem Eur J* 2023, 29 (55). https://doi.org/10.1002/chem.202301642.

(125) Warra, A. A. Transition Metal Complexes and Their Application in Drugs and Cosmetics-a Review. *J Chem Pharm Res* 2011, 3 (4), 951–958.

(126) Sodhi, R. K. Metal Complexes in Medicine: An Overview and Update from Drug Design Perspective. *Cancer Ther Oncol Int J* 2019, 14 (2). https://doi.org/10.19080/CTOIJ.2019.14.555883.

(127) Leung, C.-H.; Lin, S.; Zhong, H.-J.; Ma, D.-L. Metal Complexes as Potential Modulators of Inflammatory and Autoimmune Responses. *Chem Sci* 2015, 6 (2), 871–884. https://doi.org/10.1039/c4sc03094j.

(128) Sánchez-Delgado, R. A.; Navarro, M.; Pérez, H.; Urbina, J. A. Toward a Novel Metal-Based Chemotherapy against Tropical Diseases. 2. Synthesis and Antimalarial Activity in Vitro and in Vivo of New Ruthenium-and Rhodium-Chloroquine Complexes. *J Med Chem* 1996, 39 (5), 1095–1099. https://doi.org/10.1021/jm950729w.

(129) C.S. Rajapakse; A. Martínez; B. Naoulou; A.A. Jarzecki; L. Suárez; C. Deregnaucourt; V. Sinou; J. Schrével; E. Musi; G. Ambrosini; G.K. Schwartz; R.A. Sánchez-Delgado. Synthesis, Characterization, and in Vitro Antimalarial and Antitumor Activity of New Ruthenium(II) Complexes of Chloroquine. *Inorg. Chem*. 2009, 48 (3), 1122–1131. https://doi.org/10.1021/ic802220w

(130) Navarro, M.; Castro, W.; Biot, C. Bioorganometallic Compounds with Antimalarial Targets: Inhibiting Hemozoin Formation. *Organometallics* 2012, 31 (16), 5715–5727. https://doi.org/10.1021/om300296n.

(131) Navarro, M.; Vásquez, F.; Sánchez-Delgado, R. A.; Pérez, H.; Sinou, V.; Schrével, J. Toward a Novel Metal-Based Chemotherapy against Tropical Diseases. 7. Synthesis and in Vitro Antimalarial Activity of New Gold-Chloroquine Complexes. *J Med Chem* 2004, 47 (21), 5204–5209. https://doi.org/10.1021/jm049792o.

(132) Navarro, M.; Pekerar, S.; Pérez, H. A. Synthesis, Characterization and Antimalarial Activity of New Iridium-Chloroquine Complexes. *Polyhedron* 2007, 26 (12), 2420–2424. https://doi.org/10.1016/j.poly.2006.12.010.

(133) Ajibade, P. A.; Kolawole, G. A. Synthesis, Characterization and Antiprotozoal Studies of Some Metal Complexes of Antimalarial Drugs. *Transit Met Chem* 2008, 33 (4), 493–497. https://doi.org/10.1007/s11243-008-9070-2.

(134) van Staveren, D. R.; Metzler-Nolte, N. Bioorganometallic Chemistry of Ferrocene. *Chem Rev* 2004, 104 (12), 5931–5985. https://doi.org/10.1021/cr0101510.

(135) Biot, C.; Castro, W.; Botté, C. Y.; Navarro, M. The Therapeutic Potential of Metal-Based Antimalarial Agents: Implications for the Mechanism of Action. *Dalt Trans* 2012, 41 (21), 6335. https://doi.org/10.1039/c2dt12247b.

(136) Daher, W.; Biot, C.; Fandeur, T.; Jouin, H.; Pelinski, L.; Viscogliosi, E.; Fraisse, L.; Pradines, B.; Brocard, J.; Khalife, J.; Dive, D. Assessment of *Plasmodium falciparum* Resistance to Ferroquine (SSR97193) in Field Isolates and in W2 Strain under Pressure. *Malar J* 2006, 5 (1), 11. https://doi.org/10.1186/1475-2875-5-11.

(137) Dubar, F.; Egan, T. J.; Pradines, B.; Kuter, D.; Ncokazi, K. K.; Forge, D.; Paul, J.-F.; Pierrot, C.; Kalamou, H.; Khalife, J.; Buisine, E.; Rogier, C.; Vezin, H.; Forfar, I.; Slomianny, C.; Trivelli, X.; Kapishnikov, S.; Leiserowitz, L.; Dive, D.; Biot, C. The Antimalarial Ferroquine: Role of the Metal and Intramolecular Hydrogen Bond in Activity and Resistance. *ACS Chem Biol* 2011, 6 (3), 275–287. https://doi.org/10.1021/cb100322v.

(138) Xiao, J.; Sun, Z.; Kong, F.; Gao, F. Current Scenario of Ferrocene-Containing Hybrids for Antimalarial Activity. *Eur J Med Chem* 2020, 185, 111791. https://doi.org/10.1016/j.ejmech.2019.111791.

(139) Wani, W. A.; Jameel, E.; Baig, U.; Mumtazuddin, S.; Hun, L. T. Ferroquine and Its Derivatives: New Generation of Antimalarial Agents. *Eur J Med Chem* 2015, 101, 534–551. https://doi.org/10.1016/j.ejmech.2015.07.009.

(140) Dubar, F.; Slomianny, C.; Khalife, J.; Dive, D.; Kalamou, H.; Guérardel, Y.; Grellier, P.; Biot, C. The Ferroquine Antimalarial Conundrum: Redox Activation and Reinvasion Inhibition. *Angew Chem Int Ed* 2013, 52 (30), 7690–7693. https://doi.org/10.1002/anie.201303690.

(141) Salas, P. F.; Herrmann, C.; Cawthray, J. F.; Nimphius, C.; Kenkel, A.; Chen, J.; de Kock, C.; Smith, P. J.; Patrick, B. O.; Adam, M. J.; Orvig, C. Structural Characteristics of Chloroquine-Bridged Ferrocenophane Analogues of Ferroquine May Obviate Malaria Drug-Resistance Mechanisms. *J Med Chem* 2013, 56 (4), 1596–1613. https://doi.org/10.1021/jm301422h.

(142) Femi, A. J.; Ayoola, O. J. Co(II) Complex of Mefloquine Hydrochloride: Synthesis, Antimicrobial Potential, Antimalaria and Toxicological Activities. *E-J Chem* 2012, 9 (4), 2245–2254. https://doi.org/10.1155/2012/940258.

(143) Adediji, J. F.; Oye, T. T.; Oboirien, J. A.; Akano, I. O.; Alabi, F. A. Antimalarial, Antimicrobial, and Acute Toxicity Activities *Pf* Mefloquine-Pyrimethamine Metal Complexes. *Pac Journal Sci technol* 2012, 13 (2), 305–311. https://api.semanticscholar.org/CorpusID:44058776.

(144) Villarreal, W.; Castro, W.; González, S.; Madamet, M.; Amalvict, R.; Pradines, B.; Navarro, M. Copper (I)-Chloroquine Complexes: Interactions with DNA and Ferriprotoporphyrin, Inhibition of β-Hematin Formation and Relation to Antimalarial Activity. *Pharmaceuticals* 2022, 15 (8), 921. https://doi.org/10.3390/ph15080921.

(145) Navarro, M.; Goitia, H.; Silva, P.; Velásquez, M.; Ojeda, L. E.; Fraile, G. Synthesis and Characterization of New Copper– and Zinc–Chloroquine Complexes and Their Activities on Respiratory Burst of Polymorphonuclear Leukocytes. *J Inorg Biochem* 2005, 99 (8), 1630–1636. https://doi.org/10.1016/j.jinorgbio.2005.05.002.

(146) Navarro, M.; Pekerar, S.; Pérez, H. A. Synthesis, Characterization and Antimalarial Activity of New Iridium–Chloroquine Complexes. *Polyhedron* 2007, 26 (12), 2420–2424. https://doi.org/10.1016/j.poly.2006.12.010.

(147) Macedo, T. S.; Coliaa-Vegas, L.; DA Paxao, M.; Navarrr, M.; Barrett, B. C.; Oliveira, P. C. M.; Macambira, S. G.; Machado, M.; Predencio, M.; D'Alessandro, S.; Basilico, N.; Moreira, D. R. M.; Batista, A. A.; Sorres, M. B. P. Chloroquine-Containing Organoruthenium Complexes Are Fast-Acting Multistage Antimalarial Agents. *Parasitology* 2016, 143 (12), 1543–1556. https://doi.org/10.1017/S0031182016001153.

(148) Delhaes, L.; Biot, C.; Berry, L.; Maciejewski, L. A.; Camus, D.; Brocard, J. S.; Dive, D. Novel Ferrocenic Artemisinin Derivatives: Synthesis, in Vitro Antimalarial Activity and Affinity of Binding with Ferroprotoporphyrin IX. *Bioorg Med Chem* 2000, 8 (12), 2739–2745. https://doi.org/10.1016/S0968-0896(00)00206-6.

(149) Albertyn, C. C.; van Niekerk, A.; Duffy, S.; Avery, V. M.; Strauss, E.; Chellan, P. Investigation of Bioorganometallic Artemisinins as Antiplasmodials. *J Organomet Chem* 2023, 987–988, 122633. https://doi.org/10.1016/j.jorganchem.2023.122633.

(150) Rylands, L.; Welsh, A.; Maepa, K.; Stringer, T.; Taylor, D.; Chibale, K.; Smith, G. Structure-Activity Relationship Studies of Antiplasmodial Cyclometallated Ruthenium(II), Rhodium(III) and Iridium(III) Complexes of 2-Phenylbenzimidazoles. *Eur J Med Chem* 2019, 161, 11–21.

(151) Chellan, P.; Avery, V. M.; Duffy, S.; Triccas, J. A.; Nagalingam, G.; Tam, C.; Cheng, L. W.; Liu, J.; Land, K. M.; Clarkson, G. J.; Romero-Canelón, I.; Sadler, P. J. Organometallic Conjugates of the Drug Sulfadoxine for Combatting Antimicrobial Resistance. *Chem Eur J* 2018, 24 (40), 10078–10090. https://doi.org/10.1002/chem.201801090.

(152) Goldberg, D. E.; Sharma, V.; Oksman, A.; Gluzman, I. Y.; Wellems, T. E.; Piwnica-Worms, D. Probing the Chloroquine Resistance Locus of *Plasmodium falciparum* with a Novel Class of Multidentate Metal(III) Coordination Complexes. *J Biol Chem* 1997, 272 (10), 6567–6572. https://doi.org/10.1074/jbc.272.10.6567.

(153) Ocheskey, J. A.; Scott, H. E.; Oksman, A.; Goldberg, D. E.; Sharma, V. Metalloantimalarials: Synthesis and Characterization of a Novel Agent Possessing Activity against *Plasmodium falciparum*. *Chem comm* 2005, 15 (12), 1622–1624. https://doi.org/10.1039/B415771K.

(154) Itoh, T.; Shirakami, S.; Ishida, N.; Yamashita, Y.; Yoshida, T.; Kim, H.-S.; Wataya, Y. Synthesis of Novel Ferrocenyl Sugars and Their Antimalarial Activities. *Bioorg Med Chem Lett* 2000, 10 (15), 1657–1659. https://doi.org/10.1016/S0960-894X(00)00313-9.

(155) Wu, X.; Wilairat, P.; Go, M.-L. Antimalarial Activity of Ferrocenyl Chalcones. *Bioorg Med Chem Lett* 2002, 12 (17), 2299–2302. https://doi.org/10.1016/S0960-894X(02)00430-4.

(156) Geeth Vincent, S.; Joseph, J. Evaluation of Antioxidant Activity and Antimalarial Activity of Flavone Based Tetradentate Ligand and Its Metal Complexes. *Mater Today Proc* 2021, 45, 2159–2165. https://doi.org/10.1016/j.matpr.2020.10.008.

(157) Chellan, P.; Land, K. M.; Shokar, A.; Au, A.; An, S. H.; Taylor, D.; Smith, P. J.; Riedel, T.; Dyson, P. J.; Chibale, K.; Smith, G. S. Synthesis and Evaluation of New Polynuclear Organometallic Ru(II), Rh(III) and Ir(III) Pyridyl Ester Complexes as in Vitro Antiparasitic and Antitumor Agents. *Dalt Trans* 2014, 43 (2), 513–526. https://doi.org/10.1039/C3DT52090K.

(158) González Cabrera, D.; Douelle, F.; Younis, Y.; Feng, T.-S.; Le Manach, C.; Nchinda, A. T.; Street, L. J.; Scheurer, C.; Kamber, J.; White, K. L.; Montagnat, O. D.; Ryan, E.; Katneni, K.; Zabiulla, K. M.; Joseph, J. T.; Bashyam, S.; Waterson, D.; Witty, M. J.; Charman, S. A.; Wittlin, S.; Chibale, K. Structure–Activity Relationship Studies of Orally Active Antimalarial 3,5-Substituted 2-Aminopyridines. *J Med Chem* 2012, 55 (24), 11022–11030. https://doi.org/10.1021/jm301476b.

(159) Liang, X.; Jiang, Z.; Huang, Z.; Li, F.; Chen, C.; Hu, C.; Wang, W.; Hu, Z.; Liu, Q.; Wang, B.; Wang, L.; Qi, Z.; Liu, J.; Jiang, L.; Liu, Q. Discovery of 6′-Chloro-N-Methyl-5'-(Phenylsulfonamido)-[3,3′-Bipyridine]-5-Carboxamide (CHMFL-PI4K-127) as a Novel *Plasmodium falciparum* PI(4)K Inhibitor with Potent Antimalarial Activity against Both Blood and Liver Stages of *Plasmodium*. *Eur J Med Chem* 2020, 188, 112012. https://doi.org/10.1016/j.ejmech.2019.112012.

(160) Kaes, C.; Katz, A.; Hosseini, M. W. Bipyridine: The Most Widely Used Ligand. A Review of Molecules Comprising at Least Two 2,2'-Bipyridine Units. *Chem Rev* 2000, 100 (10), 3553–3590. https://doi.org/10.1021/cr990376z.

(161) Constable, E. C.; Housecroft, C. E. The Early Years of 2,2'-Bipyridine-A Ligand in Its Own Lifetime. *Molecules* 2019, 24 (21). https://doi.org/10.3390/molecules24213951.

(162) Shaikh, I.; Jadeja, R. N.; Patel, R. Three Mixed Ligand Mononuclear Zn(II) Complexes of 4-Acyl Pyrazolones: Synthesis, Characterization, Crystal Study and Anti-Malarial Activity. *Polyhedron* 2020, 183, 114528. https://doi.org/10.1016/j.poly.2020.114528.

(163) Kumari, G.; Gupta, A.; Sah, R. K.; Gautam, A.; Saini, M.; Gupta, A.; Kushawaha, A. K.; Singh, S.; Sasmal, P. K. Development of Mitochondria Targeting AIE-Active Cyclometalated Iridium Complexes as Potent Antimalarial Agents. *Adv Healthc Mater* 2023, 12 (9). https://doi.org/10.1002/adhm.202202411.

(164) Chellan, P.; Avery, V. M.; Duffy, S.; Land, K. M.; Tam, C. C.; Kim, J. H.; Cheng, L. W.; Romero-Canelón, I.; Sadler, P. J. Bioactive Half-Sandwich Rh and Ir Bipyridyl Complexes Containing Artemisinin. *J Inorg Biochem* 2021, 219, 111408. https://doi.org/10.1016/j.jinorgbio.2021.111408.

(165) Macedo, T. S.; Villarreal, W.; Couto, C. C.; Moreira, D. R. M.; Navarro, M.; Machado, M.; Prudêncio, M.; Batista, A. A.; Soares, M. B. P. Platinum(II)-Chloroquine Complexes Are Antimalarial Agents against Blood and Liver Stages by Impairing Mitochondrial Function. *Metallomics* 2017, 9 (11), 1548–1561. https://doi.org/10.1039/c7mt00196g.

(166) de Souza, N. B.; Carmo, A. M. L.; Lagatta, D. C.; Alves, M. J. M.; Fontes, A. P. S.; Coimbra, E. S.; da Silva, A. D.; Abramo, C. 4-Aminoquinoline Analogues and Its Platinum (II) Complexes as Antimalarial Agents. *Biomed Pharmacother* 2011, 65 (4), 313–316. https://doi.org/10.1016/j.biopha.2011.03.003.

(167) Liu, W.; Yu, C.; Wang, M.; He, Y.; Guo, Z.; He, J.; Jiang, R.; Xu, Q.; Liang, J.; Wang, S. Discovery of Platinum(IV) –Artesunate Multiaction Prodrugs as Potent Antitumor and

Antimalarial Agents. *J Med Chem* 2023, 66 (12), 8066–8085. https://doi.org/10.1021/acs.jmedchem.3c00396.

(168) Manzano, J. L.; Benito, J. J.; Hermosa, R.; Rodrı, E.; Monte, E.; Criado, J. J. Thiourea, Triazole and Thiadiazine Compounds and Their Metal Complexes as Antifungal Agents. *J Inorg Biochem* 2005, 99, 1558–1572. https://doi.org/10.1016/j.jinorgbio.2005.05.004.

(169) Nordin, N. A.; Chai, T. W.; Tan, B. L.; Choi, C. L.; Abd Halim, A. N.; Hussain, H.; Ngaini, Z. Novel Synthetic Monothiourea Aspirin Derivatives Bearing Alkylated Amines as Potential Antimicrobial Agents. *J Chem* 2017, 2017. https://doi.org/10.1155/2017/2378186.

(170) Sudzhaev, A. R.; Rzaeva, I. A.; Nadzhafova, R. A. Antioxidant Properties of Some Thiourea Derivatives. *Russ J App Chem* 2011, 84 (August), 1394–1397. https://doi.org/10.1134/S1070427211080167.

(171) Çelen, A. Ö.; Kaymakç, B.; Gümrü, S.; Toklu, H. Z.; Ar, F. Synthesis and Anticonvulsant Activity of Substituted Thiourea Derivatives. *Marmara Pharm J* 2011, 15 (20), 43–47. https://doi.org/10.12991/201115430.

(172) Vinicius, M.; Souza, N. de; Lima, M. de; Bispo, F.; Schroeder, R.; Gonçalves, B.; Kaiser, C. R. Thiourea Derivatives: A Promising Class Against HIV / TB Co-Infection. *Research* 2011, 26 (October), 127–161. https://doi.org/10.5772/23200.

(173) Shakeel, A.; Altaf, A. A.; Qureshi, A. M.; Badshah, A. Thiourea Derivatives in Drug Design and Medicinal Chemistry: A Short Review. *J Drug Design Med Chem* 2016, 2 (1), 10–20. https://doi.org/10.11648/j.jddmc.20160201.12.

(174) Zahra, U.; Saeed, A.; Abdul Fattah, T.; Flörke, U.; Erben, M. F. Recent Trends in Chemistry, Structure, and Various Applications of 1-Acyl-3-Substituted Thioureas: A Detailed Review. *RSC Adv* 2022, 12 (20), 12710–12745. https://doi.org/10.1039/D2RA01781D.

(175) Verlinden, B. K.; Niemand, J.; Snyman, J.; Sharma, S. K.; Beattie, R. J.; Woster, P. M.; Birkholtz, L. M. Discovery of Novel Alkylated (Bis)Urea and (Bis)Thiourea Polyamine Analogues with Potent Antimalarial Activities. *J Med Chem* 2011, 54 (19), 6624–6633. https://doi.org/10.1021/jm200463z.

(176) Pingaew, R.; Sinthupoom, N.; Mandi, P.; Prachayasittikul, V.; Cherdtrakulkiat, R.; Prachayasittikul, S.; Ruchirawat, S.; Prachayasittikul, V. Synthesis, Biological Evaluation and in Silico Study of Bis-Thiourea Derivatives as Anticancer, Antimalarial and Antimicrobial Agents. *Med Chem Res* 2017, 26 (12), 3136–3148. https://doi.org/10.1007/s00044-017-2008-5.

(177) El Bissati, K.; Redel, H.; Ting, L.-M.; Lykins, J. D.; McPhillie, M. J.; Upadhya, R.; Woster, P. M.; Yarlett, N.; Kim, K.; Weiss, L. M. Novel Synthetic Polyamines Have Potent Antimalarial Activities in Vitro and in Vivo by Decreasing Intracellular Spermidine and Spermine Concentrations. *Front Cell Infect Microbiol* 2019, 9. https://doi.org/10.3389/fcimb.2019.00009.

(178) Haider, N.; Eschbach, M.-L.; Dias, S. de S.; Gilberger, T.-W.; Walter, R. D.; Lüersen, K. The Spermidine Synthase of the Malaria Parasite *Plasmodium falciparum*: Molecular and Biochemical Characterisation of the Polyamine Synthesis Enzyme. *Mol Biochem Parasitol* 2005, 142 (2), 224–236. https://doi.org/10.1016/j.molbiopara.2005.04.004.

(179) Egan, T. J.; Koch, K. R.; Swan, P. L.; Clarkson, C.; Schalkwyk, D. A. Van; Smith, P. J. In Vitro Antimalarial Activity of a Series of Cationic 2, 2 ′ -Bipyridyl- and 1, 10-Phenanthrolineplatinum (II) Benzoylthiourea Complexes. *J Med Chem* 2004, 47 (2), 2926–2934. https://doi.org/10.1021/jm031132g.

(180) Koch, K. R.; Sacht, C.; Lawrence, C. Self-Association of New Mixed-Ligand Diimine–N-Acyl-N′,N′-Dialkyl Thioureate Complexes of Platinum(II) in Acetonitrile Solution. *J Chem Soc*, Dalt Trans 1998, No. 4, 689–696. https://doi.org/10.1039/a704577h.

(181) Egan, T. J.; Rossa, D. C.; Adamsb, P. A. Anti-Malarial Drugs Inhibit Spontaneous Formation of p-Haematin (Malaria Pigment). *FEBS Lett* 1994, 352, 54–57.

(182) Ncokazi, K. K.; Egan, T. J. A Colorimetric High-Throughput β-Hematin Inhibition Screening Assay for Use in the Search for Antimalarial Compounds. *Anal Biochem* 2005, 338 (2), 306–319. https://doi.org/10.1016/j.ab.2004.11.022.

(183) Hoang, A. N.; Sandlin, R. D.; Omar, A.; Egan, T. J.; Wright, D. W. The Neutral Lipid Composition Present in the Digestive Vacuole of *Plasmodium falciparum* Concentrates Heme and Mediates β-Hematin Formation with an Unusually Low Activation Energy. *Biochemistry* 2010, 49 (47), 10107–10116. https://doi.org/10.1021/bi101397u.

(184) Combrinck, J. M.; Fong, K. Y.; Gibhard, L.; Smith, P. J.; Wright, D. W.; Egan, T. J. Optimization of a Multi-Well Colorimetric Assay to Determine Haem Species in *Plasmodium falciparum* in the Presence of Anti-Malarials. *Malar J* 2015, 14 (1), 253. https://doi.org/10.1186/s12936-015-0729-9.

(185) Dziwornu, G. A.; Coertzen, D.; Leshabane, M.; Korkor, C. M.; Cloete, C. K.; Njoroge, M.; Gibhard, L.; Lawrence, N.; Reader, J.; van der Watt, M.; Wittlin, S.; Birkholtz, L.-M.;

Chibale, K. Antimalarial Benzimidazole Derivatives Incorporating Phenolic Mannich Base Side Chains Inhibit Microtubule and Hemozoin Formation: Structure–Activity Relationship and In Vivo Oral Efficacy Studies. *J Med Chem* 2021, 64 (8), 5198–5215. https://doi.org/10.1021/acs.jmedchem.1c00354.

(186) Stringer, T.; Wiesner, L.; Smith, G. S. Ferroquine-Derived Polyamines That Target Resistant *Plasmodium falciparum*. *Eur J Med Chem* 2019, 179, 78–83. https://doi.org/10.1016/j.ejmech.2019.06.023.

(187) Mambwe, D.; Korkor, C. M.; Mabhula, A.; Ngqumba, Z.; Cloete, C.; Kumar, M.; Barros, P. L.; Leshabane, M.; Coertzen, D.; Taylor, D.; Gibhard, L.; Njoroge, M.; Lawrence, N.; Reader, J.; Moreira, D. R.; Birkholtz, L.-M.; Wittlin, S.; Egan, T. J.; Chibale, K. Novel 3-Trifluoromethyl-1,2,4-Oxadiazole Analogues of Astemizole with Multi-Stage Antiplasmodium Activity and In Vivo Efficacy in a *Plasmodium Berghei* Mouse Malaria Infection Model. *J Med Chem* 2022, 65 (24), 16695–16715. https://doi.org/10.1021/acs.jmedchem.2c01516.

(188) Lawong, A.; Gahalawat, S.; Okombo, J.; Striepen, J.; Yeo, T.; Mok, S.; Deni, I.; Bridgford, J. L.; Niederstrasser, H.; Zhou, A.; Posner, B.; Wittlin, S.; Gamo, F. J.; Crespo, B.; Churchyard, A.; Baum, J.; Mittal, N.; Winzeler, E.; Laleu, B.; Palmer, M. J.; Charman, S. A.; Fidock, D. A.; Ready, J. M.; Phillips, M. A. Novel Antimalarial Tetrazoles and Amides Active against the Hemoglobin Degradation Pathway in *Plasmodium Falciparum*. *J Med Chem 2021*, 64 (5), 2739–2761. https://doi.org/10.1021/acs.jmedchem.0c02022.

(189) Ding, X. C.; Ubben, D.; Wells, T. N. A Framework for Assessing the Risk of Resistance for Anti-Malarials in Development. *Malar J* 2012, 11 (1), 292. https://doi.org/10.1186/1475-2875-11-292.

(190) Trager, W.; Jensen, J. B. Human Malaria Parasites in Continuous Culture. *Science* 1976, 193 (4254), 673–675. https://doi.org/10.1126/science.781840.

(191) Nguyen-Dinh, P.; Trager, W. Chloroquine Resistance Produced in Vitro in an African Strain of Human Malaria. *Science* 1978, 200 (4348), 1397–1398. https://doi.org/10.1126/science.351801.

(192) Ng, C. L.; Fidock, D. A. *Plasmodium Falciparum* In Vitro Drug Resistance Selections and Gene Editing. *Methods Mol Biol* 2019, 2013, 123–140. https://doi.org/10.1007/978-1-4939-9550-9_9.

(193) Ye, M.; Wilhelm, M.; Gentschev, I.; Szalay, A. A Modified Limiting Dilution Method for Monoclonal Stable Cell Line Selection Using a Real-Time Fluorescence Imaging

System: A Practical Workflow and Advanced Applications. *Methods Protoc* 2021, 4 (1), 16. https://doi.org/10.3390/mps4010016.

(194) Okombo, J.; Kanai, M.; Deni, I.; Fidock, D. A. Genomic and Genetic Approaches to Studying Antimalarial Drug Resistance and *Plasmodium* Biology. *Trends Parasitol* 2021, 37 (6), 476–492. https://doi.org/10.1016/j.pt.2021.02.007.

(195) Gilson, P. R.; Kumarasingha, R.; Thompson, J.; Zhang, X.; Penington, J. S.; Kalhor, R.; Bullen, H. E.; Lehane, A. M.; Dans, M. G.; de Koning-Ward, T. F.; Holien, J. K.; Soares da Costa, T. P.; Hulett, M. D.; Buskes, M. J.; Crabb, B. S.; Kirk, K.; Papenfuss, A. T.; Cowman, A. F.; Abbott, B. M. A 4-Cyano-3-Methylisoquinoline Inhibitor of *Plasmodium Falciparum* Growth Targets the Sodium Efflux Pump PfATP4. *Sci Rep* 2019, 9 (1), 10292. https://doi.org/10.1038/s41598-019-46500-5.

(196) Sonoiki, E.; Ng, C. L.; Lee, M. C. S.; Guo, D.; Zhang, Y.-K.; Zhou, Y.; Alley, M. R. K.; Ahyong, V.; Sanz, L. M.; Lafuente-Monasterio, M. J.; Dong, C.; Schupp, P. G.; Gut, J.; Legac, J.; Cooper, R. A.; Gamo, F.-J.; DeRisi, J.; Freund, Y. R.; Fidock, D. A.; Rosenthal, P. J. A Potent Antimalarial Benzoxaborole Targets a *Plasmodium falciparum* Cleavage and Polyadenylation Specificity Factor Homologue. *Nat Commun* 2017, 8 (1), 14574. https://doi.org/10.1038/ncomms14574.

(197) Salas, P.; Herrmann, C.; Orvig, C. Metalloantimalarials. *Chem Rev* 2013, 113. https://doi.org/10.1021/cr3001252.

(198) Yamashita, M. Auranofin: Past to Present, and Repurposing. *Int Immunopharmacol* 2021, 101, 108272. https://doi.org/10.1016/j.intimp.2021.108272.

(199) Yue, S.; Luo, M.; Liu, H.; Wei, S. Recent Advances of Gold Compounds in Anticancer Immunity. *Front Chem* 2020, 8. https://doi.org/10.3389/fchem.2020.00543.

(200) Ouji, M.; Barnoin, G.; Fernández Álvarez, Á.; Augereau, J.-M.; Hemmert, C.; Benoit-Vical, F.; Gornitzka, H. Hybrid Gold(I) NHC-Artemether Complexes to Target *Falciparum* Malaria Parasites. *Molecules* 2020, 25 (12), 2817. https://doi.org/10.3390/molecules25122817.

(201) Ertl, P. Craig Plot 2.0: An Interactive Navigation in the Substituent Bioisosteric Space. *J Cheminform* 2020, 12 (1), 10–15. https://doi.org/10.1186/s13321-020-0412-1.

(202) Ertl, P. Craig Plot 2.0: An Interactive Navigation in the Substituent Bioisosteric Space. *J Cheminform* 2020, 12 (1), 8.

https://doi.org/10.1186/s13321-020-0412-1.

(203) Morgan, G.; Burstall, F. Researches on Residual Affinity Andco-Ordination. Part XXXIV. 2, 2'-Dipyridyl Platinum Salts. *J Chem Soc* 1934, 964–971.

(204) Hocking, R. K.; Hambley, T. W. Database Analysis of Transition Metal Carbonyl Bond Lengths : Insight into the Periodicity of π Back-Bonding , σ Donation , and the Factors Affecting the Electronic Structure of the TM - C t O Moiety. *Organometallics* 2007, 2 (23), 2939–2947. https://doi.org/10.1021/om061072n.

(205) Huang, Z.; Richards, M. A.; Zha, Y.; Francis, R.; Lozano, R.; Ruan, J. Determination of Inorganic Pharmaceutical Counterions Using Hydrophilic Interaction Chromatography Coupled with a Corona® CAD Detector. *J Pharm Biomed Anal* 2009, 50 (5), 809–814. https://doi.org/10.1016/j.jpba.2009.06.039.

(206) Singh, G.; Singh, C. P.; Mannan, S. M. Kinetics of Thermolysis of Some Transition Metal Nitrate Complexes with 1,6-Diaminohexane Ligand. *J Hazard Mater* 2006, 135 (1–3), 10–14. https://doi.org/10.1016/j.jhazmat.2005.11.026.

(207) Pantelis, K. N.; Karotsis, G.; Lampropoulos, C.; Cunha-Silva, L.; Escuer, A.; Stamatatos, T. C. "Metal Complexes as Ligands" for the Synthesis of Coordination Polymers: A MnIII Monomer as a Building Block for the Preparation of an Unprecedented 1-D {MnIIMnIII}n Linear Chain. *Materials* 2020, 13 (6), 1–14. https://doi.org/10.3390/ma13061352.

(208) Aragoni, M. C.; Podda, E.; Caria, V.; Carta, S. A.; Cherchi, M. F.; Lippolis, V.; Murgia, S.; Orrù, G.; Pippia, G.; Scano, A.; Slawin, A. M. Z.; Woollins, J. D.; Pintus, A.; Arca, M. [AuIII(N^N)Br2](PF6): A Class of Antibacterial and Antibiofilm Complexes (N^N = 2,2′-Bipyridine and 1,10-Phenanthroline Derivatives). *Inorg Chem* 2023, 62 (6), 2924–2933. https://doi.org/10.1021/acs.inorgchem.2c04410.

(209) Marangoni, G.; Pitteri, B.; Bertolasi, V.; Gilli, G.; Ferretti, V. Five-Co-Ordinated Gold(III) Complexes. Part 1. Synthesis, Structure, and Properties of Bromodicyano(1,10-Phenanthroline)Gold(III)–Dimethylformamide (1/1). J. Chem. Soc., *Dalt Trans* 1986, No. 9, 1941–1944. https://doi.org/10.1039/DT9860001941.

(210) Zhu, H.; Hamachi, I. Fluorescence Imaging of Drug Target Proteins Using Chemical Probes. *J Pharm Anal*. Xi'an Jiaotong University October 1, 2020, 426–433. https://doi.org/10.1016/j.jpha.2020.05.013.

(211) Lavis, L. D.; Raines, R. T. Bright Ideas for Chemical Biology. *ACS Chem Biol* 1845, 3 (3), 144–155. https://doi.org/10.1021/cb700248m.

(212) Elbashir, A. A.; Suliman, F. E. O.; Aboul-Enein, H. Y. The Application of 7-Chloro-4-Nitrobenzoxadiazole (NBD-Cl) for the Analysis of Pharmaceutical-Bearing Amine Group Using Spectrophotometry and Spectrofluorimetry Techniques. *Appl Spectrosc Rev* 2011, 46 (3), 222–241. https://doi.org/10.1080/05704928.2011.557121.

(213) Xiao, Y.; Guo, Y.; Dang, R.; Yan, X.; Xu, P.; Jiang, P. A Dansyl-Based Fluorescent Probe for the Highly Selective Detection of Cysteine Based on a d-PeT Switching Mechanism. *RSC Adv* 2017, 7 (34), 21050–21053. https://doi.org/10.1039/c7ra00212b.

(214) Delori, F. C.; Ben-Sira, I. Excitation and Emission Spectra of Fluorescein Dye in the Human Ocular Fundus. *Reports* 1975, 14 (6), 487–492. PMID: 1132947. http://www.ncbi.nlm.nih.gov/pubmed/1132947.

(215) Queirós, C.; Vinhas, S.; Oliveira, J.; Leite, A.; Silva, A. M. G.; Rangel, M. Functionalization of Rhodamine Platforms with 3-Hydroxy-4-Pyridinone Chelating Units and Its Fluorescence Behavior towards Fe(III). *Molecules* 2022, 27 (5). https://doi.org/10.3390/molecules27051567.

(216) de Almeida, R. F. M.; Santos, T. C. B.; da Silva, L. C.; Suchodolski, J.; Krasowska, A.; Stokowa-Sołtys, K.; Puchalska, M.; Starosta, R. NBD Derived Diphenyl(Aminomethyl)Phosphane – A New Fluorescent Dye for Imaging of Low PH Regions and Lipid Membranes in Living Cells. *Dyes Pigm* 2021, 184. https://doi.org/10.1016/j.dyepig.2020.108771.

(217) Slyusareva, E. A.; Gerasimov, M. A.; Sizykh, A. G.; Gornostaev, L. M. Spectral and Fluorescent Indication of the Acidbase Properties of Biopolymer Solutions. Russ Phys J 2011, 54 (4), 485–492. https://doi.org/10.1007/s11182-011-9643-y.

(218) Tran, V. T.; Ju, H. Fluorescence Enhancement via Dual Coupling of Dye Molecules with Silver Nanostructures. *Chemosensors* 2021, 9 (8). https://doi.org/10.3390/chemosensors9080217.

(219) Mali, K. S.; Dutt, G. B. Do the Interfacial Fluidities of Cationic Reverse Micelles Enhance with an Increase in the Water Content? *J Chem Phys* 2009, 131 (17). https://doi.org/10.1063/1.3257964.

(220) Galinier, F.; Bertorelle, F.; Fery-Forgues, S. Spectrophotometric Study of the Incorporation of NBD Probes in Micelles: Is a Long Alkyl Chain on the Fluorophore an Advantage?. *C R Acad Sci* 2001; 4(12), 941–950. https://doi.org/10.1016/S1387-1609(01)01333-0

(221) Gao, Y.; Wang, C.; Chi, W.; Liu, X. Molecular Origins of Heteroatom Engineering on the Emission Wavelength Tuning, Quantum Yield Variations and Fluorogenicity of NBD-

like SCOTfluors. *Chem Asian J* 2020, 15 (23), 4082–4086. https://doi.org/10.1002/asia.202000966.

(222) Jin, S.; Guo, Y.; Guo, Z.; Wang, X. Monofunctional Platinum(II) Anticancer Agents. *Pharmaceuticals* 2021, 14 (2), 133. https://doi.org/10.3390/ph14020133.

(223) Benedetti, B. T.; Peterson, E. J.; Kabolizadeh, P.; Martínez, A.; Kipping, R.; Farrell, N. P. Effects of Noncovalent Platinum Drug-Protein Interactions on Drug Efficacy: Use of Fluorescent Conjugates as Probes for Drug Metabolism. *Mol Pharm* 2011, 8 (3), 940–948. https://doi.org/10.1021/mp2000583.

(224) Wu, S.; Zhu, C.; Zhang, C.; Yu, Z.; He, W.; He, Y.; Li, Y.; Wang, J.; Guo, Z. In Vitro and in Vivo Fluorescent Imaging of a Monofunctional Chelated Platinum Complex Excitable Using Visible Light. *Inorg Chem* 2011, 50 (23), 11847–11849. https://doi.org/10.1021/ic201506y.

(225) Woodland, J. G.; Hunter, R.; Smith, P. J.; Egan, T. J. Shining New Light on Ancient Drugs: Preparation and Subcellular Localisation of Novel Fluorescent Analogues of Cinchona Alkaloids in Intraerythrocytic *Plasmodium falciparum*. *Org Biomol Chem* 2017, 15 (3), 589–597. https://doi.org/10.1039/c6ob02110g.

(226) Woodland, J. G.; Hunter, R.; Smith, P. J.; Egan, T. J. Chemical Proteomics and Super-Resolution Imaging Reveal That Chloroquine Interacts with *Plasmodium falciparum* Multidrug Resistance-Associated Protein and Lipids. *ACS Chem Biol* 2018, 13 (10), 2939–2948. https://doi.org/10.1021/acschembio.8b00583.

(227) Greco, G.; D'Antona, N.; Gambera, G.; Nicolosi, G. Glycerophosphoinositols: Total Synthesis of the First Fluorescent Probe Derivative. *Synlett* 2014, 25 (15), 2111–2114. https://doi.org/10.1055/s-0034-1378537.

(228) Guminski, Y.; Grousseaud, M.; Cugnasse, S.; Brel, V.; Annereau, J. P.; Vispé, S.; Guilbaud, N.; Barret, J. M.; Bailly, C.; Imbert, T. Synthesis of Conjugated Spermine Derivatives with 7-Nitrobenzoxadiazole (NBD), Rhodamine and Bodipy as New Fluorescent Probes for the Polyamine Transport System. *Bioorg Med Chem Lett* 2009, 19 (9), 2474–2477. https://doi.org/10.1016/j.bmcl.2009.03.052.

(229) Yap, J. L.; Wang, H.; Hu, A.; Chauhan, J.; Jung, K. Y.; Gharavi, R. B.; Prochownik, E. V.; Fletcher, S. Pharmacophore Identification of C-Myc Inhibitor 10074-G5. *Bioorg Med Chem Lett* 2013, 23 (1), 370–374. https://doi.org/10.1016/j.bmcl.2012.10.013.

(230) Andreev, K.; Bianchi, C.; Laursen, J. S.; Citterio, L.; Hein-Kristensen, L.; Gram, L.; Kuzmenko, I.; Olsen, C. A.; Gidalevitz, D. Guanidino Groups Greatly Enhance the Action of Antimicrobial Peptidomimetics against Bacterial Cytoplasmic Membranes. *Biochim Biophys Acta Biomembr* 2014, 1838 (10), 2492–2502. https://doi.org/10.1016/j.bbamem.2014.05.022.

(231) Parola, A. J.; Lima, J. C.; Pina, F.; Pina, J.; Melo, J. S. de; Soriano, C.; García-España, E.; Aucejo, R.; Alarcón, J. Synthesis and Photophysical Properties of Dansyl-Based Polyamine Ligands and Their Zn(II) Complexes. *Inorganica Chim Acta* 2007, 360 (3), 1200–1208. https://doi.org/10.1016/j.ica.2006.11.006.

(232) Hartwig, C. L.; Rosenthal, A. S.; D'Angelo, J.; Griffin, C. E.; Posner, G. H.; Cooper, R. A. Accumulation of Artemisinin Trioxane Derivatives within Neutral Lipids of *Plasmodium falciparum* Malaria Parasites Is Endoperoxide-Dependent. *Biochem Pharmacol* 2009, 77 (3), 322–336. https://doi.org/10.1016/j.bcp.2008.10.015.

(233) Hartwig, C. L.; Lauterwasser, E. M. W.; Mahajan, S. S.; Hoke, J. M.; Cooper, R. A.; Renslo, A. R. Investigating the Antimalarial Action of 1,2,4-Trioxolanes with Fluorescent Chemical Probes. *J Med Chem* 2011, 54 (23), 8207–8213. https://doi.org/10.1021/jm2012003.

(234) Longmire, M. R.; Ogawa, M.; Hama, Y.; Kosaka, N.; Regino, C. A. S.; Choyke, P. L.; Kobayashi, H. Determination of Optimal Rhodamine Fiuorophore for in Vivo Optical Imaging. *Bioconjug Chem* 2008, 19 (8), 1735–1742. https://doi.org/10.1021/bc800140c.

(235) Tian, M.; Peng, X.; Fan, J.; Wang, J.; Sun, S. A Fluorescent Sensor for PH Based on Rhodamine Fluorophore. *Dyes Pigm* 2012, 95 (1), 112–115. https://doi.org/10.1016/j.dyepig.2012.03.008.

(236) Queirós, C.; Vinhas, S.; Oliveira, J.; Leite, A.; Silva, A. M. G.; Rangel, M. Functionalization of Rhodamine Platforms with 3-Hydroxy-4-Pyridinone Chelating Units and Its Fluorescence Behavior towards Fe(III). *Molecules* 2022, 27 (5). https://doi.org/10.3390/molecules27051567.

(237) Ren, Y.-S.; Li, H.-L.; Piao, X.-H.; Yang, Z.-Y.; Wang, S.-M.; Ge, Y.-W. Drug Affinity Responsive Target Stability (DARTS) Accelerated Small Molecules Target Discovery: Principles and Application. *Biochem Pharmacol* 2021, 194, 114798. https://doi.org/10.1016/j.bcp.2021.114798.

(238) Xiong, X.; Song, F.; Chen, G.; Sun, W.; Wang, J.; Gao, P.; Zhang, Y.; Qiao, B.; Li, W.; Sun, S.; Fan, J.; Peng, X. Construction of Long-Wavelength Fluorescein Analogues and

Their Application as Fluorescent Probes. *Chem Eur J* 2013, 19 (21), 6538–6545. https://doi.org/10.1002/chem.201300418.

(239) Xiong, X.; Yuan, Y.; Chen, G.; Li, M.; Lyu, L.; Zhao, H.; Yan, J.; Qian, Y.; Zhu, J.; Jiao, C. Construction, Photophysical Properties, Structure-Activity Relationship, and Applications of Fluorescein Analogs. *Dyes Pigm* 2023, 208, 110870. https://doi.org/10.1016/j.dyepig.2022.110870.

(240) Le Guern, F.; Mussard, V.; Gaucher, A.; Rottman, M.; Prim, D. Fluorescein Derivatives as Fluorescent Probes for PH Monitoring along Recent Biological Applications. *Int J Mol Sci* 2020, 21 (23), 9217. https://doi.org/10.3390/ijms21239217.

(241) Gupta, Y.; Sharma, N.; Singh, S.; Romero, J. G.; Rajendran, V.; Mogire, R. M.; Kashif, M.; Beach, J.; Jeske, W.; Poonam; Ogutu, B. R.; Kanzok, S. M.; Akala, H. M.; Legac, J.; Rosenthal, P. J.; Rademacher, D. J.; Durvasula, R.; Singh, A. P.; Rathi, B.; Kempaiah, P. The Multistage Antimalarial Compound Calxinin Perturbates *P. Falciparum* Ca^{2+} Homeostasis by Targeting a Unique Ion Channel. *Pharmaceutics* 2022, 14 (7). https://doi.org/10.3390/pharmaceutics14071371.

(242) Lucantoni, L.; Silvestrini, F.; Signore, M.; Siciliano, G.; Eldering, M.; Dechering, K. J.; Avery, V. M.; Alano, P. A Simple and Predictive Phenotypic High Content Imaging Assay for *Plasmodium falciparum* Mature Gametocytes to Identify Malaria Transmission Blocking Compounds. *Sci Rep* 2015, 5 (1), 16414. https://doi.org/10.1038/srep16414.

(243) Raphemot, R.; Lafuente-Monasterio, M. J.; Gamo-Benito, F. J.; Clardy, J.; Derbyshire, E. R. Discovery of Dual-Stage Malaria Inhibitors with New Targets. *Antimicrob Agents Chemother* 2016, 60 (3), 1430–1437. https://doi.org/10.1128/AAC.02110-15.

(244) Gupta, R.; Polaka, S.; Rajpoot, K.; Tekade, M.; Sharma, M. C.; Tekade, R. K. Importance of Toxicity Testing in Drug Discovery and Research. In Pharmacokinetics and Toxicokinetic Considerations; *Elsevier*, 2022; pp 117–144. https://doi.org/10.1016/B978-0-323-98367-9.00016-0.

(245) Nardon, C.; Boscutti, G.; Fregona, D. Beyond Platinums: Gold Complexes as Anticancer Agents. *Anticancer res* 2014, 34 (1), 487–492. PMID: 24403506

(246) Hemmert, C.; Fabié, A.; Fabre, A.; Benoit-Vical, F.; Gornitzka, H. Synthesis, Structures, and Antimalarial Activities of Some Silver(I), Gold(I) and Gold(III) Complexes Involving N-Heterocyclic Carbene Ligands. *Eur J Med Chem* 2013, 60, 64–75. https://doi.org/10.1016/j.ejmech.2012.11.038.

(247) Sánchez Delgado, G. Y.; Navarro, M. An Overview of Auric Compounds as Antimalarial Agents and Their Action against Essential Targets of the Parasite. *Coord Chem Rev* 2024, 503, 215633. https://doi.org/10.1016/j.ccr.2023.215633.

(248) Moreno-Alcántar, G.; Picchetti, P.; Casini, A. Gold Complexes in Anticancer Therapy: From New Design Principles to Particle-Based Delivery Systems. *Angew Chem Int Ed* 2023, 62 (22). https://doi.org/10.1002/anie.202218000.

(249) Zhang, C.; Xu, C.; Gao, X.; Yao, Q. Platinum-Based Drugs for Cancer Therapy and Anti-Tumor Strategies. *Theranostics* 2022, 12 (5), 2115–2132. https://doi.org/10.7150/thno.69424.

(250) Mario, E. A review: Enhancement of Solubility and Oral Bioavailability of Poorly Soluble Drugs. *Adv Pharm J* 2017, 2 (5), 161–173.

(251) Chillistone, S.; Hardman, J. G. Factors Affecting Drug Absorption and Distribution. *Anaes Intensive Care Med* 2017, 18 (7), 335–339. https://doi.org/10.1016/j.mpaic.2017.04.007.

(252) Saal, C.; Petereit, A. C. Optimizing Solubility: Kinetic versus Thermodynamic Solubility Temptations and Risks. *Eur J Pharm* Sci 2012, 47 (3), 589–595. https://doi.org/10.1016/j.ejps.2012.07.019.

(253) Di, L.; Kerns, E. H.; Hong, Y.; Kleintop, T. A.; McConnell, O. J.; Huryn, D. M. Optimization of a Higher Throughput Microsomal Stability Screening Assay for Profiling Drug Discovery Candidates. *J Biomol Screen* 2003, 8 (4), 453–462. https://doi.org/10.1177/1087057103255988.

(254) Parmentier, Y.; Bossant, M.-J.; Bertrand, M.; Walther, B. In Vitro Studies of Drug Metabolism. In Comprehensive Medicinal Chemistry II; *Elsevier*, 2007; pp 231–257. https://doi.org/10.1016/B0-08-045044-X/00125-5.

(255) Enlo-Scott, Z.; Bäckström, E.; Mudway, I.; Forbes, B. Drug Metabolism in the Lungs: Opportunities for Optimising Inhaled Medicines. *Expert Opin Drug Metab Toxicol* 2021, 17 (5), 611–625. https://doi.org/10.1080/17425255.2021.1908262.

(256) Knights, K. M.; Rowland, A.; Miners, J. O. Renal Drug Metabolism in Humans: The Potential for Drug-Endobiotic Interactions Involving Cytochrome P450 (CYP) and UDP-Glucuronosyltransferase (UGT). *Br J Clin Pharmacol* 2013, 76 (4), 587–602. https://doi.org/10.1111/bcp.12086.

(257) Iswandana, R.; Irianti, M. I.; Oosterhuis, D.; Hofker, H. S.; Merema, M. T.; De Jager, M. H.; Mutsaers, H. A. M.; Olinga, P. Regional Differences in Human Intestinal Drug Metabolism. *Drug Metab Dispos* 2018, 46 (12), 1879–1885. https://doi.org/10.1124/dmd.118.083428.

(258) Telaprolu, K. C.; Grice, J. E.; Mohammed, Y. H.; Roberts, M. S. Human Skin Drug Metabolism: Relationships between Methyl Salicylate Metabolism and Esterase Activities in IVPT Skin Membranes. *Metabolites* 2023, 13 (8), 934. https://doi.org/10.3390/metabo13080934.

(259) Cossum, P. A. Role of the Red Blood Cell in Drug Metabolism. *Biopharm Drug Dispos* 1988, 9 (4), 321–336. https://doi.org/10.1002/bod.2510090402.

(260) Tamargo-Rubio, I.; Simpson, A. B.; Hoogerland, J. A.; Fu, J. Human Induced Pluripotent Stem Cell–Derived Liver-on-a-Chip for Studying Drug Metabolism: The Challenge of the Cytochrome P450 Family. *Front Pharmacol* 2023, 14. https://doi.org/10.3389/fphar.2023.1223108.

(261) Almazroo, O. A.; Miah, M. K.; Venkataramanan, R. Drug Metabolism in the Liver. *Clin Liver Dis* 2017, 21 (1), 1–20. https://doi.org/10.1016/j.cld.2016.08.001.

(262) Zhao, M.; Ma, J.; Li, M.; Zhang, Y.; Jiang, B.; Zhao, X.; Huai, C.; Shen, L.; Zhang, N.; He, L.; Qin, S. Cytochrome P450 Enzymes and Drug Metabolism in Humans. *Int J Mol Sci* 2021, 22 (23), 12808. https://doi.org/10.3390/ijms222312808.

(263) Jancova, P.; Anzenbacher, P.; Anzenbacherova, E. Phase II drug metabolizing enzymes. *Drug Metab Rev* 2010, 154 (2), 103–116. https://doi.org/10.5507bp.2010.017.

(264) Perryman, A. L.; Stratton, T. P.; Ekins, S.; Freundlich, J. S. Predicting Mouse Liver Microsomal Stability with “Pruned” Machine Learning Models and Public Data. *Pharm Res* 2016, 33 (2), 433–449. https://doi.org/10.1007/s11095-015-1800-5.

(265) Jia, L.; Liu, X. The Conduct of Drug Metabolism Studies Considered Good Practice (II): In Vitro Experiments. *Curr Drug Metab* 2007, 8 (8), 822–829. https://doi.org/10.2174/138920007782798207.

(266) Barnes-Seeman, D.; Jain, M.; Bell, L.; Ferreira, S.; Cohen, S.; Chen, X. H.; Amin, J.; Snodgrass, B.; Hatsis, P. Metabolically Stable Tert-Butyl Replacement. *ACS Med Chem Lett* 2013, 4 (6), 514–516. https://doi.org/10.1021/ml400045j.

(267) Li, Y.; Meng, Q.; Yang, M.; Liu, D.; Hou, X.; Tang, L.; Wang, X.; Lyu, Y.; Chen, X.; Liu, K.; Yu, A.-M.; Zuo, Z.; Bi, H. Current Trends in Drug Metabolism and Pharmacokinetics. *Acta Pharm Sin B* 2019, 9 (6), 1113–1144. https://doi.org/10.1016/j.apsb.2019.10.001.

(268) Rimmington, F. Pharmacokinetics and Pharmacodynamics. *S Afr J Anaesth Analg* 2020, S153–S156. https://doi.org/10.36303/SAJAA.2020.26.6.S3.2562.

(269) Holt, K.; Nagar, S.; Korzekwa, K. Methods to Predict Volume of Distribution. *Curr Pharmacol Rep* 2019, 5 (5), 391–399. https://doi.org/10.1007/s40495-019-00186-5.

(270) Hann, E.; Malagu, K.; Stott, A.; Vater, H. The Importance of Plasma Protein and Tissue Binding in a Drug Discovery Program to Successfully Deliver a Preclinical Candidate. In Prog Med Chem; *Elsevier B.V.*, 2022; Vol. 61, pp 163–214. https://doi.org/10.1016/bs.pmch.2022.04.002.

(271) Smith, D. A.; Beaumont, K.; Maurer, T. S.; Di, L. Clearance in Drug Design. *J Med Chem* 2019, 62 (5), 2245–2255. https://doi.org/10.1021/acs.jmedchem.8b01263.

(272) Gao, Y.; Gesenberg, C.; Zheng, W. Oral Formulations for Preclinical Studies. In Developing Solid Oral Dosage Forms; *Elsevier*, 2017; pp 455–495. https://doi.org/10.1016/B978-0-12-802447-8.00017-0.

(273) Wei, M.; Zhang, X.; Pan, X.; Wang, B.; Ji, C.; Qi, Y.; Zhang, J. Z. H. HobPre: Accurate Prediction of Human Oral Bioavailability for Small Molecules. *J Chem inform* 2022, 14 (1). https://doi.org/10.1186/s13321-021-00580-6.

(274) Zhu, J.; Wang, J.; Yu, H.; Li, Y.; Hou, T. Recent Developments of In Silico Predictions of Oral Bioavailability. *Comb Chem High Throughput Screen* 2011, 14 (5), 362–374. https://doi.org/10.2174/138620711795508368.

(275) Smith, D. A.; Beaumont, K.; Maurer, T. S.; Di, L. Volume of Distribution in Drug Design. *J Med Chem* 2015, 58 (15), 5691–5698. https://doi.org/10.1021/acs.jmedchem.5b00201.

(276) Smith, D. A.; Beaumont, K.; Maurer, T. S.; Di, L. Relevance of Half-Life in Drug Design. *J Med Chem* 2018, 61 (10), 4273–4282. https://doi.org/10.1021/acs.jmedchem.7b00969.

(277) Menichetti, R.; Kanekal, K. H.; Bereau, T. Drug-Membrane Permeability across Chemical Space. *ACS Cent Sci* 2019, 5 (2), 290–298. https://doi.org/10.1021/acscentsci.8b00718.

(278) Wang, J.; Skolnik, S. Mitigating Permeability-Mediated Risks in Drug Discovery. *Expert Opin Drug Metab Toxicol* 2010, 6 (2), 171–187. https://doi.org/10.1517/17425250903436486.

(279) Wang, J.; Skolnik, S. Permeability Diagnosis Model in Drug Discovery: A Diagnostic Tool to Identify the Most Influencing Properties for Gastrointestinal Permeability. *Current Topics Med Chem* 2013, 13, 1308–1316. https://doi.org/10.2174/15680266113139990035.

(280) Ren, S.; Lien, E. J. Caco-2 Cell Permeability vs Human Gastrointestinal Absorption: QSPR Analysis. *Prog Drug Res* 2000, 54, 1–23. https://doi.org/10.1007/978-3-0348-8391-7_1.

(281) de Souza Teixeira, L.; Vila Chagas, T.; Alonso, A.; Gonzalez-Alvarez, I.; Bermejo, M.; Polli, J.; Rezende, K. R. Biomimetic Artificial Membrane Permeability Assay over Franz Cell Apparatus Using BCS Model Drugs. *Pharmaceutics* 2020, 12 (10), 988. https://doi.org/10.3390/pharmaceutics12100988.

(282) Buchanan, N. Protein Binding of Drugs-the Clinical Significance. *S Afr Med J* 1978, 53 (22), 883–886. PMID: 356286.

(283) Chung TDY, Terry DB, Smith LH. In Vitro and In Vivo Assessment of ADME and PK Properties During Lead Selection and Lead Optimization – Guidelines, Benchmarks and Rules of Thumb. 2015 Sep 9. In: Markossian S, Grossman A, Arkin M, Auld D, Austin C, Baell J, Brimacombe K, Chung TDY, Coussens NP, Dahlin JL, Devanarayan V, Foley TL, Glicksman M, Gorshkov K, Haas JV, Hall MD, Hoare S, Inglese J, Iversen PW, Lal-Nag M, Li Z, Manro JR, McGee J, McManus O, Pearson M, Riss T, Saradjian P, Sittampalam GS, Tarselli M, Trask OJ Jr, Weidner JR, Wildey MJ, Wilson K, Xia M, Xu X, editors. Assay Guidance Manual. Bethesda (MD): *Eli Lilly & Company and the National Center for Advancing Translational Sciences*; 2004–. PMID: 26561695.

(284) Davis, R. L. Mechanism of Action and Target Identification: A Matter of Timing in Drug Discovery. *iScience* 2020, 23 (9), 101487. https://doi.org/10.1016/j.isci.2020.101487.

(285) De Villiers, K. A.; Egan, T. J. Heme Detoxification in the Malaria Parasite: A Target for Antimalarial Drug Development. *Acc Chem Res* 2021, 54 (11), 2649–2659. https://doi.org/10.1021/acs.accounts.1c00154.

(286) Openshaw, R.; Maepa, K.; Benjamin, S. J.; Wainwright, L.; Combrinck, J. M.; Hunter, R.; Egan, T. J. A Diverse Range of Hemozoin Inhibiting Scaffolds Act on *Plasmodium falciparum* as Heme Complexes. *ACS Infect Dis* 2021, 7 (2), 362–376. https://doi.org/10.1021/acsinfecdis.0c00680.

(287) Sakata, Y.; Yabunaka, K.; Kobayashi, Y.; Omiya, H.; Umezawa, N.; Kim, H. S.; Wataya, Y.; Tomita, Y.; Hisamatsu, Y.; Kato, N.; Yagi, H.; Satoh, T.; Kato, K.; Ishikawa, H.; Higuchi, T. Potent Antimalarial Activity of Two Arenes Linked with Triamine Designed to Have Multiple Interactions with Heme. *ACS Med Chem Lett* 2018, 9 (10), 980–985. https://doi.org/10.1021/acsmedchemlett.8b00222.

(288) Berger, S. I.; Iyengar, R. Role of Systems Pharmacology in Understanding Drug Adverse Events. *Wiley Interdiscip Rev Syst Biol Med* 2011, 3 (2), 129–135. https://doi.org/10.1002/wsbm.114.

(289) Longuespée, R.; Theile, D.; Fresnais, M.; Burhenne, J.; Weiss, J.; Haefeli, W. E. Approaching Sites of Action of Drugs in Clinical Pharmacology: New Analytical Options and Their Challenges. *Br J Clin Pharmacol* 2021, 87 (3), 858–874. https://doi.org/10.1111/bcp.14543.

(290) Yayon, A.; Cabantchik, Z. I.; Ginsburg, H. Susceptibility of Human Malaria Parasites to Chloroquine Is PH Dependent. *Natl Aca Sci* 1985, 82 (9), 2784–2788. https://doi.org/10.1073/pnas.82.9.2784.

(291) Pandey, A. V.; Tekwani, B. L.; Singh, R. L.; Chauhan, V. S. Artemisinin, an Endoperoxide Antimalarial, Disrupts the Hemoglobin Catabolism and Heme Detoxification Systems in Malarial Parasite. *J Biol Chem* 1999, 274 (27), 19383–19388. https://doi.org/10.1074/jbc.274.27.19383.

(292) Edgar, R. C. S.; Counihan, N. A.; McGowan, S.; de Koning-Ward, T. F. Methods Used to Investigate the *Plasmodium falciparum* Digestive Vacuole. Frontiers in Cellular and Infection Microbiology. *Frontiers Media S.A*. January 13, 2022. https://doi.org/10.3389/fcimb.2021.829823.

(293) Brook, I. Inoculum Effect. *Clin Infect Dis* 1989, 11 (3), 361–368. https://doi.org/10.1093/clinids/11.3.361..

(294) Ferrari, V.; Cutler, D. J. Uptake of Chloroquine by Human Erythrocytes. *Biochem Pharmacol* 1990, 39 (4), 753–762. https://doi.org/10.1016/0006-2952(90)90155-E.

(295) Murithi, J. M.; Deni, I.; Pasaje, C. F. A.; Okombo, J.; Bridgford, J. L.; Gnädig, N. F.; Edwards, R. L.; Yeo, T.; Mok, S.; Burkhard, A. Y.; Coburn-Flynn, O.; Istvan, E. S.; Sakata-Kato, T.; Gomez-Lorenzo, M. G.; Cowell, A. N.; Wicht, K. J.; Le Manach, C.; Kalantarov, G. F.; Dey, S.; Duffey, M.; Laleu, B.; Lukens, A. K.; Ottilie, S.; Vanaerschot, M.; Trakht, I. N.; Gamo, F. J.; Wirth, D. F.; Goldberg, D. E.; Odom John, A. R.; Chibale, K.; Winzeler, E. A.; Niles, J. C.; Fidock, D. A. The *Plasmodium falciparum* ABC Transporter ABCI3 Confers Parasite Strain-Dependent Pleiotropic Antimalarial Drug

Resistance. *Cell Chem Biol* 2022, 29 (5), 824–839. https://doi.org/10.1016/j.chembiol.2021.06.006.

(296) Hawley, S. R.; Bray, P. G.; Mungthin, M.; Atkinson, J. D.; O'neill, P. M.; Ward, S. A. Relationship between Antimalarial Drug Activity, Accumulation, and Inhibition of Heme Polymerization in *Plasmodium falciparum* In Vitro. *Antimicrob Agents Chemother* 1998, 42 (3), 682–686.

(297) Boros, E.; Dyson, P. J.; Gasser, G. Classification of Metal-Based Drugs According to Their Mechanisms of Action. *Chem* 2020, 6 (1), 41–60. https://doi.org/10.1016/j.chempr.2019.10.013.

(298) Minić, A.; van de Walle, T.; van Hecke, K.; Combrinck, J.; Smith, P. J.; Chibale, K.; D'hooghe, M. Design and Synthesis of Novel Ferrocene-Quinoline Conjugates and Evaluation of Their Electrochemical and Antiplasmodium Properties. *Eur J Med Chem* 2020, 187 (2020), 111963. https://doi.org/10.1016/j.ejmech.2019.111963.

(299) Lai, J. W.; Maah, M. J.; Tan, K. W.; Sarip, R.; Lim, Y. A. L.; Ganguly, R.; Khaw, L. T.; Ng, C. H. Dinuclear and Mononuclear Metal(II) Polypyridyl Complexes against Drug-Sensitive and Drug-Resistant *Plasmodium falciparum* and Their Mode of Action. *Malar J* 2022, 21 (1), 386. https://doi.org/10.1186/s12936-022-04406-0.

(300) Kotzé, I. A.; Smith, V. J.; Kangara, E. F.; Koch, K. R. Rare, Hypodentate L-κ: S Coordination Mode of N, N -Dialkyl- N ′-Aroylthioureas Leads to Unprecedented Mixed-Ligand [Pt(Phen)(L-κ S)2] Complexes. *New J Chem* 2017, 41 (24), 14995–15002. https://doi.org/10.1039/c7nj03178e.

(301) Hunter, C. A.; Sanders, J. K. The Nature of Pi-Pi Interactions. *J Am Chem Soc* 1990, 112 (14), 5525–5534. https://doi.org/10.1021/ja00170a016.

(302) Rashkin, M. J.; Waters, M. L. Unexpected Substituent Effects in Offset π−π Stacked Interactions in Water. *J Am Chem Soc* 2002, 124 (9), 1860–1861. https://doi.org/10.1021/ja016508z.

(303) Egan, T. J.; Ncokazi, K. K. Quinoline Antimalarials Decrease the Rate of β-Hematin Formation. *J Inorg Biochem* 2005, 99 (7), 1532–1539. https://doi.org/10.1016/j.jinorgbio.2005.04.013.

(304) Fong, K. Y.; Sandlin, R. D.; Wright, D. W. Identification of β-Hematin Inhibitors in the MMV Malaria Box. *Int J Parasitol Drug Resis*t 2015, 5 (3), 84–91. https://doi.org/10.1016/j.ijpddr.2015.05.003.

(305) Sandlin, R. D.; Carter, M. D.; Lee, P. J.; Auschwitz, J. M.; Leed, S. E.; Johnson, J. D.; Wright, D. W. Use of the NP-40 Detergent-Mediated Assay in Discovery of Inhibitors of

β-Hematin Crystallization. *Antimicrob Agents Chemother* 2011, 55 (7), 3363–3369. https://doi.org/10.1128/AAC.00121-11.

(306) Stringer, T.; Wiesner, L.; Smith, G. S. Ferroquine-Derived Polyamines That Target Resistant *Plasmodium falciparum*. *Eur J Med Chem* 2019, 179, 78–83. https://doi.org/10.1016/j.ejmech.2019.06.023.

(307) Mackler, M. T.; Henrichs, D. J. Measurement of the Lactate Dehydrogenase Activity of *Plasmodium falciparum* as an Assessment of Parasitemia. *Am J Trop Med* 1993, 48 (2), 205–2010. https://doi.org/10.4269/ajtmh.1993.48.205.

(308) Markwalter, C. F.; Davis, K. M.; Wright, D. W. Immunomagnetic Capture and Colorimetric Detection of Malarial Biomarker *Plasmodium falciparum* Lactate Dehydrogenase. *Anal Biochem* 2016, 493, 30–34. https://doi.org/10.1016/j.ab.2015.10.003.

(309) Duraisingh, M. T.; Jones, P.; Sambou, I.; Von Seidlein, L.; Pinder, M.; Warhurst, D. C. Inoculum Effect Leads to Overestimation of in Vitro Resistance for Artemisinin Derivatives and Standard Antimalarials: A Gambian Field Study. Parasitology 1999, 119 (5), 435–440. https://doi.org/10.1017/S0031182099004953.

(310) Elgrishi, N.; Rountree, K. J.; McCarthy, B. D.; Rountree, E. S.; Eisenhart, T. T.; Dempsey, J. L. A Practical Beginner's Guide to Cyclic Voltammetry. *J Chem Educ* 2018, 95 (2), 197–206. https://doi.org/10.1021/acs.jchemed.7b00361.

(311) Mabbott, G. A. An Introduction to Cyclic Voltammetry. *J Chem Educ* 1983, 60 (9), 697–702. https://doi.org/10.1021/ed060p697.

(312) Bobbitt, J.; Willis, J. Electrochemistry of Natural Products. 7. Oxidative Decarboxylation of Some Tetrahydro-B-Carbolinecarboxylic Acids. *J Org Chem* 1980, 45(10), 1984–1986.

(313) Bollo, S.; Nunez-Vergara, L. J.; Squella, J. A. Cyclic Voltammetric Determination of Free Radical Species from Nitroimidazopyran: A New Antituberculosis Agent. *J Electroanalytical Chem* 2004, 562 (1), 9–14. https://doi.org/10.1016/j.jelechem.2003.07.031.

(314) Von Eschwege, K. G.; Conradie, J. Redox Potentials of Ligands and Complexes-a DFT Approach. *S Afr J Chem* 2011, 64, 203–209. https://api.semanticscholar.org/CorpusID:14267260.

(315) Sandford, C.; Edwards, M. A.; Klunder, K. J.; Hickey, D. P.; Li, M.; Barman, K.; Sigman, M. S.; White, H. S.; Minteer, S. D. A Synthetic Chemist's Guide to Electroanalytical Tools for Studying Reaction Mechanisms. *Chem Sci* 2019, 10 (26), 6404–6422. https://doi.org/10.1039/c9sc01545k.

(316) Wani, W. A.; Jameel, E.; Baig, U.; Mumtazuddin, S.; Ting, L. Ferroquine and Its Derivatives: New Generation of Antimalarial Agents. *Eur J Med Chem* 2015, 101 (101), 534–551. https://doi.org/10.1016/j.ejmech.2015.07.009.

(317) Coban, B.; Tekin, I. O.; Sengul, A.; Yildiz, U.; Kocak, I.; Sevinc, N. DNA Studies of Newly Synthesized Heteroleptic Platinum(II) Complexes $[Pt(Bpy)(iip)]^{2+}$ and $[Pt(Bpy)(miip)]^{2+}$. *J Biol Inorg Chem* 2016, 21 (2), 163–175. https://doi.org/10.1007/s00775-015-1317-8.

(318) Brown, A. R.; Guo, Z.; Mosselmans, F. W. J.; Parsons, S.; Schröder, M.; Yellowlees, L. J. Structural and Voltammetric Studies on the Reduction of the Bis(2,2,-Bipyridyl)Platinum(II) Cation in Aprotic Media. *J Am Chem Soc* 1998, 120 (34), 8805–8811. https://doi.org/10.1021/ja981670w.

(319) Sanna, G.; Pilo, M. I.; Minghetti, G.; Cinellu, M. A.; Spano, N.; Seeber, R. Electrochemical Properties of Gold(III) Complexes with 2,2'-Bipyridine and Oxygen Ligands. *Inorganica Chim Acta* 2000, 310, 34–40.

(320) Pantelić, N.; Stanković, D. M.; Zmejkovski, B. B.; Kaluđerović, G. N.; Sabo, T. J. Electrochemical Properties of Some Gold(III) Complexes with (S,S)-R 2 Edda-Type Ligands. *Int. J. Electrochem*. Sci 2016, 11, 1162–1171.

(321) Hayward, R.; Saliba, K. J.; Kirk, K. The PH of the Digestive Vacuole of *Plasmodium falciparum* Is Not Associated with Chloroquine Resistance. *J Cell Sci* 2006, 119 (6), 1016–1025. https://doi.org/10.1242/jcs.02795.

(322) Ruscoe, J. E.; Tingle, M. D.; O'Neill, P. M.; Ward, S. A.; Park, B. K. Effect of Disposition of Mannich Antimalarial Agents on Their Pharmacology and Toxicology. *Antimicrob Agents Chemother* 1998, 42 (9), 2410–2416. https://doi.org/10.1128/AAC.42.9.2410.

(323) Wissing, F.; Sanchez, C. P.; Rohrbach, P.; Ricken, S.; Lanzer, M. Illumination of the Malaria Parasite *Plasmodium falciparum* Alters Intracellular PH. Implications for Live Cell Imaging. *J Biol Chem* 2002, 277 (40), 37747–37755. https://doi.org/10.1074/jbc.M204845200.

(324) Gardner, M. J.; Tettelin, H.; Carucci, D. J.; Cummings, L. M.; Aravind, L.; Koonin, E. V.; Shallom, S.; Mason, T.; Yu, K.; Fujii, C.; Pederson, J.; Shen, K.; Jing, J.; Aston, C.; Lai, Z.; Schwartz, D. C.; Pertea, M.; Salzberg, S.; Zhou, L.; Sutton, G. G.; Clayton, R.; White, O.; Smith, H. O.; Fraser, C. M.; Adams, M. D.; Venter, J. C.; Hoffman, S. L. Chromosome 2 Sequence of the Human Malaria Parasite *Plasmodium falciparum*. *Science* (1979) 1998, 282 (5391), 1126–1132. https://doi.org/10.1126/science.282.5391.1126.

(325) Bowman, S.; Lawson, D.; Basham, D.; Brown, D.; Chillingworth, T.; Churcher, C. M.; Craig, A.; Davies, R. M.; Devlin, K.; Feltwell, T.; Gentles, S.; Gwilliam, R.; Hamlin, N.; Harris, D.; Holroyd, S.; Hornsby, T.; Horrocks, P.; Jagels, K.; Jassal, B.; Kyes, S.; McLean, J.; Moule, S.; Mungall, K.; Murphy, L.; Oliver, K.; Quail, M. A.; Rajandream, M.-A.; Rutter, S.; Skelton, J.; Squares, R.; Squares, S.; Sulston, J. E.; Whitehead, S.; Woodward, J. R.; Newbold, C.; Barrell, B. G. The Complete Nucleotide Sequence of Chromosome 3 of *Plasmodium falciparum*. *Nature* 1999, 400 (6744), 532–538. https://doi.org/10.1038/22964.

(326) Carucci, D. J.; Gardner, M. J.; Tettelin, H.; Cummings, L. M.; Smith, H. O.; Adams, M. D.; Hoffman, S. L.; Venter, J. C. The Malaria Genome Sequencing Project. *Expert Rev Mol Med* 1998, 1 (03), 1–9. https://doi.org/10.1017/S146239949800012X.

(327) Ng, C. L.; Fidock, D. A. *Plasmodium falciparum* In Vitro Drug Resistance Selections and Gene Editing. In Methods Mol Biol; *Humana Press Inc*., 2019; Vol. 2013, pp 123–140. https://doi.org/10.1007/978-1-4939-9550-9_9.

(328) Schenk, M.; König, N.; Hey-Hawkins, E.; Beck-Sickinger, A. G. Illuminating the Path to Enhanced Bioimaging by Phosphole-based Fluorophores. ChemBioChem 2024, 25 (5). https://doi.org/10.1002/cbic.202300857.

(329) Cowman, A. F. Mechanisms of Drug Resistance in Malaria. *Aust N Z J Med* 1995, 25 (6), 837–844. https://doi.org/10.1111/j.1445-5994.1995.tb02889.x.

(330) Duffey, M.; Blasco, B.; Burrows, J. N.; Wells, T. N. C.; Fidock, D. A.; Leroy, D. Assessing Risks of *Plasmodium falciparum* Resistance to Select Next-Generation Antimalarials. *Trends Parasitol*. Elsevier Ltd August 1, 2021, pp 709–721. https://doi.org/10.1016/j.pt.2021.04.006.

(331) Macedo-Silva, T.; Desai, S. A.; Wunderlich, G. Improved *Plasmodium falciparum* Dilution Cloning through Efficient Quantification of Parasite Numbers and C-SNARF Detection. *Malar J* 2021, 20 (1). https://doi.org/10.1186/s12936-021-03816-w.

(332) Viti, A.; Terzi, A.; Bertolaccini, L. A Practical Overview on Probability Distributions. *J Thorac Dis* 2015, 7 (3), E7–E10. https://doi.org/10.3978/j.issn.2072-1439.2015.01.37.

(333) Chavchich, M.; Gerena, L.; Peters, J.; Chen, N.; Cheng, Q.; Kyle, D. E. Role of Pfmdr1 Amplification and Expression in Induction of Resistance to Artemisinin Derivatives in *Plasmodium falciparum*. *Antimicrob Agents Chemother* 2010, 54 (6), 2455–2464. https://doi.org/10.1128/AAC.00947-09.

(334) Gil, J. P.; Krishna, S. Pfmdr1 (*Plasmodium falciparum* Multidrug Drug Resistance Gene 1): A Pivotal Factor in Malaria Resistance to Artemisinin Combination Therapies. *Expert Review of Anti-Infective Therapy*. Taylor and Francis Ltd June 3, 2017, pp 527–543. https://doi.org/10.1080/14787210.2017.1313703.

(335) Wurtz, N.; Fall, B.; Pascual, A.; Fall, M.; Baret, E.; Camara, C.; Nakoulima, A.; Diatta, B.; Fall, K. B.; Mbaye, P. S.; Diémé, Y.; Bercion, R.; Wade, B.; Pradines, B. Role of Pfmdr1 in In Vitro *Plasmodium falciparum* Susceptibility to Chloroquine, Quinine, Monodesethylamodiaquine, Mefloquine, Lumefantrine, and Dihydroartemisinin. *Antimicrob Agents Chemother* 2014, 58 (12), 7032–7040. https://doi.org/10.1128/AAC.03494-14.

(336) Pickard, A. L.; Wongsrichanalai, C.; Purfield, A.; Kamwendo, D.; Emery, K.; Zalewski, C.; Kawamoto, F.; Miller, R. S.; Meshnick, S. R. Resistance to Antimalarials in Southeast Asia and Genetic Polymorphisms in Pfmdr1. *Antimicrob Agents Chemother* 2003, 47 (8), 2418–2423. https://doi.org/10.1128/AAC.47.8.2418-2423.2003.

(337) Adamu, A.; Jada, M. S.; Haruna, H. M. S.; Yakubu, B. O.; Ibrahim, M. A.; Balogun, E. O.; Sakura, T.; Inaoka, D. K.; Kita, K.; Hirayama, K.; Culleton, R.; Shuaibu, M. N. *Plasmodium falciparum* Multidrug Resistance Gene-1 Polymorphisms in Northern Nigeria: Implications for the Continued Use of Artemether-Lumefantrine in the Region. *Malar J* 2020, 19 (1), 439–449. https://doi.org/10.1186/s12936-020-03506-z.

(338) Price, R. N.; Uhlemann, A. C.; Brockman, A.; McGready, R.; Ashley, E.; Phaipun, L.; Patel, R.; Laing, K.; Looareesuwan, S.; White, N. J.; Nosten, F.; Krishna, S. Mefloquine Resistance in *Plasmodium falciparum* and Increased Pfmdr1 Gene Copy Number. *Lancet* 2004, 364 (9432), 438–447. https://doi.org/10.1016/S0140-6736(04)16767-6.

(339) Borges, S.; Cravo, P.; Creasey, A.; Fawcett, R.; Modrzynska, K.; Rodrigues, L.; Martinelli, A.; Hunt, P. Genomewide Scan Reveals Amplification of Mdr1 as a Common Denominator of Resistance to Mefloquine, Lumefantrine, and Artemisinin in *Plasmodium chabaudi* Malaria Parasites. *Antimicrob Agents Chemother* 2011, 55 (10), 4858–4865. https://doi.org/10.1128/AAC.01748-10.

(340) Shafik, S. H.; Richards, S. N.; Corry, B.; Martin, R. E. Mechanistic Basis for Multidrug Resistance and Collateral Drug Sensitivity Conferred to the Malaria Parasite by Polymorphisms in PfMDR1 and PfCRT. *PLoS Biol* 2022, *20* (5), e3001616. https://doi.org/10.1371/journal.pbio.3001616.

(341) Soldati, D.; Foth, B. J.; Cowman, A. F. Molecular and Functional Aspects of Parasite Invasion. *Trends Parasitol*. December 2004, pp 567–574. https://doi.org/10.1016/j.pt.2004.09.009.

(342) Aikawa, M.; Miller, L. H.; Rabbege, J. R.; Epstein, N. Freeze-Fracture Study on the Erythrocyte Membrane during Malarial Parasite Invasion materials and methods. *J Cell Biol* 1981, 91, 55–62.

(343) Gao, H.; Yang, Z.; Wang, X.; Qian, P.; Hong, R.; Chen, X.; Su, X. zhuan; Cui, H.; Yuan, J. ISP1-Anchored Polarization of GCβ/CDC50A Complex Initiates Malaria Ookinete Gliding Motility. *Curr Biol* 2018, 28 (17), 2763–2776. https://doi.org/10.1016/j.cub.2018.06.069.

(344) Zeeshan, M.; Rashpa, R.; Ferguson, D. J. P.; Abel, S.; Chahine, Z.; Brady, D.; Vaughan, S.; Moores, C. A.; Le Roch, K. G.; Brochet, M.; Holder, A. A.; Tewari, R. Genome-Wide Functional Analysis Reveals Key Roles for Kinesins in the Mammalian and Mosquito Stages of the Malaria Parasite Life Cycle. *PLoS Biol* 2022, 20 (7), e3001704. https://doi.org/10.1371/journal.pbio.3001704.

(345) Tolić, I. M. Mitotic Spindle: Kinetochore Fibers Hold on Tight to Interpolar Bundles. *Eur Biophys J*. Springer Verlag April 1, 2018, pp 191–203. https://doi.org/10.1007/s00249-017-1244-4.

(346) Liu, T.; Shilliday, F.; Cook, A. D.; Zeeshan, M.; Brady, D.; Tewari, R.; Sutherland, C. J.; Roberts, A. J.; Moores, C. A. Mechanochemical Tuning of a Kinesin Motor Essential for Malaria Parasite Transmission. *Nat Commun* 2022, 13 (1), 6988–7004. https://doi.org/10.1038/s41467-022-34710-x.

(347) Lorusso, P. M.; Goncalves, P. H.; Casetta, L.; Carter, J. A.; Litwiler, K.; Roseberry, D.; Rush, S.; Schreiber, J.; Simmons, H. M.; Ptaszynski, M.; Sausville, E. A. First-in-Human Phase 1 Study of Filanesib (ARRY-520), a Kinesin Spindle Protein Inhibitor, in Patients with Advanced Solid Tumors. *Invest New Drug J* 2015, 33 (2), 440–449. https://doi.org/10.1007/s10637-015-0211-0.

(348) Marconi, G. D.; Carradori, S.; Ricci, A.; Guglielmi, P.; Cataldi, A.; Zara, S. Kinesin Eg5 Targeting Inhibitors as a New Strategy for Gastric Adenocarcinoma Treatment. *Molecules* 2019, 24 (21), 3948–3961. https://doi.org/10.3390/molecules24213948.

(349) Sakowicz, R.; Finer, J. T.; Beraud, C.; Crompton, A.; Lewis, E.; Fritsch, A.; Lee, Y.; Mak, J.; Moody, R.; Turincio, R.; Chabala, J. C.; Gonzales, P.; Roth, S.; Weitman, S.; Wood, K. W. Antitumor Activity of a Kinesin Inhibitor. *Cancer Res* 2004, 64, 3276–3280.

(350) Blagden, S. P.; Molife, L. R.; Seebaran, A.; Payne, M.; Reid, A. H. M.; Protheroe, A. S.; Vasist, L. S.; Williams, D. D.; Bowen, C.; Kathman, S. J.; Hodge, J. P.; Dar, M. M.; De

Bono, J. S.; Middleton, M. R. A Phase I Trial of Ispinesib, a Kinesin Spindle Protein Inhibitor, with Docetaxel in Patients with Advanced Solid Tumours. *Br J Cancer* 2008, 98 (5), 894–899. https://doi.org/10.1038/sj.bjc.6604264.

(351) Siddik, Z. H. Cisplatin: Mode of Cytotoxic Action and Molecular Basis of Resistance. *Oncogene* 2003, 22 (6), 7265–7279. https://doi.org/10.1038/sj.onc.1206933.

(352) Fanning, J.; Biddle, W. C.; Goldrosen, M.; Crickard, K.; Crickard, U.; Piver, M. S.; Foon, K. A. Comparison of Cisplatin and Carboplatin Cytotoxicity in Human Ovarian Cancer Cell Lines Using the MTT Assay. *Gynecol Oncol* 1990, 39 (2), 119–122. https://doi.org/10.1016/0090-8258(90)90416-i.

(353) Haas, K. L.; Franz, K. J. Application of Metal Coordination Chemistry to Explore and Manipulate Cell Biology. *Chem Rev* 2009, 109 (10), 4921–4960. https://doi.org/10.1021/cr900134a.

(354) Xia, Z.; Smith, C. D. Efficient Synthesis of a Fluorescent Farnesylated Ras Peptide. *J Org Chem* 2001, 66 (15), 5241–5244. https://doi.org/10.1021/jo015526w.

(355) Horinouchi, T.; Nakagawa, H.; Suzuki, T.; Fukuhara, K.; Miyata, N. A Novel Mitochondria-Localizing Nitrobenzene Derivative as a Donor for Photo-Uncaging of Nitric Oxide. *Bioorg Med Chem Lett* 2011, 21 (7), 2000–2002. https://doi.org/10.1016/j.bmcl.2011.02.027.

(356) Yap, J. L.; Wang, H.; Hu, A.; Chauhan, J.; Jung, K.-Y.; Gharavi, R. B.; Prochownik, E. V.; Fletcher, S. Pharmacophore Identification of C-Myc Inhibitor 10074-G5. *Bioorg Med Chem Lett* 2013, 23 (1), 370–374. https://doi.org/10.1016/j.bmcl.2012.10.013.

(357) Abney, K. K.; Ramos-Hunter, S. J.; Romaine, I. M.; Goodwin, J. S.; Sulikowski, G. A.; Weaver, C. D. Selective Activation of N,N'-Diacyl Rhodamine Pro-Fluorophores Paired with Releasing Enzyme, Porcine Liver Esterase (PLE). *Chemistry* 2018, 24 (36), 8985–8988. https://doi.org/10.1002/chem.201801409.

(358) Woodcock, J. W.; Sheridan, R. J.; Beams, R.; Stranick, S. J.; Mitchell, W. F.; Brinson, L. C.; Gudapati, V.; Hartman, D.; Vaidya, A.; Gilman, J. W.; Holmes, G. A. Damage Sensing Using a Mechanophore Crosslinked Epoxy Resin in Single-Fiber Composites. *Compos Sci Technol* 2020, 192, 108074. https://doi.org/10.1016/j.compscitech.2020.108074.

(359) Ke, H.; Sigala, P. A.; Miura, K.; Morrisey, J. M.; Mather, M. W.; Crowley, J. R.; Henderson, J. P.; Goldberg, D. E.; Long, C. A.; Vaidya, A. B. The Heme Biosynthesis

Pathway Is Essential for *Plasmodium falciparum* Development in Mosquito Stage but Not in Blood Stages. *J Biol Chem* 2014, 289 (50), 34827–34837. https://doi.org/10.1074/jbc.M114.615831.

(360) Remcho, T. P.; Guggilapu, S. D.; Cruz, P.; Nardone, G. A.; Heffernan, G.; O'Connor, R. D.; Bewley, C. A.; Wellems, T. E.; Lane, K. D. Regioisomerization of Antimalarial Drug WR99210 Explains the Inactivity of a Commercial Stock. *Antimicrob Agents Chemother* 2020, 65 (1). https://doi.org/10.1128/AAC.01385-20.

(361) Aragoni, M. C.; Podda, E.; Caria, V.; Carta, S. A.; Cherchi, M. F.; Lippolis, V.; Murgia, S.; Orrù, G.; Pippia, G.; Scano, A.; Slawin, A. M. Z.; Woollins, J. D.; Pintus, A.; Arca, M. [AuIII(N^N)Br2](PF6): A Class of Antibacterial and Antibiofilm Complexes (N^N = 2,2′-Bipyridine and 1,10-Phenanthroline Derivatives). *Inorg Chem* 2023, 62 (6), 2924–2933. https://doi.org/10.1021/acs.inorgchem.2c04410.

(362) Gonzalez, F. S.; Mateo, F. H.; Jaramillo, J. L.; Sanfrutos, J. M.; Munoz, M. O. Compound for Labelling Biomolecules Based on Vinylsulphone, *Preparation and Uses*. WO2009144344A2, 2009. patents.google.com/patent/WO2009144344A2 (accessed 2024-02-14).

(363) Gruzdev, M. S.; Chervonova, U. V.; Sorokina, I. A.; Ksenofontov, A. A.; Alexandrov, A. I.; Pashkova, T. V. Synthesis and Emissive Properties of Bi-Directed Azomethine Iron(III) Complexes Based on Salicylidene-4-Biphenylcarboxylic Acid. *J Mol Struct* 2019, 1176, 529–537. https://doi.org/10.1016/j.molstruc.2018.09.005.

(364) Lambros, C. and Vanderberg, J.P. Synchronization of Plasmodium falciparum Erythrocytic Stages in Culture. *J Parasitol* 1979, 65, 418-420. http://dx.doi.org/10.2307/3280287.

(365) Reader, J.; Botha, M.; Theron, A.; Lauterbach, S. B.; Rossouw, C.; Engelbrecht, D.; Wepener, M.; Smit, A.; Leroy, D.; Mancama, D.; Coetzer, T. L.; Birkholtz, L. M. Nowhere to Hide: Interrogating Different Metabolic Parameters of *Plasmodium falciparum* Gametocytes in a Transmission Blocking Drug Discovery Pipeline towards Malaria Elimination. *Malar J* 2015, 14 (1). https://doi.org/10.1186/s12936-015-0718-z.

(366) Reader, J.; van der Watt, M. E.; Birkholtz, L.-M. Streamlined and Robust Stage-Specific Profiling of Gametocytocidal Compounds Against *Plasmodium falciparum*. *Front Cell Infect Microbiol* 2022, 12. https://doi.org/10.3389/fcimb.2022.926460.

(367) Zhou, L.; Yang, L.; Tilton, S.; Wang, J. Development of a High Throughput Equilibrium Solubility Assay Using Miniaturized Shake-Flask Method in Early Drug Discovery. J Pharm Sci 2007, 96 (11), 3052–3071. https://doi.org/10.1002/jps.20913.

(368) Le Manach, C.; Dam, J.; Woodland, J. G.; Kaur, G.; Khonde, L. P.; Brunschwig, C.; Njoroge, M.; Wicht, K. J.; Horatscheck, A.; Paquet, T.; Boyle, G. A.; Gibhard, L.; Taylor, D.; Lawrence, N.; Yeo, T.; Mok, S.; Eastman, R. T.; Dorjsuren, D.; Talley, D. C.; Guo, H.; Simeonov, A.; Reader, J.; Van Der Watt, M.; Erlank, E.; Venter, N.; Zawada, J. W.; Aswat, A.; Nardini, L.; Coetzer, T. L.; Lauterbach, S. B.; Bezuidenhout, B. C.; Theron, A.; Mancama, D.; Koekemoer, L. L.; Birkholtz, L. M.; Wittlin, S.; Delves, M.; Ottilie, S.; Winzeler, E. A.; Smith, D.; Fidock, D. A.; Street, L. J.; Basarab, G. S.; Duffy, J.; Chibale, K. Identification and Profiling of a Novel Diazaspiro[3.4]Octane Chemical Series Active against Multiple Stages of the Human Malaria Parasite *Plasmodium falciparum* and Optimization Efforts. *J Med Chem* 2021, 64 (4), 2291–2309. https://doi.org/10.1021/acs.jmedchem.1c00034.

(369) Combrinck, J. M.; Fong, K. Y.; Gibhard, L.; Smith, P. J.; Wright, D. W.; Egan, T. J. Optimization of a Multi-Well Colorimetric Assay to Determine Haem Species in *Plasmodium falciparum* in the Presence of Anti-Malarials. *Malar J* 2015, 14 (1), 253. https://doi.org/10.1186/s12936-015-0729-9.

(370) Kuhn, Y.; Rohrbach, P.; Lanzer, M. Quantitative PH Measurements in *Plasmodium falciparum*-Infected Erythrocytes Using PHluorin. *Cell Microbiol* 2007, 9 (4), 1004–1013. https://doi.org/10.1111/j.1462-5822.2006.00847.x